



National Library
of Canada

Bibliothèque nationale
du Canada

Canadian Theses Service

Service des thèses canadiennes

Ottawa, Canada
K1A 0N4

NOTICE

The quality of this microform is heavily dependent upon the quality of the original thesis submitted for microfilming. Every effort has been made to ensure the highest quality of reproduction possible.

If pages are missing, contact the university which granted the degree.

Some pages may have indistinct print especially if the original pages were typed with a poor typewriter ribbon or if the university sent us an inferior photocopy.

Previously copyrighted materials (journal articles, published tests, etc.) are not filmed.

Reproduction in full or in part of this microform is governed by the Canadian Copyright Act, R.S.C. 1970, c. C-30.

AVIS

La qualité de cette microforme dépend grandement de la qualité de la thèse soumise au microfilmage. Nous avons tout fait pour assurer une qualité supérieure de reproduction.

S'il manque des pages, veuillez communiquer avec l'université qui a conféré le grade.

La qualité d'impression de certaines pages peut laisser à désirer, surtout si les pages originales ont été dactylographiées à l'aide d'un ruban usé ou si l'université nous a fait parvenir une photocopie de qualité inférieure.

Les documents qui font déjà l'objet d'un droit d'auteur (articles de revue, tests publiés, etc.) ne sont pas microfilmés.

La reproduction, même partielle, de cette microforme est soumise à la Loi canadienne sur le droit d'auteur, SRC 1970, c. C-30.

**Elasto-Plastic Two Surface Soil Model
and its Finite Element
Formulation and Application**

Vladimir Gocevski

**A Thesis
in
The Faculty
of
Engineering**

**Presented in Partial Fulfillment of the Requirements
for the degree of Doctor of Philosophy at
Concordia University
Montréal, Québec, Canada**

**November 1984
© Vladimir Gocevski 1984**

Permission has been granted to the National Library of Canada to microfilm this thesis and to lend or sell copies of the film.

The author (copyright owner) has reserved other publication rights, and neither the thesis nor extensive extracts from it may be printed or otherwise reproduced without his/her written permission.

L'autorisation a été accordée à la Bibliothèque nationale du Canada de microfilmer cette thèse et de prêter ou de vendre des exemplaires du film.

L'auteur (titulaire du droit d'auteur) se réserve les autres droits de publication; ni la thèse ni de longs extraits de celle-ci ne doivent être imprimés ou autrement reproduits sans son autorisation écrite.

ISBN 0-315-41593-2


ABSTRACT

**Elasto-Plastic Two Surface Soil Model and its
Finite Element Formulation and Application**

Vladimir Gocevski, Ph.D.
Concordia University, 1984

This study formulates elasto-plastic constitutive relations for weakly naturally or artificially cemented soil deposits. For vanishing cohesion the model proves to be applicable for both loose and dense states of packing of a pure sand. It is based on the theory of bounding surface plasticity employing an isotropic-kinematic hardening rule. It incorporates a non-associated flow rule and the concept of reflected plastic potential surface. The predicted soil behavior is then compared with observed response from drained and undrained tests under monotonic and cyclic loading programs.

Quadrilateral parabolic isoparametric finite element using the derived constitutive relations is formulated and incorporated in a general purpose computer program MIXDYN. The model is then employed for the analysis of a footing on sand and an earth dam during construction. In the case of the footing analysis the obtained results are compared with those from an experiment and another analytical procedure, whereas, for the dam problem the comparison is made only with a nonlinear-elastic finite element procedure.



The applicability of the proposed model in solving complex engineering problems is evaluated by analysis of problems of static elasto-plastic soil-structure interaction. The analysis of a mat foundation of an eight story building founded on clay-silt is presented first, and results are compared with those obtained by conventional methods and other finite element methods.

The behavior of a concrete gravity dam founded on "soft" foundation medium is analysed next. The influence of a cyclic load due to the water fluctuation in the reservoir on the overall deformations of the dam and soil plastification is further examined.

Moreover, for each of the above mentioned structures the effects of an elasto-plastic soil on the structural behavior is discussed in detail. The influence of various important parameters in the performed analyses is also discussed.

ACKNOWLEDGEMENTS

The author wishes to thank his supervisor, Professor O.A. Pekau for his guidance during the development of this thesis.

Special thanks are extended to Dr. H.B. Poorooshasb and Dr. S. Pietruszczak for their guidance and advice in development of Chapter II, and to Mr. A. Lee for taking the time to edit part of the thesis.

The author is grateful to the software group of Concordia University Computer Center for their help and use of the computing facilities.

Thanks are also due to Miss. L. Giguere for typing the thesis.

Many thanks to Vesna and Irena whose patience and understanding extend far beyond what one would expect.

This work was supported by the National Research Council of Canada under Grant No. A8258.

TABLE OF CONTENTS

	<u>Page</u>
ABSTRACT	(i)
ACKNOWLEDGEMENTS	(iii)
TABLE OF CONTENTS	(iv)
ENGLISH-INTERNATIONAL SYSTEM (SI) CONVERSIONS	(vi)
LIST OF TABLES	(vii)
LIST OF FIGURES	(viii)
LIST OF SYMBOLS	(xiv)
 CHAPTER I - INTRODUCTION	
1.1 General	1
1.2 Review of Previous Work	3
1.2.1 Soil Modeling	4
1.2.2 Numerical Techniques	10
1.2.3 Application to Engineering Problems	12
1.2.4 Need for Further Work	17
1.3 Scope of the Present Study	18
1.4 Organisation of Thesis	19
 CHAPTER II - FORMULATION OF AN ELASTO-PLASTIC WORK-HARDENING MODEL FOR GRANULAR SOIL WITH COHESION	
2.1 Introduction	21
2.2 Formulation of the Constitutive Law	24
2.2.1 Conceptual Baseline	24
2.2.2 Mathematical Formulation	25
2.2.3 Relation to the Work by Poorooshasb and Pietruszczak	41
2.3 Numerical Examples	43
2.3.1 General Procedure for Evaluation of Parameters Required by the Model	43
2.3.2 Monotonic Loading	46
2.3.2.1 Comparison with Experimental Results	46
2.3.2.2 Parametric Study	49

TABLE OF CONTENTS (Cont'd)

CHAPTER II. - (Cont'd) page	<u>Page</u>
2.3.3 Reversal Loading	53
2.3.3.1 Comparison with Experimental Results	53
2.3.3.2 Parametric Study	54
2.4. Concluding Remarks	55
 CHAPTER III - FINITE ELEMENT FORMULATION	
3.1. Introduction	82
3.2. Review of Finite Element Analysis	83
3.2.1 Formulation of the Element-stiffness Matrix	83
3.2.2 Numerical Procedure	88
3.3. Implementation of the Developed Finite Element to Computer Program MIXDYN	90
3.3.1 Features of the program MIXDYN	90
3.3.2 Implementation of the Element	91
3.4. Evaluation of Soil Parameters	93
3.4.1 Description of Required Parameters	93
3.4.2 Tests for Soil Properties	94
3.4.3 Procedure for Evaluation Model Parameters	96
 CHAPTER IV - VERIFICATION OF THE MODEL; SOLUTION TO CHOSEN PROBLEMS RELATED TO GEOMECHANICS	
4.1. Introduction	103
4.2. Footing on Sand	106
4.3. Analysis of Earth Dam During Construction	109
4.4. Conclusions	115
 CHAPTER V - MODELING OF NONLINEAR SOIL-STRUCTURE INTERACTION PROBLEMS	
5.1. Introduction	144
5.2. Mat Foundation on Clayey-Silt	144
5.3. Concrete Gravity Dam on Elasto-Plastic Soil	150
5.3.1 Construction Stresses and Deformations	152
5.3.2 Effect of Water Fluctuation and Uplift Pressure	152
5.4. Conclusions	155
 CHAPTER VI - SUMMARY AND CONCLUSIONS	
6.1. Recommendations for Future Study	187
REFERENCES	192
APPENDIX A - Listing of the Modified Subroutine RESEPL	194
APPENDIX B - Input for Material Parameters	204
	210

ENGLISH - INTERNATIONAL SYSTEM (SI)

CONVERSION FACTORS

This list below gives the conversion factors for all Imperial units used in this study.

<u>TO CONVERT</u>	<u>TO</u>	<u>MULTIPLY BY</u>
inches (in.)	millimetres (mm)	25.4
feet (ft)	meters (m)	0.3048
square inches (sq. in)	square millimetres (mm ²)	645.16
square feet (sq. ft)	square meters (m ²)	0.0929
pound-force (lbf)	newton (N)	4.4482
kip (k)	newton (N)	4448.2
pound-force-inch (lbf-in.)	newton-metre (Nm)	0.1130
pound-force-foot (lbf-ft)	newton-metre (Nm)	1.3558
kip/inch (k/in)	kilonewton/metre (KN/m)	175.1
pound-force/square inch (psi)	newton/square metre (N/m ²)	6895

LIST OF TABLES

	<u>Page</u>
Table 2-I: Values of parameters for proposed elasto-plastic model for weakly naturally cemented sands.	57
Table 2-II: Values of parameters for proposed elasto-plastic model for artificially cemented sands with 2% cement and relative density of 74%.	57
Table 2-III: Values of parameters for proposed elasto-plastic model for artificially cemented sands with 5% cement and 100% Maximum Proctor Density.	58
Table 2-IV: Values of parameters for proposed elasto-plastic model for pure sand of Ref. 2.20.	58
Table 2-V: Values of parameters for proposed elasto-plastic model for pure sand of Ref. 2.21.	59
Table 4-I(a): Values of parameters used in the nonlinear-elastic analysis of the footing.	119
Table 4-I(b): Values of parameters for proposed elasto-plastic model in the footing analysis.	119
Table 4-II(a): Values of stress-strain parameters for nonlinear elastic analysis of the earth dam.	120
Table 4-II(b): Values of parameters for elasto-plastic analysis of the earth dam.	120
Table 5-I: Values of parameters for (a) conventional methods and nonlinear FE analysis (b) proposed elasto-plastic analysis for the mat foundation.	160
Table 5-II: Values of parameters for elasto-plastic analysis of the concrete gravity dam.	161

LIST OF FIGURES

	<u>Page</u>
Fig. 2.1:	The yield and the bounding surface in principal stress space. 60
Fig. 2.2:	(a) The bounding $F=0$, the plastic potential $\phi=0$ surfaces, and (b) the location of the conjugate and datum stress points in the meridional plane $(q/g(\theta), p)$. 61
Fig. 2.3:	Comparison of model behavior with experimental data for naturally weakly cemented sand, (a) stress difference versus axial strain, (b) volumetric versus axial strain. 62
Fig. 2.4:	Comparison of model behavior with experimental data; Artificially cemented sand with 2% cement at 74% relative density, (a) stress difference versus axial strain, (b) volumetric versus axial strain. 63
Fig. 2.5:	Comparison of model behavior with experimental data; Artificially cemented sand with 5% cement at 100% Proctor Density. 64
Fig. 2.6:	Comparison of model behavior with experimental data on loose sand; (a) effective stress paths (b) stress difference versus axial strain for the stress paths in (a). 65
Fig. 2.7:	Influence of the cohesion on drained material behavior at different confining pressure for, (a) naturally cemented sand with 2% cement (Ref. 2.3) 66
Fig. 2.8:	Influence of cohesion on drained behavior of artificially cemented sand with 5% cement at different confining pressures. 67
Fig. 2.9:	Influence of cohesion on the response under undrained constraint of loose sand at initial confining pressure of 275 kPa (Ref. 2.20), (a) Effective stress paths, (b) stress difference versus axial strain for the stress paths in (a). 68
Fig. 2.10:	Influence of cohesion on the response under undrained constraint of loose sand (Ref. 2.20) at initial confining pressure of 550 kPa (a) Effective stress paths, (b) stress difference versus axial strain for the stress paths in (a). 69

LIST OF FIGURES(cont'd)

	<u>Page</u>	
Fig. 2.11:	Influence of the parameter m_c on the prediction of drained behavior of, (a) and (b) artificially cemented sand 2%, (c) and (d) naturally cemented sand (Ref. 2.3).	70
Fig. 2.12:	Influence of m_c on the effective stress paths of undrained behavior of sand (Ref. 2.20) with added cohesion $c=40$ kPa and initial confining pressure, (a) 275 kPa, (b) 550 kPa.	71
Fig. 2.13:	Influence of the bulk modulus on the prediction of drained behavior of; (a) and (b) artificially cemented sand with 2% cement; (c) and (d) naturally cemented sand (Ref. 2.3).	72
Fig. 2.14:	Influence of the bulk modulus on the predictions of undrained behavior of loose sand (Ref. 2.20) with added cohesion $c=40$ kPa and initial confining pressure of 275 kPa, strain for the stress paths in (a).	73
Fig. 2.15:	Influence of the bulk modulus on the prediction of undrained behavior of loose sand (Ref. 2.20) with added cohesion $c=40$ kPa and initial confining pressure of 550 kPa (a) Effective stress paths, (b) stress difference versus axial strain for the stress paths in (a).	74
Fig. 2.16:	Influence of the hardening parameter A on drained behavior of, (a) and (b) naturally cemented sand, (c) and (d) artificially cemented sand; both at initial confining pressure of 207 kPa.	75
Fig. 2.17:	Effective stress path for strain controlled cyclic undrained test; Effective stress paths for shear modulus. (a) $G=160$ kg/cm ² , (b) $G=120$ kg/cm ² ; Stress-strain diagrams, (c) Experiment (Ref. 2.21); (d) Model Simulation for shear modulus $G=120$ kg/cm ² .	76
Fig. 2.18:	Effective stress path for an undrained two-way strain controlled test; on loose and cemented Fuji river sand (Ref. 2.21) for kinematic hardening parameter. $\gamma=2.0$.	77
Fig. 2.19:	Effective stress paths for an undrained two-way strain controlled test; on loose and cemented Fuji river sand (Ref. 2.21), for kinematic hardening parameter. $\gamma=4.0$.	78

LIST OF FIGURES(cont'd)

	<u>Page</u>	
Fig. 2.20:	Effective stress paths for an undrained two-way strain controlled test on loose and cemented Fuji river sand (Ref. 2.21) for kinematic hardening parameter $\gamma=8.0$.	79
Fig. 2.21:	Influence of the bulk modulus on the effective stress path on cemented Fuji river sand (Ref. 2.21), with assumed cohesion $c=30$ kPa and kinematic hardening parameter $\gamma=4.0$. (a) $G/K=1$; (b) $G/K=0.75$; (c) $G/K=0.5$, and (d) $G/K=0.33$.	80
Fig. 2.22:	Effective stress path for (a) loose sand (Ref.2.20) compressed at virgin loading; (b) loose sand (Ref. 2.20) expands at virgin loading; and stress strain diagram for strain controlled test in (b) for (c) cohesion of $c=0$ kPa; and (d) cohesion of $c=50$ kPa.	81
Fig. 3.1	Overall structure of the computer program MIXDYN (Ref. 1.54) with implemented modifications for the developed finite element.	99
Fig. 3.2	Flow chart for integration of stress histories penetrating the bounding surface.	100
Fig. 3.3:	Evaluation of model parameters, (a) typical results of standard triaxial test at low confining pressure (Test No. B-10 Ref. 3.11), (b) slopes for failure and zero dilatancy lines.	101
Fig. 3.4:	(a) Plots of $q-\epsilon_q$ and $\epsilon_v-\epsilon_q$ required for evaluation of elastic parameters G and K , (b) Plot $m-\epsilon_q^p$ used to evaluate the hardening parameter A .	102
Fig. 4.1:	Finite element mesh of model footing in sand.	121
Fig. 4.2:	Comparison of results for settlement of model footing.	122
Fig. 4.3:	Settlement under model footing for proposed analysis.	123
Fig. 4.4:	Vertical pressures under footing from proposed analysis.	124
Fig. 4.5:	Contours of: (a) minor principal stress (kPa); (b) accumulated plastic strain (%) - vertical footing pressure of 172 kPa.	125

LIST OF FIGURES(cont'd)

	<u>Page</u>
Fig. 4.6:	Effect of cohesion on footing settlement 126
Fig. 4.7:	Model footing on loose sand covered by layer of artificially cemented sand. 127
Fig. 4.8:	Influence of degree of cementation of top layer on settlement of footing. 128
Fig. 4.9:	Embankment structure: (a) dam cross-section with points where comparisons are made; (b) finite element mesh with layers of soil fill during construction. 129
Fig. 4.10:	Settlement at points 1 to 8 of prototype dam after application of construction layers 4(case a) to 8 (case e) and 5 (case a') to 8 (case d'). 130
Fig. 4.11:	Horizontal movement of points 1, 2 and 3 at EL. 0.0 m and different construction stages. 131
Fig. 4.12:	Settlement and horizontal movement at points 1, 2 and 3 for different construction stages from proposed elasto-plastic analysis. 132
Fig. 4.13:	Effects of cohesion c (kPa) on settlement and horizontal movement for elasto-plastic analysis. 133
Fig. 4.14:	Contours of settlements (mm) during construction obtained with: (a) nonlinear elastic analysis; (b) proposed elasto-plastic analysis ($\phi = 43.5^\circ$). 134
Fig. 4.15:	Contours of settlement (mm) if single layer is considered: (a) proposed analysis; (b) nonlinear elastic analysis. 135
Fig. 4.16:	Contours of minor principal stresses (kPa) determined by: (a) nonlinear elastic analysis; (b) proposed analysis. 136
Fig. 4.17:	Contours of major principal stresses (kPa) determined by: (a) nonlinear elastic analysis; (b) proposed analysis. 137
Fig. 4.18:	Principal stresses from: (a) nonlinear analysis; (b) proposed analysis. 138
Fig. 4.19:	Contours of shear stress τ_{xy} (kPa): (a) nonlinear elastic analysis; (b) proposed analysis. 139

LIST OF FIGURES(cont'd)

	<u>Page</u>
Fig. 4.20:	Contours of maximum shear stress (kPa): (a) non-linear elastic analysis; (b) proposed analysis. 140
Fig. 4.21:	(a) Dam cross-section and (b) movement of dam profile with water level at EL. 50.0 m. 141
Fig. 4.22:	Contours of (a) major and (b) minor principal stresses from proposed analysis with water level at EL. 50.0 m. 142
Fig. 4.23:	Contours of maximum shear stress for proposed elastó-plastic analysis. 143
Fig. 5.1:	Building and the mat foundation 162
Fig. 5.2:	Idealisation for FE analysis (a), and discretization of mat and subsoil (b). 163
Fig. 5.3:	Discretization test: (a) contact pressure; (b) bending moment 164
Fig. 5.4:	Comparison with conventional methods: (a) contact pressure; (b) bending moment. 165
Fig. 5.5:	Comparison with other FE analysis: (a) contact pressure; (b) bending moment. 166
Fig. 5.6:	Effect of the initial elastic modulus on: (a) contact pressure; (b) bending moment. 167
Fig. 5.7:	Effect of hardening constant A on: (a) contact pressure; (b) bending moment. 168
Fig. 5.8:	Effect of footing thickness t on: (a) contact pressure (b) bending moment. 169
Fig. 5.9:	Average contact pressure-settlement diagram for load up to local shear failure in the soil. 170
Fig. 5.10:	Concrete gravity dam: (a) dam and subsoil, (b) cross-section dimensions. 171
Fig. 5.11:	(a) Finite element model used in analysis; (b) and (c) assumed water pressure diagrams. 172
Fig. 5.12:	Construction terminated: (a) deformation (b) zones with tensile major principal stresses (kPa). 173

LIST OF FIGURES(cont'd)

	<u>Page</u>
Fig. 5.13:	Construction terminated: (a) contours of minor principal stresses (kPa); (b) contours of accumulated plastic strain (%) corresponding to stresses in (a). 174
Fig. 5.14:	Dam deformation due to first load cycle-water fluctuation 40 m. Uplift pressure with cut-off. 175
Fig. 5.15:	Reservoir filled with water, first cycle: (a) contours of minor principal stresses; (b) contours of vertical stresses. Uplift pressure with cut-off. 176
Fig. 5.16:	Dam deformation due to different water pressures (water fluctuation 20 m): (a) first loading cycle; (b) twelfth load cycle. 177
Fig. 5.17:	Dam deformation at different loading cycles (water fluctuation of 20 m): (a) uplift pressure neglected; (b) uplift pressure with cut-off. 178
Fig. 5.18:	Load-displacement relations for crest (water fluctuation of 20 m): (a) uplift pressure neglected; (b) uplift pressure with cut-off. 179
Fig. 5.19:	Dam displacement at (a) first, (b) fifth and (c) tenth cycles (water fluctuation 40 m). 180
Fig. 5.20:	Cyclic deformation of dam: (a) and (b) load displacement relation for crest (water fluctuation 40 m). Uplift pressure with cut-off. 181
Fig. 5.21:	Contours of minor principal stresses: (a) first load cycle; (b) twelfth load cycle (for water fluctuation 20 m). 182
Fig. 5.22:	Contours of minor principal stresses at twelfth load cycle (water fluctuation of 40 m). 183
Fig. 5.23:	Tension zones in dam (kPa): (a) first load cycle; (b) twelfth load cycle 184
Fig. 5.24:	Contours of maximum shear stresses (kPa): (a) first load cycle; (b) twelfth load cycle. 185
Fig. 5.25:	Contours of accumulated plastic strain (%) corresponding to stresses in Fig. 5.24: (a) first load cycle; (b) twelfth load cycle. 186

LIST OF SYMBOLS

Symbols are defined where they first appear in the text. These symbols which appear often in the text are defined below:

- A = constant for the hardening rule
- B = matrix of the derivatives of the shape functions
- c = cohesion in the soil
- D_{ij} = elastic constitutive matrix
- D^{ep} = elasto-plastic constitutive matrix
- E = modulus of elasticity
- F = bounding surface
- f = inner yield surface
- G = elastic shear modulus
- H_e = elastic hardening parameter
- H_p = plastic hardening parameter
- J_3 = third stress invariant
- \tilde{K} = element stiffness matrix
- h = plastic hardening modulus
- h_e, h_B = values of h_p at yield and bounding surface, respectively.
- K = elastic bulk modulus
- K_B = structural stiffness matrix
- m = slope of state line-bounding surface
- m_c = slope of state line at zero dilatancy
- m_f = slope of state line at failure
- m_o = slope of state line-yield surface
- n_i = vector normal to yield surface
- \bar{n}_i = vector normal to plastic potential surface

- P = stress point on the yield surface
- p = hydrostatic stress axis relative to Σ_1
- p_0 = $p(c, \phi)$
- p' = yield surface hydrostatic axis relative to Σ_1'
- p_c = constant mean effective stress (specifies position of plastic potential surface)
- P = nodal force vector
- q = deviatoric stress axis relative to Σ_1
- q' = yield surface deviatoric stress axis relative to Σ_1'
- R = conjugate point on the boundin surface
- \dot{W} = rate of work performance
- α_1 = unit vector specifying the position of the yield surface
- T_{ij} = transformation tensor between Σ_1, Σ_1'
- γ = kinematic hardening constant
- δ = angle between the stress and the conjugate stress vector
- δ_0 = maximum value of δ
- $\tilde{\delta}$ = nodal displacement vector
- $\epsilon_1, \epsilon_2, \epsilon_3$ = principal strain components
- ϵ_q = distortional strain
- $\dot{\epsilon}$ = distortional strain rate
- ϵ_v (= volumetric strain
- $\dot{\epsilon}_v$ = volumetric strain rate
- $\epsilon_q^p, \epsilon_q^e$ = plastic and elastic components of ϵ_q
- ϵ_1^p = plastic strain vector
- $\epsilon_v^p, \epsilon_v^e$ = plastic and elastic components of ϵ_v
- ϵ_{ijk} = alternating tensor
- $d\epsilon_{ij}$ = total strain increments

- $\dot{\epsilon}_1^p, \dot{\epsilon}_1^e$ = plastic and elastic strain increments
- λ = positive parameter in the flow rule-monotonic loading
- λ_1 = conjugate stress vector
- θ = angle measures the orientation in the π -plane
- ν = Poisson's ratio
- Σ_1, Σ_1^1 = effective stress space sets of axes
- $\sigma_1, \sigma_2, \sigma_3$ = principal effective stress components
- σ_1 = principal stress tensor.
- σ_1^d = location vector for point R on bounding surface
- $\dot{\sigma}_1$ = stress rates
- ϕ = angle of friction for triaxial conditions
- ϕ_f = ultimate internal frictional angle
- ψ = residual force vector
- ψ = plastic potential surface
- $g(\theta)$ = function specifies shape of the π -plane

CHAPTER I

1.0 INTRODUCTION

1.1 GENERAL

Engineering structures often are located in the areas where the foundation medium is not pure sand, gravel or clay but a mixture of minerals of different physical and chemical properties. Naturally cemented sands are found at various places on earth and the cementation is generally attributed to a small amount of agents at the point of contact. Cementation or cementation-like effects can also be produced artificially by a dense packing of sand grains with cement or by a matrix of silt and clay particles.

With the constitutive relations developed to date these types of soils are not modeled to the extent where the more significant aspects in soil behavior such as nonlinearity, inelasticity, shear dilatancy, and path dependency, can be simulated for either monotonic or cyclic loading programs. Therefore, the need for such a model is apparent.

The stress-strain relations for soils, either theoretical or empirical, constitute only one element in the total design procedure that involves analysis, adequate judgement of parameters, quality control, and monitoring of structural performance. The analysis of any continuum mechanics problem requires that the field equations must be solved with respect to the appropriate boundary conditions. Also, in soil mechanics the effects of the initial state of stress and the

stress history of in situ soils have to be considered in a realistic analysis. The finite element method is a well recognised numerical technique able to provide answers to all these questions. Therefore, successful application of any new constitutive law in solution of actual engineering problems is related to its appropriate finite element implementation.

The process of verification of any soil model includes two steps: (a) comparison of the result obtained with appropriate soil tests to demonstrate the validity of the model, and (b) analysis of an actual engineering problem and comparison of results with those obtained by field observation or other reliable analytical techniques. However, the verification of a soil model is not an easy process particularly in the case of cemented sand deposits. Due to the difficulties associated with representative sampling and sample disturbances, results of laboratory tests of cemented sands under monotonic loading are rare. At the present, the test data of cemented sands under cyclic loading conditions is not available. Similar difficulties are encountered when attempting to simulate results of an actual engineering problem published in the literature. The reported soil properties or soil tests of the analysed problem do not usually provide sufficient data for evaluation of the parameters required by the model used in the present study. Therefore, the verification process should include an elaborate parametric study in addition to soil test simulation and analysis of actual engineering problems.

The applicability of a constitutive law and the reliability of a finite element program should be verified by analysing different types of problems. The verification program may include problems related to

geotechnical engineering and soil-structure interaction, in order to show the capabilities and limitations of the model. For instance, a model capable of simulating shear coupling effect of soil is necessary for use in the analysis of embankment structures during construction. This is especially true if the foundation under the embankment is sloping. On the other hand, a model capable of simulating soil plastification due to cyclic loading in the low range of stresses is mandatory in the case of a concrete gravity dam on "soft" foundation, subjected to fluctuation of water in the reservoir. Data obtained from the analysis of these types of structures may demonstrate the necessity of a more elaborate elasto-plastic soil model.

The preceding discussions form the general framework of the present study. An attempt is made to:

- (a) develop an elasto-plastic constitutive law for naturally and artificially cemented sand deposits;
- (b) incorporate the constitutive law into a finite element analysis algorithm;
- (c) verify the correctness of the soil model by means of test simulations and by analyses of real engineering problems;
- and
- (d) investigate the effect of soil plastification on nonlinear soil-structure interaction problems.

1.2 REVIEW OF PREVIOUS WORK

A number of authors have endeavored to present some insight into the real soil behavior. Many different types of soil models have been developed. Some of them were implemented into appropriate numerical

procedures, however, only few of the advanced constitutive laws are applied to the analysis of actual engineering problems.

1.2.1 Soil Modeling

Constitutive laws play a significant role in providing reliable results from any solution procedure. Their importance has been enhanced with the increase in development of many modern computer-based numerical techniques such as finite elements, finite differences and boundary elements. Very often, results from a numerical analysis that may have used a less appropriate constitutive law can be of doubtful validity. Realization of this fact invoked active research and interest in the theoretical formulation of constitutive laws and determination of their parameters.

For a long time, Soil Mechanics has been based on Hooke's law of linear elasticity. In mathematical terms, the minimal requirement for a material to qualify as elastic is that there exists a one-to-one correspondence between stress increment and strain increment. Thus, a body consisting of this material returns to its original state of deformation whenever completely unloaded. The use of linear elasticity laws is restricted to a very limited class of materials and certainly is questionable in the context of geological media.

For soils sustaining proportional loading the modelling via non-linear elasticity can be quite accurate. Non-linear elasticity models are the simplest of all models that can be used for closer representation of geotechnical materials. Two elastic parameters are required to vary with stress and/or strain. This pair can be

chosen arbitrarily out of E , ν , K or G . It is convenient and logical in many instances to use the bulk modulus, K , and shear modulus, G , instead of elastic modulus, E , and Poisson's ratio, ν . The reason for this is that the behaviour of soil under changing confining stress measured by K is quite different from that under distortion measured by G . Furthermore, in isotropic elastic models these two modes are decoupled, i.e., changes in mean stress do not cause distortion nor does deviatoric stress (pure shear) cause volume change. Models of this type have been discussed in numerous papers [1.1 to 1.11].

The most popular models in this category appear to be: bilinear elastic model, K-G model, and hyperbolic model. The bilinear and K-G models are preferred to the hyperbolic on the ground that they are simpler and involve fewer constants in their definition. The bilinear requires only four constants (K_e , G_e , c , ϕ) to be defined as against the five (K , G , α_k , α_g , β_g) for K-G models and nine in the case of the hyperbolic model. However, due to the fact the hyperbolic model was extensively developed by Duncan and his associates [1.11] and successfully tested on numerous practical problems (ex. in the analysis of Oroville Dam, Ref. 1.12), it is very popular. There are serious objections to the use of nonlinear elasticity models.

The main one is that, although consistent in a mechanical sense, they may predict an unrealistic material response for some loading paths, in which case uniqueness in the solution of boundary value problems cannot generally be assured. The formulations based on nonlinear elasticity fail to identify irreversible deformations when

unloading takes place. This can, to some extent, be rectified by introducing loading criteria as in the deformation theory of plasticity. In practical implementations of this theory such a loading condition can be applied only after the solution to a boundary value problem has been obtained.

Thus, some a priori assumptions as to loading and unloading regions have to be made in order to obtain the solution. Moreover, the theory is formulated in such a manner that there is no continuity between elastic and plastic regions for neutral change of stress.

In spite of all these inconsistencies the deformation theory is still a very attractive alternative for the solution of large classes of soil and soil-structure interaction problems. A summary of advantages and limitations of these models is presented in Ref. 1.13.

The flow theory of plasticity represents a necessary and correct extension of elastic stress-strain relations into the plastic range at which permanent plastic strain can be admitted. Perhaps the first reference in the history of plasticity can be attributed to Coulomb (1773), who proposed a yield criterion for soils. Since that time a considerable amount of work has been done in this area, however, a unified flow theory began to evolve only around 1945. A detailed history of this review is provided in the text by Hill [1.14]. In the area of Soil Mechanics early developments were based on elastic-perfectly plastic formulations incorporating Mohr-Coulomb or Drucker-Prager yield criteria together with an associated or non-associated flow rule. In these formulations the yield surface was assumed to

remain stationary and no hardening/softening effects were admitted. A study of strain hardening phenomenon in soils started with the works of Rendulic [1.15] and Hvorslev [1.16]. Subsequently, the findings of both researchers were investigated by Roscoe [1.17, 1.18, 1.19] who proposed a model based on the theory of plasticity incorporating an isotropic hardening rule. The concept developed by Roscoe's group is known in the literature as the Critical State model.

In this concept the evolution of the yield surface is assumed to depend on irreversible void ratio variation which is proportional to the plastic volumetric strain. The model allows for both stable and unstable behavior and assumes the existence of a critical state surface defining an instantaneous locus of elasto-perfectly plastic response combined with no plastic volume change. Several different forms of the yield criterion known as Cam-clay, cap model, etc., have been used so far.

The Critical State concept is applicable to normally consolidated clays subjected to monotonic load. For overconsolidated material the predictions are poor and for sands the concept is virtually not applicable.

An alternative description for simulating sand behaviour is the one in which deviatoric plastic strain is assumed to act as the hardening parameter (Poorooshasb et al. [1.20]). In general, both the volumetric and deviatoric components of plastic strain can act simultaneously as a combined hardening parameter. In this way, for instance, the applicability of the Critical State model can be extended to both overconsolidated clays and dense sands (Nova and Wood-

[1.21], Wilde [1.22]). Finally, in another category of constitutive concepts the multi yield-loci theories are implemented (Porooshab and Young [1.23], Prevost and Hoeg [1.24]). In most of these formulations the mode of yielding is assumed to be governed by two different mechanisms; the first responsible for plastic volumetric strains and the second associated with plastic distortions. Thus, both hardening parameters act independently of each other.

In general, the combined hardening parameter of multi yield-loci theories was intended to improve the accuracy of predictions based on a single hardening parameter. All these concepts are applicable for monotonic loading conditions as they all assume purely elastic behaviour for stress paths penetrating the interior of the yield surface. Recent developments in constitutive modelling based on plasticity have focused mainly on modelling of soil response to fluctuating loading. A very convenient way of formulating such a generalized constitutive law is to extend some of the isotropic hardening descriptions to include the aspect of reverse plastic flow (Pietruszczak and Porooshab [1.25]). A number of existing formulations utilize the isotropic hardening surface as a so-called "bounding surface" (Krieg [1.26], Dafalias and Popov [1.27, 1.28]) and the response of the material during a stress reversal is modelled using isotropic and/or kinematic hardening. Among the formulations maintaining irreversible void ratio variations as the isotropic hardening parameter those due to Dafalias and Herrmann [1.29], Carter et al. [1.30] and Mroz et al. [1.31, 1.32] are noticeable. Bounding surface formulations admitting plastic distortions as the hardening parameter are due to Porooshab, Pietruszczak [1.33] and Ghaboussi,

Momen [1.34]. Finally, Nova and Hueckel [1.35] use a combined deviatoric/volumetric hardening together with a "paraelastic" (i.e., path independent between suitably defined stress reversal points) description for stress reversals.

The theory of plastic flow is, at present, the most extensively used framework for formulating constitutive relations for soils. In 1971 Valanis [1.36] proposed endochronic plasticity as an alternative theory to classical plasticity for the description of rate independent response of the material. The two theories differ in certain important aspects such as:-

- (i) The endochronic theory does not require the concept of the yield surface for its development.
- (ii) The physical assumptions that underline the theory have their origin in irreversible thermodynamics of internal variables.
- (iii) The material memory is defined in terms of an intrinsic time scale which is considered to be a material property.

Since 1971 endochronic plasticity has undergone a significant evolution. The original work by Valanis has been extended by Bazant and Bhat [1.37] for concrete and Bazant and Krizek (1.38) for soils. In general, there are a lot of arguments for and against the validity of endochronic theory. The models involve a large number of material parameters and, at present, are not used extensively.

The response of geological materials is sensitive to the strain rate. Such sensitivity cannot be modelled via plasticity as the governing equations are homogeneous in time. Rate sensitive plastic

material is referred to as a viscoplastic one. Theory of elasto-viscoplasticity has been formulated by Perzyna [1.39] and incorporated into a numerical code by Zienkiewicz and Corneau [1.40]. Other visco-plastic models for geological materials have been discussed by Akai et al. [1.41].

Numerical methods allied to powerful digital computers allow today the possibility of solving almost all well defined physical problems within any accuracy desirable. The finite element process of discretising and approximating continuous problems has proved itself to be one of the most general and useful procedures [1.42]. It is therefore natural to seek solution with this numerical process when analysing behavior of important structures such as dams.

1.2.2 Numerical Techniques

The analysis of continuum structures involves generally differential equations or integral statements for which closed form processes involving discretisation are employed. The finite ~~difference~~ difference process, boundary integral procedures, and trial function methods are three fairly general techniques that exist for such discretisation.

The analysis of the problems chosen in this study may be performed by any of the above numerical techniques. Therefore a short review of the main advantages and limitations of these methods are outlined below.

The finite difference method is a relatively old numerical technique. It was first written in 1872 [1.43] and is well reported in the literature. Only recently [1.44] however it was applied in analysis of complex engineering structures. The main advantage is

found in its generality, however the requirements for relatively regular mesh pattern, and the difficulty in introducing boundary conditions in the local differential equations governing the problem, are considered as limitations.

The "boundary integral procedure" is considered as a mathematically favorable method. Its use in stress analysis however is not extensive [1.45, 1.46, 1.47]. Similar difficulties as in the case of the finite difference method, related to the geometry of the boundaries are encountered here also. The analysis becomes very complex for situations other than linear and homogeneous.

The finite element method in its classical form appeared first at the beginning of this century as the Rayleigh-Ritz procedure, or Galerkin method [1.48, 1.49]. From energy or virtual work principles a global integral statement related to the analysed problem is defined first. For the domain of interest unknown functions are assumed. The functions are such that they approximately satisfy the interior as well as the boundary conditions. The concept of finite elements employed today is relatively new [1.50]. In this new concept the medium is discretized into finite elements and the trial functions are specified locally. The advantage of this is seen in the evaluation of properties on the element level only, and in the replacement of a global integral statement with a system of algebraic equations following the rules of structural assembly.

Different forms of elements are used in the finite element procedure. The particularity of the problem dictates which type of element will be employed. For the problems related to geotechnical

engineering probably the most efficient of the elements currently in use are the isoparametric parabolic elements [1.41, 1.51, 1.52]. Accompanied by the elaborate constitutive relations closely describing the elasto-plastic nature of the soil behavior these elements provide the possibility of accurately solving almost all well defined problems in geotechnical engineering.

A limited number of advanced constitutive relations for soil have been implemented in the development of new finite elements. A literature survey [1.13, 1.53] shows that only a few of them are included as part of a general purpose finite element program. The results of these implemented models generally indicate good agreement with experiments. However, the use of these models in engineering practice is limited. This can be due to either of the problems analysed, which were designed for simulation of triaxial tests, small-scale tests of a footing on soil, or passive pressure on a vertical plate.

Extensive work in the direction of implementing elasto-plastic constitutive relations in a finite element algorithm was performed at University College, Swansea. The algorithms of the program "MIXDYN" ("Finite Elements in Plasticity" [1.54], Critical State Model, Infinite Number of Surfaces Model, etc. were formulated by Zienkiewicz, Naylor, Tabb, Pande, Pietruszczak, Paul, and Simpson [1.53]).

1.2.3 Application to Engineering Problems

The usefulness of a soil model can be assessed by its applicability to actual engineering problems. In classical soil

mechanics, the problems of deformation and stability are treated separately. Past experience demonstrates that the treatments are in general satisfactory. However, the behavior of soil as structural material or as a foundation medium is a continuous process and therefore the deformation and stability problems cannot be treated separately. In classical soil mechanics the achievement of a high safety factor does not eliminate the possibility of local yielding, or the state of collapse does not automatically demonstrate that failure occurred in all soil elements. The application of an appropriate deformation analysis is hence a logical approach for evaluation of stresses in all loading stages prior to instability. The integral analysis of deformation and stability forms part of the non-classical or modern soil mechanics. It requires a constitutive relationship suitable for modelling a correct stress-strain behavior, necessary for a fundamental understanding of the mechanical behavior of soils.

There is no single constitutive law which describes adequately all features of soil behavior. When compared to other engineering materials even under controlled laboratory conditions the behavior of soil is extremely complex. Consequently, the application of the constitutive laws which aim to model most aspects of soil behavior for actual engineering structures is difficult. Despite these facts, the need of a more detailed soil model for analysis is apparent in the study of (among others) the following engineering problems: (a) mat foundation under a highrise building, (b) embankment structures during and after construction, and (c) concrete gravity dam on a "soft" foundation medium.

Mat Foundations

A mat or raft foundation is a large concrete slab and usually supports the entire structure. Like other types of foundations it must satisfy the following basic requirements: it must have a sufficient factor of safety against overall shear failure, and it must not cause excessive settlements [1.55]. The methods of design of mat foundations are classified as [1.56]: conventional methods known as the rigid method [1.57], and "simplified elastic foundation methods" [1.58, 1.59, 1.60]; and numerical methods represented by finite difference and finite element methods [1.61]. Generally, in the conventional methods the subsoil is represented by an infinite number of elastic springs (subgrade reaction method) or it is considered as an elastic half-space (compression index analysis). The representation of the subsoil by a system of independent springs implies that the load distribution is not considered in the analysis, while the elastic halfspace model, although describing the inter dependence between the structure and subsoil, leads to results predicting unrealistically high stresses under the edge of the raft.

Methods using finite element analysis assume elastic, nonlinear elastic or elastic-perfectly plastic (von Mises) material behavior of the subsoil (1.55). There are many objections to the use of the methods based on nonlinear elasticity or elastic-plastic (von Mises) models. The main ones were discussed in Subsection 1.2.1.

Analysis of Embankments

Analytical methods employed in the past for the design of dams were simple plane analyses. They involved calculation of force resultants required to satisfy various design criteria. The middle-

third rule [1.62] was one of the most frequently used criteria in the design of concrete gravity dams.

The development of digital computers provided a base for application of various numerical methods. Stress analysis of different types of dams have been made by employing finite difference [1.63] and finite element [1.64] methods. The material was assumed elastic and a set of new design criteria related to the maximum allowable direct and shear stresses were defined.

The development of the finite element method was prerequisite to its application in analysis of earth dams. The calculation of stresses and deformations was lately extended to stability analysis as well [1.65]. The results obtained from various analyses are being constantly improved by developments in discretization, solution algorithm, and particularly by development in the constitutive law to model soil properties.

The effect of incremental construction on the stresses and deformations developed in an embankment was studied by Clough and Woodward [1.66] and the significance of layered as compared to single step loading was examined. The same effect and using nonlinear characteristics was evaluated by Alberro [1.67] in the finite element analysis of the El-Infieruillo dam, and by Kulhawy and Duncan [1.68] in the study of stresses and movements of the Oroville dam. The latter assumed nonlinear-elastic material properties. The work was later extended by Nobary and Duncan [1.69] to compute the effect of reservoir filling on the redistribution of stresses and movements in the Oroville Dam. The finite element method was used also for

evaluation of the factor of safety of slope stability. Resendis and Romeo [1.70] established a potential failure zone by a curve connecting the points of major principal strains, and compared the factor of safety with conventional methods. The accuracy of equilibrium methods used in the past was examined by Wright, Kulhawy and Duncan [1.71]. They employed a finite element method and the obtained factor of safety did not differ much from the one found with equilibrium methods. The effect of foundation compressibility on the development of cracks in the Duncan Dam was examined by Eisenstein, Krishnayya and Morganstern [1.72]. Here, the tensile zones obtained from the finite element analysis compared well with observations. The finite element method was also used by Takahashi and Nakayawa [1.73] to determine the optimum location of the core of a high rockfill dam. They simulated construction in layers and the material was assumed to be visco-elastic.

Gravity Dams on "Soft" Foundations

Gravity dams founded on "soft" foundations such as weak rock or soils having horizontal clay seams or shales with poor shear strength characteristics present a major design problem. Such foundations have been met all over the world: (a) in India [1.74] at the sites of Kadana Dam, Barna Dam, Dudganga Dam, and Hidkol Dam; (b) Warragamba Dam in Australia [1.75]; (c) Maquinenza Dam in Spain [1.76]; (d) Meadow bank in Tasmania [1.71]; (e) Green Peter Dam in U.S.A. [1.78]; and (f) in other places [1.79, 1.80]. The design of gravity dams on such foundations encountered several difficulties due to the complex three dimensional character of the formations and the heterogeneity of the materials.

The simplest procedure for computing the sliding stability is to divide the base into a number of two-dimensional vertical slices and to add up the contribution to the sliding resistance of each slice [1.74, 1.78]. Safety factors varying from 4 to 1.5 are usually assumed [1.81].

Recently, there is a growing trend to use the finite element analysis or photoelastic methods which take into account the compatibility of deformations in preference to simple force equilibrium analysis [1.80, 1.82, 1.83]. However, the effect of permanent (plastic) deformations of the soft subsoil due to static or fluctuating loads of the water was not considered so far.

~~1.2.4~~ Need for Further Work

From the preceding review of previous work one may conclude that further research is required in all the areas discussed. New constitutive laws incorporating the most significant aspects of soil behavior are obviously needed. They should provide the capability to predict accurately the behavior of soils, such as cemented sands which has not been analytically modeled previously. Implementation of newly developed models into the algorithms of existing numerical techniques such as the finite element method is essential in the validation process of any constitutive law. Today, very few models have been successfully implemented and further work in this direction is required. The influence of soil plastification on the behavior of actual structures, in both geotechnical engineering as well as the study of nonlinear soil structure interaction, is not adequately investigated, and therefore more research is needed.

1.3 SCOPE OF THE PRESENT STUDY

The primary purpose of this study is to develop a constitutive model for a granular medium with cohesion. Such a formulation will be applicable to geological materials composed of sand and gravel particles cemented naturally or artificially with calcite (CaCO_3), gypsum ($\text{CaSO}_4 \cdot 2\text{H}_2\text{O}$), cement, or other agents. In recent years these materials have been extensively used in engineering practice [2.4, 2.5] and the need for an appropriate constitutive description (which has been lacking so far) seems quite evident.

The formulation presented in the thesis constitutes an extension of the work by Poorooshasb and Pietruszczak [1.33]. The model is based on the theory of bounding surface plasticity incorporating a non-associated flow rule and the concept of reflected plastic potential. Details of the mathematical description are provided in Chapter 2. The present formulation is more comprehensive than that discussed in Ref. 1.33 and differs from it in a number of aspects, which include for example,

- (i) the form of the yield surface and plastic potential
- (ii) mode of accumulation of plastic distortions
- (iii) generalized form of the local plastic potential, etc.

Also, the present formulation is more detailed as it provides explicit analytical expressions for the gradient tensors, location of the conjugate stress point, etc., which are required for implementation in a computer code.

The usefulness of elaborated constitutive relations is seen only if they can be incorporated into a numerical procedure suitable for analysing boundary value problems. Hence, the second purpose of this

study is to incorporate the derived elasto-plastic relationships in a general purpose finite element computer program.

The third purpose of this study is to solve a number of boundary value problems of practical significance. These include typical problems related to geomechanics (footing on subsoil, analysis of an earth dam during construction) and problems of soil-structure interaction (mat foundation, concrete gravity dam on "soft" foundation).

An elaborate soil model which accounts for important soil properties such as path dependency, dilatancy and soil hardening becomes an important part of any refined analysis. Therefore, the final purpose of this study is to demonstrate the need to use an elaborate model in analysis of very important structures such as dams or mat foundations.

1.4 ORGANIZATION OF THESIS

The development of the analysis and investigation reported herein is organized in the following manner:

The formulation of the constitutive equations for work hardening granular elasto-plastic material with cohesion between the particles is presented in Chapter II. Also, the comparison of the derived relations with experimental results is evaluated.

Chapter III is partially devoted to the development of a finite element which includes the relations defined in the previous chapter. The finite element is then attached to a general purpose computer program. A detailed procedure for evaluation of required model parameters is presented in the second half of Chapter III.

The finite element implemented in a general purpose computer program is validated in Chapter IV by solving problems related to geotechnical engineering. A footing problem is examined and results are compared with experiments. A comparison with another finite element model (nonlinear-elastic) of a large embankment is performed.

The study of nonlinear static soil-structure interaction is presented in Chapter V. Here, the influence of elasto-plastic soil on a mat foundation is examined first and results are compared with those obtained by conventional methods and other finite element methods. The effect of water fluctuations and uplift water pressures on the behavior of concrete gravity dam is analysed next.

Finally, general conclusions are listed in Chapter VI.

CHAPTER II

2.0 FORMULATION OF AN ELASTO-PLASTIC WORK-HARDENING MODEL FOR GRANULAR SOIL WITH COHESION

2.1 INTRODUCTION

Many numerical techniques for the solution of load-deformation problems in Soil Mechanics satisfy the equations of equilibrium, equations of compability and boundary conditions in a routine manner. It is the choice of an appropriate constitutive relation which determines whether the solution obtained is realistic and meaningful. The existing phenomenological concepts describing the behaviour of soil are based on different fundamental theories. These include nonlinear elasticity, hypoelasticity, so-called endochronic theory, and finally the theory of plasticity. Among the existing concepts, those built within the framework of plasticity are, in the author's opinion, of advantage. The theory has a considerable flexibility to enable modelling of complex behaviour of different types of soil. It also proves to be very convenient in incorporating the memory rules of particular loading events.

The mathematical theory of elasto-plasticity is well established and has been used extensively in many branches of engineering. The theory postulates the existence of a yield locus which represents the limit of elasticity. During the deformation process this locus either remains stationary (perfect plasticity) or undergoes evolution

(work-hardening). The flow rule is formulated in such a manner that the direction of plastic strain rate is uniquely determined by the stress state itself.

In Soil Mechanics various combinations of the yield functions and hardening rules have been used so far. Isotropic hardening, kinematic hardening and mixed hardening rules with hardening due to plastic volumetric strains and plastic shear strains gave rise to models of varying complexities. The Critical State Model, models due to Mroz et al [1.31] [1.32], Lade [2.1], Nova [1.35], Pgorooshasb and Pietruszczak [1.33] are a few examples of such concepts.

The present chapter is concerned with the establishment of incremental stress-strain relations for granular soil with cohesion. Typical examples of this type of soil are naturally or artificially cemented sand deposits. Cemented sands are found in many areas of the world. The cementation is provided by small amounts of agents, such as silica, hydrous silicates, hydrous iron oxides, and carbonates deposited at the points of contact between sand particles [2.2, 2.3]. Cementation or cementation-like effects can also be produced by a dense packing of sand grains [2.4], or by a matrix of silt and clay particles. Natural cementation is not uniformly distributed within the soil [2.5]. It varies over the entire stratigraphical interval of any formation. It also varies on a small scale within any testing sample, and unequal distribution of cementation agents is considered as a main reason.

By adding a small amount of cement to the sand it is possible to obtain a material with strong enough chemical bond between the sand

grains to increase its strength characteristics and to prevent possible liquefaction.

Static and dynamic strain properties of naturally and artificially cemented sands have been studied by different investigators [2.6 to 2.11]. The difficulties related to appropriate undisturbed sampling and testing of naturally cemented sand requires use of artificially cemented specimens. They are used for better understanding of the behavior of naturally cemented deposits [2.3, 2.9], and also they provide enough information for defining design criteria in the stabilization of liquefiable sand deposits [2.4].

These initial studies indicate that artificially cemented sands simulate the behavior of naturally cemented sands [2.9]. Recent research [2.12, 2.13] supports the conclusions of previous work [2.14, 2.15, 2.16, 2.17] that the properties of cemented sands change with time period. For example the stiffness and the strength of cemented sands increase with time. Therefore, an understanding of the effect of cementation on static and dynamic strength and the deformation behavior of sands is becoming increasingly important in design and analysis within geotechnical engineering.

For vanishing cohesion the concept presented in this chapter will describe the behavior of pure (uncemented) sand. The model is based on the theory of bounding surface plasticity [1.26, 1.27, 1.31, 1.32, 2.18, 2.19], incorporating a non-associated flow rule and the idea of reflected plastic potential.

The next section provides the derivation of the general three-dimensional constitutive relationships. In the subsequent section a comparison of the predicted behavior and observed response is examined. This includes: (a) comparison with results of drained triaxial tests on naturally weakly-cemented sands as reported in Ref. 2.3; (b) comparison with results of drained triaxial test on artificially cemented sand with 2% cement reported in Ref. 2.3; (c) comparison of results of drained triaxial tests on artificially cemented sand with 5% cement reported in Ref. 2.4; (d) comparison of results of undrained triaxial test for a cohesionless granular medium as reported in Ref. 2.20; (e) comparison of results of predicted behavior and observed response for cohesionless granular medium under cyclic loading as reported in Ref. 2.21; and (f) parametric study of the effect of different parameters (employed in the model) on the results obtained for cemented and cohesionless sand behavior under monotonic as well as cyclic loading.

2.2 FORMULATION OF THE CONSTITUTIVE LAW

2.2.1 Conceptual Baseline

The constitutive concept described in this section represents an extension of the model proposed by Poorooshasb and Pietruszczak [1.33] to simulate the behavior of naturally or artificially cemented sand deposits. The conceptual baseline adopted here is that the response of a loose cemented sand is, in the mechanical sense, similar to that of pure sand with higher relative density and inherent cohesion. The applicability of the model discussed in Ref. 1.33 extends to pure sand in a wide spectrum of initial void ratios, ranging from a very loose to a very dense one. Therefore, the mathematical framework

chosen is analogous to that proposed in Ref. 1.33, and applies to cemented sands with the same wide spectrum of initial void ratios.

2.2.2 Mathematical Formulation.

The formulation of the constitutive law is presented in relation to the principal effective stresses σ_i ($i=1,2,3$). The three stress invariants p , q and J_3 are defined as follows:

$$\begin{aligned} p &= -(\sigma_1 + \sigma_2 + \sigma_3)/3 \\ q &= \sqrt{\frac{3}{2}} [(\sigma_1 + p)^2 + (\sigma_2 + p)^2 + (\sigma_3 + p)^2]^{\frac{1}{2}} \\ J_3 &= \frac{1}{3} [(\sigma_1 + p)^3 + (\sigma_2 + p)^3 + (\sigma_3 + p)^3] \end{aligned} \quad (2.1)$$

The state of stress in a "triaxial" loading test is commonly defined as $\sigma_1 > \sigma_2 = \sigma_3$. Hence; it follows that these invariants become

$$\begin{aligned} p &= -(\sigma_1 + 2 \sigma_3)/3 \\ q &= \sigma_3 - \sigma_1 \\ J_3 &= -\frac{2}{27} (\sigma_3 - \sigma_1)^3 \end{aligned} \quad (2.2)$$

For convenience, the angle measure of the third stress invariant (analogous to Lode's angle) is introduced and defined by

$$\theta = \frac{1}{3} \sin^{-1} \left(-\frac{27}{2} \frac{J_3}{q^3} \right); \quad -\frac{\pi}{6} \leq \theta < \frac{\pi}{6} \quad (2.3)$$

The angle θ can be directly identified in the so-called π -plane, i.e. $\sigma_1 + \sigma_2 + \sigma_3 = \text{const.}$ The volumetric strain rate $\dot{\epsilon}_v$ and the distortional strain rate $\dot{\epsilon}$ represent the strain rate invariants which are compatible

with the above stress invariants p and q . $\dot{\epsilon}_v$ and $\dot{\epsilon}$ are expressed as follow:

$$\begin{aligned} \dot{\epsilon}_v &= -(\dot{\epsilon}_1 + \dot{\epsilon}_2 + \dot{\epsilon}_3) \\ \dot{\epsilon} &= \sqrt{\frac{2}{3}} [(\dot{\epsilon}_1 + \dot{\epsilon}_v/3)^2 + (\dot{\epsilon}_2 + \dot{\epsilon}_v/3)^2 + (\dot{\epsilon}_3 + \dot{\epsilon}_v/3)^2]^{1/2} \end{aligned} \quad (2.4)$$

For conventional 'triaxial' loading equations (2.4) reduce to

$$\begin{aligned} \dot{\epsilon}_v &= -(\dot{\epsilon}_1 + 2\dot{\epsilon}_3) \\ \dot{\epsilon} &= \frac{2}{3} (\dot{\epsilon}_1 - \dot{\epsilon}_3) \end{aligned} \quad (2.5)$$

and the rate of work performance \dot{W} is equal to

$$\dot{W} = p\dot{\epsilon}_v + q\dot{\epsilon} = \sigma_1\dot{\epsilon}_1 + 2\sigma_3\dot{\epsilon}_3 \quad (2.6)$$

The constitutive concept, as described below, is based on the following assumptions:

- (i) Active loading process imposed upon virgin material results in creation of a so-called "bounding" surface. This surface reflects isotropic properties of the material and is assumed to undergo deviatoric hardening.
- (ii) The yield surface, enclosing the domain of elastic response, is assumed to be activated during stress-reversal programs. This surface is allowed to translate and rotate within the domain occupied by the bounding surface (kinematic hardening).
- (iii) The hardening modulus of the material varies along the stress path from its initial very large value (corresponding to the

first stress reversal) to a prescribed value on the bounding surface. The appropriate interpolation rule is provided later in this section.

- (iv) Plastic flow is governed by a non-associated flow rule that implies the existence of a potential function which differs from the yield function.
- (v) The viscous effects are neglected.

For a given loading path ξ , with no stress reversal, the bounding surface expands with increasing load and is confined within a failure state. At the onset of stress reversal, a yield surface is created which is permitted only to translate and rotate within the bounding surface. For the state of stress enclosed by the yield surface the behavior is purely elastic. Once the stress path ξ departs the yield surface the behavior becomes elasto-plastic. The mode of accumulation of plastic distortions during the stress reversal process dictates the contraction or expansion of the bounding surface. If the stress point reaches and tends to move beyond the bounding surface during stress reversal programs, the behavior is again governed by the bounding surface. Both surfaces and the loading path are presented in Fig. 1.1.

Consider first an active loading process during which the stress point is located on the bounding surface. The equation of this surface is assumed in the form

$$F = q - mg(\theta)(p + p_0) \quad (2.7)$$

where the parameter $m = m(\epsilon^P)$ describes the history of plastic distortion ϵ^P

$$\epsilon^P = \int \dot{\epsilon}^P dt' \quad (2.8)$$

The bounding surface in the q-p space is presented in Fig. 2.2(a). In the effective stress space, Σ_1 , equation (2.7) represents an irregular cone having its apex displaced by p_0 from the origin and its axis coinciding with the diagonal of Σ_1 -space.

The function $g(\theta)$ is postulated in the form (William, Warnke [272])

$$g(\theta) = \frac{(1 - k^2)a + (2k - 1)[(2 + b)(1 - k^2) + 5k^2 - 4k]^{\frac{1}{2}}}{(1 - k^2)(2 + b) + (1 - 2k)^2} \quad (2.9)$$

where

$$a = \sqrt{3} \cos \theta - \sin \theta$$

$$b = \cos 2\theta - \sqrt{3} \sin 2\theta$$

$$k = (3 + \sin \phi_f) / (3 - \sin \phi_f)$$

and ϕ_f represents the ultimate internal friction angle.

The parameter p_0 reflects the tensile strength of the material under hydrostatic conditions and is a function of the cohesion c and the angle of internal friction ϕ_f and is expressed as $p_0 = c \cot \phi_f$.

To define the function $m = m(\epsilon^P)$, a simple hyperbolic form is used, viz.

$$m = m_f \frac{\epsilon^P}{A + \epsilon^P} \quad (2.10)$$

where A is a positive constant and $m_f = 6 \sin \phi_f / (3 - \sin \phi_f)$. Although other functions allow strain hardening as well as strain softening behavior (Ghaboussi, Momen [1.34], Prevost, Hoeg [1.24], Vernier [2.237]), this type of function describes only strain hardening.

The derivation of the corresponding constitutive relations is presented next. Assume a non-associated flow rule

$$\dot{\epsilon}_i^p = \lambda \frac{\partial \Psi}{\partial \sigma_i} \quad (2.11)$$

in which $\Psi = 0$ represents the plastic potential postulated in the form

$$\Psi = q + m_c (p + p_0) g(\theta) \ln \left(\frac{p + p_0}{p_c} \right) = 0 \quad (2.12)$$

In equation (2.12) m_c and p_c are constants. The parameter p_c has the dimension of stress representing the size of the plastic potential and m_c defines the value of $q/g(\theta)p$ for which $\dot{\epsilon}_v^p = 0$ (by analogy to Critical State concept). The consistency condition, requiring the state of stress σ_i to remain on the bounding surface, reads

$$d\hat{F} = \frac{\partial F}{\partial \sigma_i} \dot{\sigma}_i + \frac{\partial F}{\partial \epsilon^p} \dot{\epsilon}^p = 0 \quad (2.13)$$

Writing the second equation in (2.4) in the form

$$\dot{\epsilon}^p = \sqrt{\frac{2}{3}} (\dot{e}_i^p \dot{e}_i^p)^{\frac{1}{2}} \quad (2.14)$$

where \dot{e}_i^p represents the deviator of plastic strain rate, and utilizing equation (2.11) one obtains

$$\dot{\epsilon}^p = \sqrt{\frac{2}{3}} \dot{\lambda} \left[\left(\text{dev} \frac{\partial \Psi}{\partial \sigma_i} \right) \left(\text{dev} \frac{\partial \Psi}{\partial \sigma_i} \right) \right]^{\frac{1}{2}} \quad (2.15)$$

Substitution of equation (2.15) in the consistency condition (2.13) yields

$$\dot{\lambda} = \frac{\frac{\partial F}{\partial \sigma_i} \dot{\sigma}_i}{H_p} \quad (2.16)$$

where

$$H_p = -\sqrt{\frac{2}{3}} \frac{\partial F}{\partial m} \frac{\partial m}{\partial \epsilon^p} \left[\left(\text{dev} \frac{\partial \Psi}{\partial \sigma_i} \right) \left(\text{dev} \frac{\partial \Psi}{\partial \sigma_i} \right) \right]^{\frac{1}{2}} \quad (2.17)$$

and H_p represents the plastic hardening modulus.

After differentiation of equations (2.7) and (2.10) (with respect to m and ϵ^p , respectively), the relation (2.17) takes the form

$$H_p = -\sqrt{\frac{2}{3}} g(\theta)(p + p_0) \frac{(m_f - m)^2}{Am_f} \left[\left(\text{dev} \frac{\partial \Psi}{\partial \sigma_i} \right) \left(\text{dev} \frac{\partial \Psi}{\partial \sigma_i} \right) \right]^{\frac{1}{2}} \quad (2.18)$$

so that $H_p \rightarrow 0$ for $m \rightarrow m_f$.

In order to derive the stress-strain relations, assume the additivity between reversible (elastic) and irreversible (plastic) strain rates

$$\dot{\epsilon}_i = \dot{\epsilon}_i^e + \dot{\epsilon}_i^p \quad (2.19)$$

Writing the stress rates in the form

$$\dot{\sigma}_i = D_{ij}(\dot{\epsilon}_j - \dot{\epsilon}_j^p) \quad (2.20)$$

where D_{ij} is the elastic constitutive matrix, and utilizing equations (2.13) and (2.11) one arrives at

$$\dot{\sigma}_i = \left(D_{ij} - \frac{D_{ip} \frac{\partial \Psi}{\partial \sigma_p} \frac{\partial F}{\partial \sigma_q} D_{qj}}{H_e + H_p} \right) \dot{\epsilon}_j \quad (2.21)$$

with

$$H_e = \frac{\partial F}{\partial \sigma_1} D_{ij} \frac{\partial \Psi}{\partial \sigma_1}$$

The above constitutive relation holds good whenever the state of stress is located on the bounding surface $F = 0$. Note that according to equation (2.7) the expression for the gradient tensor $(\partial F)/(\partial \sigma_1)$ takes the form

$$\frac{\partial F}{\partial \sigma_1} = \frac{\partial F}{\partial q} \frac{\partial q}{\partial \sigma_1} + \frac{\partial F}{\partial p} \frac{\partial p}{\partial \sigma_1} + \frac{\partial F}{\partial \theta} \frac{\partial \theta}{\partial \sigma_1} \quad (2.22)$$

Differentiating equation (2.3) one obtains

$$\frac{\partial \theta}{\partial \sigma_1} = \frac{\partial \theta}{\partial p} \frac{\partial p}{\partial \sigma_1} + \frac{\partial \theta}{\partial J_3} \frac{\partial J_3}{\partial \sigma_1} \quad (2.23)$$

where

$$\frac{\partial \theta}{\partial q} = \frac{\tan 3\theta}{q}; \quad \frac{\partial \theta}{\partial J_3} = -\frac{9}{2q^3 \cos 3\theta}$$

Thus, equation (2.22) can be rearranged to the form

$$\frac{\partial F}{\partial \sigma_1} = c_1 \frac{\partial p}{\partial \sigma_1} + c_2 \frac{\partial q}{\partial \sigma_1} + c_3 \frac{\partial J_3}{\partial \sigma_1} \quad (2.24)$$

in which

$$c_1 = \frac{\partial F}{\partial p}; \quad c_2 = \frac{\partial F}{\partial q} - \frac{\tan 3\theta}{q} \frac{\partial F}{\partial \theta}; \quad c_3 = -\frac{9}{2q^3 \cos 3\theta} \frac{\partial F}{\partial \theta} \quad (2.25)$$

and according to eqn. (2.1)

$$\frac{\partial p}{\partial \sigma_1} = -\frac{1}{3} \begin{bmatrix} 1 \\ 1 \\ 1 \end{bmatrix}; \quad \frac{\partial q}{\partial \sigma_1} = \frac{1}{\sqrt{6}q} \begin{bmatrix} 2\sigma_1 - \sigma_2 - \sigma_3 \\ 2\sigma_2 - \sigma_1 - \sigma_3 \\ 2\sigma_3 - \sigma_1 - \sigma_2 \end{bmatrix}; \quad \frac{\partial J_3}{\partial \sigma_1} = \frac{1}{3} \begin{bmatrix} 2(\sigma_1+p)^2 - (\sigma_2+p)^2 - (\sigma_3+p)^2 \\ 2(\sigma_2+p)^2 - (\sigma_1+p)^2 - (\sigma_3+p)^2 \\ 2(\sigma_3+p)^2 - (\sigma_1+p)^2 - (\sigma_2+p)^2 \end{bmatrix} \quad (2.26)$$

The gradient vector $(\partial \Psi)/(\partial \sigma_1)$ can be evaluated in a similar manner to that outlined above.

Consider now the stress reversal process. The plastic flow may be described by the evolution of the yield surface which is created inside the bounding surface. Initially, the yield surface remains tangential to the bounding surface at the stress reversal point. For subsequent loading, it undergoes both translation and rotation within the domain enclosed by the bounding surface.

Define a new set of stress invariants, p' , q' and θ' , which are related to a new axis system \sum_1' . The latter is related to the original system \sum_1 through the transformation tensor T_{1j} , and has its diagonal coincident with the axis of the yield surface. Thus

$$p' = -(\sigma_1' + \sigma_2' + \sigma_3')/3$$

$$q' = \sqrt{\frac{3}{2}} [(\sigma_1' + p')^2 + (\sigma_2' + p')^2 + (\sigma_3' + p')^2]^{1/2} \quad (2.27)$$

$$J_3' = \frac{1}{3} [(\sigma_1' + p')^3 + (\sigma_2' + p')^3 + (\sigma_3' + p')^3]$$

$$\theta' = \frac{1}{3} \sin^{-1} \left(-\frac{27}{2} \frac{J_3'}{(q')^3} \right) \quad (2.28)$$

where $\sigma_i' = T_{ij} \sigma_j$ (2.29)

and σ_i' represents the components of the stress vector relative to the new coordinate system Σ_1' .

The equation of the yield surface is postulated in the form

$$f = q' - m_0 g(\theta')(p' + p_0') = 0 \quad (2.30)$$

where $m_0 = \text{constant}$ ($m_0 \ll m_f$) and

$$p_0' = p_0 T_{ij} \delta_i \delta_j ; \quad \delta_i = \begin{Bmatrix} 1 \\ 1 \\ 1 \end{Bmatrix} \quad (2.31)$$

The translation and the rotation of the yield surface is guided by a conjugate stress vector σ_1^c . This stress vector is on the bounding surface and its intersection with the current π -plane is called the conjugate stress point. For any state of stress σ_i on the yield surface the stress invariants p^c , q^c and θ^c satisfying

$$p^c = p; \quad q^c = mg(\theta)(p^c + p_0); \quad \theta^c = \theta' \quad (2.32)$$

define the conjugate stress vector σ_1^c . The location of the conjugate stress point for a current state of stress σ_i is presented in Fig. 2.2(b).

Note that, according to equation (2.32), the parameter θ^c corresponding to the conjugate point coincides with θ' i.e. local 'Lode' parameter (in Σ'_1 system). Based on relations (2.32), the location of the conjugate stress point σ_1^c is defined by (see Ref. 1.54 for the details of transformation)

$$\sigma_1^c = \frac{2}{3} q^c a_i - p \delta_i \quad (2.33)$$

where

$$a_i = \begin{cases} \sin(\theta + \frac{2\pi}{3}) \\ \sin \theta \\ \sin(\theta + \frac{4\pi}{3}) \end{cases}$$

The form of the translation rule for the yield surface is identical to that in Ref. 1.33. For clarity and continuity of the presentation the derivation is taken here in its entire form from the above reference.

"The mode of translation and rotation of the yield surface is governed by the following rules

- (1) The axis of the yield surface (which coincides with the space diagonal of Σ'_1 coordinate system) moves parallel to a plane containing the stress vector and the conjugate stress vector, i.e. the plane passing through the origin, point σ_1 and point σ_1^c - hereafter referred to as the $\theta \sigma_1 \sigma_1^c$ plane.

(ii) The rotation of the yield surface is such that the 'Lode' parameter corresponding to the set of stress points common to the plane $\theta \sigma_1 \sigma_1^c$ and the new yield surface (the yield surface resulting from the incremental change in stress point σ_1) remains equal to the 'Lode' parameter of the conjugate stress vector σ_1^c .

In order to satisfy (i), let the vector normal to the stress vector and the conjugate stress vector be denoted by λ_1

$$\lambda_1 = \epsilon_{ijk} \sigma_j^c \sigma_k \quad (2.34)$$

where ϵ_{ijk} is the alternating tensor. Also, denote by α_1 the unit vector long the space diagonal in Σ_1' system

$$\alpha_1 = T_{ij} \alpha_j \quad (2.35)$$

with

$$\alpha_j' = \frac{1}{\sqrt{3}} \delta_j \quad (2.36)$$

According to (i) the condition $\lambda_1 \alpha_1 = 0$ must be satisfied, in which

$$\alpha_1 = T_{ji} \alpha_j' \quad (2.37)$$

This leads to the first equation in terms of nine unknowns T_{ji} :

$$\epsilon_{ijk} \sigma_j^c \sigma_k T_{li} \alpha_l' = 0 \quad (2.38)$$

Consider a stress point $\sigma_1 + \dot{\gamma}_1 dt'$ in the neighbourhood of σ_1 chosen in such a way that

$$\sigma_1 \dot{\gamma}_1 = 0 \quad (2.39)$$

If the stress point is to be located on the new yield surface as well as on the $\theta \sigma_1 \sigma_1^c$ plane, the following two relationships must hold:

$$\dot{f} = \frac{\partial f}{\partial T_{ij}} T_{ij} + \frac{\partial f}{\partial \sigma_1} \dot{\gamma}_1 = 0 \quad (2.40)$$

$$\epsilon_{ijk} \sigma_j^c \sigma_k \dot{\gamma}_1 = 0 \quad (2.41)$$

Combining equations (2.39), (2.40), (2.41) and (2.34) yields

$$\dot{\gamma}_1 = -\epsilon_{ijk} \lambda_j \sigma_k \left(\frac{\partial f}{\partial T_{mn}} \right) T_{mn} / \Delta \quad (2.42)$$

where

$$\Delta = \epsilon_{ijk} \sigma_j \left(\frac{\partial f}{\partial \sigma_k} \right) \lambda_i$$

But $\theta = \theta' = \theta(T_{ij}, \sigma_1)$ and hence

$$\dot{\theta} = \frac{\partial \theta}{\partial T_{ij}} T_{ij} + \frac{\partial \theta}{\partial \sigma_1} \dot{\gamma}_1 \quad (2.43)$$

Therefore rule (ii) which demands $\dot{\theta} = 0$ yields for the present case

$$\left[\frac{\partial \theta}{\partial T_{ij}} - \epsilon_{pqr} \frac{\partial \theta}{\partial \sigma_q} \lambda_p \sigma_r \left(\frac{\partial f}{\partial T_{ij}} \right) / \Delta \right] T_{ij} = 0 \quad (2.44)$$

In general, one more equation may be obtained from the consistency condition

$$\frac{\partial f}{\partial T_{ij}} \dot{T}_{ij} + \frac{\partial f}{\partial \sigma_1} \dot{\sigma}_1 = 0 \quad (2.45)$$

and six more relations from the identities

$$T_{ij} \dot{T}_{ik} + T_{ik} \dot{T}_{ij} = 0 \quad (2.46)$$

To recapitulate: to locate the new yield surface, the new local coordinate system (Σ'_1 with direction cosines $T_{ij} + T_{dt}$) is to be specified. This is done using the relations (2.38), (2.44), (2.45) and (2.46).

The local plastic potential $\Psi' = 0$ is postulated in the form of a surface of revolution about α_1 axis having one of its generating curves in common with the global plastic potential surface $\Psi = 0$, equation (2.12). To obtain the invariants q, p in terms of q' and p' the following transformation is made, viz.

$$\begin{aligned} q &= q' \alpha^* + \frac{3}{\sqrt{2}} p \alpha^{**} \\ p &= p' \alpha^* - \frac{\sqrt{2}}{3} q \alpha^{**} \end{aligned} \quad (2.47)$$

where

$$\alpha^* = -\alpha_1 \delta_1 / \sqrt{3}; \quad \alpha^{**} = (\bar{\alpha}_1 \bar{\alpha}_1)^{1/2} \quad (2.48)$$

and

$$\bar{\alpha}_1 = \alpha_1 + \alpha^* \delta_1 / \sqrt{3} \quad (2.49)$$

Writing eq. (2.12) in the form

$$\Psi = q + \beta_1 (p + p_0) \ln \left(\frac{p + p_0}{p_c} \right) \quad (2.50)$$

with

$$\beta_1 = m_c g(\theta) \quad (2.51)$$

and utilizing relations (2.47), we can express the local plastic potential $\Psi' = 0$ as

$$\Psi' = q' + \frac{3}{\sqrt{2}} p' \beta_2 + \beta_1 \left[(p' + p'_0) - \frac{\sqrt{2}}{3} q' \right] \ln \frac{[(p' + p'_0) - \frac{\sqrt{2}}{3} q']}{\beta_3} = 0 \quad (2.52)$$

where

$$\beta_2 = \alpha^*/\alpha^{**} \quad \text{and} \quad \beta_3 = p_c/\alpha^* \quad (2.53)$$

To complete the formulation the rule for variation of the plastic hardening modulus in the course of deformation should be specified. For the considered reverse loading process the non-associated flow rule can be conveniently expressed by

$$\dot{\epsilon}_i^p = h(n_k \dot{\sigma}_k) \bar{n}_i \quad (2.54)$$

Here n_i and \bar{n}_i represent the unit vector normal to the yield and plastic potential surface respectively

$$n_i = \frac{\frac{\partial f}{\partial \sigma_i}}{\left(\frac{\partial f}{\partial \sigma_k} \frac{\partial f}{\partial \sigma_k} \right)^{1/2}} ; \quad \bar{n}_i = \frac{\frac{\partial \Psi'}{\partial \sigma_i}}{\left(\frac{\partial \Psi'}{\partial \sigma_k} \frac{\partial \Psi'}{\partial \sigma_k} \right)^{1/2}} \quad (2.55)$$

where

$$\frac{\partial f}{\partial \sigma_i} = T_{ij} \frac{\partial f}{\partial \sigma'_j} \quad \text{and} \quad \frac{\partial \Psi'}{\partial \sigma_i} = T_{ij} \frac{\partial \Psi'}{\partial \sigma'_j} \quad (2.56)$$

Three stress vectors, the current stress vector σ_i on the yield surface, the conjugate σ_i^c and the datum stress vector σ_i^d on the bounding surface

define the magnitude of the parameter, h . The datum stress vector is coplanar with the stress and the conjugate stress vector.

Introduce the angle measures, δ and δ_0 where

$$\delta = \cos^{-1} \frac{\sigma_1 \sigma_1^c}{[\sigma_k \sigma_k] (\sigma_p^c \sigma_p^c)} \quad (2.57)$$

is the angle between the stress and conjugate stress vectors, and δ_0 is the maximum angle between the conjugate and the datum stress vectors.

To obtain the magnitude of the hardening parameter the following type of interpolation rule is introduced

$$h = h_B \left(1 - \frac{\delta}{\delta_0}\right)^\gamma \quad (2.58)$$

where γ is a constant and h_B is the hardening modulus on the bounding surface defined as

$$h_B = \left(\frac{\partial F}{\partial \sigma_i} \frac{\partial F}{\partial \sigma_i}\right)^{\frac{1}{2}} \left(\frac{\partial \Psi}{\partial \sigma_k} \frac{\partial \Psi}{\partial \sigma_k}\right)^{\frac{1}{2}} / H_p \quad (2.59)$$

with H_p given by equation (2.18) and evaluated at conjugate stress point σ_i^c . According to equation (2.58), $h \rightarrow h$ as $\delta \rightarrow 0$ (the case when the yield surface approaches the bounding surface), whereas for $\delta \rightarrow \delta_0$ (stress reversal) we have $h \rightarrow 0$.

Thus for all stress paths penetrating the interior of the bounding surface the constitutive relation takes the form

$$\dot{\sigma}_i = (D_{ij} - \frac{D_{ip} \bar{n}_p n_q^D q_j}{h_e + 1/h}) \dot{\epsilon}_j \quad (2.60)$$

where

$$h_e = n_i^D D_{ij} \bar{n}_i \quad (2.61)$$

Note that the unit vectors \bar{n}_i and n_i appearing in equation (2.60) can be evaluated from equations (2.55) and (2.56). For example, the expression for the gradient vector $(\partial f)/(\partial \sigma_i)$ takes the form (equation 2.56)

$$\frac{df}{\partial \sigma_i} = T_{ji} \frac{\partial f}{\partial \sigma'_j} \quad (2.62)$$

where, by analogy, to equation (2.24), we have

$$\frac{\partial f}{\partial \sigma'_i} = c_1 \frac{\partial p'}{\partial \sigma'_i} + c_2 \frac{\partial q'}{\partial \sigma'_i} + c_3 \frac{\partial J_3}{\partial \sigma'_i} \quad (2.63)$$

with

$$c_1 = \frac{\partial f}{\partial p'} ; \quad c_2 = \frac{\partial f}{\partial q'} - \frac{\tan 3\theta'}{q'} \frac{\partial f}{\partial \theta'} ; \quad c_3 = - \frac{9}{2(q')^3 \cos 3\theta'} \frac{\partial f}{\partial \theta'} \quad (2.64)$$

The derivatives of the invariants p' , q' and J_3 with respect to σ'_i are given by relations similar to equation (2.26) (with all the variables primed).

Finally, it should be noted that during stress reversal programs the bounding surface can expand or contract depending on the mode of accumulation of plastic distortions, ϵ^p . Herein, the following criterion has been adopted (after Ref. 2.19):

$$\underline{\varepsilon}^P = \int \dot{\varepsilon}^P dt' \quad ; \quad \dot{\varepsilon}^P = \pm \dot{\varepsilon}^P \quad (2.65)$$

$$\dot{\varepsilon}^P > 0 \quad \text{for} \quad s_i \dot{s}_i > 0$$

where $s_i = \sigma_i - p\delta_i$ represents the stress deviator vector.

The above presented constitutive relations were derived under the restriction regarding the fixity of the principal axes of stress with respect to the material element. If such relations are to be implemented in the finite element code certain coaxiality postulates have to be imposed. Hereafter, it is assumed that the principal axes of the plastic strain rate coincide with the principal axes of total stress tensor. This postulate enables the concepts discussed above to be directly extended to cover any (general) loading program.

2.2.3 Relation to the Work by Poorooshab and Pietruszczak

The formulation presented in the previous section is based on the stress invariants p , q and θ which are defined in a different way than in the work by Poorooshab and Pietruszczak [1.33]. This is, to a large extent, a question of convenience. Here, θ is defined as the angle measure of the third stress invariant and is explicitly related to J_3 and q . The function $g(\theta)$, equation 2.9, is postulated in the elliptical form suggested by Willam and Warnke [2.22]. Such formulation leads always to a convex π -plane section (regardless of the value of ϕ_f), whereas the Fourier cosine series proposed in Ref. 1.33 gives the convex shape only for an infinite number of terms. The hardening function $m = m(\varepsilon^P)$ is selected in a hyperbolic form analogous to that proposed in Ref.

1.33. It seems that this form is suitable for relatively loose deposits and it is recommended that this equation be generalized to, for example, an exponential form which will allow for a smooth transition from a stable to unstable response (typical for dense deposits).

Derivation of constitutive relation, presented in Section 2.2.2, follows (as in Ref. 1.33) the convention of theory of plasticity. The equations of the yield surface and plastic potential incorporate parameter p_0 reflecting the tensile strength (under hydrostatic conditions) of cemented granular material. The section concerning the formulation of bounding surface is concluded by specifying the explicit mathematical form of gradient vectors $\partial F/\partial \sigma_1$, $\partial \psi/\partial \sigma_1$ (not provided in Ref. 1.33) which is convenient in the context of future numerical implementations.

For stress-reversal histories, again a different notation as compared to Ref. 1.33 is adopted. Local stress invariants p' , q' , θ' , are defined in consistency with previously introduced measures and appropriate transformation equations are provided (e.g. Equation 2.31). The translation and the rotation rule of the yield surface is identical to that of Ref. 1.33 and also presented here. An explicit mathematical definition of the conjugate point (lacking in Ref. 1.33), in terms of the current state of stress, is given, viz. equations 2.32 and 2.33. The equation of the local plastic potential, as proposed in Ref. 1.33 leads to a discontinuous transition between the states inside and on the bounding surface when m is constant. For this reason a modified form of this equation is proposed (conceptually similar to that in Ref. 2.19) in which $\Psi' = 0$ is postulated in a form of a surface of revolution about the

α_1 axis having one of its generating curves in common with $\Psi = 0$. Detailed mathematical transformation is provided, viz. Equations 2.47 to 2.52. Finally, an explicit mathematical form for the gradient vector $\partial f / \partial \sigma_1$ (not given in Ref. 1.33) is derived, which again is convenient in the context of numerical implementation.

2.3 NUMERICAL EXAMPLES

To demonstrate the capability of the proposed constitutive model for both monotonic and cyclic loading, the drained and undrained triaxial tests on naturally and artificially cemented sands reported in Refs. 2.3 and 2.4, and uncemented (pure) sands reported in Refs. 2.20 and 2.21 are simulated. The effects of various parameters employed in the model on the predictions of the material behavior is further examined.

2.3.1 General Procedure for Evaluation of Parameters Required by the Model

The following parameters must be specified:

- 1) elastic modulus E and Poisson's ratio ν or equivalently G and K , where G is the shear modulus and K is the so-called bulk modulus,
- 2) parameters identifying the tensile strength of cemented granular material ($p_0 = c \cot \phi$), the failure envelope (m_f) and the zero dilatancy envelope (m_c),
- 3) isotropic hardening parameter A (Eq. 2.10) and the kinematic hardening parameter γ of Eq. 2.58.

Elastic constants G and K may be evaluated from known values of E and ν by employing relations from the theory of elasticity. The existence of a small elastic domain allows evaluation of shear modulus G from the initial portion of the stress strain curve of uniaxial compression/-extension test.

Alternatively, a more accurate estimate of the value of G can be obtained from the unloading branch of this curve, if such results are available with known values of G. The bulk modulus is evaluated from the relation:

$$K = \frac{2(1 + \nu)G}{3(1 - 2\nu)}$$

Or in the case of known axial strain ϵ versus volumetric strain ϵ_v plot:

$$K = \left(\frac{\Delta \epsilon}{\Delta \epsilon_v} \right) \cdot G$$

where $\left(\frac{\Delta \epsilon}{\Delta \epsilon_v} \right)$ represents the strain ratio evaluated at either an early stage of loading or during a unloading phase.

For a given angle of internal friction ϕ_f , the parameter m_f indicating the position of the failure line in p-q space may be obtained from:

$$m_f = \frac{6 \sin \phi_f}{3 - \sin \phi_f}$$

The value of m_c defining the location of zero dilatancy line is evaluated from p-constant test.

The parameter A of the hardening rule may be obtained from either:

- i) Conventional triaxial compression test by plotting the results of such a test in q-ε space and then applying the constitutive law (Eq. 2.21) to match the experimental data in a trial and error process; or
- ii) from the strain hardening rule expressed by Eq. 2.10, where for plastic strain $\epsilon^p=0$, it follows that

$$\frac{dm}{d\epsilon} = \frac{m_f}{A}$$

Since $m = \frac{q}{p}$ one obtains

$$\frac{dm}{d\epsilon^p} = \frac{1}{p} \left(\frac{\partial q}{\partial \epsilon^p} - m \frac{\partial p}{\partial \epsilon^p} \right); \quad \text{and} \quad \frac{\partial q}{\partial \epsilon^p} = 3G_0 \quad \text{at} \quad q = 0$$

This gives

$$\frac{m_f}{A} = \frac{3G_0}{P}$$

Therefore,

$$A = m_f \frac{P}{3G_0}$$

where p is the applied effective pressure in a P-constant test, and G_0 represents the initial elastic shear modulus.

Finally, the kinematic hardening parameter γ can be determined by a process of trial and error by fitting any reverse-compression curve. In general, the results of either drained or undrained compression test can be used for evaluation purposes. Alternatively, γ can be evaluated from an undrained cyclic test by matching the actual rate of pore pressure generation.

2.3.2 Monotonic Loading

2.3.2.1 Comparison with Experimental Results

Test results of naturally and artificially cemented sand deposits reported in Refs. 2.3 and 2.4 present a base for comparison with results obtained by the proposed constitutive law. The properties of the examined materials are well documented in the above references (Tables 1 and 2 of Ref. 2.3, and Table 5 and Fig. 7 of Ref. 2.4). From the presented data it can be seen that the cohesion c (peak and residual) varies between 0 kPa and 365 kPa, and the friction angle ϕ_f varies between 20° and 49° .

Comparisons of stress-strain and volume change curves for naturally weakly cemented sand deposits, as tested by Clough et al. [2.3], are shown in Figs. 2.3(a) and 2.3(b) respectively. Five sets of results corresponding to confining pressures of 69 kPa, 138 kPa, 207 kPa, 276 kPa and 414 kPa, as employed in the test are presented. The model parameters are evaluated from the soil properties described in Ref. 2.3 and are shown in Table 2-I. The common characteristic of the predicted and evaluated results is that the stiffness and peak strength increases with

increasing confining pressure. Also, strong volumetric expansion is seen to occur during shear at the lower confining pressure levels.

The numerical predictions are in close agreement with the experimental behavior especially at the lower confining pressure levels. At higher confining pressure levels the model predicts sharper transition from moderate to excessive plastic flow compared with the results obtained in the tests.

Figures 2.4(a) and 2.4 (b) simulate the behavior of artificially-cemented sand prepared to 74% relative density, D_r , using 2% cement by weight. The test data are reported in Ref. 2.3. Three sets of results corresponding to confining pressures of 103 kPa, 207 kPa, and 414 kPa as employed in the test are presented. The parameters characterizing the material properties as evaluated from these tests are shown in Table 2-II. The basic trend observed for the stress-strain and volume change data of the naturally cemented sands in Fig. 2.3 is also exhibited by the artificially-cemented sands. Here, the numerical predictions are in reasonably close agreement with the experimental behavior.

Figure 2.5 shows the comparison of results obtained by the proposed model and those obtained from drained triaxial tests on sand-cement samples of Ref. 2.4. The cement content in the prepared samples is 5% of the dry weight. The samples were compacted to 100% Maximum Proctor density (American Society for Testing and Materials, ASTM, D558) and cured under water in the mold for 180 days in an attempt to duplicate the field conditions. The model parameters are evaluated from the soil

properties in Ref. 2.4 and are shown in Table 2-III. Three sets of results corresponding to confining pressures of 100 kPa, 200 kPa and 500 kPa are presented. Close agreement between the numerical results and test observations for the three confining pressure levels is observed.

It should be noted that the drained behavior of weakly cemented sands presented in the above examples demonstrates the tendency of slight material softening after the failure load is reached. Due to the nature of the hardening function employed in the model which simulate only strain hardening behavior, the stress-strain curves after the failure occurs are not closely followed. This can be corrected simply by assuming a different hardening rule.

Figures 2.6(a) and 2.6(b) simulate the undrained behavior of a loose sand as tested by Townsend and Mulilis and reported in Ref. 2.20. Two sets of results corresponding to confining pressures $p_c = 275$ kPa and $p_c = 550$ kPa, as employed in the test are presented. Bulk moduli of $K = 300$ at. and $K = 600$ at. correspond to the above confining pressures, respectively. From the test data, the values $m_f = 1.2$ and $m_c = 1.15$ were evaluated. The analysis was performed assuming $c = 0$, with the angle of internal friction $\phi = 30^\circ$. The model parameters are summarized in Table 2-IV.

The effective stress paths are plotted in Fig. 2.6(a), and the corresponding stress strain curves are plotted in Fig. 2.6(b). The numerical predictions and the experimental behavior are in fairly close agreement. The numerically predicted stress path differs from the experimental one only when the failure line is approached.

2.3.2.2 Parametric Study

For the selected examples, the parameters used by the model are derived from the material properties as reported in the appropriate references. Due to the difficulties associated with representative sampling and sample disturbances the soil properties obtained from tests should always be critically examined. Therefore, the sensitivity of each soil parameter to any slight variation in soil properties should be fully investigated. Following is a parametric study of all the important parameters used by the model in test simulation under monotonic loading programs.

The influence of cohesion c expressed through parameter $p_o = c \cot \phi$ on the response under drained conditions of both naturally and artificially cemented sands is shown in Figs. 2.7 and 2.8. The values of the cohesion c evaluated by the tests and reported in Refs. 2.3 and 2.4 are 25 kPa for naturally cemented sand, 46 kPa and 220 kPa for artificially cemented sands with 2% and 5% cement respectively. Ignoring the presence of the cohesion between the sand particles ($p_o = 0$ kPa) leads to reduction in the magnitude of the failure loads, whereas the overall stress-strain characteristics shows no significant difference. The reduction of the failure load is more pronounced at lower confining pressures and for sands with a higher percentage of cementation.

Figures 2.9 and 2.10 simulate the undrained behavior of loose sand (2.20) with cohesion. Two sets of results corresponding to confining pressures $p_c = 275$ kPa and $p_c = 550$ kPa and cohesion of $c = 0$ kPa to $c = 100$ kPa are presented.

The sand properties reported in Ref. 2.20 are for cohesionless loose sand. The range of cohesion $c = 0$ kPa to $c = 100$ kPa employed in the parametric study is obtained through analysis of the data for both naturally and artificially cemented sands, reported in Refs. 2.3 and 2.4. The magnitude of the cohesion in naturally cemented sands varies from $c = 0$ kPa to $c = 175$ kPa (Table 2. Ref. 2.3), while, in the artificially cemented sands the cohesion is a function of the percentage of agents providing the cementation, and is regulated by the designer of the mixture.

The effective stress paths for monotonic loading are plotted in the q - p stress space in Figs 2.9(a) and 2.10(a), while the plots of corresponding stress differences q versus axial strain ϵ_1 , are presented in Figs 2.9(b) and 2.10(b).

The influence of cohesion on the response under undrained constraint is as expected. For different confining pressures undrained strength increases with increasing cohesion. It can be further concluded that qualitatively similar response is observed for both confining pressures with undrained strength increasing with increasing confining pressure.

Identical response of cemented loose sand as the one presented above is observed in the results of the undrained triaxial tests performed by Saxena and Lastico in Ref. 2.5. The findings reported are based on the properties of formation called Vincentown Formation, located on a man-made artificial island on the east bank of the Delaware River, within the New Jersey outer coastal plain. The Vincentown Formation is composed of

a cemented fine to medium greenish gray sand with a varying silt content. Due to a lack of sufficient soil properties in Ref 2.5, the evaluation of the required elastoplastic model parameters was not possible. Therefore, the reported undrained triaxial tests are not simulated. However, the results of these tests when compared with the results obtained by simulating the undrained behavior of loose sand (Ref. 2.20) and with added cohesion, lead to the same observations as concluded in Ref. 2.5: "(a) the stress-strain behavior, the pore pressure response, and the stress paths indicate that the cemented loose sands are strain dependent; (b) the cemented soil skeleton initially compresses under a load, with further straining it tends to dilate as demonstrated on the stress path plots; (c) at low axial strain ($\epsilon_1 = 1\%$) Figs. 2.9 and 2.10, the cohesion caused by the cement bonding between particles is the major contributor of strength. The cohesion strength is destroyed around a 1% strain and at the same time the frictional strength becomes predominant."

The influence of m_c (slope of zero dilatancy line) on drained and undrained response of cemented dense (Ref. 2.3) and loose (Ref. 2.20) sands under different confining pressure is presented in Figs. 2.11, and 2.12 respectively. The actual values of parameters m_c and m_f for the examined materials are shown in Table 2-II and Table 2-IV. Numerical predictions on dense naturally or artificially weakly cemented sands at confining pressure of 207 kPa, and cemented loose sand with cohesion $c = 40$ kPa and confining pressures of 275 kPa and 550 kPa are plotted. From the data presented it is evident that the confining pressure does not influence the qualitative material response. A decrease of m_c does not

affect the stress-strain drained behavior, but influences significantly the volumetric changes in the material. It can also be observed that for loose cemented sands by reducing m_c the undrained shear strength increases.

Figure 2.13 describes the influence of varying bulk modulus K on the drained behavior of naturally or artificially cemented (2%) sands. Here, the volumetric strain change is affected by increasing the value of K , while no effect on the stress-strain behavior is observed.

Figures 2.14 and 2.15 describe the undrained behavior of loose sand with cohesion of 40 kPa and varying bulk modulus K for confining pressures of 275 kPa and 550 kPa respectively. The value of the material shear modulus G was kept constant. The corresponding stress difference versus axial strain ϵ_1 , are presented in Figs. 2.14(b) and 2.15(b) for both confining pressures. The results show the same qualitative trend. Increase in the value of K results in more significant generation of pore pressure prior to subsequent reduction.

A common conclusion for all the undrained cases examined under monotonic load increase, for material with or without cohesion, is that initial generation of pore pressure is followed by subsequent reduction due to plastic dilatancy of the material.

The influence of A (hardening constant) on drained response of the naturally weakly cemented sand and artificially cemented (2%) sand under confining pressure of 207 kPa is presented in Fig 2.16. Numerical predictions on naturally and artificially cemented sand for $A = 0.0001$ and $A = 0.01$ are plotted. From the data presented it is evident that the

hardening constant A strongly influences the stress-strain as well as the volumetric change behavior.

2.3.3 Reversal Loading

2.3.3.1 Comparison with Experimental Results

The results of model simulation of a cyclic triaxial test reported by Ishihara, Tasuoka, and Yasuda (2.21) are summarized in Figs 2.29 and 2.30. The physical properties of the Fuji sand are reported in the above reference and material properties used in model simulation are determined from monotonic test results. The material parameters which could not be directly determined from the test results are estimated.

Figure 2.17 represents comparisons of measured and predicted undrained paths in strain-controlled static test cycled with constant amplitude. The sensitivity of the predictions to the value of elastic shear modulus G was examined by employing $G = 160 \text{ kg/cm}^2$ (Fig. 2.17a) and $G = 120 \text{ kg/cm}^2$ (Fig. 2.17b).

The corresponding stress-strain diagram of this strain-controlled cyclic undrained test and the model simulation are presented in Figs. 2.17(c) and 2.17(d).

The overall quality of simulation results are reasonable. Pore pressure is generated upon both loading and unloading. The rate of pore pressure generation gradually decreases. Stress amplitudes decrease with decreasing effective confining pressure.

By analyzing the experimental results a conflicting behavior can be observed as:

- 1) during the loading phase negative pore pressure develops within the material (which is unusual), and
- ii) the number of cycles to produce liquefaction seems excessive and the latter is very sensitive to methods of sample preparation.

2.3.3.2 Parametric Study

Parameters influencing the cyclic behavior of pure and cemented sand are evaluated next. The effect of the cohesion c , bulk modulus K , and the kinematic hardening γ are examined on the behavior of two samples of loose sand, reported in Refs. 2.20 and 2.21. Cementation is artificially introduced by assuming different values of cohesion. All the other parameters remain the same as those defined in Tables 2-IV and 2-V.

Effective stress paths for an undrained two-way strain controlled test on loose (Ref. 2.21) and cemented Fuji sand are presented in Figs. 2.18, 2.19 and 2.20. The confining pressure in all of the examined cases is $p_c = 156.6$ kPa, the considered cohesion is $c = 0.0$ kPa, $c_s = 30$ kPa and $c = 50$ kPa, and the value of the kinematic hardening parameter γ is 2, 4 and 8.

From the presented results it can be observed that increase in the value of γ decreases the rate of pore pressure generation in both loose and cemented sand. Also the rate of pore pressure generation is reduced by larger cohesion between the particles of the examined sand. The reduction is quite significant during the early stages of loading program.

As in the case of monotonic loading programs presented previously the effect of the G/K ratio on the cyclic behavior of cemented sand is shown in Fig. 2.21. For the value of $\gamma = 4$ and $c = 30$ kPa the plots of effective stress paths are presented. An increase of K (decrease of G/K) decreases the rate of pore pressure generation. This is more pronounced in the early stages of the loading program.

Fig. 2.22 simulates the behavior of cemented sand of Ref. 2.20. Effective stress paths for strain-controlled cyclic undrained test with cohesion of $c = 0$ kPa and $c = 50$ kPa and initial confining pressure of $p_c = 550$ kPa are presented. Two different types of loading programs are presented: (a) material compressed at the virgin loading Fig. 2.22(a); and (b) material expands at the virgin loading Fig. 2.22(b). The stress-strain diagrams corresponding to the above effective stress paths are shown in Figs. 2.22(c) and 2.22(d). In both cases of loading the rate of pore pressure generation is the same. However, in the case of initial expansion of the material during the loading process the decrease of the stress amplitudes is more regular.

2.4 CONCLUDING REMARKS

The constitutive relation presented in this chapter allows modelling the behaviour of naturally or artificilly cemented sand with calcite, gypsum cement or other agents. For vanishing cohesion the model proves to be applicable for both loose and dense states of packing of a pure sand.

The formulation utilizes a combined isotropic-kinematic hardening law. Such a law allows modelling anisotropy resulting from nonhomogeneity of deformation at the microscale (residual stress anisotropy). The yield locus is assumed to be geometrically similar to the bounding surface and is allowed to translate and rotate within the domain enclosed by the bounding surface. The kinematic constraints imposed on the evolution of the yield surface are such that at the limit both the yield and the bounding surface became tangential to each other, the common point being the stress point itself.

The numerical examples provided in Section 2.3 support the major conceptual assumption involved. Cemented sand of a certain initial density can be modelled as a pure sand of a higher density with internal cohesion. In the present framework the differences in qualitative trends between loose and dense sand are largely affected by the degree of separation between the zero-dilatancy and failure envelopes. It seems that, in order to improve the effectiveness of the present concept, Eq. 2.10 defining the strain-hardening characteristics should be re-examined. In cemented material the characteristics may display sensitivity to the confining pressure and transition from stable to unstable response. Unfortunately, due to lack of appropriate experimental data, such assessment is at present impossible.

The above described concept has been implemented in a finite element code. Subsequent chapters specify the details of finite element formulation and provide the solutions to a number of boundary-value problems of practical significance.

PARAMETERS	CONFINING PRESSURES				
	69 kPa	138 kPa	207 kPa	276 kPa	414 kPa
failure line m_f	1.68	1.56	1.53	1.64	1.52
dilatancy line m_c	1.50	1.42	1.32	1.36	1.35
parameter p_o (kPa)	29.7	29.7	29.7	29.7	29.7
shear modulus G (kPa)	25112	38062	48546	57693	73583
bulk modulus K (kPa)	33487	50750	64728	76924	110374
hardening constant A	0.0014	0.0014	0.0014	0.0014	0.0018

TABLE 2-I. Values of parameters for proposed elasto-plastic model of weakly naturally cemented sands

PARAMETERS	CONFINING PRESSURES		
	103 kPa	207 kPa	414 kPa
slope of the failure line m_f	1.51	1.51	1.39
slope of the dilatancy line m_c	0.91	1.20	1.05
parameter p_o (kPa)	54.8	54.8	54.8
initial shear modulus (kPa)	35117	46925	61087
initial bulk modulus (kPa)	45017	61466	81087
hardening constant A	0.0012	0.0012	0.0012

TABLE 2-II. Values of parameters for proposed elasto-plastic model for artificially cemented sands with 2% cement at relative density 74%

PARAMETERS	CONFINING PRESSURES		
	0.1 MPa	0.3 MPa	0.5 MPa
slope of the failure line m_f	1.72	1.74	1.72
slope of the dilatancy line m_c	1.69	1.65	1.69
parameter p_0 (kPa)	260	260	260
initial shear modulus (kPa)	185000	280000	555000
initial bulk modulus (kPa)	209000	295000	585000
hardening constant A	0.0014	0.0018	0.0018

TABLE 2-III. Values of parameters for proposed elasto-plastic model for artificially cemented sands with 5% cement at 100% Maximum Proctor density

PARAMETERS	CONFINING PRESSURES	
	275 kPa	550 kPa
slope of the failure line m_f	1.2	1.2
slope of the dilatancy line m_c	1.15	1.15
parameter p_0 (kPa)	0	0
initial shear modulus (kPa)	29430	29430
initial bulk modulus (kPa)	29430	58800
hardening constant A	0.0015	0.0015

TABLE 2-IV. Values of parameters for proposed elasto-plastic model for pure sands of Ref. 2.20.

PARAMETERS	VALUE
slope of the failure line m_f	1.56
slope of the dilatancy line m_c	1.29
parameter p_0 (kg/cm ²)	0.0
initial shear modulus (kg/cm ²)	160
initial bulk modulus (kg/cm ²)	240
hardening constant A	0.0025
kinematic hardening γ	8.0
initial confining pressure (kg/cm ²)	1.595

Table 2-V. Values of parameters for proposed elasto-plastic model for pure sand of Ref. 2.21

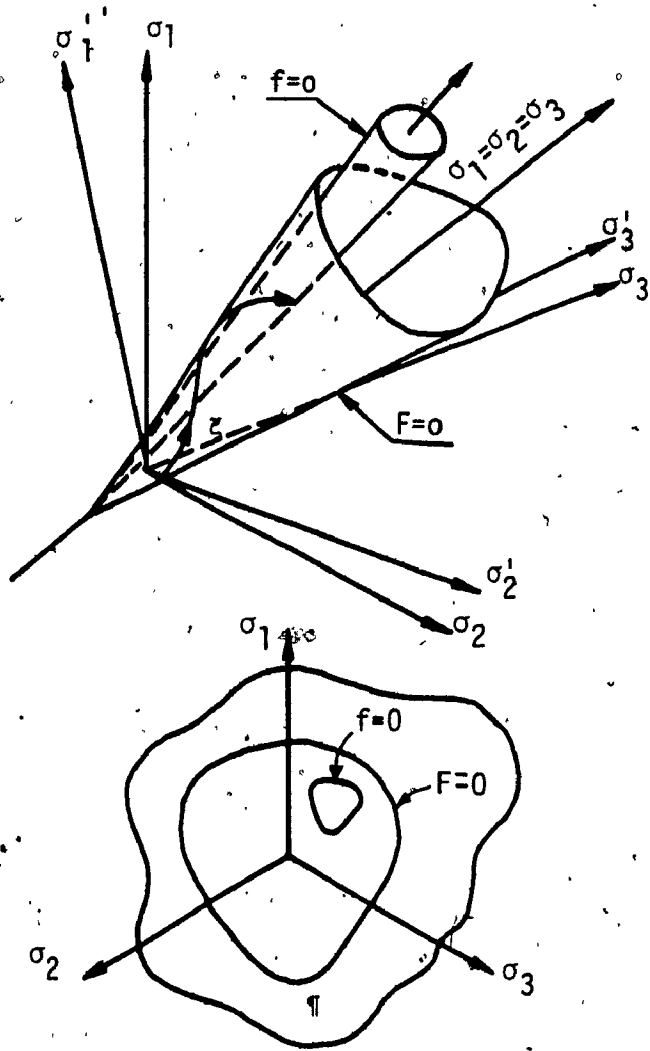


FIG. 2.1: The yield and the bounding surface in principal stress space

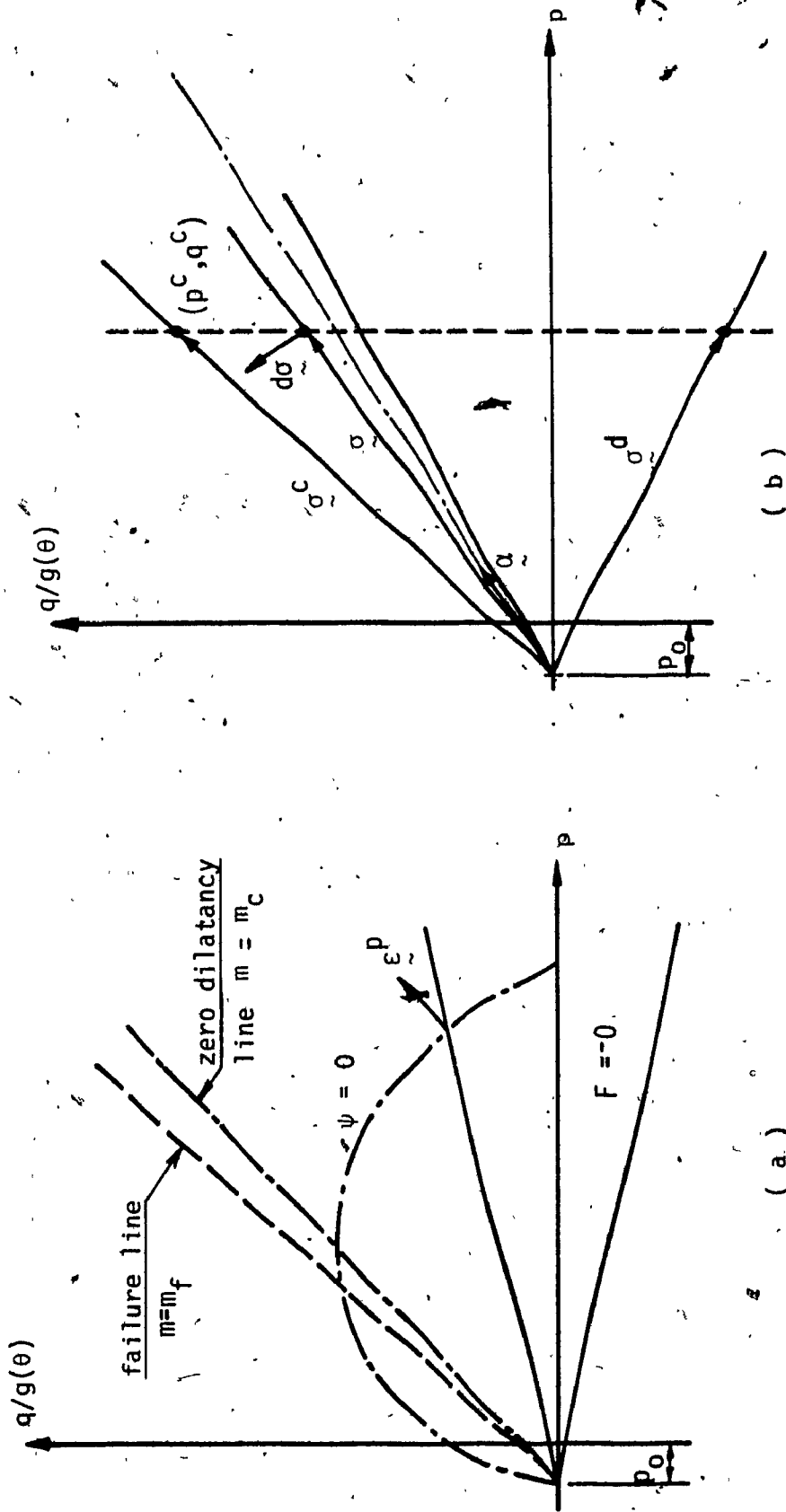


FIG. 2.2; (a) The bounding $F=0$, the plastic potential $\psi=0$ surfaces, and, (b) the location of the conjugate and datum stress points in the meridional plane ($q/g(\theta), p$)

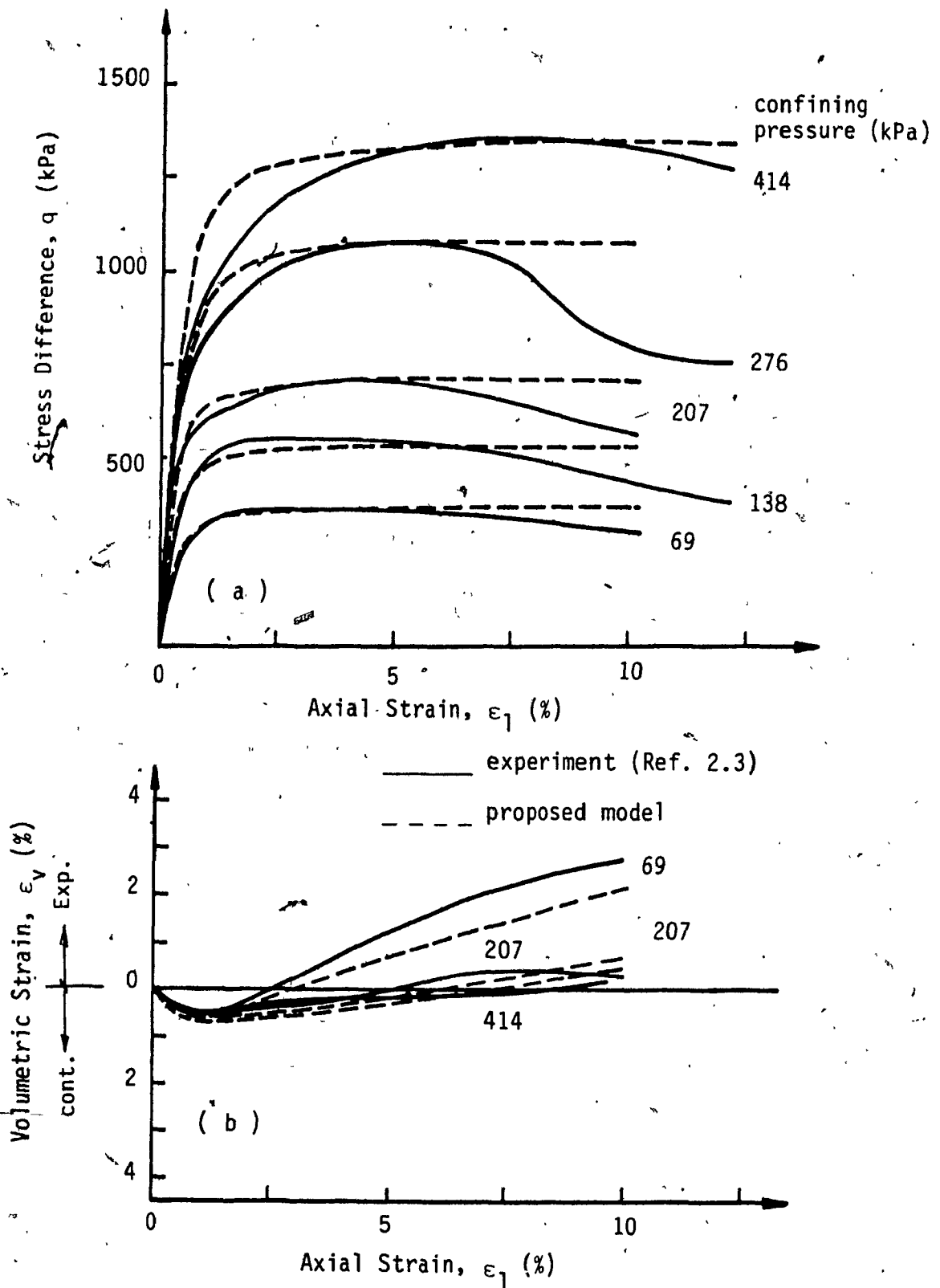


FIG. 2.3: Comparison of model behavior with experimental data for naturally weakly cemented sand, (a) Stress difference versus axial strain, (b) volumetric versus axial strain

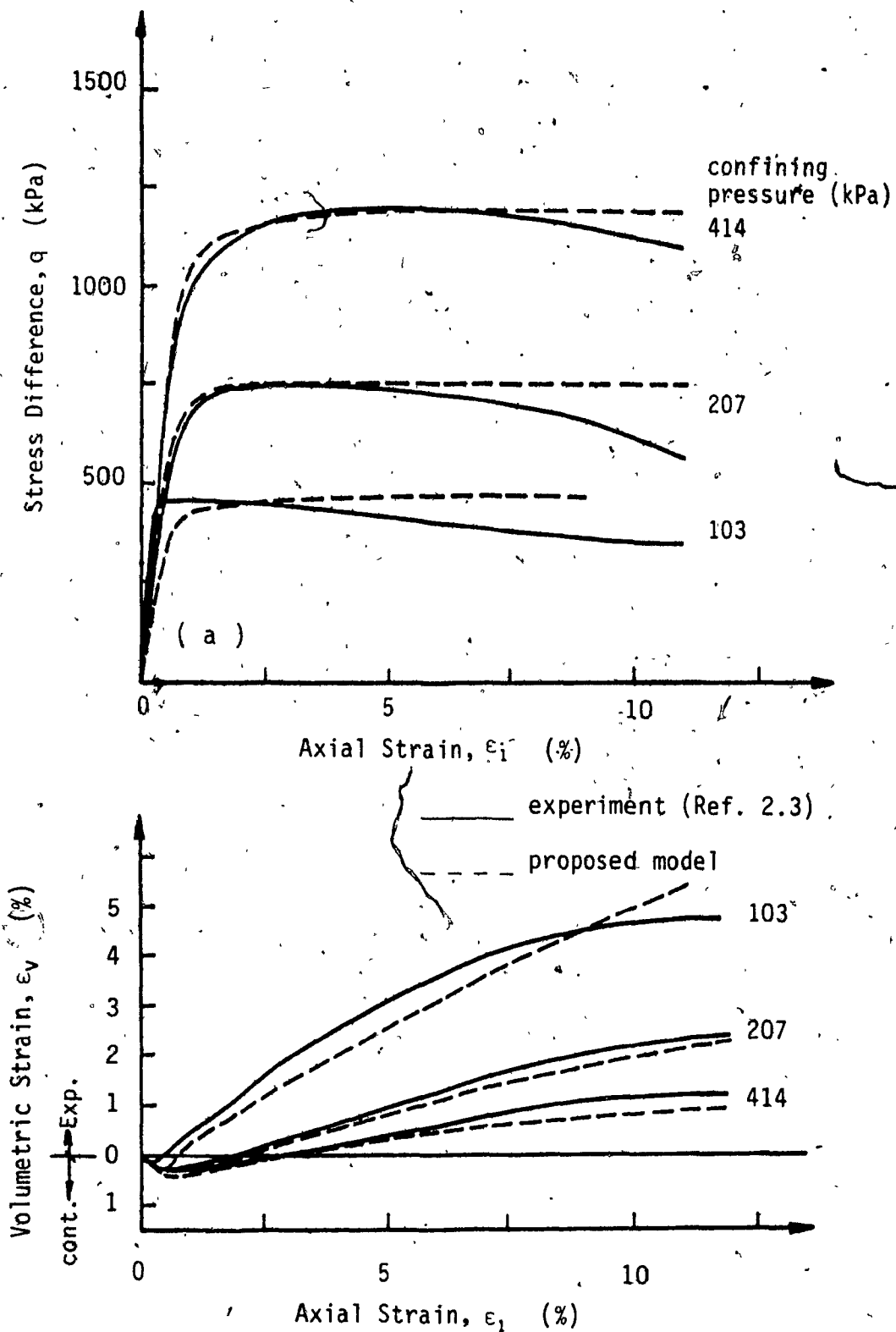


FIG. 2.4: Comparison of model behavior with experimental data; Artificially cemented sand with 2% cement at 74% relative density, (a) Stress difference versus axial strain, (b) volumetric versus axial strain.

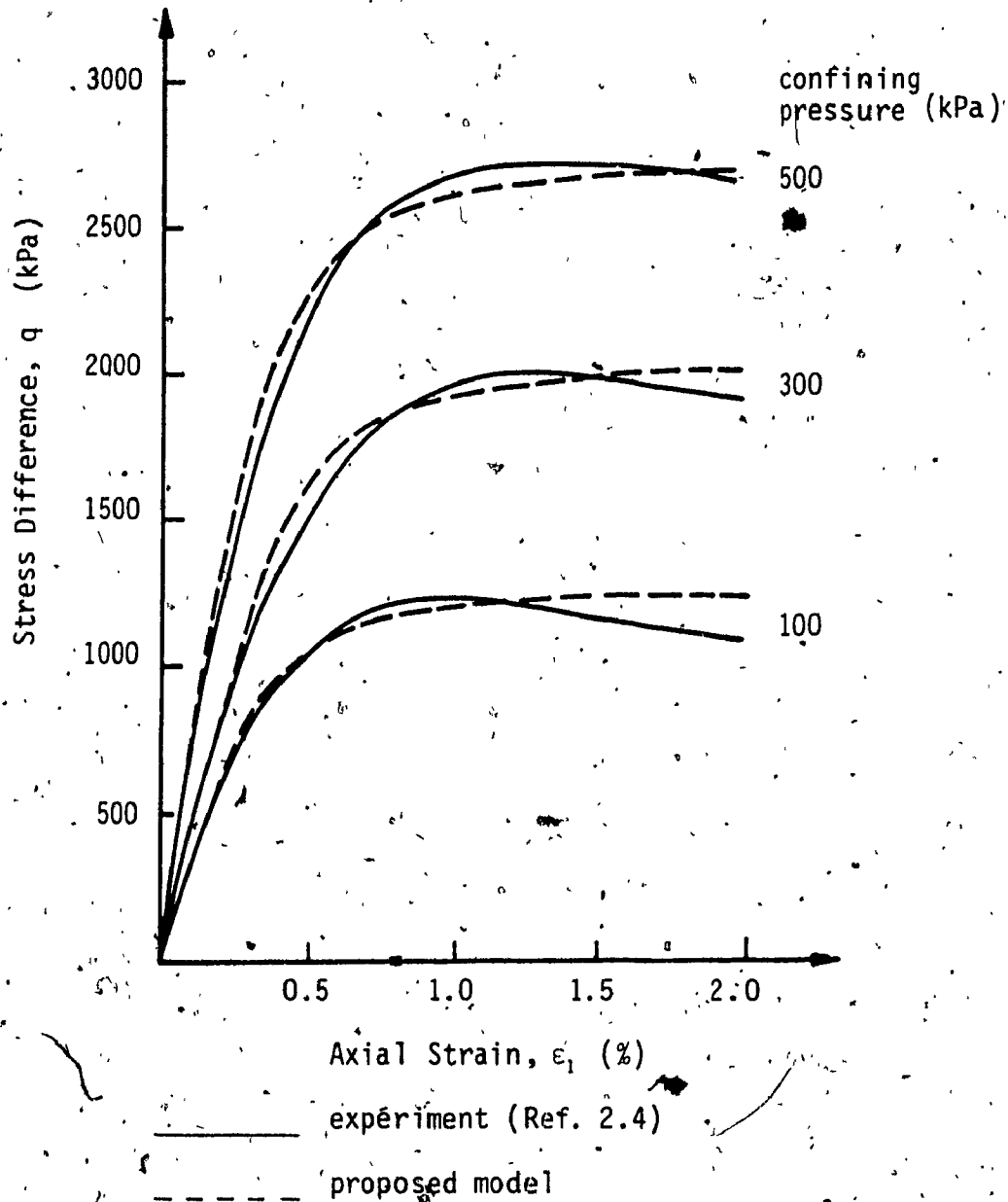


FIG. 2.5: Comparison of model behavior with experimental data; Artificially cemented sand with 5% cement at 100% Proctor Density

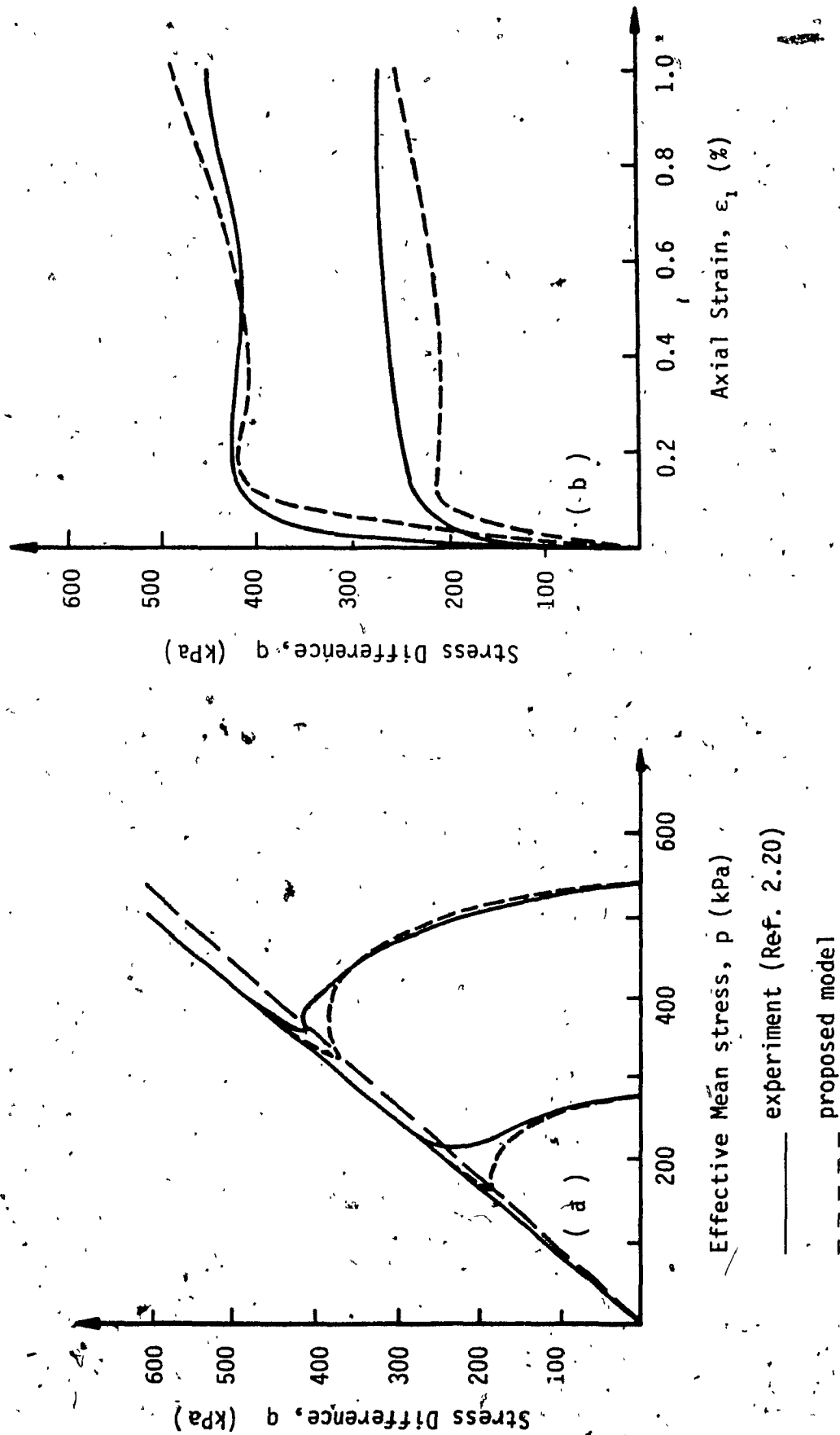


FIG. 2.6: Comparison of model behavior with experimental data on loose sand; (a) Effective stress paths (b) stress difference versus axial strain for the stress paths in (a).

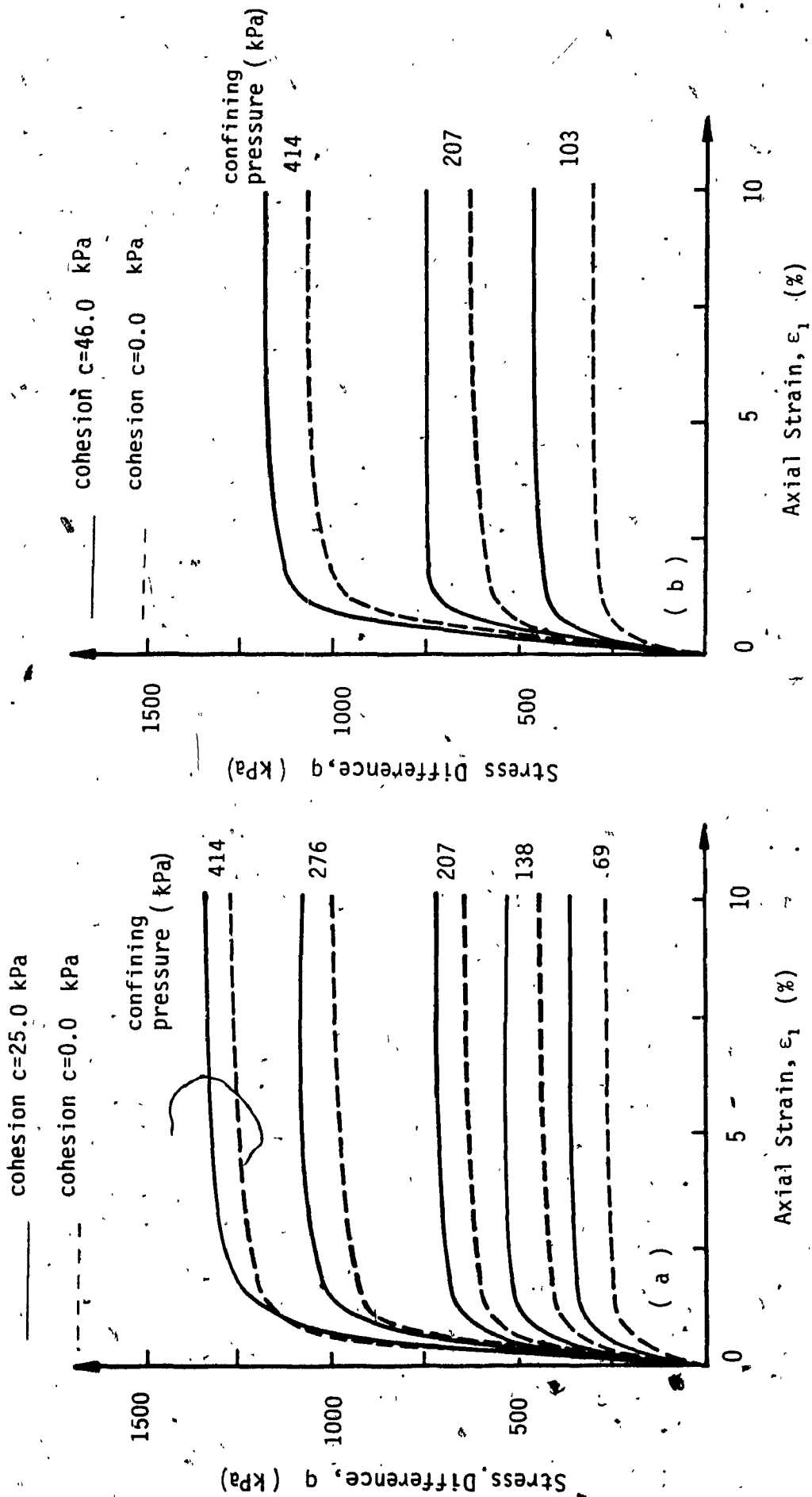


FIG. 2.7: Influence of the cohesion on drained material behavior at different confining pressure for, (a) naturally cemented sand (Ref. 2.3) and (b) artificially cemented sand with 2% cement (Ref. 2.3)

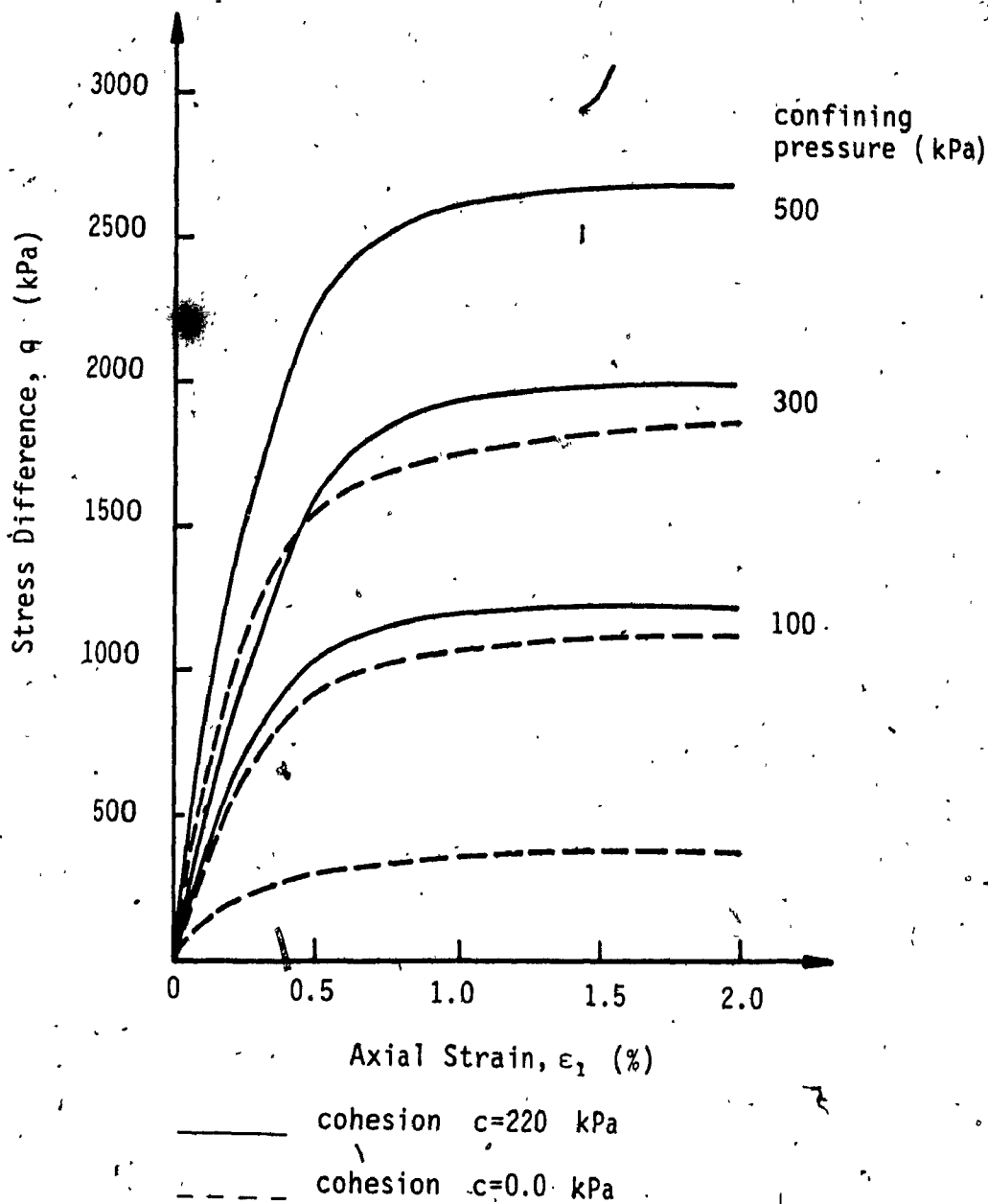


FIG: 2.8: Influence of cohesion on drained behavior of artificially cemented sand with 5% cement at different confining pressures.

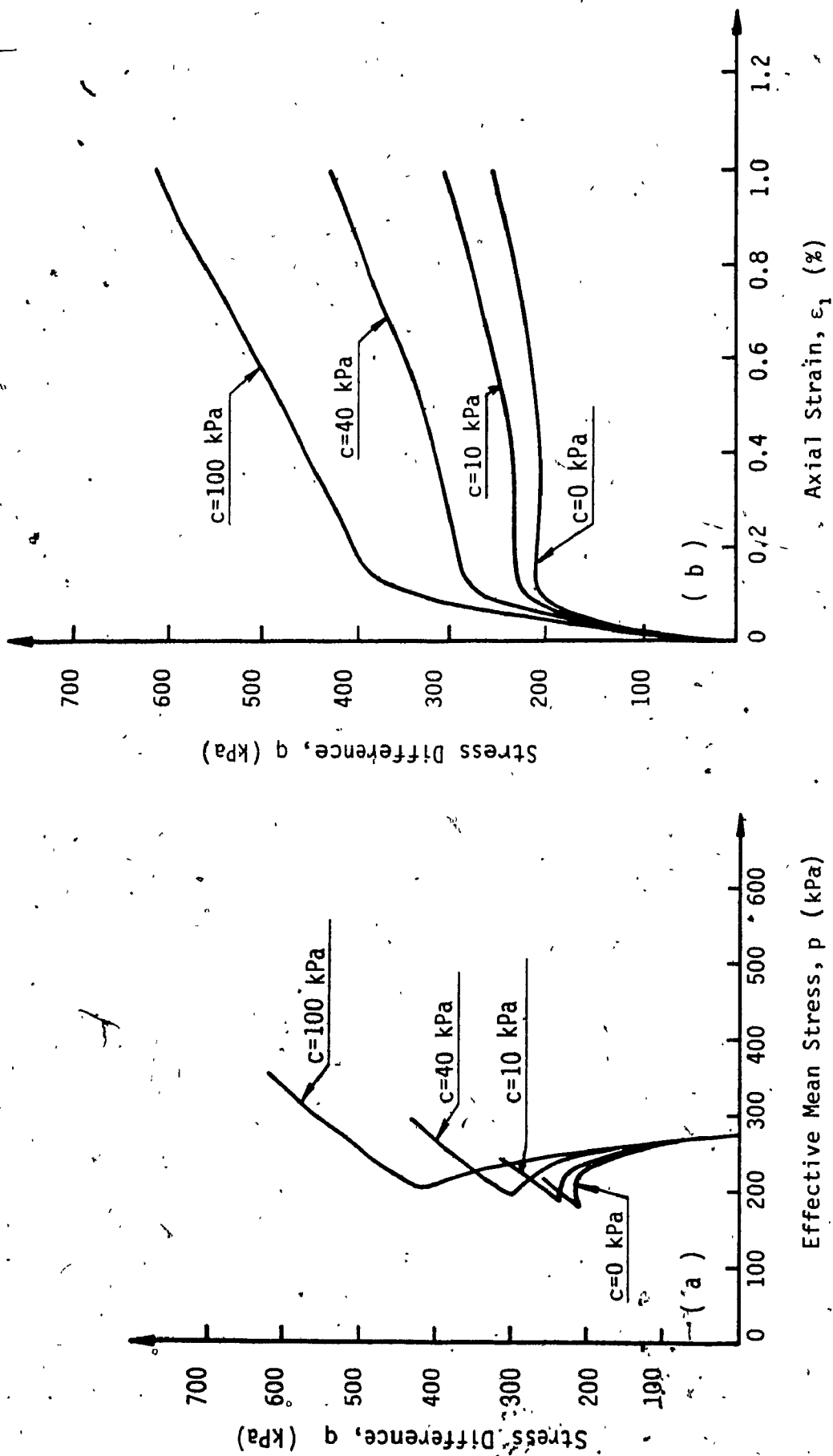


FIG. - 2.9: Influence of cohesion on the response under undrained constraint of loose sand at initial confining pressure of 275 kPa (Ref. 2.20), (a) Effective stress paths, (b) stress difference versus axial strain for the stress puts in (a).

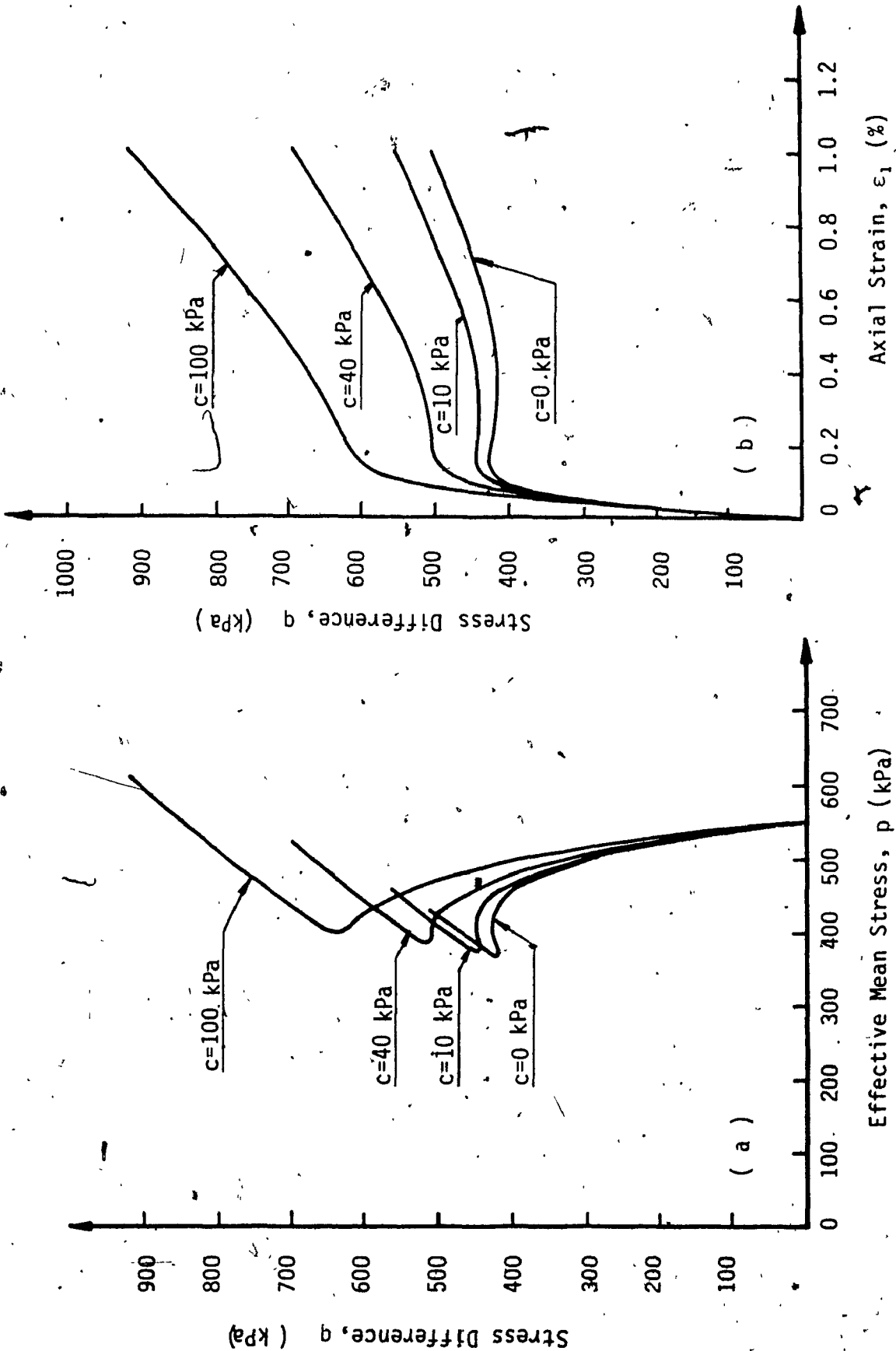


FIG. 2.10: Influence of cohesion on the response under undrained constraint of loose sand (Ref. 2.20) at initial confining pressure of 550 kPa
(a) Effective stress paths, (b) stress difference versus axial strain for the stress paths in (a).

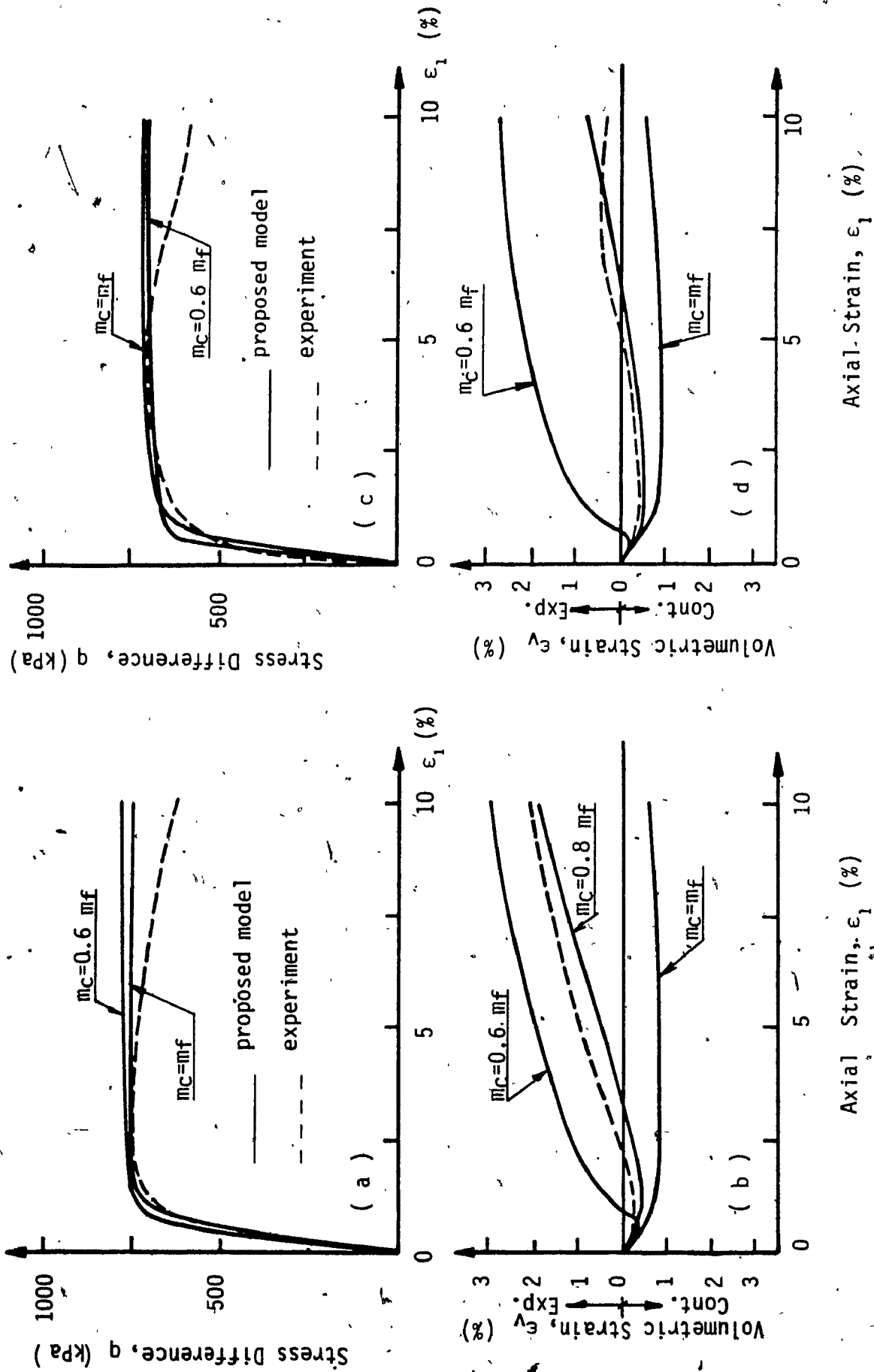


FIG. 2.11: Influence of the parameter m_c on the prediction of drained behavior of, (a) and (b) artificially cemented sand 2%, (c) and (d) naturally cemented sand (Ref. 2.3).

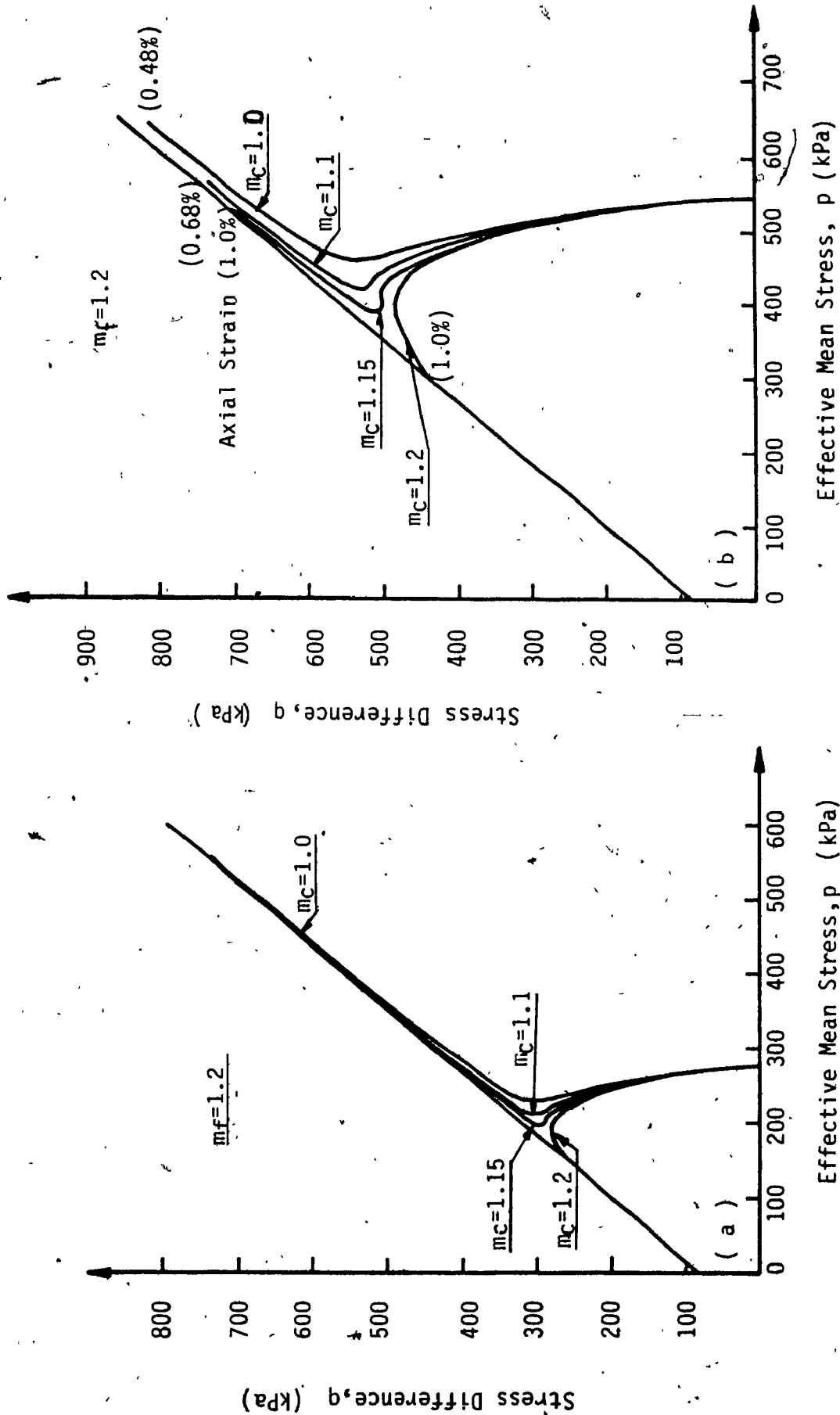


FIG. 2.12: Influence of m_c on the effective stress paths of undrained behavior of sand (Ref. 2.20) with added cohesion $c=40$ kPa and initial confining pressure, (a) 275 kPa, (b) 550 kPa.

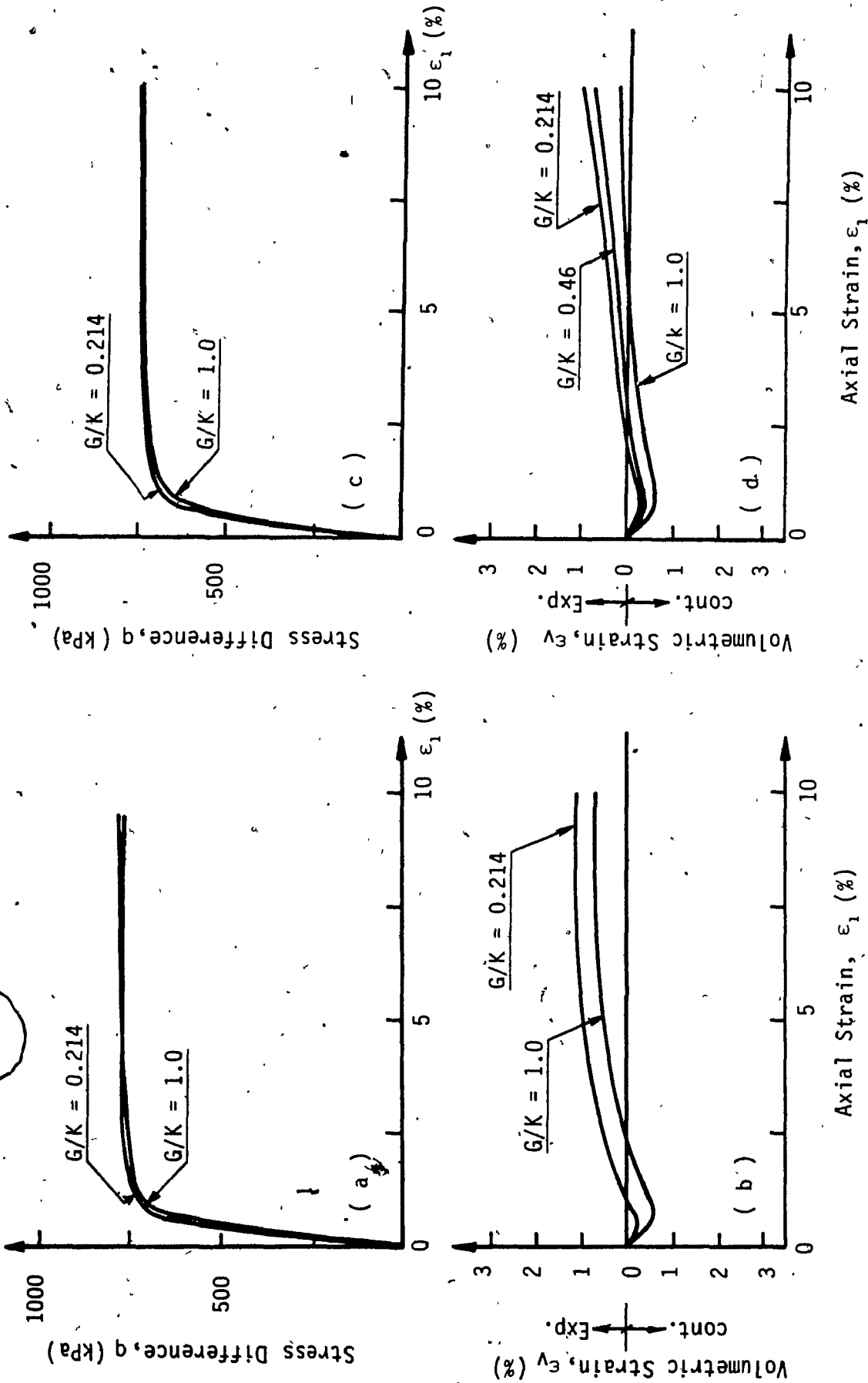


FIG. 2.13: Influence of the bulk modulus on the prediction of drained behavior of; (a) and (b) artificially cemented sand with 2% cement; (c) and (d) naturally cemented sand (Ref. 2.3).

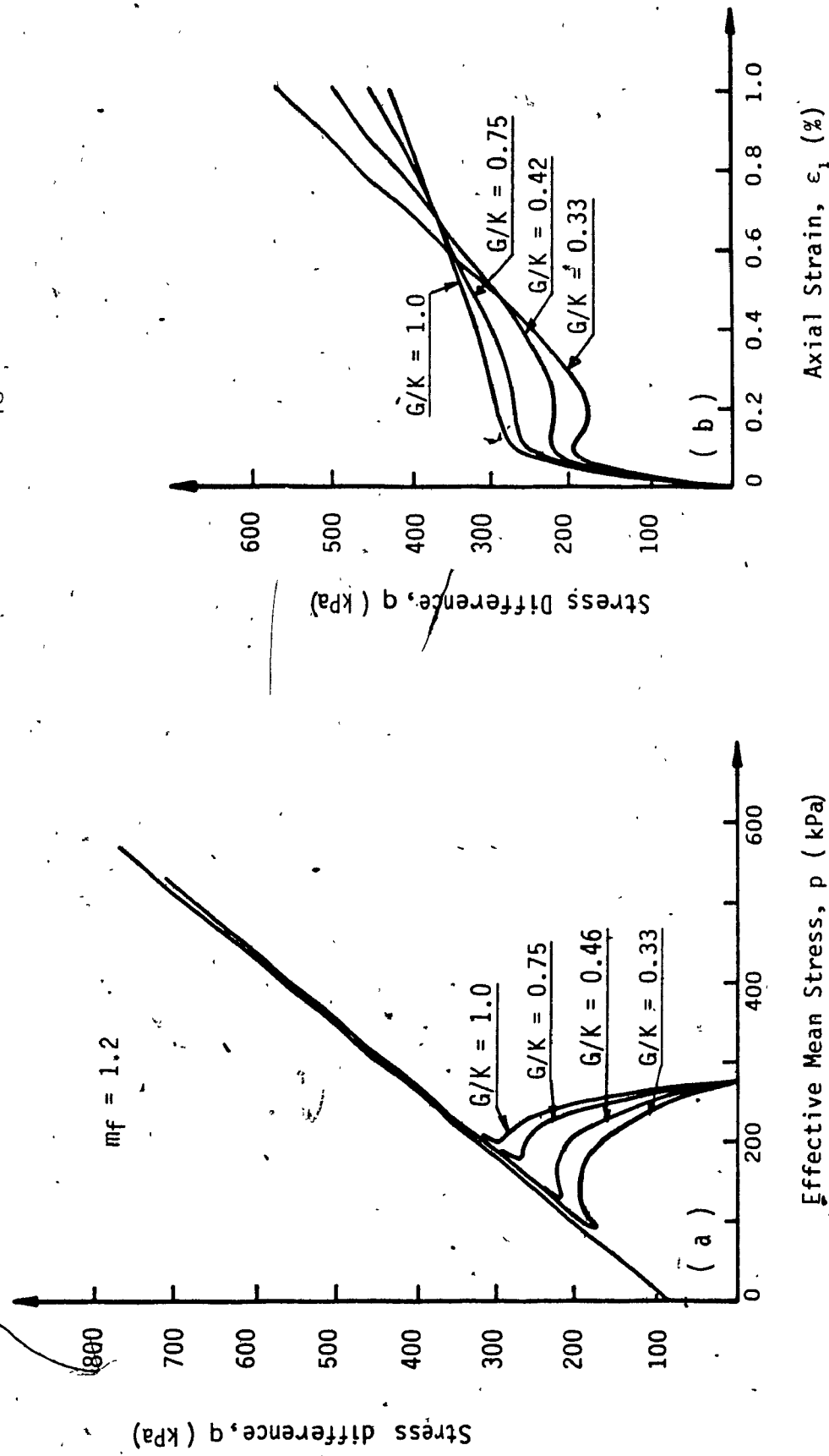


FIG. 2.14: Influence of the bulk modulus on the prediction of undrained behavior of loose sand (Ref. 2.20) with added cohesion $c=40$ kPa and initial confining pressure of 275 kPa strain for the stress paths in (a).

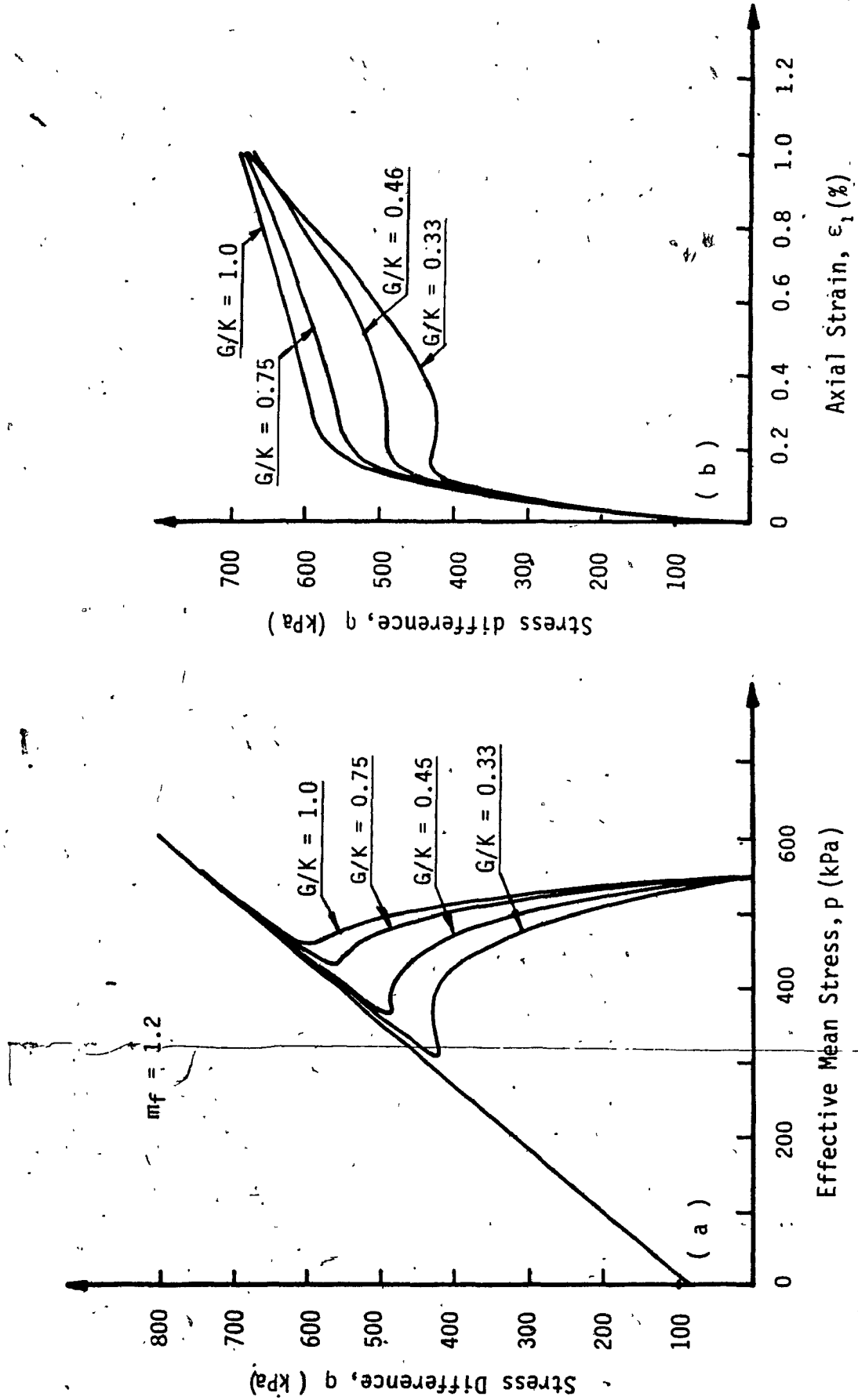


FIG. 2.15: Influence of the bulk modulus on the prediction of undrained behavior of loose sand (Ref. 2.20) with added cohesion $c=40$ kPa and initial confining pressure of 550 kPa (a) Effective stress paths, (b) stress difference versus axial strain for the stress paths in (a).

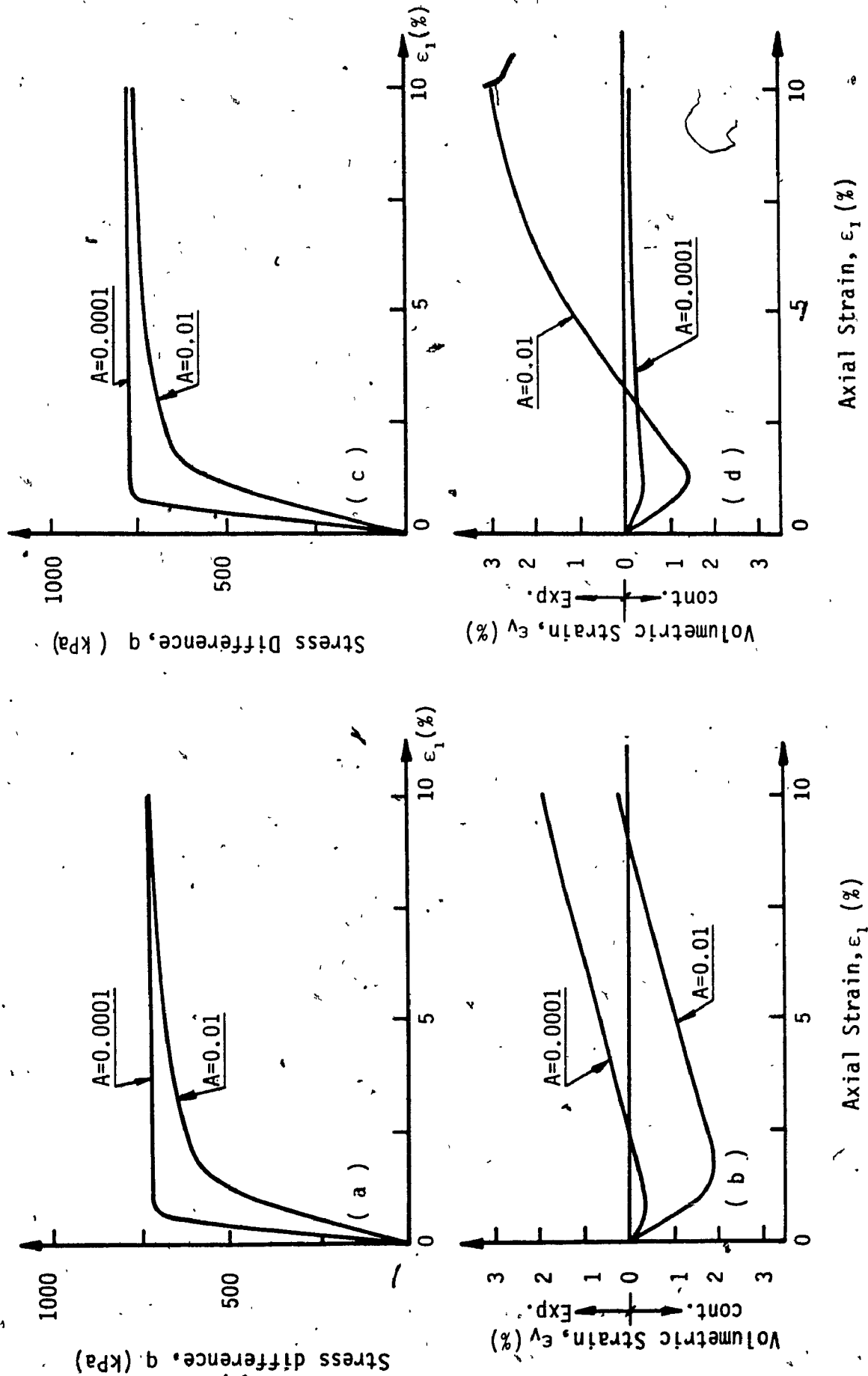


FIG. 2.16: Influence of the hardening parameter A on drained behavior of, (a) and (b) naturally cemented sand, (c) and (d) artificially cemented sand; both at initial confining pressure of 207-kPa

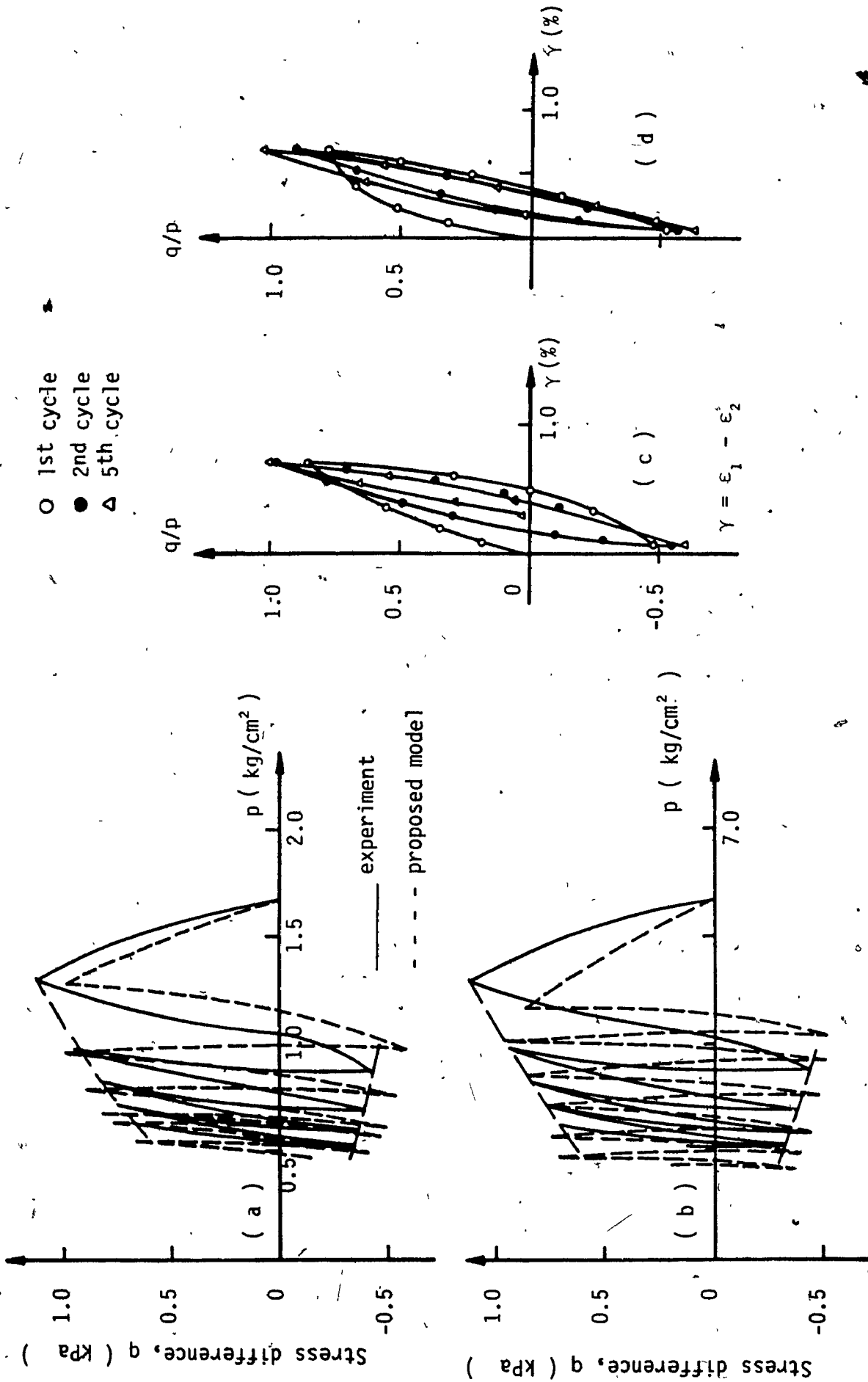


FIG. 2.17: Effective stress path for strain controlled cyclic undrained test; Effective stress paths for shear modulus. (a) $G=160$ kg/cm² (b) $G=120$ kg/cm²; Stress-Strain diagrams, (c) Experiment (Ref. 2.21); (d) Model Simulation for shear modulus $G=120$ kg/cm².

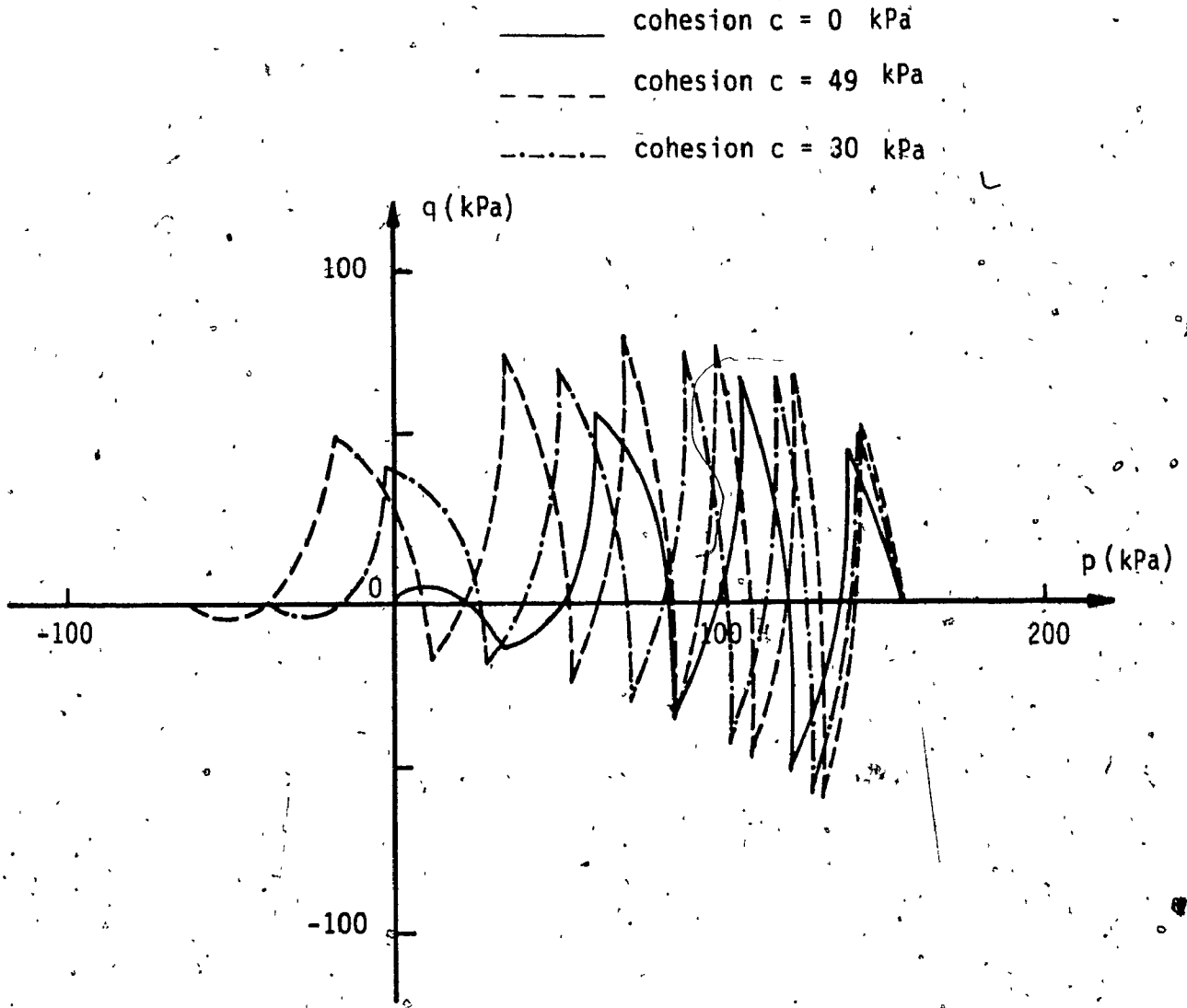


FIG. 2.18: Effective stress path for an undrained two-way strain controlled test; on loose and cemented Fuji river sand (Ref. 2.21), for kinematic hardening parameter $\gamma = 2.0$.

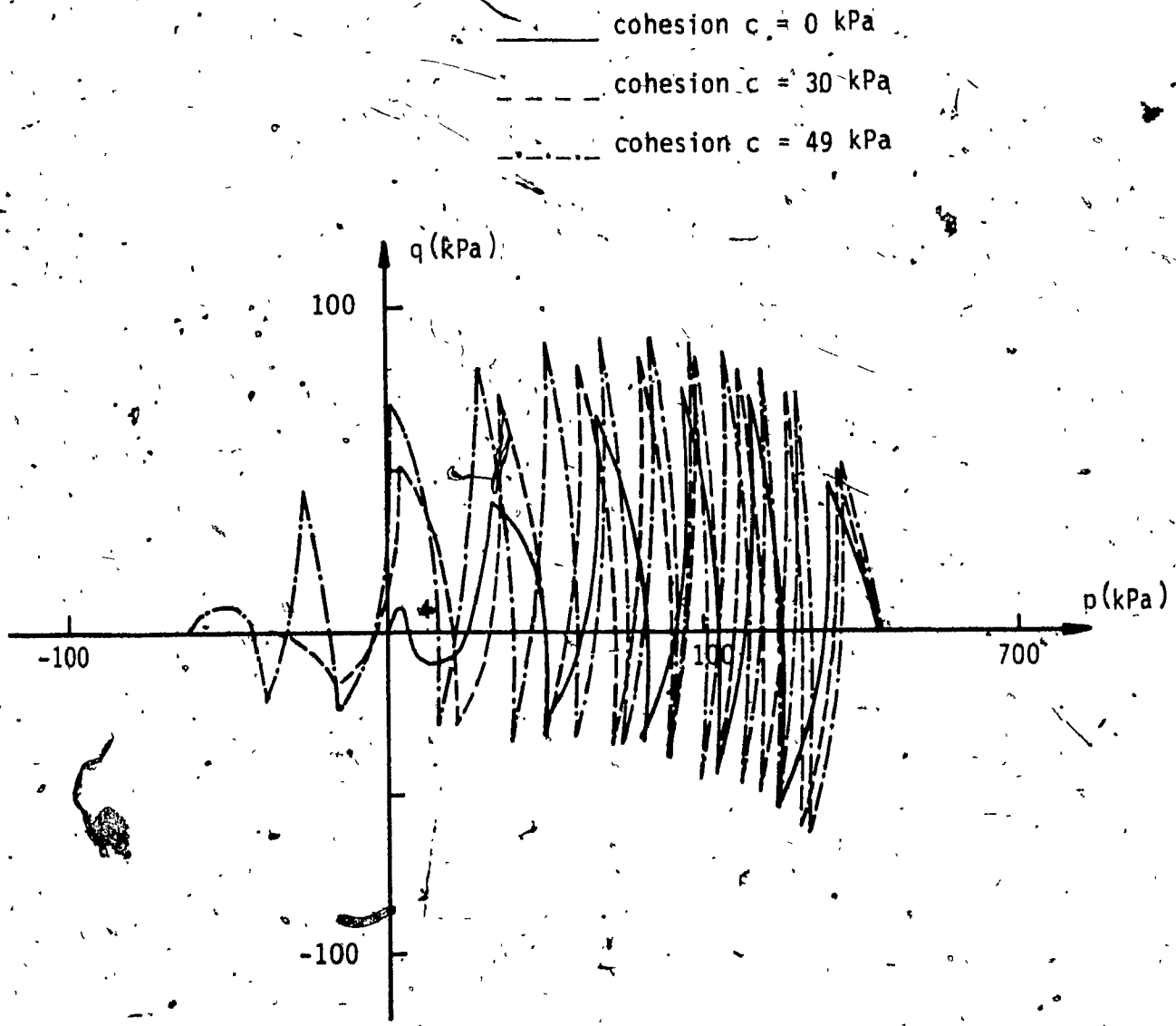


FIG. 2.19: Effective stress paths for an undrained two-way strain controlled test; on loose and cemented Fuji river sand (Ref. 2.21), for kinematic hardening parameter $\gamma = 4.0$.

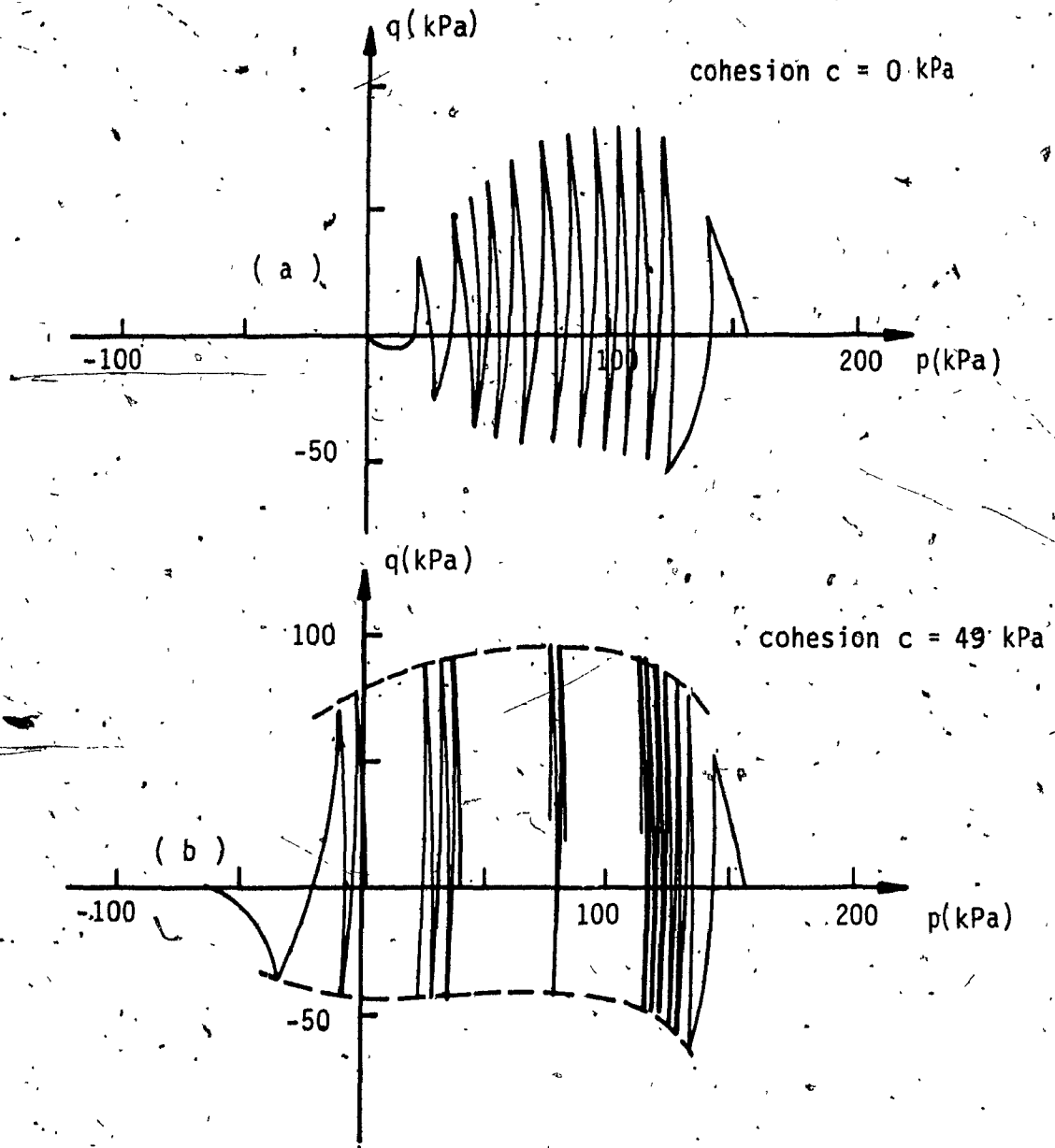


FIG. 2.20: Effective stress paths for an undrained two-way strain controlled test on loose and cemented Fuji river sand (Ref. 2.21), for kinematic hardening parameter $\gamma = 8.0$.

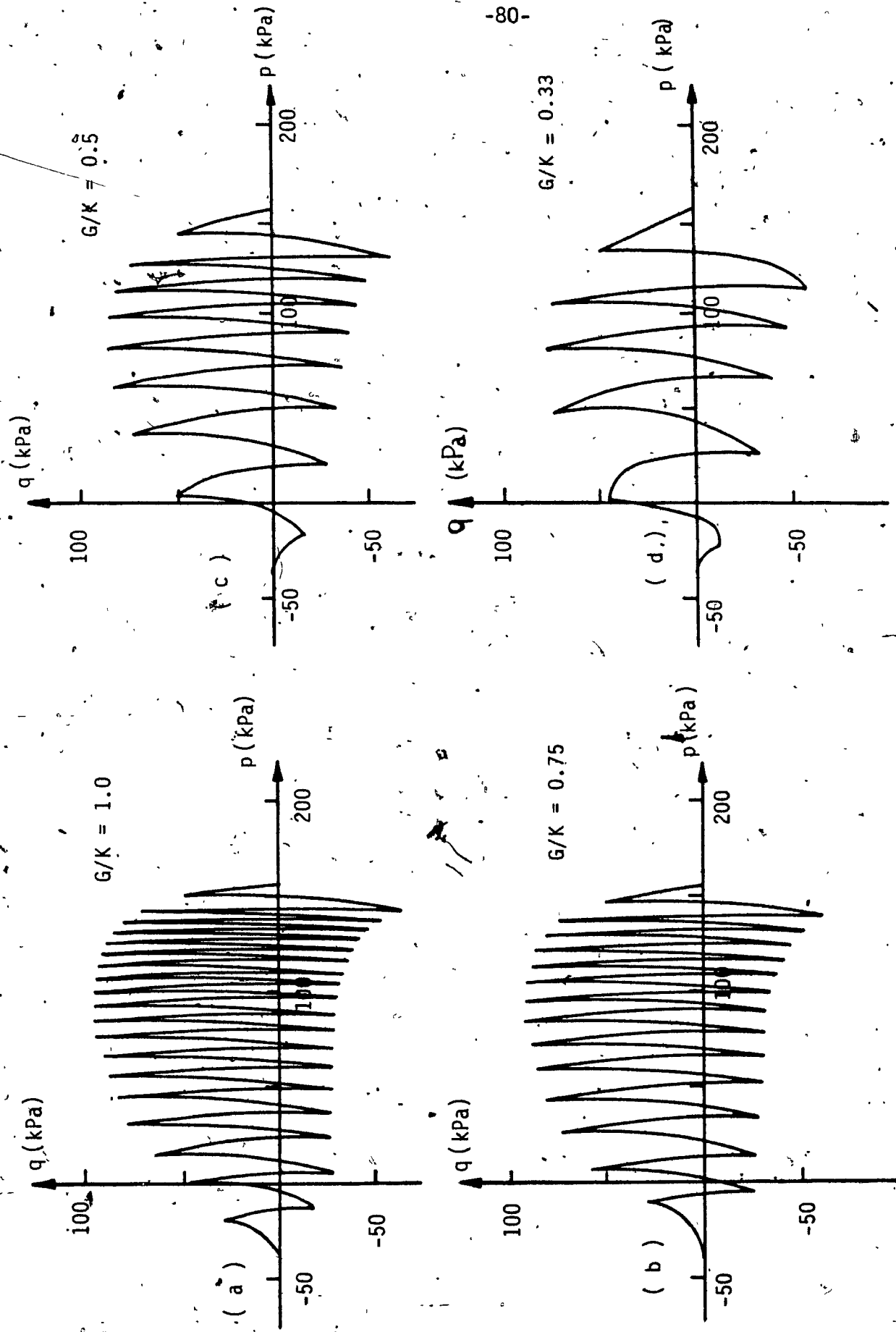


FIG. 2.21: Influence of the bulk modulus on the effective stress path on cemented Fuji river sand (Ref. 2.21), with assumed cohesion $c = 30$ kPa and kinematic hardening parameter $\gamma = 4.0$. (a) $G/K = 1$; (b) $G/K = 0.75$; (c) $G/K = 0.5$, and (d) $G/K = 0.33$.

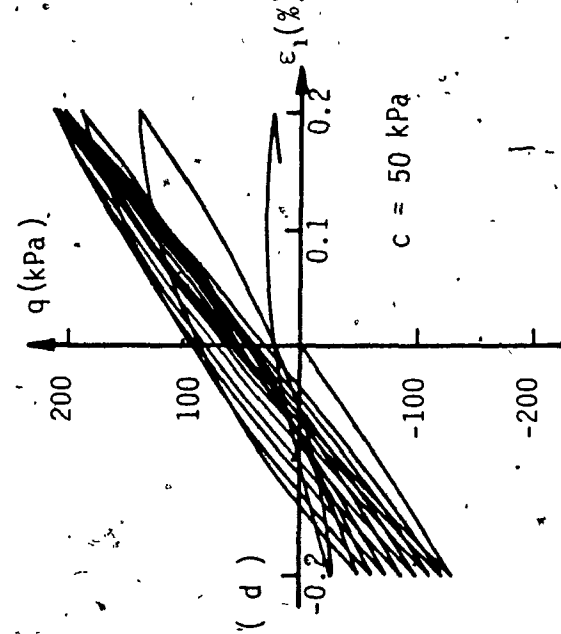
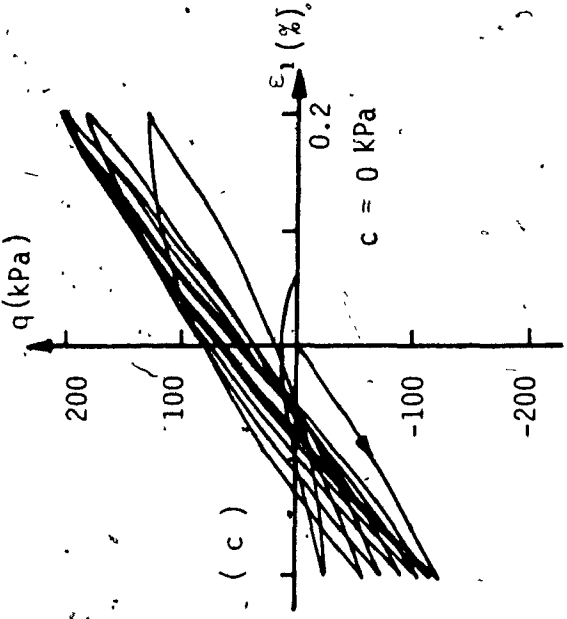
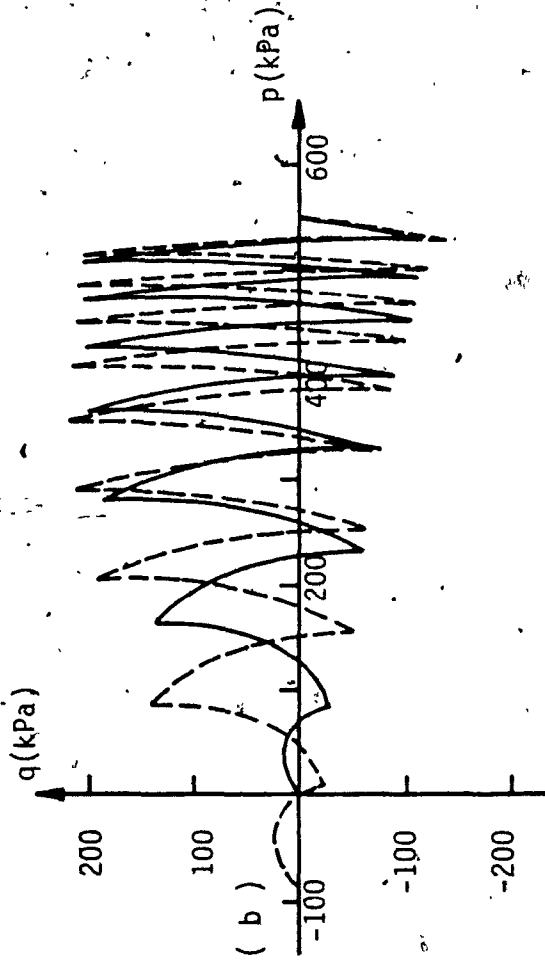
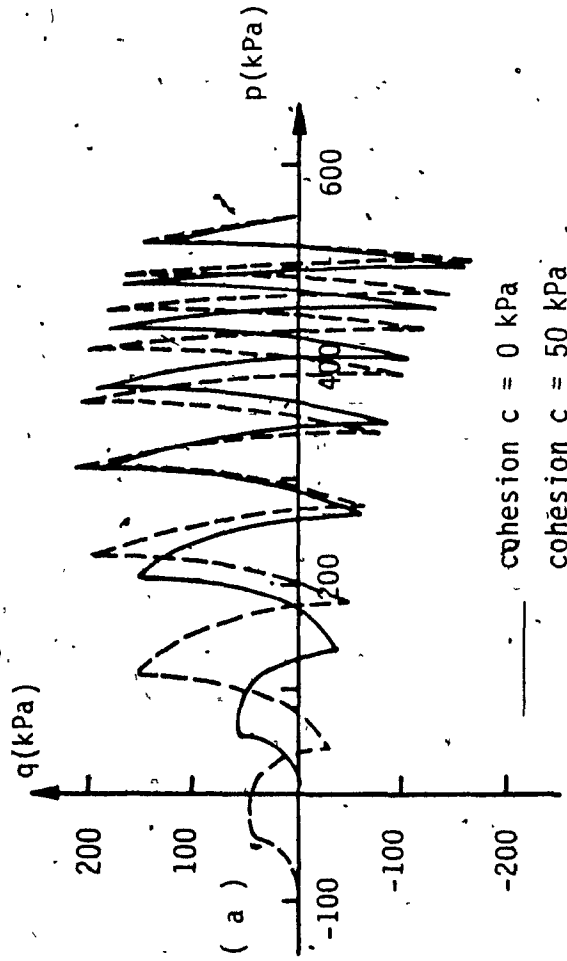


FIG. 2.22: Effective stress paths for (a) loose sand (Ref. 2.20) compressed at virgin loading; (b) loose sand (Ref. 2.20) expands at virgin loading; and stress strain diagram for strain controlled test in (b) for (c) cohesion of $c=0$ kPa; and (d) cohesion of $c=50$ kPa.

CHAPTER III

3.0 FINITE ELEMENT FORMULATION

3.1 INTRODUCTION

With the present state of development in computational methods, inadequate material models are often the major factor in limiting the capability of stress analysis for soils. Unfortunately, generally accepted constitutive relations for soil under triaxial states of stress do not exist. Nevertheless, there exists a large variety of models which have been proposed in recent years to model the most significant aspects of soil behavior such as nonlinearity, path dependency and shear dilatancy, among others [1.13. 1.53].

The development of constitutive relations to express real soil behavior is a difficult task. The complexity of the model requires considerable effort in its implementation to any numerical algorithm. Finite element techniques employing elastic or nonlinear elastic models have been used widely in the past [1.54, 1.64] and considerable experience has been accumulated in this area. For elasto-plastic constitutive relations (including the proposed model), on the other hand, the complexities of existing formulations and the problems with the identification of soil parameters make many of these models rather difficult to implement in practical problems.

Therefore, the objective of this chapter is to incorporate into an existing finite element the elasto-plastic constitutive relations derived in Chapter II, to implement the resulting finite element in a

computer program, and to present an elaborate procedure for evaluation of soil parameters required by the model.

The verification phase of the developed model outlined two critical points in the analytical proceedings simulating reversal loading programs. At the onset of unloading following loading step, and at the onset of reloading following unloading step, either divergence or considerably large number of iterations for convergence were required. To prevent divergence and reduce the required execution time a modification of the computation process is introduced. At the end of any loading or unloading phase the state of stress is memorized (stored on tape). In the following unloading or reloading step of the loading program the memorized state of stress is introduced as an initial condition, and the bounding and the yield surface are adjusted accordingly.

The implemented modification limits the application of the proposed formulation to monotonic and relatively regular cyclic loading programs. Also a pure elastic behavior of the soil during reversal loading cannot be simulated.

3.2 REVIEW OF FINITE ELEMENT ANALYSIS

3.2.1 Formulation of the Element Stiffness Matrix

The basic step in the formulation of a model in any finite-element analysis is the derivation of element stiffness matrix K . This matrix relates the nodal displacement vector δ to the nodal force vector p . In the case of incremental stress-strain relations of an element the element stiffness matrix relates the increments of nodal displacement vector $d\delta$

to the increments of nodal force vector $d\mathbf{p}$. To derive this relation the compatibility of strains, equilibrium of stresses, and stress-strain relations must be satisfied. The formulation described below is the same as the one adopted in Ref. 1.54 and relates to the computer program MIXDYN adopted for implementation of the proposed model.

To approximate the true displacement behavior of the element in a continuum, shape functions \underline{N} are assumed. These functions relate the increment of internal displacement vector $d\mathbf{u}$ at any point within the element with increment of nodal displacement vector $d\mathbf{\delta}$; thus

$$d\mathbf{u} = \underline{N} \cdot d\mathbf{\delta} \quad (3.1)$$

For finite element applications it is necessary to relate strain to the displacement at element nodes. With known displacements within the element the increment of strain vector $d\mathbf{\epsilon}$ at any point can be obtained by taking suitable derivatives of Eq. 3.1. If the derivatives of the shape functions are composed in the matrix \underline{B} then the incremental strain-displacement relationship is expressed as:

$$d\mathbf{\epsilon} = \underline{B} \cdot d\mathbf{\delta} \quad (3.2)$$

The matrix \underline{B} for an element comprises a row of n (the number of nodes in the element) submatrices \underline{B}_i which for plane problems take the form:

$$\underline{B}_i = \begin{bmatrix} \partial N_i / \partial x & 0 \\ 0 & \partial N_i / \partial y \\ \partial N_i / \partial y & \partial N_i / \partial x \end{bmatrix} \quad (3.3)$$

Now the principle of virtual work is used to establish the incremental equilibrium relation between the increment of nodal force vector $d\mathbf{p}$ and internal stress vector $d\mathbf{g}$. The virtual work equation in classical textbooks on the finite element method is normally used on total stresses and forces rather than on incremental forces since the latter are just a numerical approximation technique. However, in the recent textbooks and papers related to the incremental flow theory of plasticity [1.54, 3.12], the virtual work equation is used on incremental stresses and forces. This procedure is adopted here. Also as in Ref. 3.12 the procedure is further simplified by assuming that all forces acting on an element are concentrated at the nodes.

A set of virtual displacements $d\bar{\delta}$ is applied to the nodes. Let the incremental stress at a point in the element be $d\mathbf{g}$, and the strain corresponding to the virtual displacements be $d\bar{\epsilon}$. Equating the work done externally (at the nodes) to that done internally gives:

$$d\bar{\delta}^T \cdot d\mathbf{p} = \int_V d\bar{\epsilon}^T \cdot d\mathbf{g} \cdot dv \quad (3.4)$$

When Eq. (3.2) is substituted into Eq. (3.4), we have:

$$d\bar{\delta}^T \cdot d\mathbf{p} = d\bar{\delta}^T \int_V \mathbf{B}^T \cdot d\mathbf{g} \cdot dv \quad (3.5)$$

Using the fact that the coefficients of $d\bar{\delta}$ are independent (which allows $d\bar{\delta}$ to be effectively cancelled), we obtain:

$$d\mathbf{p} = \int_V \mathbf{B}^T \cdot d\mathbf{g} \cdot dv \quad (3.6)$$

This important relation is used whenever a set of nodal forces is required which are to be equivalent to (or in an overall sense to be in equilibrium with) the internal element stresses.

To proceed further with a solution requires a constitutive relationship between $d\sigma$ of Eq. 3.6 and $d\epsilon$ of Eq. 3.7 to be established. The incremental form of the stress-strain relation is expressed as

$$d\sigma = D^{ep} \cdot d\epsilon \quad (3.7)$$

where D^{ep} is the elasto-plastic constitutive matrix for the current stress level.

The expression for $d\delta$ (Eq. 3.7) substituted in Eq. 3.6 and introducing Eq. 3.2 into Eq. 3.7 gives for each element

$$dP = \left(\int_V \underline{B}^T \cdot D^{ep} \cdot \underline{B} \, dv \right) d\delta \quad (3.8)$$

or
$$dP = K \cdot d\delta \quad (3.9)$$

where

$$K = \int_V \underline{B}^T \cdot D^{ep} \cdot \underline{B} \cdot dy \quad (3.10)$$

is the desired element stiffness matrix.

Commonly in geotechnical problems strains are zero at the start of loading so that the initial strain increments are equal to the total strains.

The corresponding stress increments are $d\sigma = \sigma - \sigma_0$ (σ_0 being the initial stresses). Strains can, however, occur due to causes other than load application, e.g. by temperature change in structures, or by creep or saturation in soils. Such strains ϵ_0 can be viewed as "initial" strains which are subsequently increased by the load-induced strains. Consequently, the $d\epsilon$ for use in the constitutive law Eq. 3.7 is more generally defined as

$$(\sigma - \sigma_0) = D^{ep}(\epsilon - \epsilon_0) \quad (3.11)$$

Re-arranging, eliminating ϵ by Eq. 3.2 and substituting in Eq. 3.6:

$$d\bar{p} = \int_V \bar{B}^T \cdot D^{ep} \cdot \bar{B} \cdot d\delta \cdot dv + \int_V \bar{B}^T \cdot \sigma_0 \cdot dv - \int_V \bar{B}^T \cdot D^{ep} \cdot \epsilon_0 \cdot dv \quad (3.12)$$

Note that $d\delta$ is now the actual but not the virtual set of displacements. Denoting the last two terms of Eq. 3.12 by \bar{p}_{σ_0} and \bar{p}_{ϵ_0} respectively we have:

$$d\bar{p} = \bar{K} \cdot d\delta + \bar{p}_{\sigma_0} - \bar{p}_{\epsilon_0} \quad (3.13)$$

Once the element stiffness matrices have been derived and transformed from the local to global coordinate system, the structure stiffness matrix \bar{K}_s which relates the load increment $d\bar{r}_s$ to the nodal displacement increment $d\delta_s$ of the complete structure can be formed by addition of element stiffness

$$d\bar{r}_s = \bar{K}_s \cdot d\delta_s \quad (3.14)$$

By solving Eq. (3.14) the modal displacement vector $d\delta$ is found.

The stresses within each element are obtained from:

$$d\tilde{g} = \tilde{D}^{ep} \cdot \tilde{B} \cdot d\tilde{\delta} \quad (3.15)$$

3.2.2 Numerical Procedure

A solution scheme for the nonlinear analysis involves three major computational steps [1.54]: (1) linearization which constitutes the evaluation of the tangent stiffness matrix as part of Eq. 3.14, (2) equation solution, which is the computation of an effective load vector, and the solution of a set of linear equations, and (3) state determination which involves computation of increments in stress and strain that correspond to the displacement increments obtained after Eq. 3.14 has been solved.

The structure tangent stiffness matrix in a finite element formulation is generated by assembly of the element stiffness matrices, and requires the material constitutive relationship as stated in the previous section. For elasto-plastic materials, the latter varies with the state of stress and strain within the element. A numerical procedure is then employed to establish the element stiffness by evaluating the constitutive relationships at selected integration points.

For the analysis of nonlinear elasto-plastic problems different approaches have been suggested. They can be iterative, incremental or combination of both. For work-hardening elasto-plastic materials, the most suitable approach seems to be the incremental application of load and by iterating within the increment to satisfy equilibrium. By applying load in increments and following plastic action as it develops one may properly account for the path-dependent nature of plasticity.

The structure is loaded in small increments, and for every step of loading a new structural stiffness matrix is calculated from the updated material matrices \underline{D}^{ep} . All of the techniques using either incremental or iterative or combination of both run into the problem of an appropriate error control of the numerical results. According to the combined procedure the total load \underline{P} is added in increments and for every such load step the residual force $\underline{\psi}(\delta)$ is calculated, as follows,

$$\underline{\psi}^{\delta} = \int_V \underline{B}_S^T \cdot \underline{\sigma}_S \cdot dv - \underline{P} \quad (3.16)$$

Here, \underline{P} denotes the total level of externally applied loads, and $\underline{\sigma}_S$ denotes the actual stress level reached at the end of the step. The correction (the residual force) vector $\underline{\psi}^{\delta}$ may be applied in the subsequent load step or may be corrected within the current load step such that essentially zero $\underline{\psi}^{\delta}$ exist at the beginning of the following load increment. Thus, within a step one analyzes for the successive loads $d\underline{p}$, $\underline{\psi}^{\delta 1}$, $\underline{\psi}^{\delta 2}$, $\underline{\psi}^{\delta 3}$, etc., updating stiffness, strains, and stresses each time. This procedure is known as the "incremental within one-step Newton-Raphson correction" [1.54].

As correction loads $\underline{\psi}^{\delta}$ serve to return drifting values to the proper path, it is not essential that the tangent stiffness matrix be used. We may use the original elastic structure stiffness matrix in all load steps. This form of solution has been called the "initial stress" method.

After the displacement increments are obtained by solving Eq. 3.14, it is necessary to compute the corresponding increments in stress and strain and hence arrive at a new state. This is the state determination phase, and is as important as the linearization phase. However, it has received considerably less attention in the past. Computation of strain increments from displacement increments involves only kinematics, specifically the strain-displacement transformation. The problem of computing the stress increment from a given strain increment involves the material constitutive relationship.

3.3 IMPLEMENTATION OF THE DEVELOPED FINITE ELEMENT TO THE COMPUTER PROGRAM MIXDYN

3.3.1 Features of the Program MIXDYN

The finite element program MIXDYN [1.54], has many attractive features from the point of research related applications. The program written in modular form with the various main finite element operations being performed by separate subroutines. Also, it considers geometric or elasto-plastic material nonlinearity. A total Lagrangian formulation using four, eight-, and nine-noded quadrilateral isoparametric elements is adopted to model the geometric nonlinear behavior, and four types of standard elasto-plastic material models can be considered (von Mises, Tresca, Mohr-Coulomb, Drucker-Prager). The computer program is based on the Implicit-Explicit time integration scheme of Hughes and Liu [3.1]. The profile solvers DECOMP and REDBAC and a few other subroutines are based on those given by Bathe and Wilson in reference [3.2].

The elasto-plastic, quadrilateral isoparametric finite element developed in this study is added to the existing element library. This will provide a solution for many geotechnical as well as soil-structure interaction problems.

3.3.2 Implementation of the Element

All of the existing constitutive concepts for soil are first formulated and verified in the triaxial configuration $\sigma_1, \sigma_2 = \sigma_3$. Especially at the early stage of development, none of these formulations have been verified in truly triaxial conditions (because of lack of appropriate experimental data). Subsequently, the stress-strain measures are generalized to incorporate the general state of stress configuration and various boundary value problems are solved to confirm the validity of the concept.

The model presented in this study is applicable for general state of stress and as such is incorporated in the finite element formulation after being extensively verified in triaxial configuration in Chapter II. Plane strain condition is achieved by imposing appropriate constraints on the general formulation [1.54].

Any nonlinear finite element program must essentially contain all the subroutines necessary for elastic analysis. These consist of a subroutine to accept the input data, a subroutine for element stiffness formulation, subroutines for equation assembly and solution and subroutine for output of the final results.

In order to implement the solution algorithms for nonlinear problems additional subroutines are required. This consists of subroutines to evaluate the residual forces and also to monitor convergence of the solution and DO LOOPS are necessary to iterate the solution until convergence of the solution occurs and to increment the applied loading, if appropriate.

The flow diagram for MIXDYN is shown in Fig. 3.1. The master routine organizes the calling of the main routines as outlined in the flow diagram. The formation of the new elasto-plastic material matrix D^{ep} (and its incorporation in Eq. 3.10 to form the element stiffness matrix) was introduced within the subroutine RESEPL which calculates the nodal forces that are statically equivalent to the stress field satisfying elasto-plastic conditions. Since the constitutive model has no linear range for start of loading, all elements are characterized by elasto-plastic behavior and D^{ep} must be evaluated for even the first load increment.

All stress and strain quantities are monitored at each Gaussian integration point and therefore one can determine the magnitude of plastic deformations at such points. The flow chart for integration of stress histories penetrating the bounding surface is shown in Fig. 3.2

The integration of the stress histories penetrating the yield surface during the unloading and reloading programs follow the same flow chart, however, the equations used are those of Chapter II related to the yield surface.

Elaborate description of all the subroutines composed in the program MIXDYN is presented in Ref. 1.54 and hence not repeated here. The program code of the subroutine RESERL which incorporates major part of the modifications is listed in Appendix A.

3.4 EVALUATION OF SOIL PARAMETERS

3.4.1 Description of Required Parameters

To perform a finite element analysis by means of the proposed elasto-plastic model, the required material parameters and their evaluation from a triaxial test are defined in this section. The material parameters for the proposed model can be classified into the following categories: elastic moduli, failure parameters, hardening (or deformation) parameters and dilatancy parameters.

The elastic constants E and ν , with E representing the initial elastic modulus, and ν Poisson's ratio, or alternatively G and K where G is the shearing modulus and K is the bulk modulus, represent the category of elastic moduli. Two elastic parameters are required to vary with stress and/or strain. This pair can be chosen arbitrarily out of E , ν , K or G .

Two parameters m_f and p_0 define the failure parameters. The parameter m_f defines the slope of state line at failure, p_0 is a parameter related to the cohesion c , and both parameters are related to the internal angle of friction.

The three parameters required for the isotropic and kinematic hardening functions are A , γ and δ_p . The hardening parameter A is a positive constant used in Eq. 2.10 which describes strain hardening only. The

parameters γ and δ_0 play an important role in the cyclic behavior of the material. They control the kinematic hardening and reduction of hysteresis with increase of number of cycles.

The material parameter controlling the dilatancy is m_c and represents the slope of state line at zero dilatancy.

3.4.2. Tests for Soil Properties

Among construction materials used in structural and geotechnical engineering the soil is the most variable material. Its properties change irregularly in all directions and therefore, are difficult to be determined. The other factors directly influencing the evaluation of soil properties are [3.3]: (a) factors related to the sampling procedure, and (b) the sophistication of the employed testing method. There are many different techniques employed for sample extraction and conservation [3.3]. The advantages and limitations of these techniques are well reported in standard books in soil mechanics.

Common tests frequently employed for evaluation of soil properties are: (a) direct shear test [3.6], (b) triaxial test [3.7], (c) borehole shear test [3.8], and, (d) vane shear test [3.9]. They are all suitable for evaluation of the properties related to the strength parameters of the model. Other tests may provide more realistic values for properties such as compressibility indexes, permeability, volumetric data such as void ratio, and gravimetric data such as unit weight.

Different groups of parameters described in Subsection 3.4.1 depend on various factors related to the method of testing and the characteristics of the tested soil sample. For example the failure

(strength) parameters m_f , ϕ_f and c are strongly influenced by [3.3, 3.4, 3.5]: (a) method of testing, (b) confining (cell) pressure, and (c) size of soil particles, their shape, density, moisture content, and mineral composition. In particular, the value of the angle of internal friction ϕ_f for example increases with increase of the grain size and angularity, lower water content, and for tests conducted under low confining pressure.

The elastic parameters E , ν or G , K obtained from various tests depend on the following factors [3.3]: (a) method of testing, (b) cell pressure, (c) material composition, its density and moisture.

For the two groups of parameters describe above the method of testing appears to be the critical element in adequate evaluation of their characteristics. Different tests, as reported above, employed to evaluate a particular parameter may produce relatively different values for the same parameter. For example, the investigations reported in the literature [3.10] agree that under drained conditions the plane strain angle of internal friction obtained from a triaxial test may be up to 8° lower than the actual value or that obtained from a plane strain test. The difference is more pronounced for dense sands tested under low confining pressure, while small difference is associated with loose sands, or dense sands at high confining pressure [3.10].

At the present time the triaxial test has been widely accepted for design problems and for research in soil mechanics. It provides useful data and is popular in the practicing engineering offices. Many important structures were designed in the past on data obtained from

triaxial test. They are simple to perform, the interpretation of the results is in relation to Mohr-Coulomb failure criterion, and the intermediate principle stress is not considered. However, in many cases the triaxial test results do not represent the actual field condition. This is particularly true in cases of plane strain behavior (landslide problems, strip footing, retaining wall, long earth or concrete gravity dams) where single plane shear failure is typical. Therefore, the plane strain test for strength evaluation seems more appropriate.

The plane strain tests are usually more difficult to perform than triaxial tests (3.10), and unless it can be shown that the plane strain results are significantly different from those obtained by triaxial tests, it is unlikely that plane strain will become widely accepted in routine soil mechanics investigations. Discussion related to different testing methods is not in the scope of this work and therefore will not be provided here.

3.4.3. Procedure for Evaluation Model Parameters

The following example demonstrates detailed procedure for evaluation of required parameters for the proposed elasto-plastic model.

The results of triaxial test at low confining pressure on Chatahooche River sand which were conducted by Vesic and Clough (3.11) are shown in Fig. 3.3. This sand was extensively tested in the past and was used in the footing test conducted by Duncan and Chang [1.11] and simulated by the proposed model in the following Chapter. On the combined diagram both stress difference-axial strain, and volumetric strain-axial

strain paths are presented. From the test data the deviatoric stress at state of failure q_f and state of zero dilatancy q_c are evaluated as 2.32 kg/cm^2 and 2.25 kg/cm^2 respectively. The value of q_c represents the stress difference at the onset of large plastic strain increase.

Fig. 3.4 represents a q - p stress space with q representing deviatoric and p hydrostatic stress. Line n represents the effective stress path for the triaxial test performed at initial confining pressure of 1.0 kg/cm^2 . Also shown are lines $q_f = 2.32 \text{ kg/cm}^2$ and $q_c = 2.25 \text{ kg/cm}^2$. The slope of state line at failure m_f and the slope of state line at zero dilatancy m_c are obtained as slopes of lines passing through the origin and intersection points of lines q_f - n and q_c - n respectively. All the required data for Fig. 3.4 is easily obtainable from Fig. 3.3. In the present example of Chatahoochi River sand the values of m_f and m_c are evaluated as 1.34 and 1.308 respectively.

The value of the angle of internal friction ϕ obtained by using the relation $m_f = 6 \sin \phi / (3 - \sin \phi)$ is $\phi = 33.2^\circ$.

The same triaxial test data are further used for evaluation of elastic constants G and K . In Fig. 3.5 the q - ϵ_q and ϵ_v - ϵ_q diagrams are presented. The deviatoric strain component ϵ_q and the volumetric strain component ϵ_v are defined with Eq. 2.5. The initial slopes of the presented curves are directly related to G and K . Both, the shear and bulk modulus for the considered sand are 55 kg/cm^2 and 75.26 kg/cm^2 respectively.

The hardening constant A is defined from Fig. 3.6. Here, based on the triaxial test data $m-\epsilon_q^P$ diagram is plotted. The slope of the state-line bounding surface $m = q/p$, and the deviatoric plastic strain component ϵ_q^P are evaluated at different stress levels. With a trial and error procedure the parameter A is used so the hardening function $m = m_f \epsilon_q^P / (A + \epsilon_q^P)$ best fits the $m-\epsilon_q^P$ plot. In Fig. 3.6 three plots of the hardening rule with values for A of 0.12, 0.012 and 0.0012 are presented. It can be seen that for the value of $A=0.012$ the best fit is obtained.

The kinematic hardening parameter γ is determined from any reverse-compression curve obtained of either drained or undrained compression test. For the sand described here these tests were not available. Also due to the modifications introduced in the computational phase and discussed above (clause 3.1), this parameter will not be employed in the model.

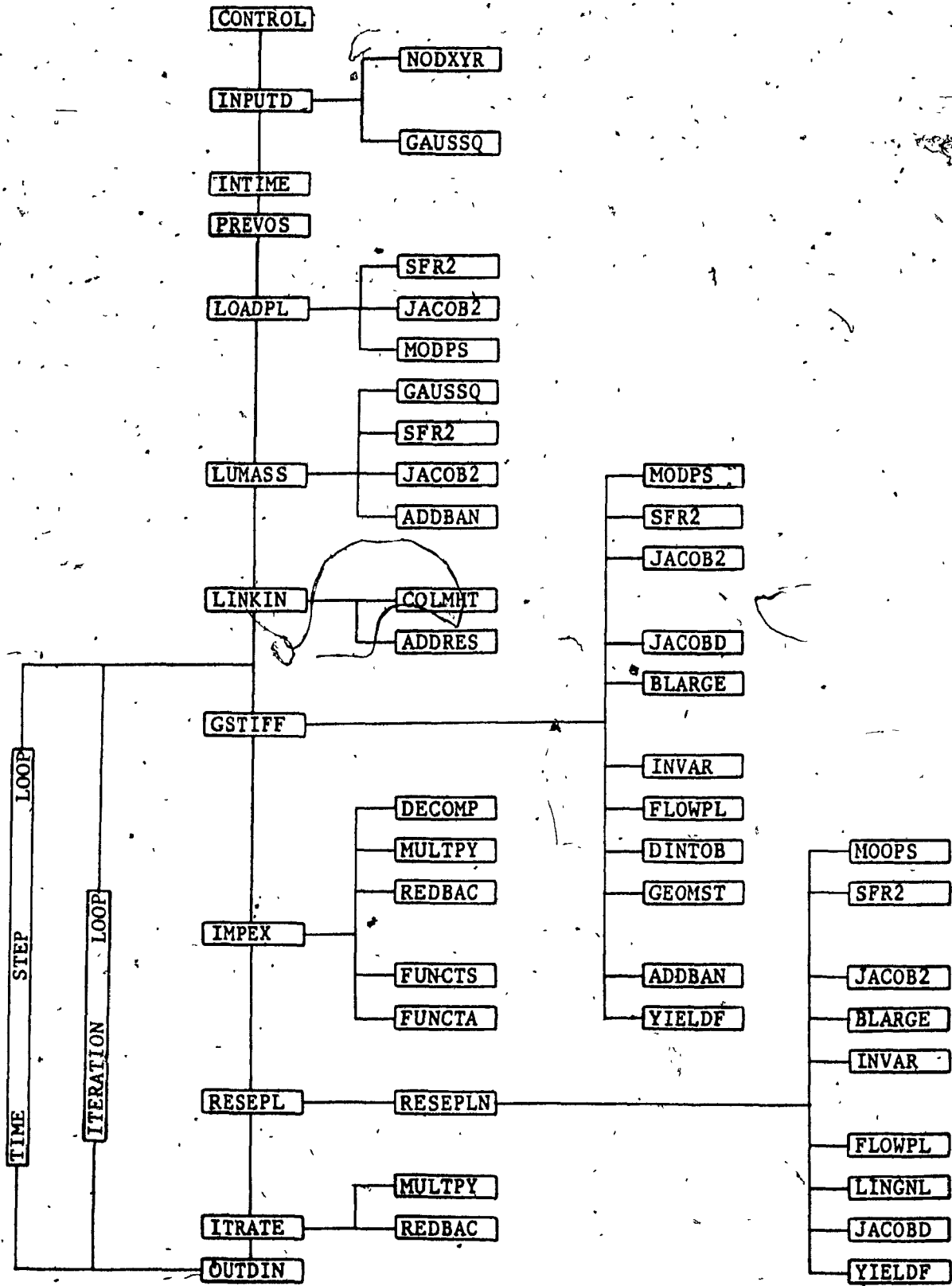


Fig. 3.1 Overall structure of the computer program MIXDYN (Ref. 1,54) with implemented modifications for the developed finite element.

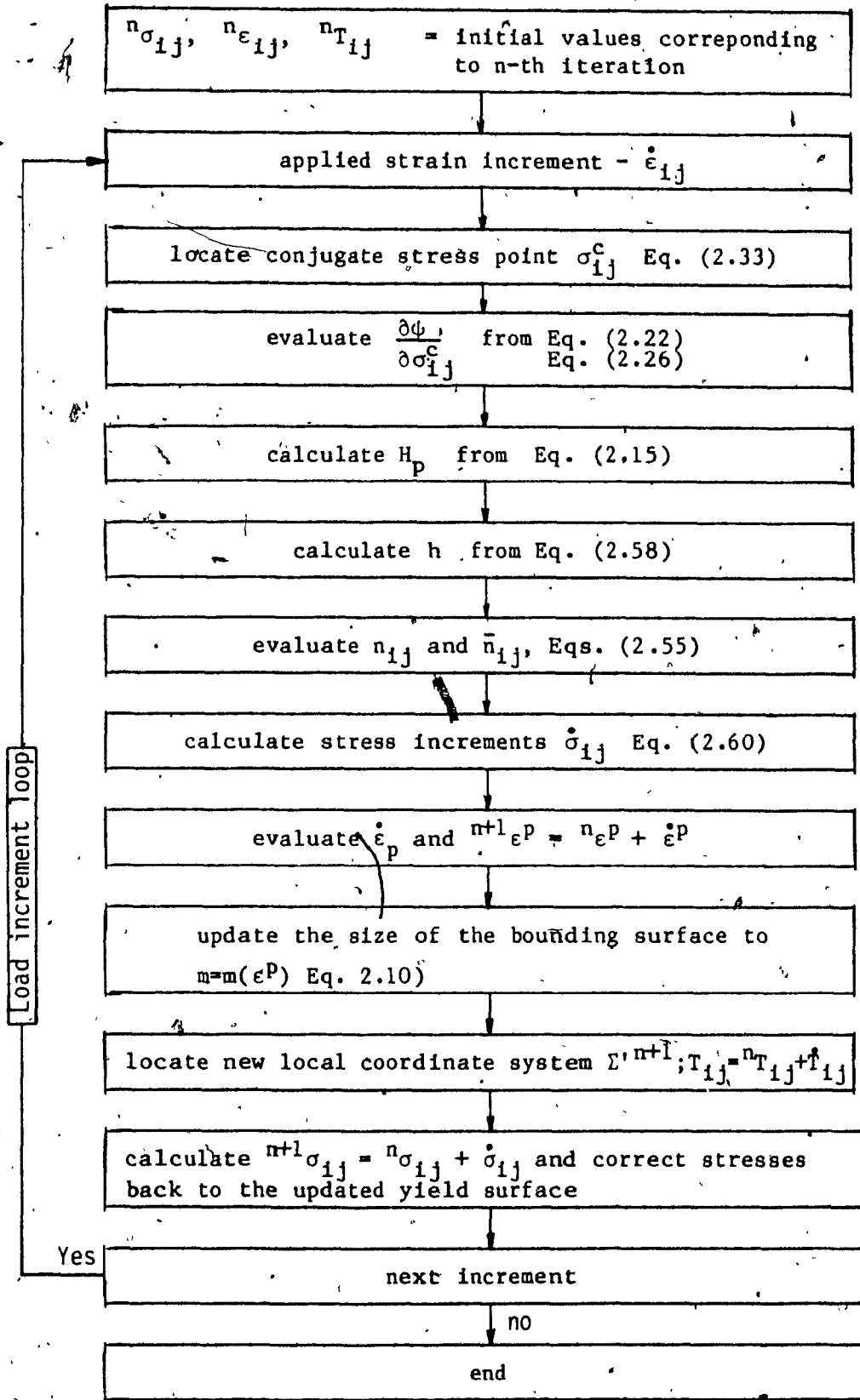


Fig. 3.2. Flow chart for integration of stress histories penetrating the bounding surface

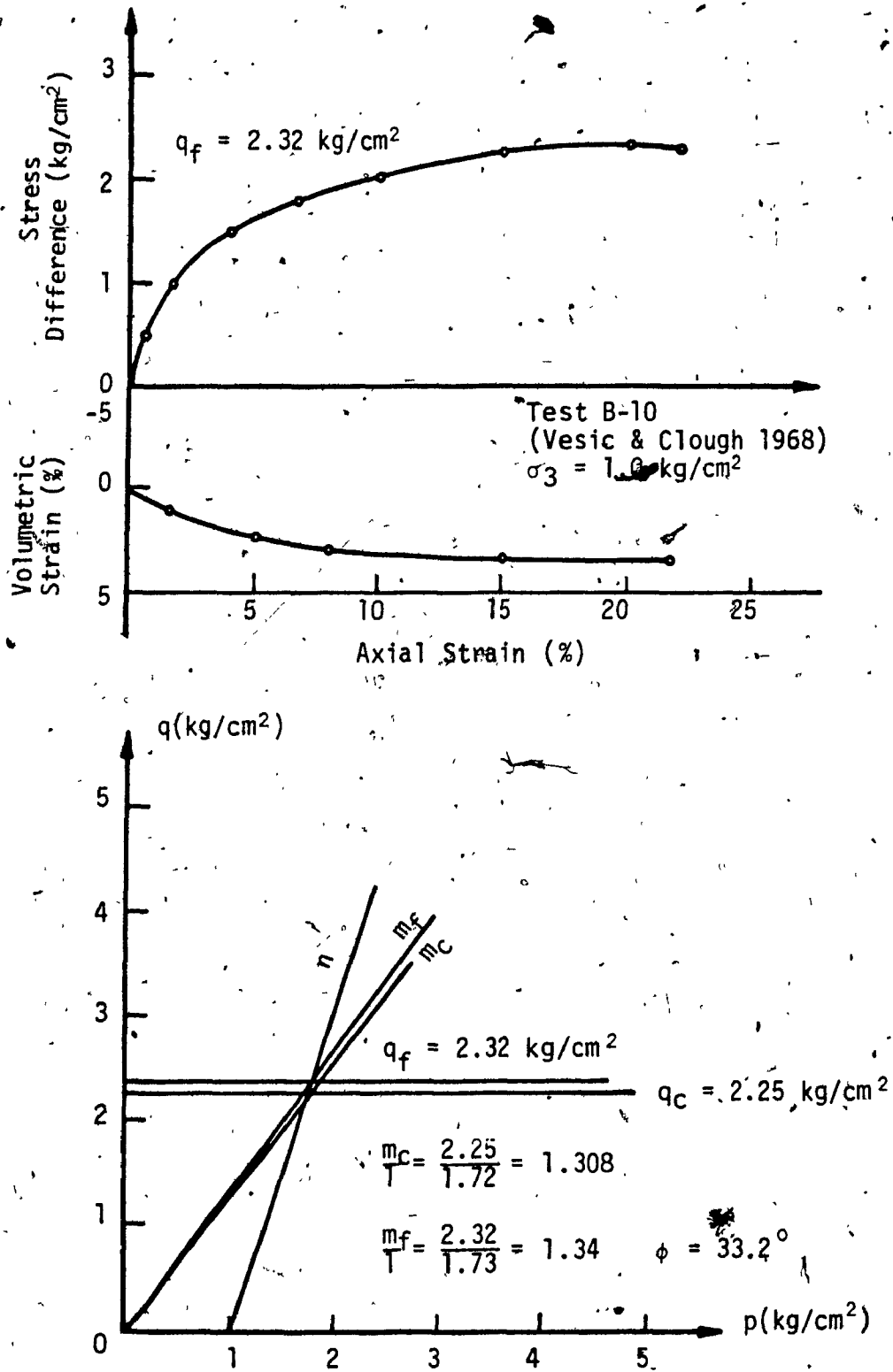


FIG. 3.3: Evaluation of model parameters: (a) typical results of standard triaxial test at low confining pressure (Test no. B-10 Ref. 3.11); (b) slopes for failure and zero dilatancy lines.

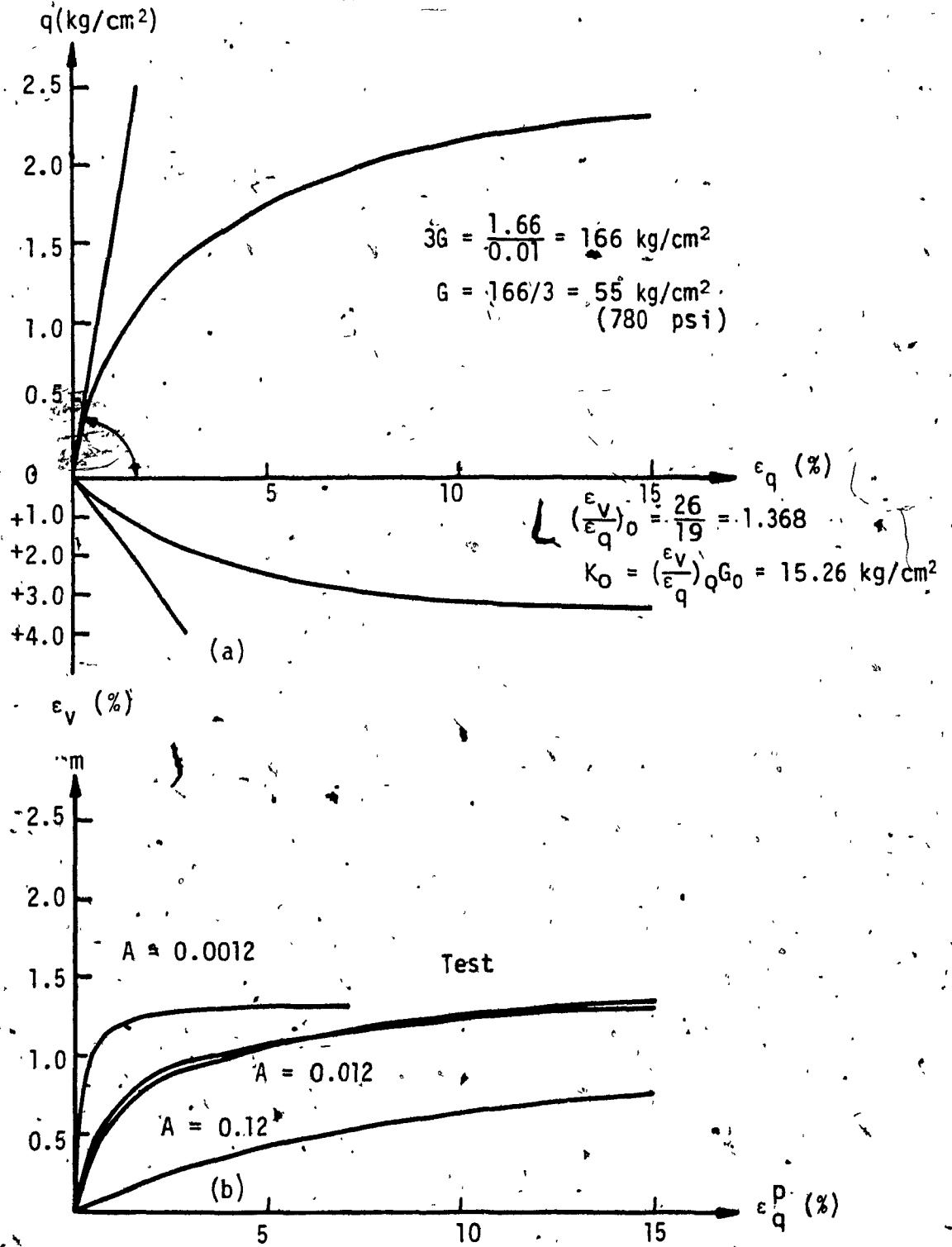


FIG. 3.4: (a) Plots of q - ϵ_q and ϵ_v - ϵ_q required for evaluation of elastic parameters G and K ; (b) Plot of m - ϵ_q^p used to evaluate the hardening parameter A

CHAPTER IV

4.0 VERIFICATION OF THE MODEL; SOLUTION OF CHOSEN PROBLEMS RELATED TO GEOMECHANICS

4.1 INTRODUCTION

In order to ensure reliability, the newly developed elasto-plastic finite element must be verified. The nature of the soil behavior and the complexity of the model demand extensive testing of the adopted finite element procedure before its results can be relied upon.

A limited number of advanced constitutive relations for soil have been implemented in the development of new finite elements. A literature survey by Saleeb and Chen [1.13], and Pande and Pietruszczak [1.53] shows that only a few of them are included as part of a general purpose finite element program. The results from these implemented models generally indicate good agreement with experiments. However, the use of these models in engineering practice today is not extensive. The reason is that many of them were only applied to simulate small-scale tests and not on large engineering structures, thus they were not adequately tested.

The existing formulations cannot describe adequately the response for a wide range of initial void ratios. In the context of cyclic loading they either predict complete liquefaction or cyclic mobility. In the case of monotonic loading a number of proposed formulations can perform satisfactorily provided the stress path is close to proportional. This includes nonlinear elasticity formulations for properly defined elastic parameters.

The proposed model describes irreversible deformations on the stress reversal. There are other models capable of describing the same effect. To provide convincing arguments which one is the most effective requires extensive numerical verification. A number of international workshops were organized with the objective to compare the performance of various models. The existing experimental evidence is very fragmentary at the moment and objective evaluation is difficult if not impossible.

The proposed model is capable of predicting all the fundamental trends of the response of granular materials to both monotonic and fluctuating load. These include transition from compaction to dilatancy, liquefaction and cyclic mobility effects.

The footing problem published by Duncan and Chang [1.11] is first chosen for comparison. The data reported in this reference is based on small-scale tests and analytical solutions. Their analytical approach employs the finite element procedure assuming nonlinear elastic material behavior.

In order to verify the general applicability of the present model, it is imperative to perform analysis on an actual engineering boundary-value problem, as for example an embankment structure. Unfortunately, a review of the literature on elastic-plastic boundary-value problems reveals that closed form solutions or experimental data for such complex structures are uncommon or not reported in detail. Experimental data reported in Ref. 1.68 for the stresses and movements of the Oroville Dam is extensive. However the complexity of this structure and the variety

of the materials used in its construction make it unsuitable for the purpose of verification of a newly developed elasto-plastic model. This leads to the fact that the results from the present model may only be compared with those from other numerical procedures applied to embankment structures which are relatively less complex and smaller in scale.

The finite element method using a nonlinear elastic material model developed by Kulhawy et al. [4.2, 1.12] in the late 1960's has been applied extensively on many structures, and the results are generally considered acceptable. In this regard the analysis of an embankment structure is selected as the basis for comparison of results obtained from both procedures.

Experimental evidence shows that shear stress induces volume changes. This could be either compaction or dilation depending on the actual confining pressure. Any of the existing nonlinear elastic formulations can take this effect into account. Displacement field as predicted by an elasto-plastic constitutive model is far more accurate than that predicted by linear or nonlinear elasticity [4.5]. This applies also to the stress field. Therefore, the shear coupling will have significant impact on the predicted displacement field in the context of boundary value problems.

The proposed formulation incorporates the intermediate principal stress through definition of stress invariants and the function $g(\theta)$. Numerical evidence [4.5] demonstrates that this principal stress has a significant influence on the predicted strength of the soil. However, there is no appreciable experimental evidence related to the effect of

the intermediate principal stress on the material response. Triaxial tests do not provide any since $\sigma_2 = \sigma_3$.

The influence of introducing cohesion in the sands used in the analysed footing and embankment is further examined. The latter investigation is purely qualitative in nature as there is no experimental evidence of cemented granular materials available in the literature.

4.2 FOOTING ON SAND

For the nonlinear-elastic analysis of the footing by Duncan and Chang [1.11], the values of the parameters required are evaluated from the data of Ref. 3.11. The same reference is used for evaluation of the required parameters for the proposed elasto-plastic analysis and the detailed procedure for their evaluation has been presented in previous chapter. Table 4-1 summarizes the values of all parameters used in both analyses of the model footing.

The footing is 62 mm wide and 320 mm long and for the experiment it was installed at a depth of 508 mm within the sand [4.3].

The finite element mesh used in the analysis is shown in Fig. 4.1. The mesh size is coarser than the one used in Ref. 1.11. It contains 44 elements and 161 nodal points. The reduction of the mesh size is justified by the use of 8-node instead of 4-node elements. Each node has two translational degrees of freedom.

The nodal points along the centerline beneath the footing and those on the right vertical boundary are constrained to move only in vertical direction, whereas those on the bottom boundary are constrained from both

horizontal and vertical movement. The rest of the nodal points are unconstrained. Eight node quadrilateral isoparametric finite elements with plane-strain behavior are used.

The stresses due to gravity loads of the sand are introduced in the proposed analysis as initial stresses.

Loads are applied to the elements representing the footing in increments of 6.89 kPa. Typical results generated from this analysis are shown in Figs. 4.2, 4.3 and 4.4.

Fig. 4.2 shows the load-displacement curves produced from the test and from both analytical procedures. It should be noted that in the analysis the footing is considered rigid and therefore equal settlements are expected for any contact point under the footing. The load-displacement diagram indicates close agreement between the present results and those from the experiment. At the early loading stage, the computed settlement is 30% larger than that from experiment. This indicates the significance of the estimated initial modulus E on the behavior during the initial phase of loading. Although there is only a small difference in the overall load-displacement characteristics between the two finite element models, the prediction of the load at large values of settlement for the final portion of the curve is clearly seen to be different. The load at the end of the experiment predicted by the proposed elastoplastic analysis coincides with the value from the experiment, whereas the analysis using nonlinear elastic model underestimates this load by 30 percent.

Fig. 4.3 shows the mode of deformation of the sand medium under the loaded footing while Fig. 4.4 represents the vertical pressure distribution plotted along vertical sections at large values of settlement at the end of the experiment (170 kPa). The results presented in both Fig. 4.3 and 4.4 are obtained from the performed elasto-plastic analysis. Similar data for the footing behavior is not reported in the literature and therefore cannot be compared. The aim of the presentation of these results is to show the versatility of the program. Also, by inspection of the magnitudes of the stresses and deformations close to the boundaries it can be concluded that the size of the defined finite element mesh is appropriate and the boundaries do not have an effect on the obtained results.

The contours of the minor principal stresses and accumulated plastic strain below the footing are shown in Fig. 4.5. The presented stresses are due to a load of 170 kPa near the end of the experiment as defined in Fig. 4.2. According to Eq. 4.2, σ_1 is assumed to be the major principal stress. The sign convention used is tension positive, and σ_1 is greater algebraically than that of σ_3 . The minus sign in the figures showing stress magnitudes is omitted. A variation of minor principal stresses, Fig. 4.5(a), from 7 kPa to 211 kPa is observed. Fig. 4.5(b) represents the contours of accumulated plastic strain for the stress level shown in Fig. 4.5(a). The diagram shown is only a local zone under the footing. The plastic strain concentration around the edges of the footing is clearly shown. Very high plastic strain of 19.08 percent is developed at the edges, whereas only 0.5 percent is observed at the center line under the footing.

Fig. 4.6 presents a comparison of the load-settlement characteristics of cemented sands. By simple variation of the cohesion from $c = 0.0$ kPa to $c = 14.5$ kPa different degrees of cementation are simulated. Although there is no difference in the overall load-settlement characteristics between the cases analyzed, the loads at the end of the analysis vary from 200 kPa to 2100 kPa for cemented sands with cohesion $c = 0.0$ kPa and $c = 14.5$ kPa respectively. In all cases, the computation was terminated by divergence of the results in the last loading increment after a large number of iterations.

Fig. 4.7 represents the model footing on two different layers of soil. The top layer depth equals 0.7 of the footing width. The soil properties for this layer are assumed the same as those for the sand in Table 4-I with the addition of $c = 7.25$ kPa and $c = 20.0$ kPa for cohesion. The lower layer is sand with properties described in Table 4-I. Fig. 4.8 shows a comparison of load-settlement characteristics for the footing. Improvement of the strength characteristics of the top layer by increasing the material cohesion to 7.25 kPa and 20.0 kPa leads to significant increase of the failure loads, by 50 and 125 percent respectively.

4.3 ANALYSIS OF AN EARTH DAM DURING CONSTRUCTION

For both finite element procedures employed here in the analysis of a dam during construction, the properties of the rockfill material used for the Oroville Dam [1.68] form the basis for evaluation of required parameters. Prior to the construction of the Oroville Dam extensive

material testing was performed and the results are published in Refs. 4.2, 1.68 and 4.4. The program "LSBUILD" [1.68] for nonlinear elastic analysis of embankments was used in the analysis phase of the Oroville dam. For comparison this program is also used for the analysis of the present dam, in which the required soil parameters are based upon the Oroville Dam taken from Ref. [1.68] and presented in Table 4-II (a).

The necessary soil parameters for the present model are derived from Refs. 1.68, 4.4 and tabulated in Table 4-II (b). The values of the angle of internal friction ϕ and Poisson's ratio ν are employed as calculated in Ref. 1.68, whereas the other required parameters are calculated using the relations described in Chapter II. For the value of $\phi = 43.5^\circ$ as estimated in Ref. 1.68 the slope of the failure line m_f is calculated using the relation $m_f = 6 \sin \phi / (3 - \sin \phi)$. Analysing the tests performed on the shell material of Oroville Dam as reported in Ref. 4.4, the slope of the zero dilatancy line m_c is evaluated to be $0.89 m_f$. The value of E , the initial elastic modulus, is evaluated based on the values of the modulus number K and modulus exponent n reported in Ref. 1.68 ($E = K p_a (\frac{\sigma_3}{p_a})^n$). With the two elastic constants E and ν known, the initial shear modulus G can be calculated by using the relation from the theory of elasticity. The hardening parameter A is then evaluated as $A = m_f p_1 / 3G$ where p_1 is the value of the confining pressure of the low confining P -constant test. Due to the lack of this type of tests a value of $p_1 = 13.7$ kPa corresponding to the in-situ pressure within a layer immediately after placement is employed and justified by the fact that the magnitude of stresses in an embankment are generally relatively low and as demonstrated in the parametric studies performed in Chapter II,

the hardening constant A at low stress ranges has no effect on the model predictions.

The cross-section of the dam under investigation is shown in Fig. 4.9(a). The width of the dam is 273.0 m at the base and 15.0 m at the crest, with an overall height of 80.0 m. The slopes of the upstream and downstream faces are both at a ratio of 1:2. As can be seen in the diagram, the base is sloped at approximately 10° for half of its width. Characteristically, this inclination will produce relatively high shear stresses near this region. Due to the dilatancy effect, the latter will in turn induce higher normal stresses. This is known as a coupling effect. It is noted that the coupling effects of normal and shear stresses, which are accounted for in the present model, has not been included in the nonlinear elastic model. Therefore, it can be expected that the proposed model will predict higher normal and shear stresses, hence higher deformations.

The finite element mesh, as shown in Fig. 4.9(b), consists of a total of 36 elements and 51 nodal points. Eight node quadrilateral finite elements with plane-strain behavior are used. Each node has two translational degrees of freedom.

The construction of an embankment structure is carried out by successive placement of layers of fill.

The number of layers, to some degree, affects the behavior of the dam during as well as after the completion of construction [1.68]. In this comparative study eight construction sequences are considered.

Results generated from both analyses are shown in Figs. 4.10 to 4.20. The displacement curves shown in Fig 4.10(a) to 4.10(e) represent the settlement induced at points 1 to 4, (Fig. 4.9(a)) when successive layers four to eight (Fig. 4.9(b)) are applied. Also, the settlement at points 5 to 8 are shown in Fig. 4.10(a') to 4.10(d'). The data shown in these diagrams indicate a close agreement between the results obtained from the nonlinear elastic and the proposed elasto-plastic analysis. Specifically, for the points 1 to 4 above the sloped base, the settlement obtained by the proposed analysis are larger than those by the nonlinear elastic analysis. This increase in settlement is believed to be due to the shear coupling effect, considered only by the proposed model.

The influence of the successive placements of layers 4 to 8 on the horizontal displacements at points 1, 2 and 3 are demonstrated in Fig. 4.11. The results show larger horizontal movements when compared with those from nonlinear elastic model.

From the formulation of the constitutive relations in Chapter II, it was shown that the angle of internal friction ϕ and the cohesion c , have an influence on the magnitude of plastic flow. Figs. 4.12 and 4.13 show comparisons of calculated movements when values of $\phi = 43.5^\circ$ and $\phi = 30.0^\circ$ with $c = 0$ to $c = 75$ kPa are considered. The vertical and horizontal movements are found to differ by up to 50%.

Fig. 4.14 illustrates the contours of calculated settlements in the analyzed dam. Here, as well as in the following figures, the contours of deformations and stresses are related to the final phase of the construction sequence. The contours in Fig. 4.14(a) are obtained from the non-

linear elastic analysis and they are approximately 30% lower than those calculated with the proposed model in Fig. 4.14(b).

In analyzing the present structure, if the effects due to the successive placements of fill layers were not considered, the contours of settlements would be as those presented in Fig. 4.15. These contours are seen to be significantly different than those shown on Fig. 4.14. This clearly indicates the importance of considering the influence of construction sequence in the analytical solution, as also demonstrated in Ref. 1.66.

The stresses calculated by means of these two analysis procedures are shown in Fig. 4.16 to Fig. 4.20. Contours of minor principal stress, shown in Fig. 4.16 are nearly the same for both methods of analysis. The stresses obtained by the proposed elasto-plastic analysis are slightly higher (13%). The contours of the major principal stress determined by both nonlinear elastic and elasto-plastic analysis are shown in Figs. 4.17(a) and 4.17(b) respectively. The stresses at the base of the embankment are 30% higher when obtained by the proposed analysis. Fig. 4.18 represent the magnitudes and orientations of principal stresses determined by both analyses. As discussed previously, their magnitudes differ (13% and 39%), however, their orientations are similar for both methods. Contours of calculated shear stresses are shown in Figs. 4.19 and 4.20 for both nonlinear elastic and elasto-plastic analysis. Here, both the maximum shear stresses (Fig. 4.20) as well as τ_{xy} stresses (Fig. 4.19) are compared. From the concentration of the maximum shear stresses the location of the potential sliding plane is easily identified. The purpose of comparison of the shear stress contours of τ_{xy} is that the

concentration of these stresses on the side of the dam with a sloped foundation base is strongly emphasized when the proposed analysis is used. In both cases, the diagrams indicate the incidence of high shear stress zones in the embankment. However, the maximum shear stresses obtained with the proposed analysis are found to be approximately 60 percent higher. The higher values of the shear stresses determined by the proposed analysis is believed to be due to the shear coupling effect considered only by the present elasto-plastic model.

Similar findings resulted from the dilatancy effects are reported in Ref. 4.5 where the calculated stress paths when nonlinear elastic analysis is used differ considerably from those obtained by an elasto-plastic analysis capable of simulating dilatant behavior.

The results from both analyses presented above are now discussed with relation to the conclusions stated in Ref. 1.68. There, the field measurements of the stresses and movements in Oroville Dam are compared with results obtained from the same nonlinear elastic analysis used here. For the shell material, considered also in the embankment structure analysed, it was found that the magnitudes of the settlements and horizontal movements, measured after the construction was terminated, are 25% larger than those obtained by the nonlinear elastic analysis. Further, it was also found that the measured stresses are up to 41% higher than that calculated by the analysis.

Comparison of the results obtained here shows the same trend. Namely the magnitudes of the stresses and movements in the analysed

embankment are higher by the same percentage range when calculated by the proposed elasto-plastic analysis.

The behavior of the embankment due to horizontal water pressure after the reservoir is filled is examined next. The cross-section of the embankment with the maximum water level in the reservoir is shown in Fig. 4.21(a).

Fig. 4.21(b) shows the calculated movement of the dam surface for the maximum water level, and Figs. 4.22 and 4.23 represent contours of major principal stresses, minor principal stresses, and maximum shear stresses respectively.

A considerable increase in all three types of stresses is observed. It should be noted that the last set of results is obtained with the proposed elasto-plastic analysis.

4.4 CONCLUSION

The procedure adopted in this chapter in order to verify the applicability of the new model consists of:

- (a) analysis of a footing on sand; and
- (b) analysis of an embankment during construction.

In the case of the footing, the analytical results obtained were compared with available experimental data, and those from another finite element procedure. Also, in the analysis of the dam, the results were compared only with those obtained from another finite element procedure.

Based on the numerical results for the footing, the following conclusions are made:

- (1) A close agreement of the results was obtained between the present analysis and the experiments. This demonstrates the validity of the present model.
- (2) As expected, it was shown that the value of the elastic modulus influence the material load deflection behavior considerably during the initial phase of loading. Therefore, the predictions in the early loading stages are largely affected by the proper evaluation of the elastic parameters.
- (3) At large values of settlement both the experimental and the calculated load-settlement curves exhibit similar characteristics.
- (4) At low magnitude of the settlements the overall load-displacement characteristics from both finite element procedures are approximately the same. However, at large values of settlement they differ considerably.
- (5) The contours of plastic strains show high plastic strain accumulation around the edges of the footing. This is in agreement with experimental observations where extensive platification occurred at the edges of a rigid footing on sand. This again demonstrates the validity of the proposed model.

- (6) The comparison of load-settlement characteristics of cemented sands with various degrees of cementation shows no difference in the overall behavior. The degree of cementation simulated by the material cohesion, as expected, produces considerable difference in the magnitude of the failure load.
- (7) Improvement of the strength characteristics of the soil layer under the footing increases significantly the failure load. The influence of this layer, frequently used in engineering practice, on the bearing capacity of the foundations, can be closely determined by the proposed model.

From the results obtained in the analysis of an embankment structure during construction, the following conclusions are noted:

- (1) The settlements calculated with the proposed model are larger than those obtained from the nonlinear elastic procedure, This difference is more pronounced on the sloping side of the base and therefore higher shear stresses have develop. The shear coupling effect is considered as being the main factor. The higher settlements as predicted by the model are in accordance with the observations stated in Ref. 1.68.
- (2) The horizontal movements are found to be larger when the proposed elasto-plastic model is used. Here, the sloped side also shows relatively higher horizontal displacements when compared with those on the levelled side of the dam.

- (3) A good judgment in selecting material properties and a proper evaluation of model parameters are found to be an important factor in determining the validity of the results. Hence, a variety of soil tests must be conducted prior to the evaluation of parameters.
- (4) For the proposed elasto-plastic model the contours of calculated settlements and shear stresses show increases of 30% and 60% respectively. This is in accordance with the findings in Ref. 1.68 where the measured settlements and stresses are found respectively 25% and 41% higher than calculated by the nonlinear elastic analysis.
- (5) It was demonstrated that the effects of successive placements of fill layers must be considered in the analysis of a dam during construction. The proposed model behaved satisfactorily in the process of simulation of construction sequences.
- (6) The effect of the angle of internal friction and cohesion on the displacements was found significant. For soils having low angle of internal friction a trace of cementation (cohesion) may have an influence of up to 30% on the movements.

PARAMETER	SYMBOL	VALUE
modulus number	K	300
modulus exponent	n	0.55
failure ratio	R_f	0.83
cohesion	C	0.0
friction angle (deg.)	ϕ	35.5
unit weight KN/m ³)	γ	14.3
poisson's ratio	ν	0.35

TABLE 4-I.(a): Values of parameters used in the nonlinear elastic analysis of the footing

PARAMETER	SYMBOL	VALUE
young's mod. (KPa)	E	1882
poisson's ratio	ν	0.35
friction angle (deg.)	ϕ	35.5
failure line	m_f	1.34
dilatancy line	m_c	1.308
hardening constant	A	0.012
cohesion	C	0.0

TABLE 4-I.(b): Values of parameters for proposed elastoplastic model in the footing analysis

PARAMETER	SYMBOL	VALUE
unit weight (KN/m ³)	γ	23.57
cohesion (KN/m ²)	c	0.0
friction angle (deg.)	ϕ	43.5
modulus number	K	3780
modulus exponent	n	0.19
failure ratio	R_f	0.76
poisson's ratio	ν	0.43
parameters	F	0.19
	d	14.8

TABLE 4-II.(a): Values of stress-strain parameters for non-linear elastic analysis of the earth dam.

PARAMETER	SYMBOL	VALUE
initial young's mod (KN/m ²)	E	335000
initial poisson's ratio	ν	0.43
frictional angle (deg.)	ϕ	43.5
failure line	m_f	1.786
dilatancy line	m_c	1.6
hardening constant	A	0.00007
cohesion (kN/m ²)	c	0.0

TABLE 4-II.(b): Values of parameters for proposed elasto-plastic analysis of the earth dam.

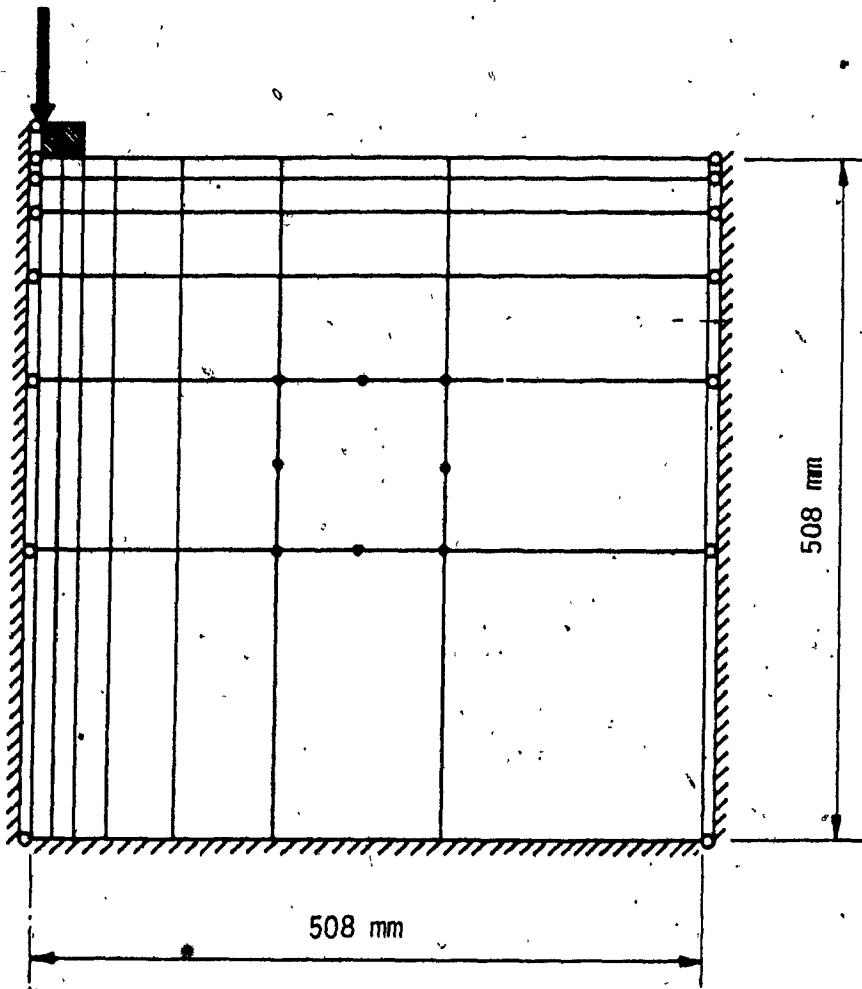


FIG. 4.1: Finite element mesh of model footing in sand

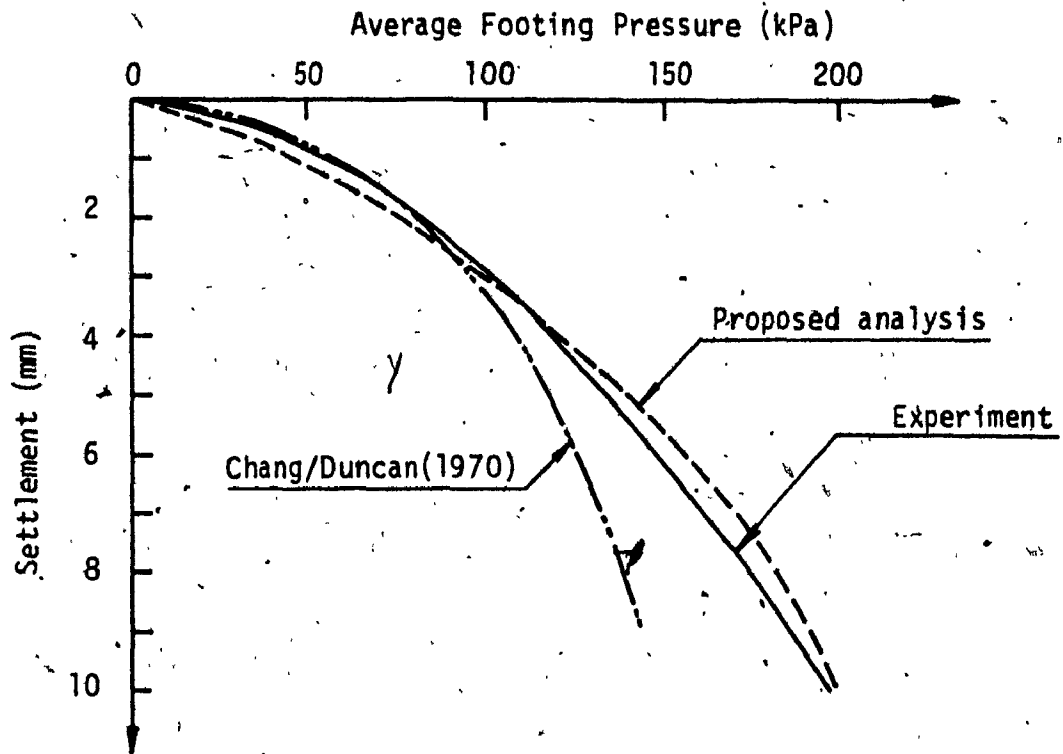


FIG. 4.2: Comparison of results for settlement of model footing

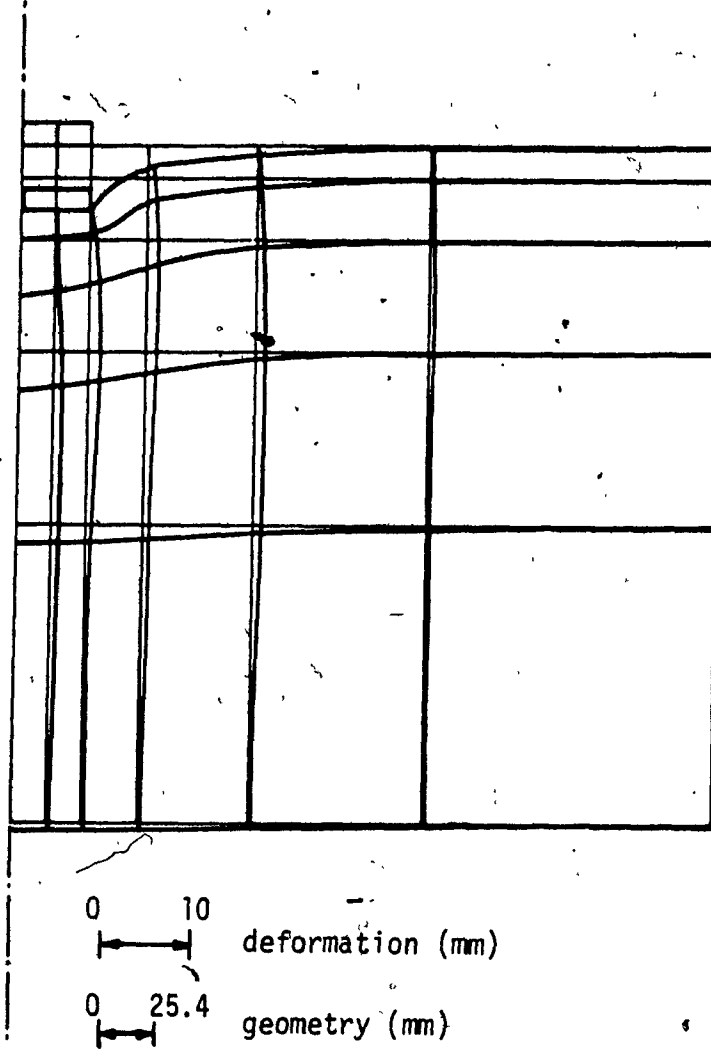


FIG. 4.3: Settlement under model footing for proposed analysis

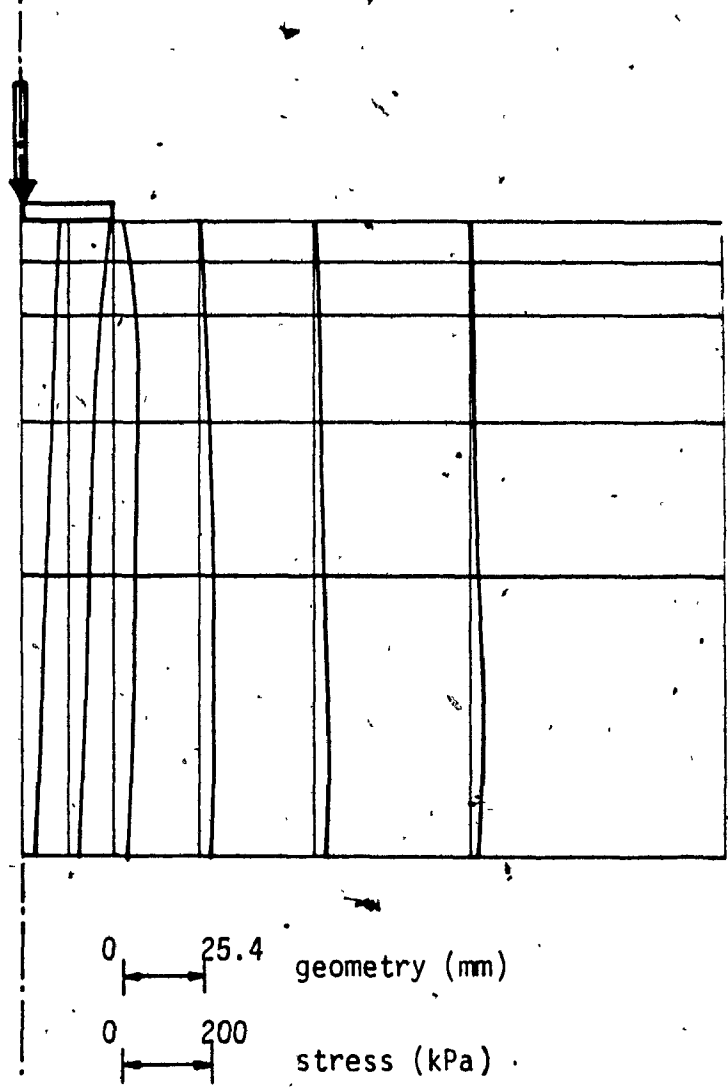


FIG. 4.4: Vertical pressures under footing from proposed analysis

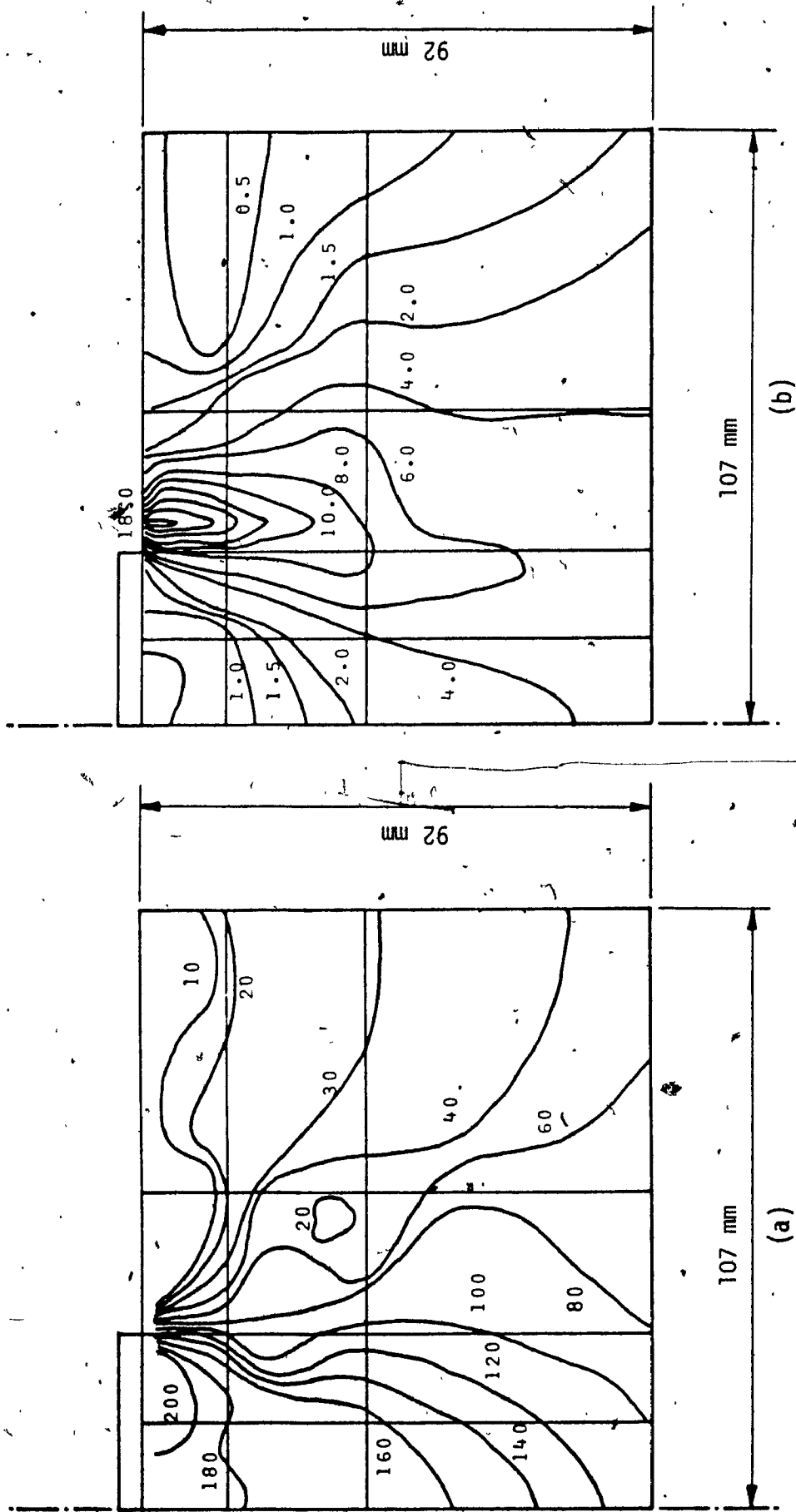


FIG. 4.5: Contours of: (a) minor principal stress (kPa); (b) accumulated plastic strain (%) - vertical footing pressure of 172 kPa.

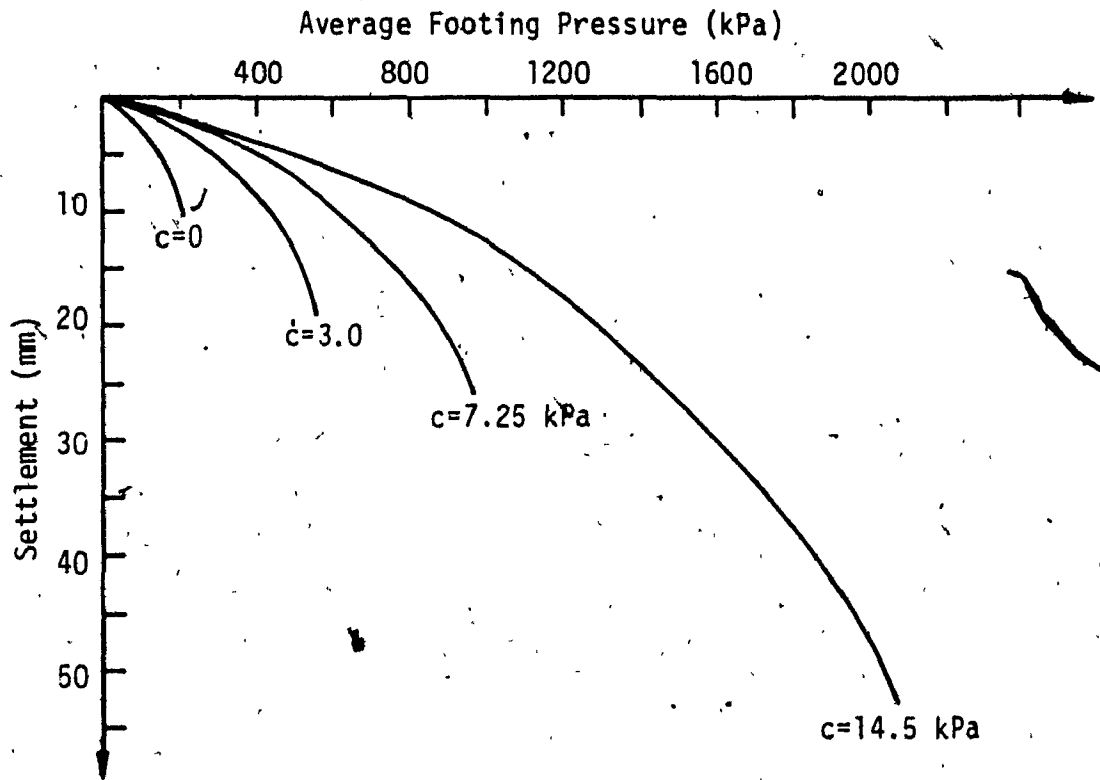


FIG. 4.6: Effect of cohesion on footing settlement

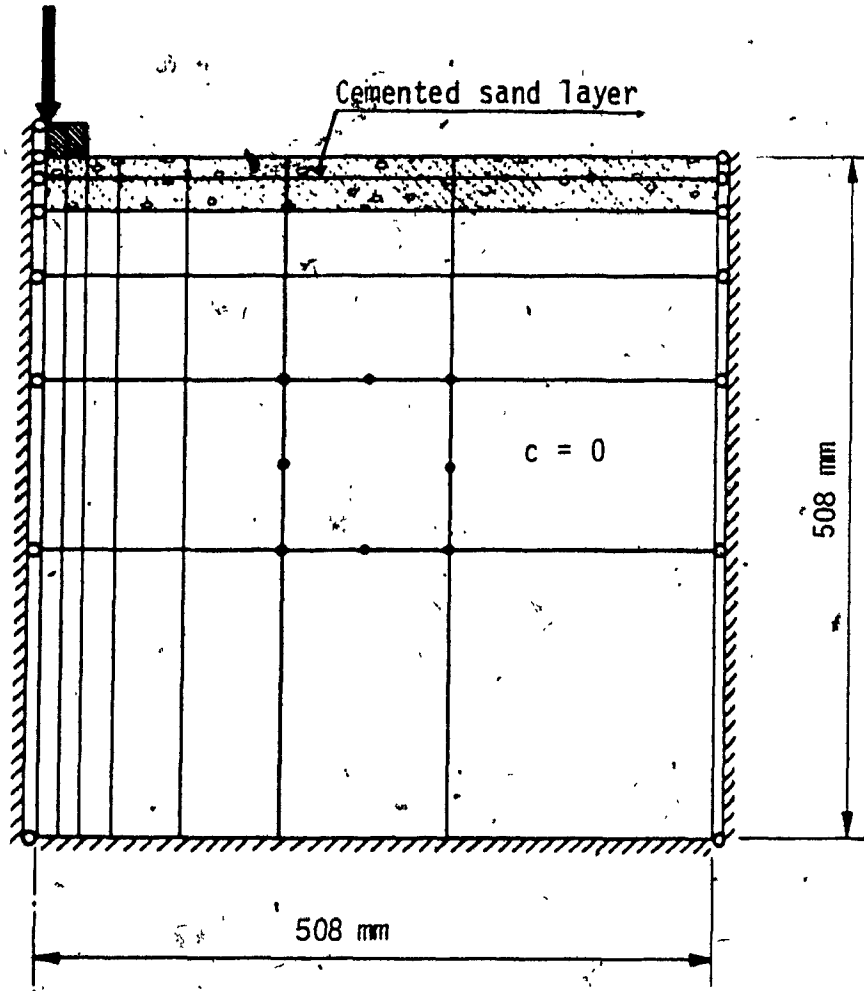


FIG. 4.7: Model footing on loose sand covered by layer of artificially cemented sand

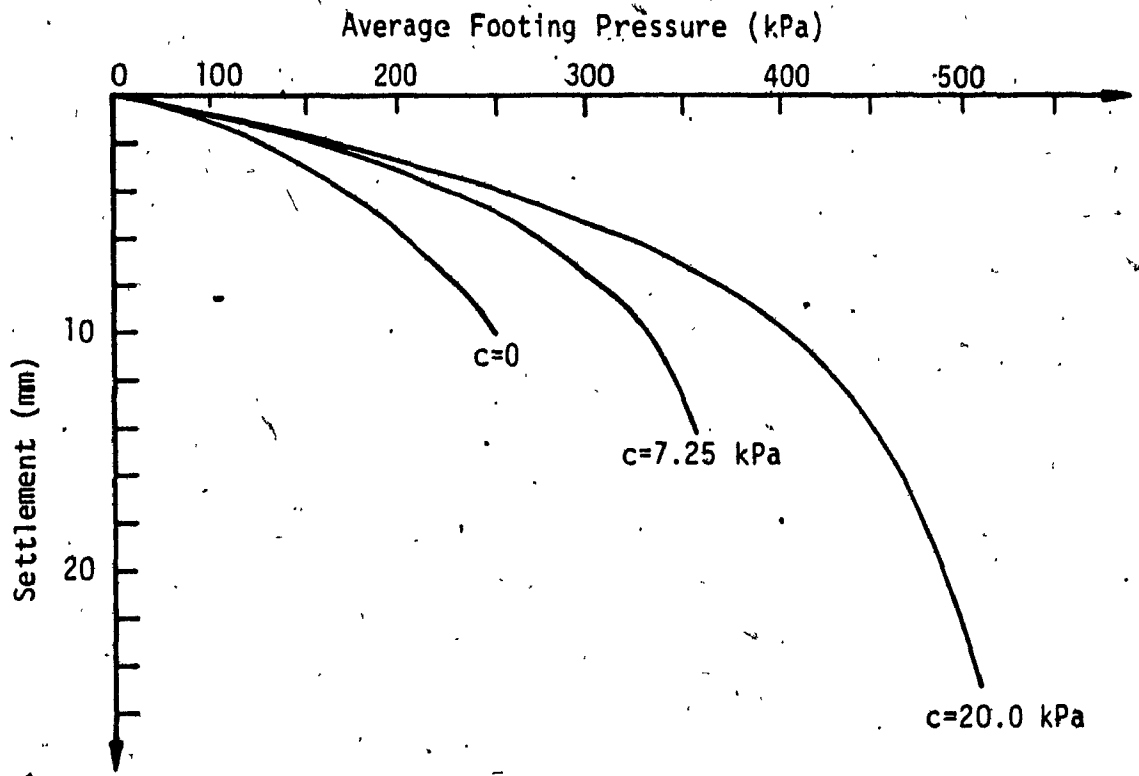


FIG. 4.8: Influence of degree of cementation of top layer on settlement of footing.

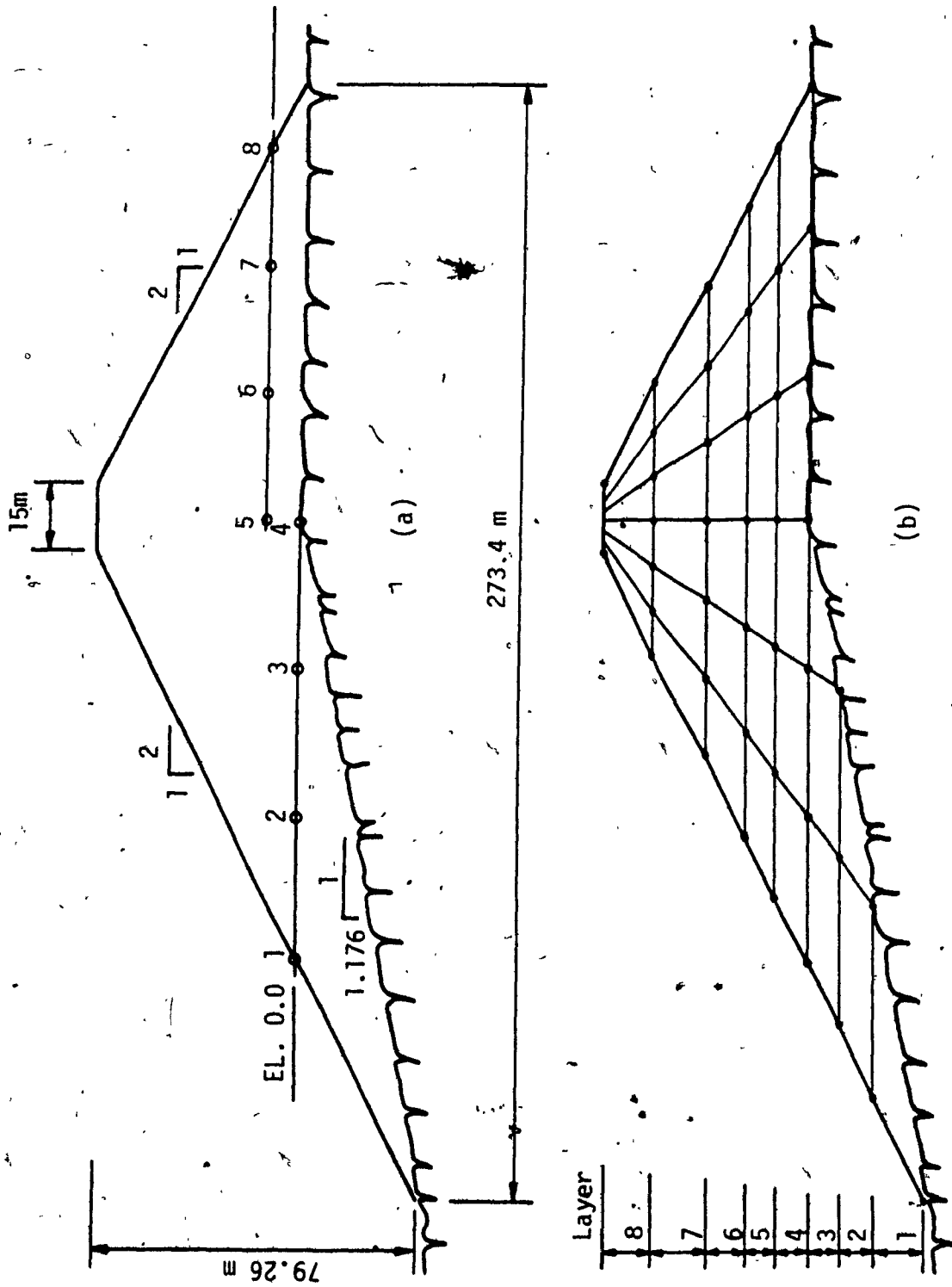


FIG. 4.9: Embankment structure: (a) dam cross-section with points where comparisons are made; (b) finite element mesh with layers of soil fill during construction

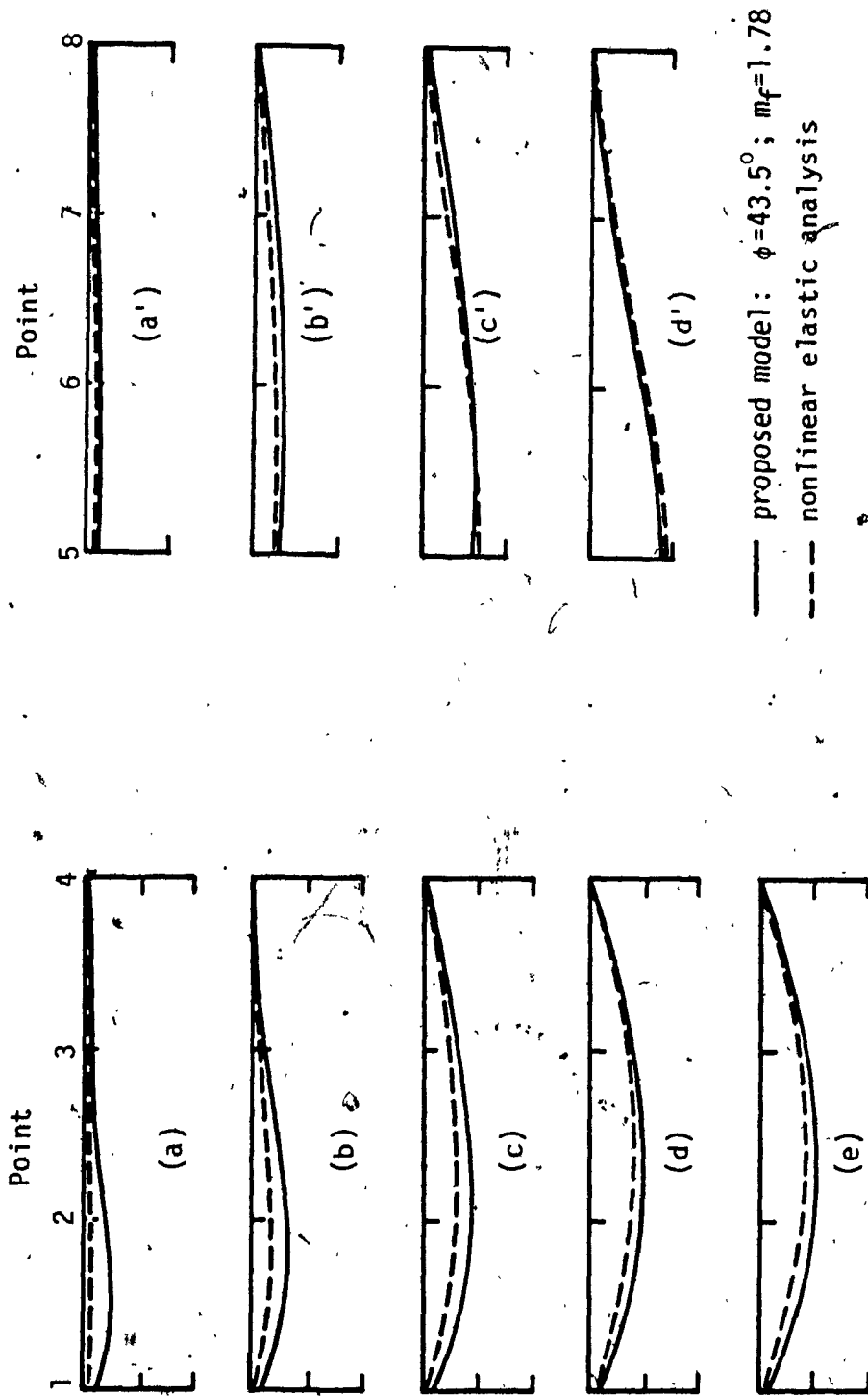


FIG. 4.10: Settlement at points 1 to 8 of prototype dam after application of construction layers 4 (case a) to 8 (case e) and 5 (case a') to 8 (case d').

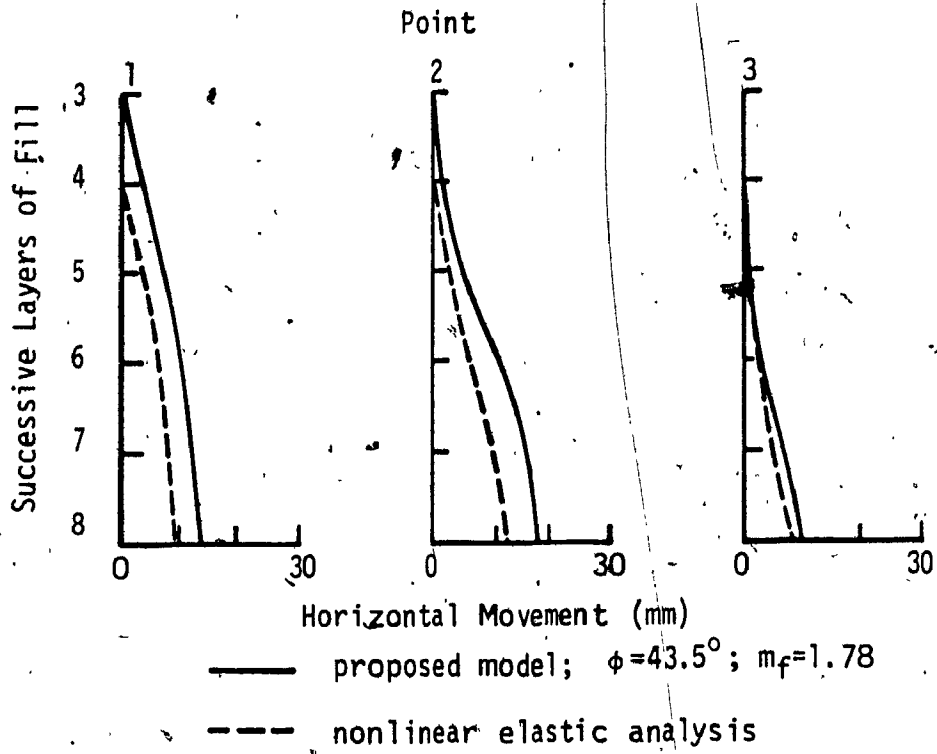


FIG. 4.11: Horizontal movement of points 1, 2 and 3 at EL. 0.0 m and different construction stages.

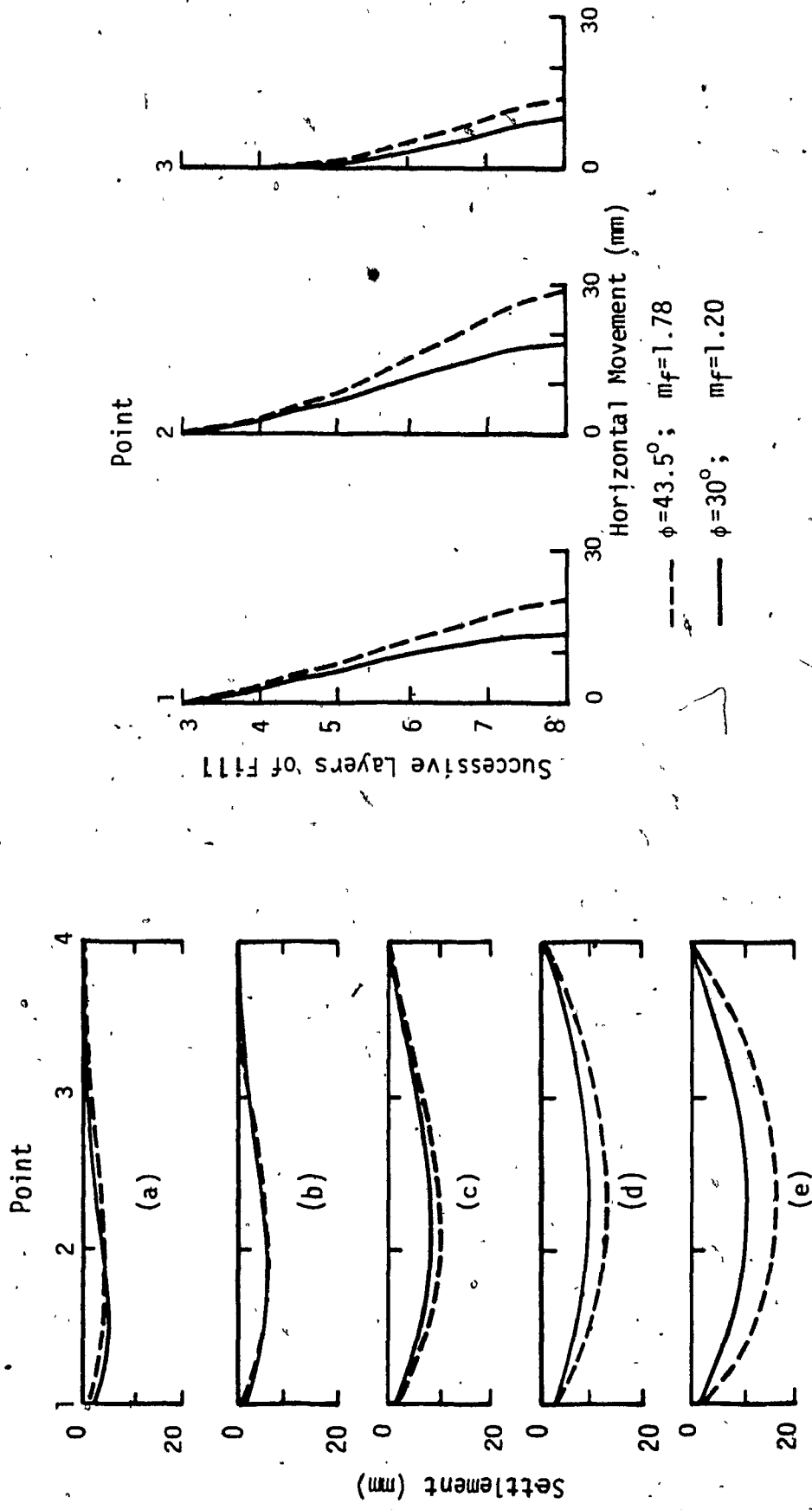


FIG. 4.12: Settlement and horizontal movement at points 1, 2 and 3 for different construction stages from proposed elasto-plastic analysis

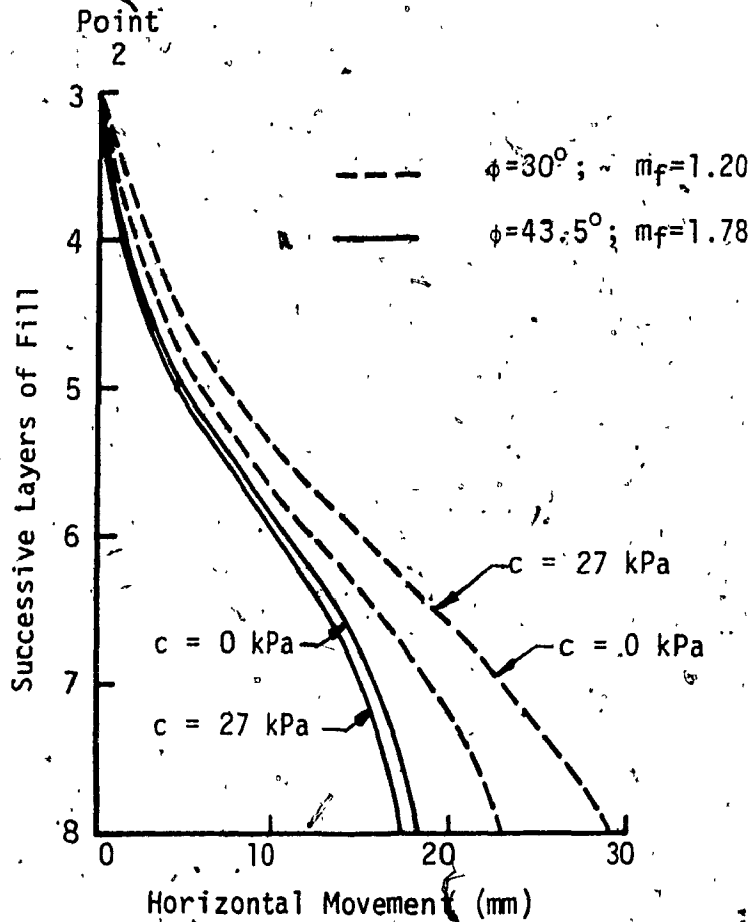
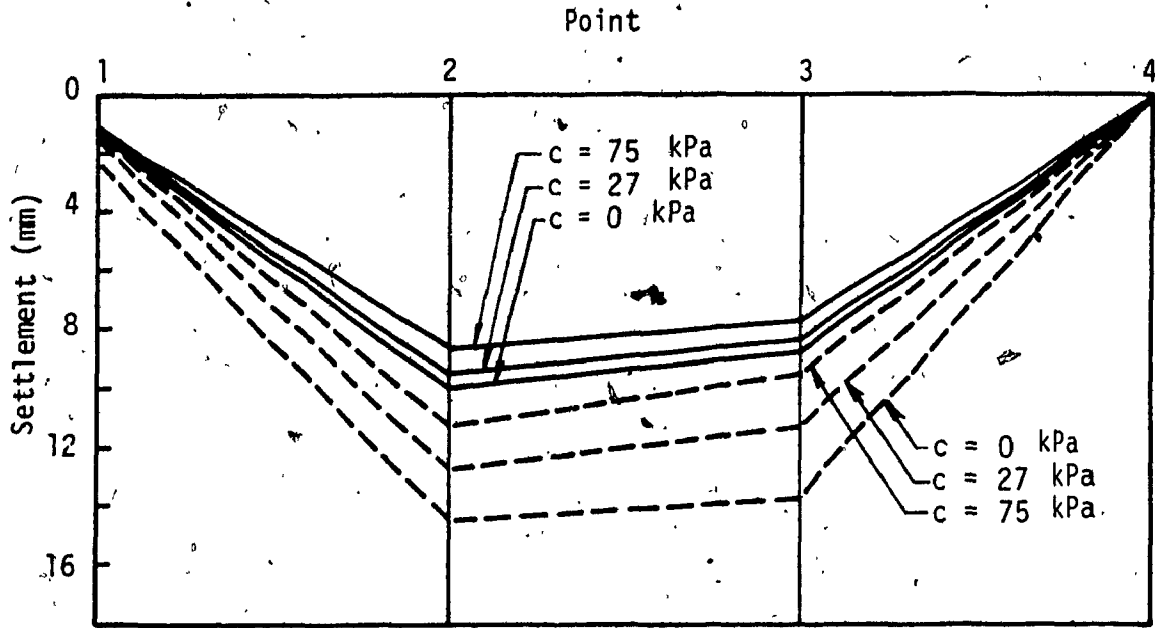


FIG. 4.13: Effects of cohesion c (kPa) on settlement and horizontal movement for elasto-plastic analysis

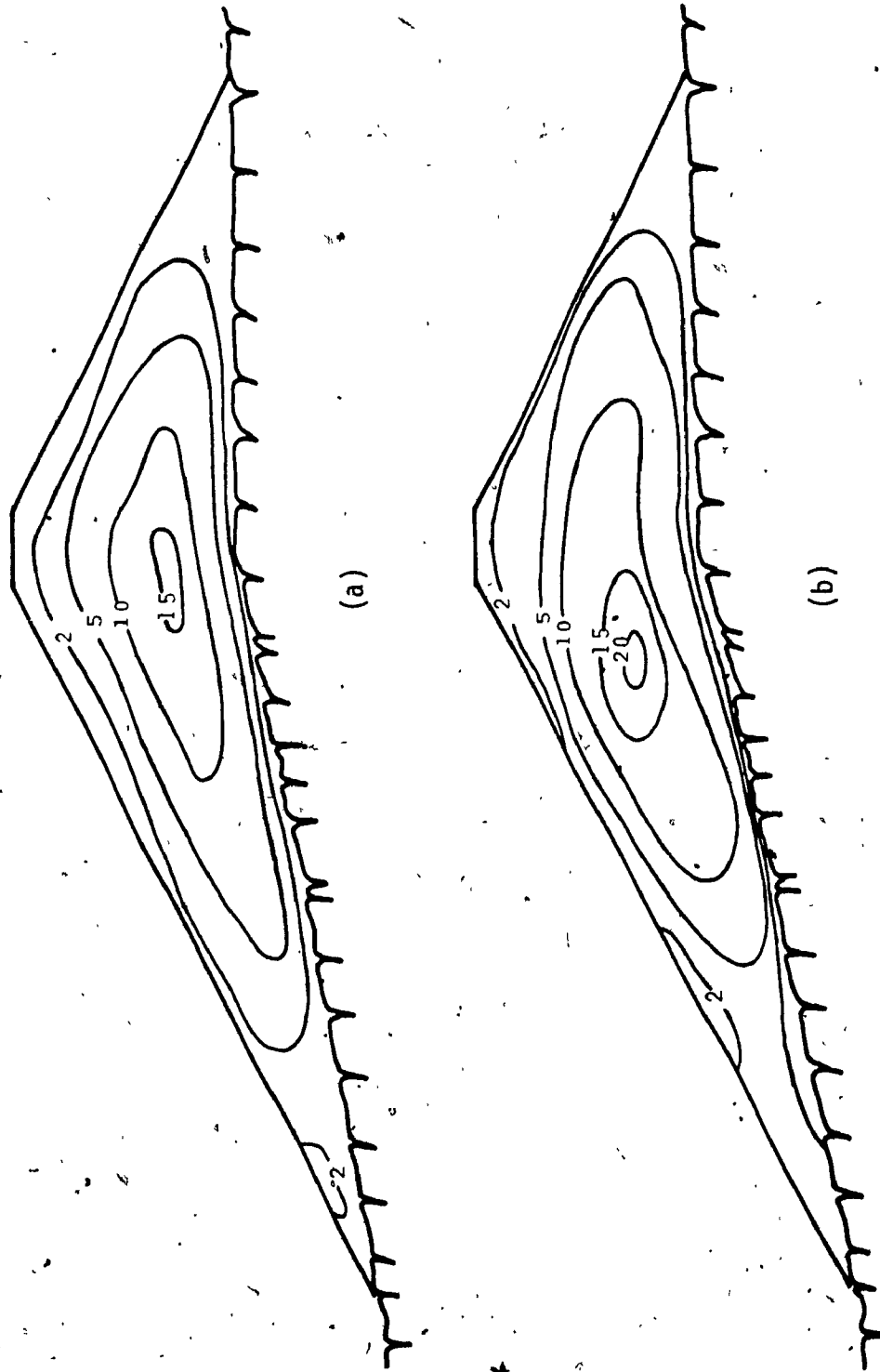


FIG. 4.14: Contours of settlements (mm) during construction obtained with:
(a) nonlinear elastic analysis; (b) proposed elasto-plastic analysis ($\phi = 43.5^\circ$)

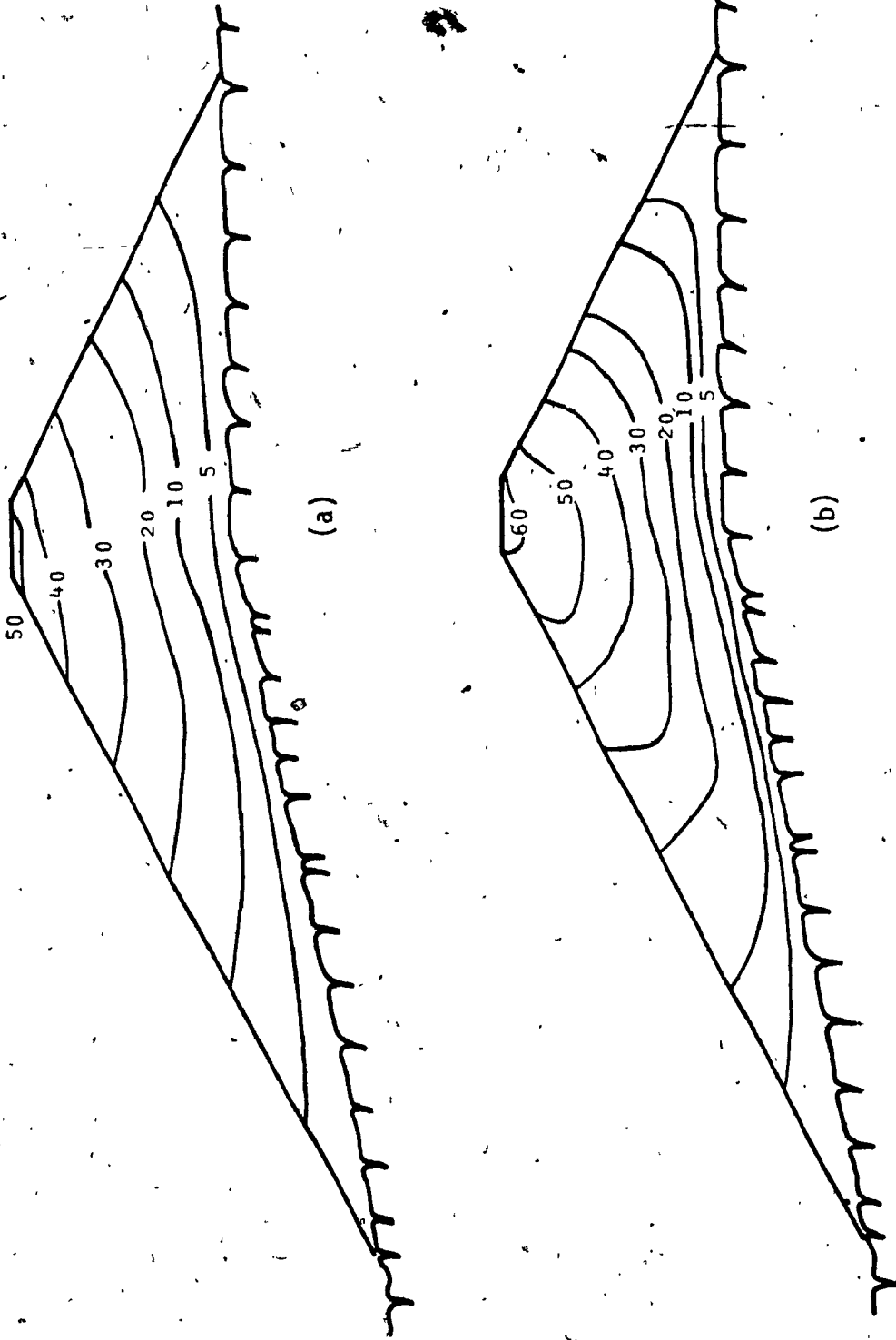


FIG. 4.15: Contours of settlement (mm) if single layer is considered: (a) proposed analysis; (b) nonlinear elastic analysis

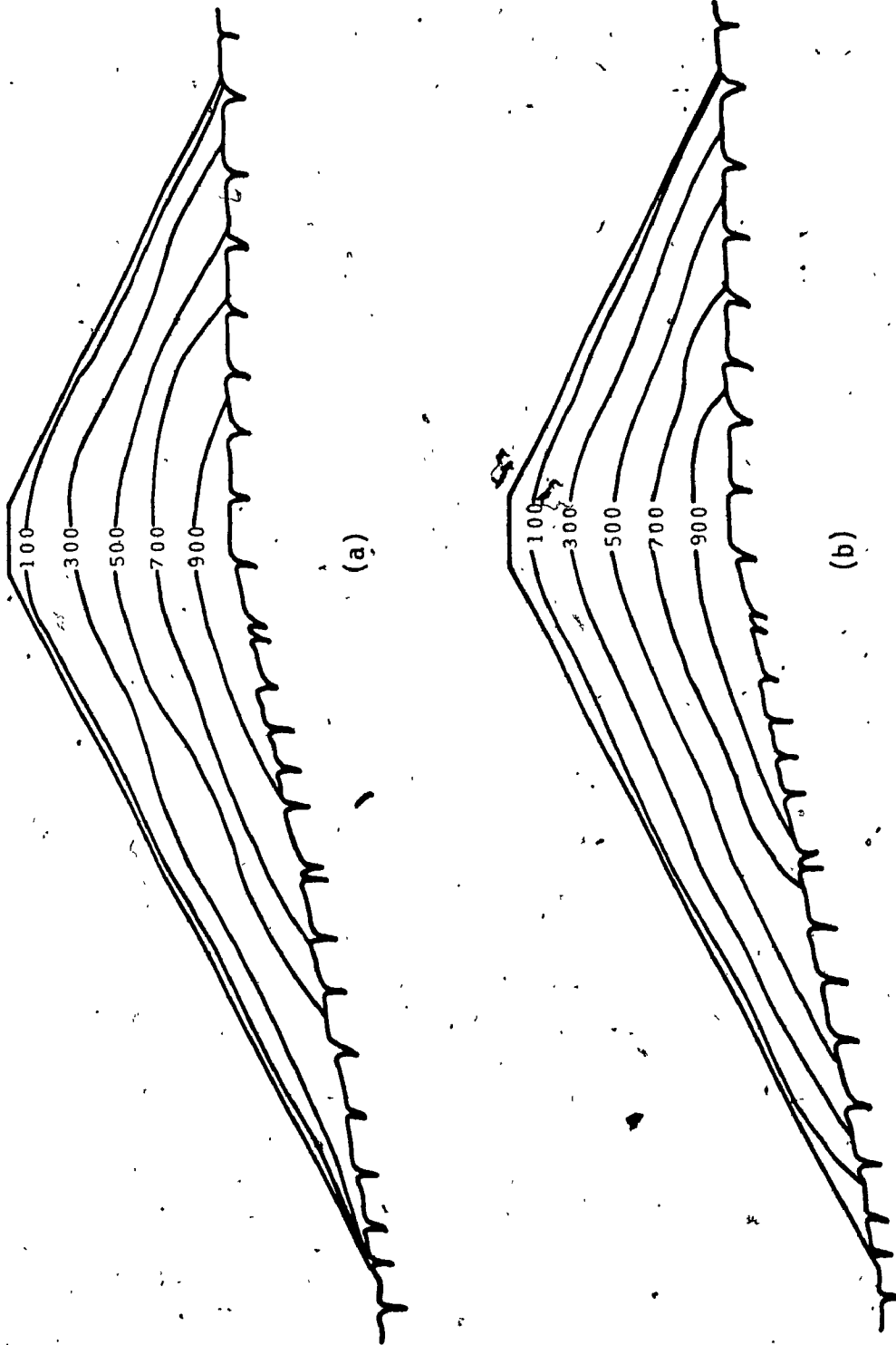


FIG. 4.16: Contours of minor principal stresses (kPa) determined by: (a) non-linear elastic analysis; (b) proposed analysis

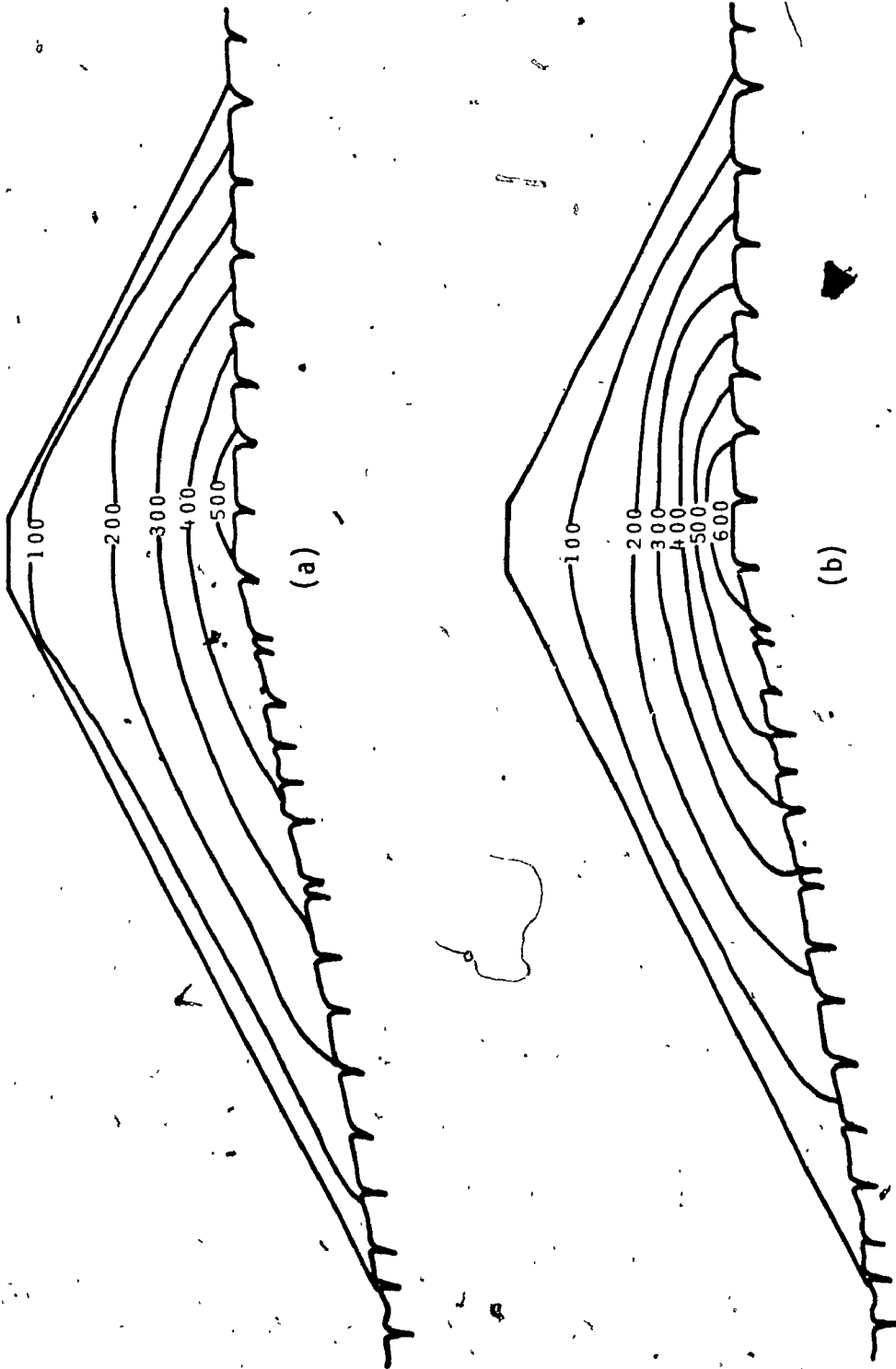


FIG. 4.17: Contours of major principal stresses (kPa) determined by: (a) nonlinear elastic analysis; (b) proposed analysis

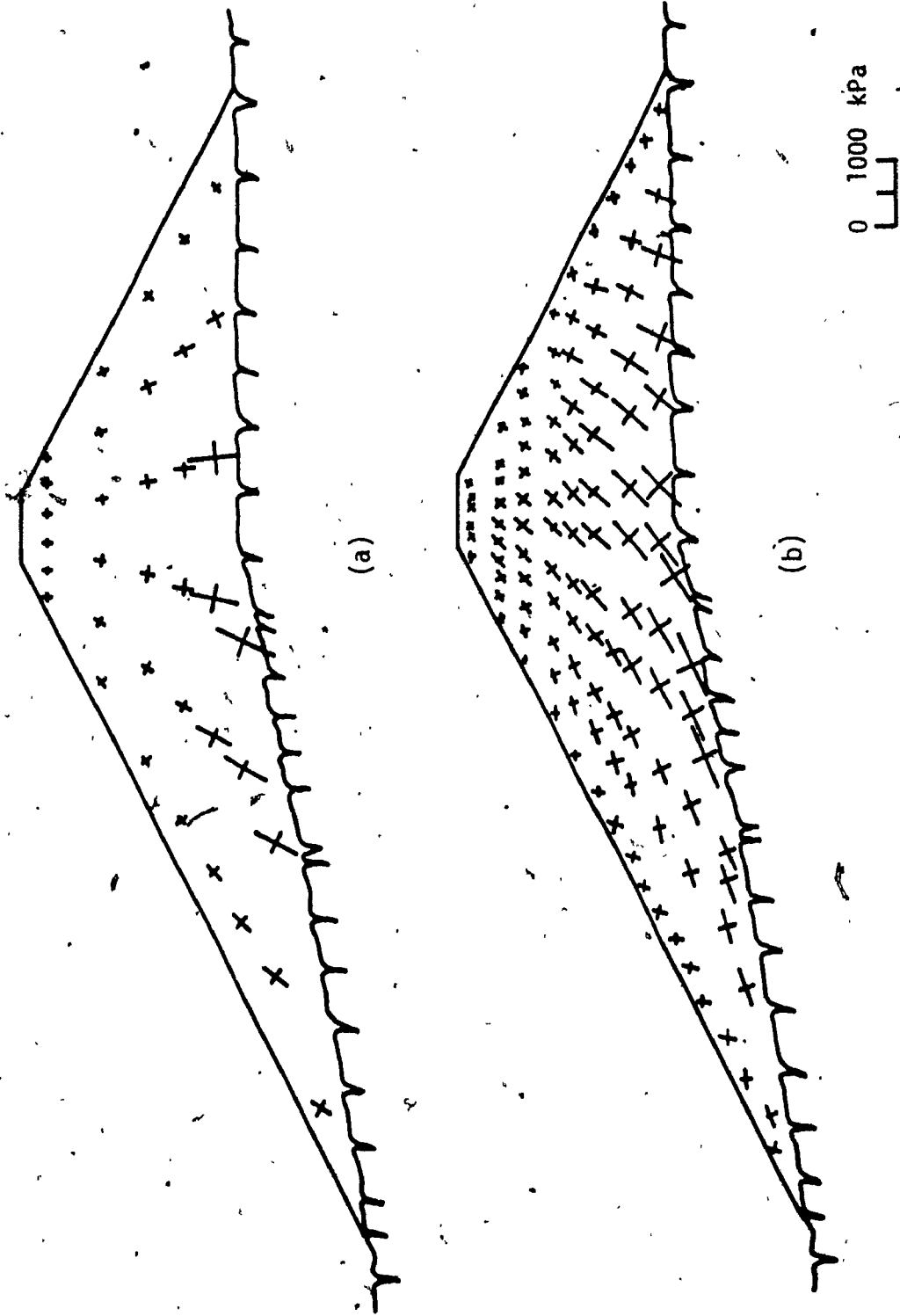


FIG. 4.18: Principal stresses from: (a) nonlinear analysis; (b) proposed analysis

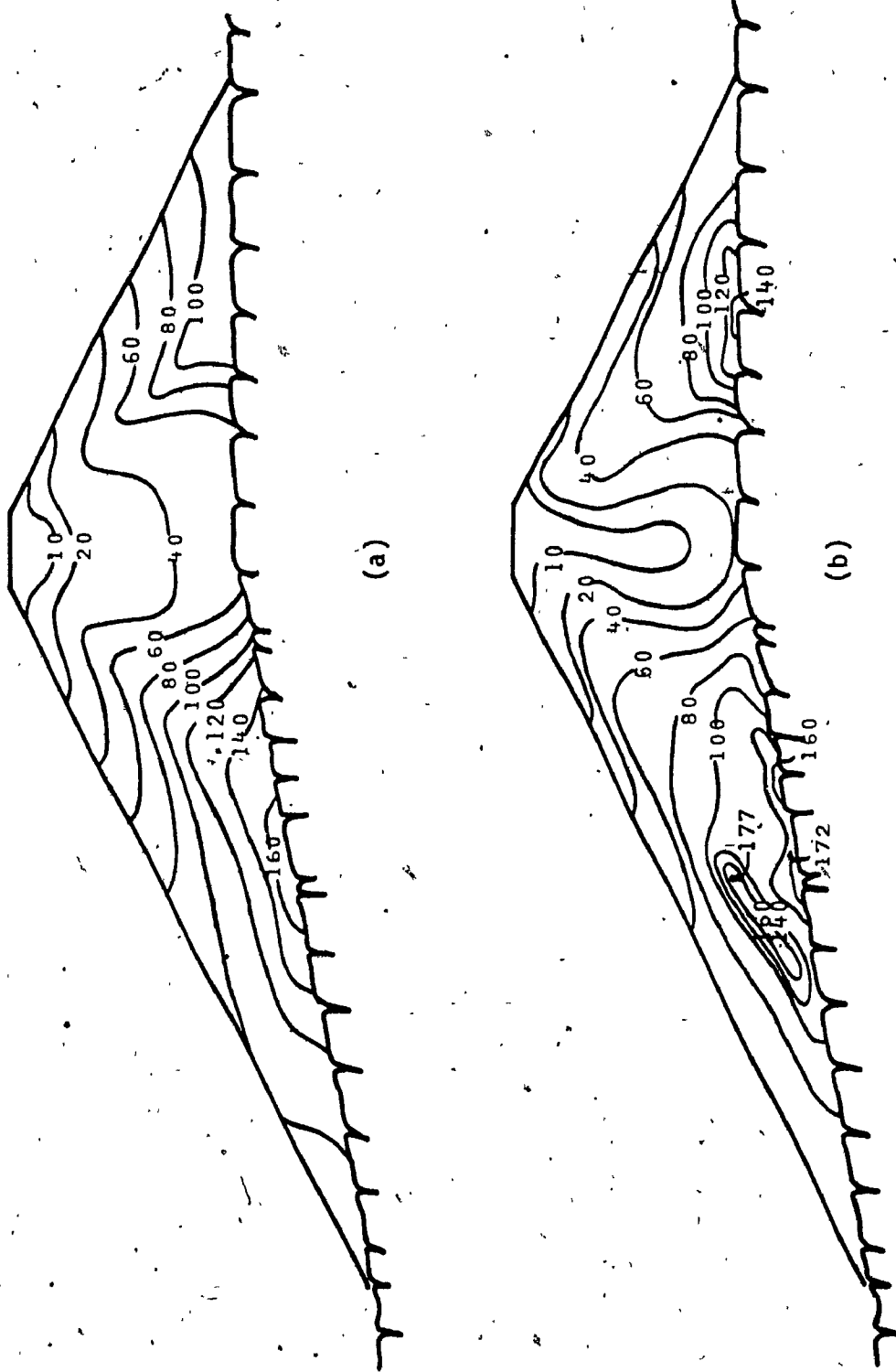


FIG. 4.19: Contours of shear stress τ_{xy} (kPa): (a) non-linear elastic analysis; (b) proposed analysis

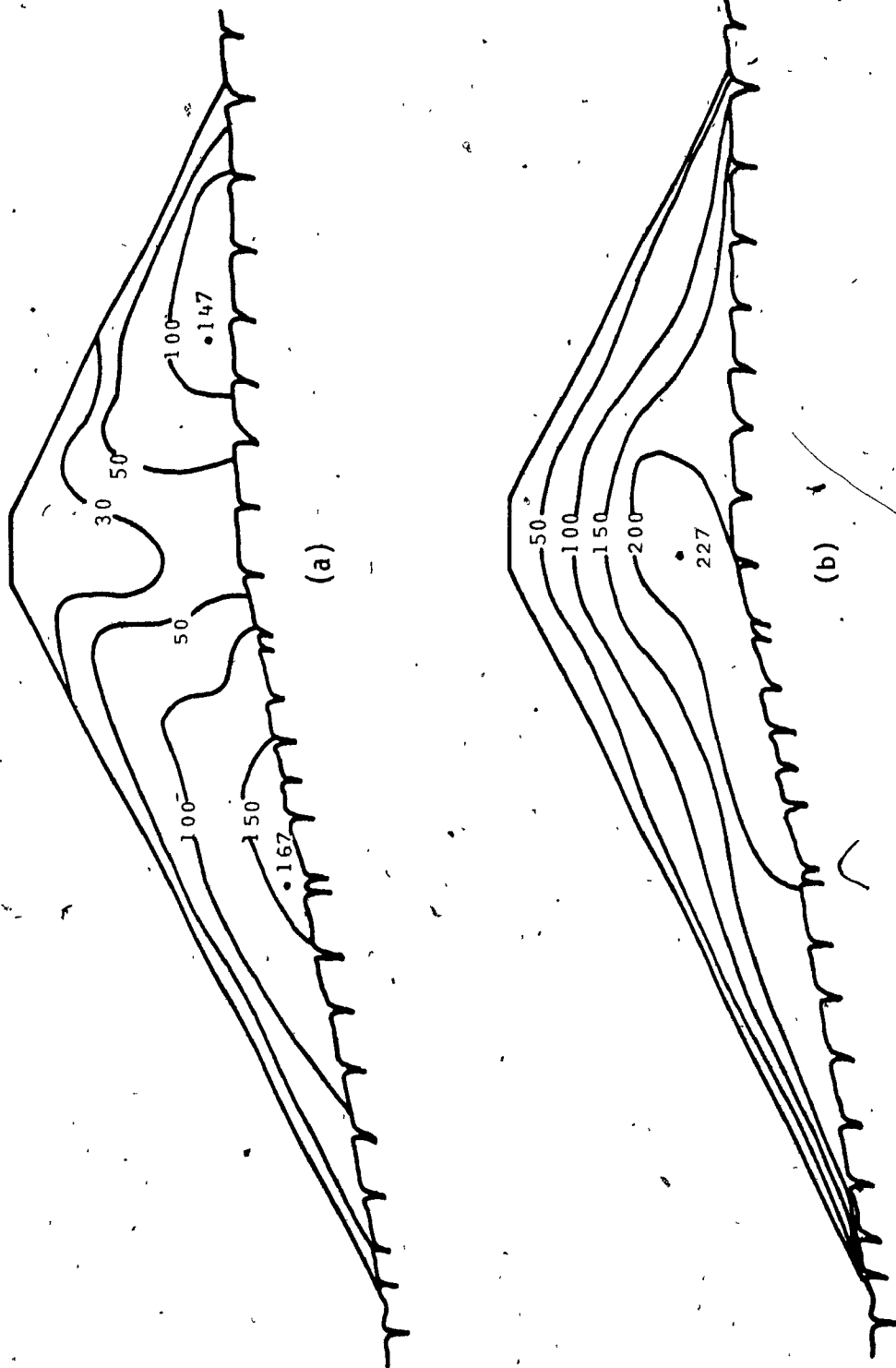


FIG. 4.20: Contours of maximum shear stress (kPa): (a) nonlinear elastic analysis; (b) proposed analysis

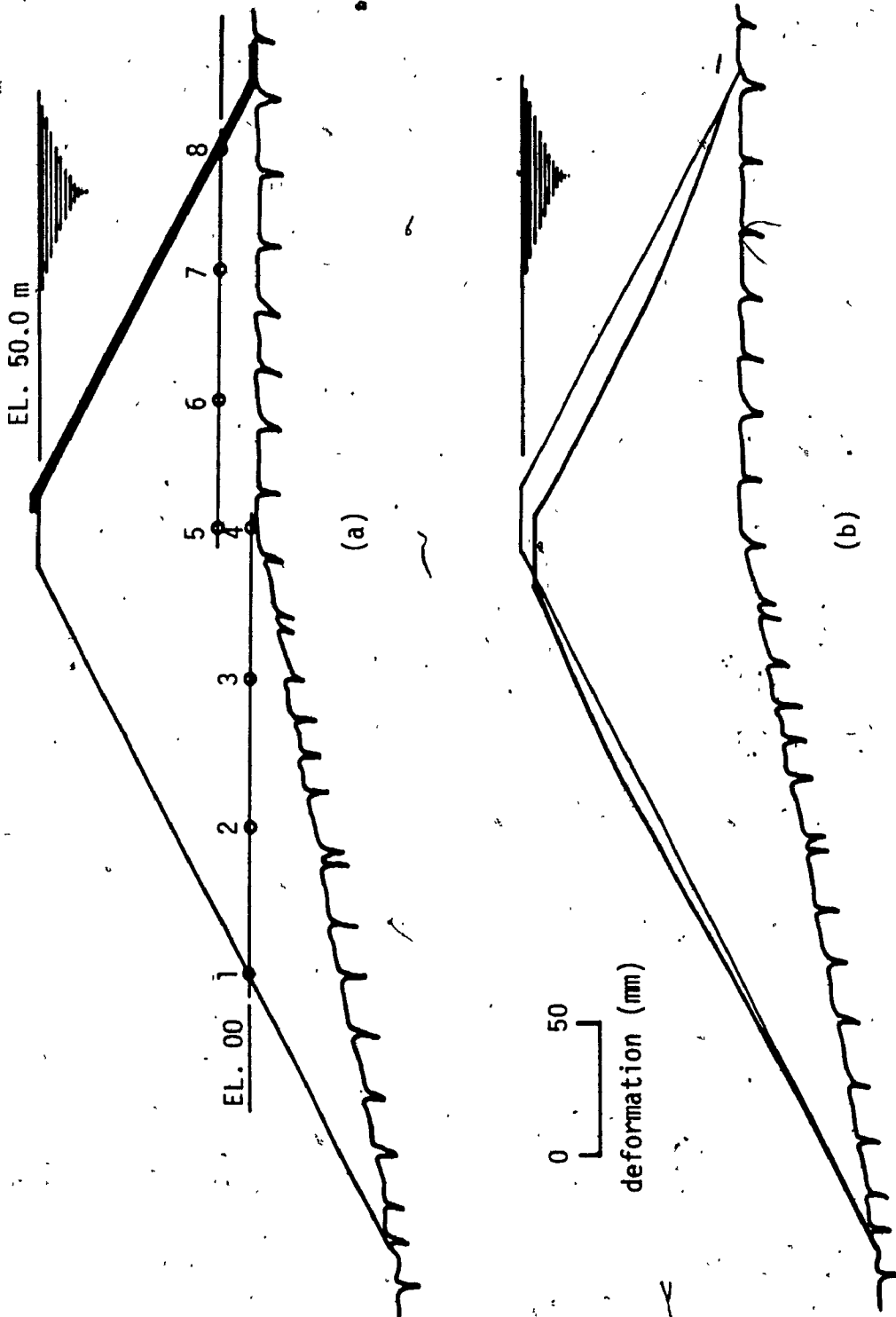


FIG. 4.21: (a) Dam cross-section and (b) movement of dam profile with water level at EL. 50.0 m

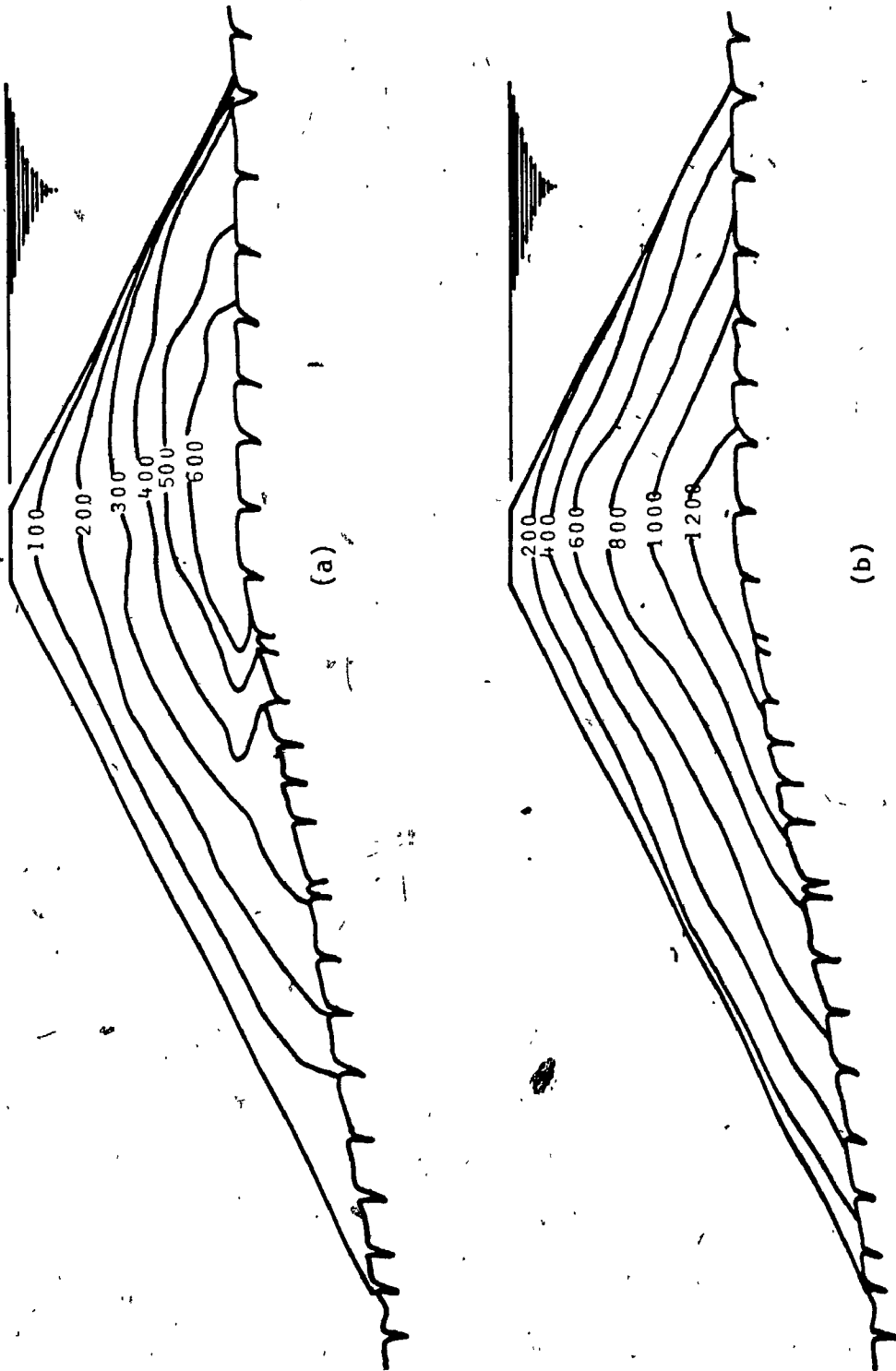


FIG. 4.22: Contours of (a) major and (b) minor principal stresses from proposed analysis with water level at EL. 50.0 m

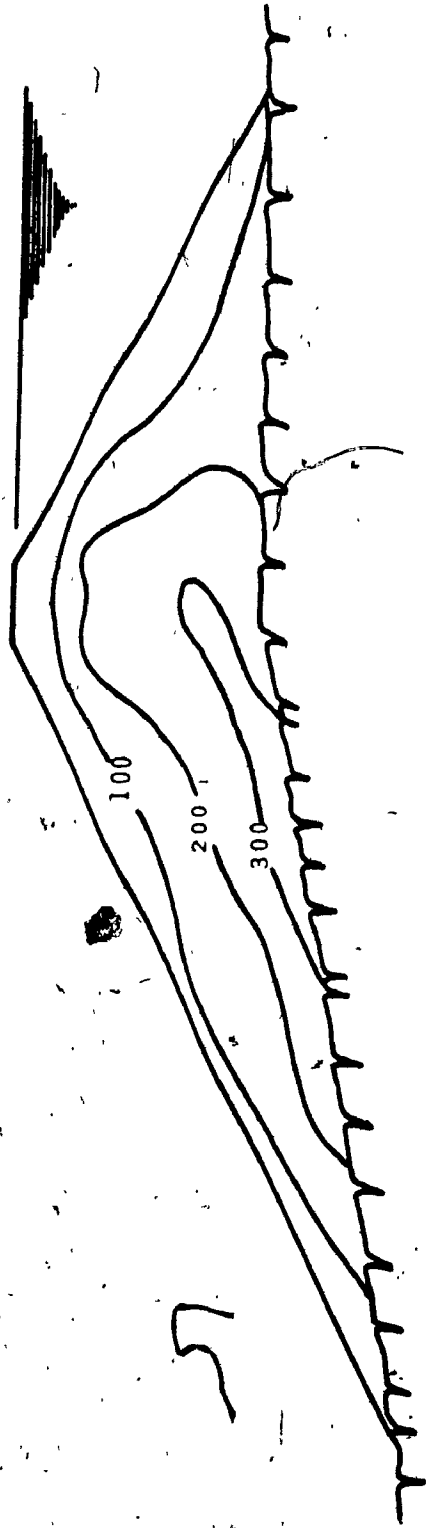


FIG. 4.23: Contours of maximum shear stress for proposed elasto-plastic analysis

5.0 MODELING OF NONLINEAR SOIL-STRUCTURE INTERACTION PROBLEMS

5.1 INTRODUCTION

In order to describe the behavior of structures founded on elasto-plastic soil, two static soil-structure interaction problems are analysed and presented in this chapter. The analysis of a mat foundation of an eight storey building reposing on clayey-silt [1.55] is presented first. The results obtained when the proposed model is used are compared with those reported in Ref. 1.55 where the mat was analysed by the conventional methods (subgrade reaction method, and compression index analysis), and also the finite element methods considering nonlinear elastic and elastic-plastic material behavior of the subsoil. The behavior of a concrete gravity dam on an elasto-plastic "soft" subsoil is analysed next. The principal parameters examined are the effects of the construction process, uplift water pressure, and cycling loading due to fluctuation of the retained water level.

5.2 MAT FOUNDATION ON CLAYEY-SILT

An eight storey prefabricated office building with a plan area of 60 m by 20.4 m, founded on alluvial clayey silt of 30 m deep, is shown in Fig. 5.1. The floor loads are transferred to the mat foundation by the use of concrete walls. The prefabricated concrete floor slabs are assumed hinged to their supports. This implies that the stiffness of the upper storeys has no influence on the mat foundation.

The required soil parameters for the conventional methods of analysis and the finite element nonlinear-elastic and elastic-plastic (von Mises) analysis are reported in Ref. 1.55. The soil properties are typical for silts or clayey silts. The title of the Ref. 1.55 clearly states that. However in the text of the same reference the material is mistakenly referred as clay. The reported data in Ref. 1.55 is used for the evaluation of required parameters for the proposed elasto-plastic analysis. The conducted tests used for evaluation of the soil properties are not reported. Therefore, the values of the initial elastic modulus and the hardening constant required by the proposed analysis are approximately evaluated from the parameters specified for the nonlinear elastic analysis, while the values of m_f and m_c are calculated with the relations described in Chapter II. The values of all parameters used in the analyses are summarized in Table 5-I.

The finite element structural representation of the mat and the subsoil is shown in Fig. 5.2. Due to the symmetry of loading, only half of the structure is modelled. The finite element mesh contains 53 isotropic eight-node plane-strain elements with a total of 188 nodal points. Each node has two translational degrees of freedom. At the silt-rock boundary both the horizontal and vertical movements of the boundary nodes are constrained. Along the vertical boundaries the nodes are constrained to move only in the vertical direction. The soil above the foundation level is accounted for by considering the equivalent vertical pressure due to the weight of soil. The initial analysis is performed by assuming a 300 mm thick mat.

The finite element mesh used in Ref. 1.55 is composed of triangular elements and differs from the mesh used in the present calculation. To evaluate the accuracy of the proposed finite element discretization, separate analyses are carried out using different mesh sizes and elements. Fig. 5.3 represents the significance of different finite element discretizations on contact pressure distributions and bending moments in the mat. It is thus concluded that satisfactory precision can be achieved by using a mesh containing 53 - 8-node elements.

The stresses due to gravity loads of the subsoil are introduced in the analysis as initial stresses. They were calculated previously without considering any loads from the structure. Drained condition of the subsoil is investigated in the present analysis.

The working loads of the structure as evaluated in Ref. 1.55 are applied to the elements representing the mat foundation in 40 increments, shown in Fig. 5.2 (a).

The results calculated by the proposed method are first compared with those reported in Ref. 1.55 and were evaluated by conventional methods. The subgrade reaction method was extensively used in the past to evaluate the distribution of the contact pressure under the strip or mat foundations. The subsoil in this method is simulated by elastic springs for which the stiffness is related to the subgrade modulus of the soil. The other conventional method used for comparison of the results is the compression index analysis. Here, the subsoil is considered as an elastic isotropic halfspace. Both classical methods are well explained in the literature and need not be discussed here.

Fig. 5.4 shows the comparisons of contact pressure distributions and bending moments between the proposed analysis and conventional methods. Since the conventional methods predict unrealistic results at the edges of footings (i.e. pressure = ∞), hence comparison will be made at interior points. The proposed elasto-plastic analysis indicates comparatively higher stress concentrations beneath the interior walls and the edges of the raft, which lead to smaller bending moments between the walls and larger bending moments under the walls in the mat. The maximum calculated contact stresses by the proposed analysis are 22.5 % and 27% higher than the stresses calculated with the compression index and subgrade reaction analysis respectively. The resulting bending moments in the mat footing between the walls, evaluated by the proposed analysis are 52% lower than those calculated with the subgrade modulus analysis, and 35% lower than moments obtained with the compression index analysis. Under the walls however, the bending moments in the mat calculated by the proposed analysis are higher. Compared with those obtained by the subgrade modulus method and compression index analysis the moments under the interior walls are higher by 34% and 12% and under the exterior walls are higher by 90% and 44% respectively. It should be noted that the above differences in either contact stresses or bending moments pertain only to a specific mat thickness and soil characteristics. Thus the interaction between mat foundation having other thicknesses and subsoil characteristics will be examined.

The comparison of contact stresses obtained with the current analysis and other finite element procedures is shown in Fig. 5.5. The finite element procedures employed in Ref. 1.55 and used for comparison of results assume nonlinear elastic or elastic-plastic soil behavior. The

nonlinear elastic procedure is based on the constitutive model incorporated in the computer program LSBUILD [1.68] by Kulhawy and Duncan, while the elastic-plastic procedure uses as a failure criterion the von Mises yield criterion incorporated in a separate computer finite element algorithm. Similar contact stress distributions are observed in all analyses. The maximum stresses obtained from the elasto-plastic model under the interior wall are found to be 15% and 9% higher than those from the von Mises yield criterion and the nonlinear elastic models respectively. At the edge of the mat foundation the contact pressure calculated by the proposed analysis is similar to the one obtained by the nonlinear elastic procedure, however it is 10% higher than the pressure calculated by the elastic-plastic procedure assuming von Mises yield criterion. It can be seen from Fig. 5.5(b) that the differences in the bending moments developed in the mat are negligible. A maximum difference of only 1.2% in the bending moments is observed between those calculated by the present model and that of the von Mises yield criterion.

Due to lack of laboratory test data of soil properties as reported in Ref. 1.55, the values of the initial elastic modulus and the hardening constant used in the present analysis were approximated. Therefore, analyses are performed to evaluate the sensitivity of the results to these parameters.

Fig. 5.6 shows the effect of the subsoil initial elastic modulus on the magnitude and distributions of the contact pressure and bending moments. A difference of 270% in the initial elastic modulus produces a relatively small maximum difference of 12% in the contact stresses and,

less than 1% in bending moments. Similar comparison of contact stresses and bending moments is shown in Fig 5.7 where the hardening constant "A" in the proposed constitutive relations is varied. Here, a variation of 100% in the hardening constant results in a maximum change of 18% and 30% in contact stresses and bending moments respectively.

Figs. 5.8 presents the contact pressure distribution in the subsoil and the bending moments in the mat foundation obtained with the elasto-plastic analysis. From the results it is apparent that with an increase of a 100% in the mat thickness, the maximum stress concentration in the subsoil under the interior bearing wall reduce by 17.5% , whereas the maximum bending moment in the mat at the same location increases by 30%.

Fig: 5.9 shows the differential settlement, between the center and the edge of the mat foundation, as a function of the mean contact stress calculated by the elasto-plastic analysis. The settlements due to the actual (working) load are found to be 121 mm at the center and 112 mm at the edge of the mat. Thus the differential settlement is only 9 mm.

Generally speaking, the strength of a mat foundation is governed by the following limiting states:

- i) Maximum permissible settlement;
- ii) Ultimate strength of the reinforced concrete mat;
- iii) Local shear failure of the soil; and
- iv) General shear failure of the soil.

The ultimate strength of the analysed mat foundation is attained at a bending moment of 370 kN.m, for a slab thickness of 300 mm, and at a bending moment of 200 kN.m for a slab thickness of 600 mm. The values were calculated using the National Building Code of Canada (Ref.5.1) with a concrete strength of $f'_c = 30$ MPa and a reinforcement ratio $\rho_s = 0.75 \rho_b$. For the 300 mm slab the ultimate moment of 370 kN.m corresponds to a mean contact pressure of approximately 120 kPa. Using Terzaghi's bearing capacity equation (Ref.5.2), the conditions of local shear failure (large soil compaction under the entire footing) and general shear failure (soil undergoes sudden failure) of the soil are reached at mean contact pressure of 614 kPa and 1754 kPa, respectively. It can therefore be concluded that the ultimate strength of mat foundations is governed by the concrete strength and that local, as well as general shear failures cannot occur.

For the ultimate loading (120 kPa) the observed maximum settlement is 190 mm (Fig. 5.9). Depending on the structural application of the building under consideration, this magnitude of settlement may or may not be acceptable.

5.3 CONCRETE GRAVITY DAM ON ELASTO-PLASTIC SOIL

In this section, the soil-structure interaction between a typical concrete gravity dam and its supporting soil exhibiting elasto-plastic behavior is described. The configuration of a typical concrete gravity dam and foundation is illustrated in Fig. 5.10. The width of the dam is 50.0 m at the base and 9.0 m at the crest, with an overall height of 50.0 m. To prevent sliding a 10.0 m deep shear key is incorporated at the base of the dam. If required, a water barrier and a drainage system may be installed on the shear key.

The material properties used in the analysis are similar to those used for the Oroville Dam (Ref. 1.12). The required parameters for the present model are derived directly from these material properties and tabulated in Table 5-II. The cementation in the soil masses is simulated by introducing cohesion of 20 kPa. This value is within the range of cohesion for naturally cemented sands as reported in Ref. 2.3.

The depth of the cemented alluvial sand and gravel deposit is assumed 70.0 m. It possesses low permeability and is bounded at the bottom with impermeable rock.

The finite element mesh, as shown in Fig. 5.11(a), consists of a total of 38 elements and 143 nodal points. Both the gravity dam and the foundation are idealized by two-dimensional, plane-strain, 8-noded isoparametric elements. A 2x2 Gauss integration rule is used for the stiffness evaluation. The model base is assumed to be fixed in both horizontal and vertical directions, and side boundaries are represented by vertical rollers, i.e. restrained in the horizontal direction.

The water pressure loads considered in the analysis are shown in Figs. 5.11(b) and 5.11(c). Three types of uplift pressure patterns are shown: (i) no uplift pressure (neglected due to complete impermeability), (ii) uplift pressure with cutoff based on a normal design practice, and (iii) complete uplift pressure without cutoff with its maximum value at the toe and zero at the heel.

5.3.1 Construction Stresses and Deformations

The construction process of the dam is simulated by applying 40 successive layers of concrete of equal weight. Deformation of the dam upon completion of construction is shown in Fig. 5.12(a). It is worth noting that in practice this deformation is normally adjusted during construction and hence the analysis is based on the undeformed geometry. The contours of maximum tensile stresses (major principal stresses) are shown in Fig. 5.12(b). The developed tensile stresses may be avoided or reduced at this stage by proper modification of the dam geometry.

The contours of maximum compressive stresses (minor principal stresses) of the dam upon completion are plotted in Fig. 5.13(a). The corresponding plastic strains are shown in Fig. 5.13(b). It should be noted that at the vertical subsoil boundary on the reservoir side the values of the accumulated plastic strains are higher than normally expected. The reason being is the effect of the boundary conditions assumed for the finite element mesh.

5.3.2 Effect of Water Fluctuation and Uplift Pressure

Consider the dam subjected to a rise in water level to EL. 50.0 m and an uplift pressure with cutoff, the resulting deformation and stress contours are shown in Figures 5.14 and 5.15. It should be noted that the previously obtained stresses (Figure 5.13) are prescribed as initial stresses for the present analysis. Due to the fluctuation of the water level in the reservoir, it is apparent that the dam will be subjected to a loading of cyclic nature. For convenience initial filling of the reservoir is defined as the first load cycle, following each fall and rise constitutes an additional cycle of loading. Fig. 5.14 shows the

deformation of the structure after the first load cycle.

The response of the dam to three different uplift pressure distributions and cyclic loads is presented in Fig. 5.16. In Fig. 5.16(a), the effect of uplift pressure on the overall deformation of the dam after the first load cycle is clearly demonstrated. The horizontal displacement of the crest increases by 39% for full uplift, and by 30% for uplift with cutoff. On the other hand, the difference in crest displacement between full uplift and uplift with cutoff is about 7% after the first cycle, and 36% after the twelfth cycle (Fig. 5.16(b)).

The permanent dam deformations after the first, fifth, tenth, and twelfth load cycles with and without uplift, are shown in Figs. 5.17(a) and 5.17(b) respectively. The water fluctuation of 20.0 m for each loading cycle is considered. In both instances it is shown that the deformation increases with progressing load cycles, with larger deformations observed for the case when uplift pressure is considered. The load-displacement relations at the crest of the dam are shown in Figs. 5.18(a) and 5.18(b). The total load W_T is related to the water at El. 50.0 m while W is the current elevation load. These curves illustrate the accumulation of plastic deformations with increasing load cycles, regardless of the presence of uplift.

It can be expected that the effect of plastification of the soil is more pronounced if the amplitudes of the load cycles are increased. Consider that the fluctuation in water level increases to 40.0 m and remains constant for each load cycle, the modes of deformation of the dam and the upper layers of the foundation for the first, fifth and tenth

loading cycles are shown in Figs. 5.19(a), 5.19(b) and 5.19(c) respectively. The accumulated plastic displacement of the concrete dam is presented in Fig. 5.20(a), and the complete load-displacement history of the crest of the dam is shown in Fig. 5.20(b). These results when compared with those obtained with water fluctuations of 20.0 m show considerably larger plastification of the foundation soil. Specifically the horizontal displacement of the dam at the crest, after twelve load cycles, is found to be 269.0 mm or 38% larger.

The contours of the minor principal stresses (compression) developed in the dam after the first and twelfth loading cycles, for two amplitudes of water fluctuation (20.0 m and 40.0 m) are shown in Figs. 5.21 and 5.22.

The minor principal stresses of the dam after twelve loading cycles increase (in zones with stress concentration) by 30% to 42% and 47% to 75% when water fluctuations in the reservoir are considered 20.0 m and 40.0 m respectively.

The tensile stress zones of the concrete dam are shown in Fig. 5.23. After the first cycle a maximum tensile stress of 1140 kPa is developed at the middle of the base of the dam (Fig. 5.23(a), whereas after the twelfth cycle a maximum tensile stress of 3548 kPa is observed at the toe of the dam. The latter indicates cracking of the concrete in the toe area, since the rupture strength has been exceeded ($f_t = 2.7$ MPa for concrete $f'_c = 20$ MPa).

The sliding stability of a gravity dam is directly related to the shear strength of the foundation soil. Fig. 5.24(a) shows the contours of maximum shear stresses in the subsoil subsequent to the first loading cycle. As shown in Fig. 5.24(b), after twelve loading cycles, the zones with high shear stresses are clearly marked, indicating possible sliding planes.

Figs. 5.25(a) and 5.25(b) present the contours of accumulated plastic strains in the foundation. After twelve loading cycles an increase of 27% in the maximum plastic strain is observed. The zones with high soil plastification occur around the heel and the shear key of the concrete gravity dam.

5.4 CONCLUSION

The behavior of structures founded on elasto-plastic soil was examined in this chapter. The static nonlinear soil-structure interaction examples were:

- (a) analysis of mat foundation; and
- (b) analysis of concrete gravity dam on soft foundation.

In the case of the mat foundation the results obtained were compared with those predicted by conventional analytical procedures and from another finite element procedure. The concrete gravity dam was analysed with the proposed elasto-plastic analysis and the effect of the permanent soil deformations due to water fluctuation in the reservoir was examined.

Based on the numerical results obtained for the mat foundation analysis the following conclusions are made:

- (1) The maximum stress concentrations beneath the mat, calculated with the proposed model, are 22.5% and 27% higher than those obtained by the compression index and subgrade reaction modulus analyses respectively.

Consequently, the bending moments in the foundation between the walls calculated by the present analysis are respectively 52% and 35% smaller than those obtained by the subgrade reaction and compressed index analyses. Under the interior walls the moments calculated by the proposed model are higher by 34% and 12% and under the exterior walls by 90% and 44% compared with those obtained by the subgrade modulus method and compression index analysis respectively. Both conventional methods assume elastic soil behavior. Therefore, the more realistic soil modeling procedure of the proposed model is regarded as the main reason for the difference in the predicted response.

From the point of view of a design engineer the found difference does not affect the overall quantity of the required reinforcement, and therefore will not optimise the design process.

- (2) The comparison of the present results with those obtained by the other finite element procedures show a smaller difference in both contact stresses (9% to 15%) and bending moments (1.2%).

- (3) The initial elastic modulus does not have a significant effect on the results obtained by the present analysis. However, in order to reduce the error in the calculated stresses and moments care must be taken in evaluating the hardening constant of the model.
- (4) An increase in the mat thickness results in a better distribution of contact stresses but larger bending moments. A 100% increase of the mat thickness (from 300 mm to 600 mm) reduces the maximum contact stress by 7.5% while the bending moment in the mat increases by 33%.
- (5) The failure loads corresponding to the local shear failure or overall shear failure in the soil are respectively 8 to 20 times higher than those based upon the ultimate strength of concrete. Similarly, these loads will produce settlements larger than those acceptable for majority of the structures. Hence, they do not govern the ultimate capacity of this type of foundations.

From the results obtained in the analysis of the concrete gravity dam, the following conclusions are noted:

- (1) Proper geometry of the gravity dam is necessary to reduce or avoid tensile stresses in the concrete gravity dam during the construction phase.
- (2) Depending upon the compressibility of the foundation soil considerable settlement of the dam may occur during the construction period.

- (3) The overall stress distribution in the foundation is similar for both the construction phase and the first application of loading due to the water in reservoir.
- (4) The influence of uplift pressure on the calculated displacements is significant. The horizontal displacement at the crest of the dam is 30% and 39% higher when calculated considering full or partial uplift pressures respectively, than those when the uplift pressure is neglected.
- (5) Variations in the uplift pressure pattern due to the water barrier underneath the dam does not significantly affect the magnitude of displacements. A maximum difference of 7% was observed between those complete and partial uplift pressure cases.
- (6) The fluctuation of the water in the reservoir is found to have considerable effect on both (a) the permanent dam deformation, and (b) on the magnitude and distribution of stresses in the dam and the foundation.
- (7) With or without uplift pressure underneath the dam, permanent plastic deformation accumulates following any loading cycle.
- (8) The magnitude of accumulated plastic deformation is directly related to the amplitude of water fluctuations. The calculated plastic deformation was found to differ by 38% between the cases analysed with variations of 20.0 m and 40.0 m.

- (9) The magnitude of stresses and the stress distribution in the dam and foundation are influenced by the water fluctuation. A 75% increase in stress in the dam after the twelfth load cycle is observed. Zones with tensile stresses develop in the concrete dam after a few loading cycles. These tensile stresses exceed the rupture strength of concrete and hence cracking was predicted.
- (10) The magnitude of shear stresses in the foundation which relates directly to the sliding stability of the gravity dam, increases with successive load cycles. An average increase of 50% in the maximum shear stress in the soil occurs after twelve loading cycles.
- (11) The accumulated plastic strains that relate to the shear stress increase by 27% after a twelve loading cycles.

PARAMETERS	SYMBOLS	VALUE
SOIL		
SUBGRADE REACTION MODULUS (kH/m^3)	k_s	520.0
COMPRESSION INDEX MODULUS (kH/m^2)	c_r	2060.0
depth: from 0.0 to 10.5 m		3460.0
from 10.5 to 30.0 m		3.5
COHESION (kH/m^2)	c	27
FRICTION ANGLE (degrees)	ϕ	125
MODULUS NUMBER	K	0.5
MODULUS EXPONENT	n	0.9
FAILURE RATIO	R_f	0.354
POISSON'S RATIO	ν	
CONCRETE		
YOUNG'S MODULUS (kH/m^2)	E_c	2.1(10)
POISSON'S RATIO	ν_c	0.2

(a)

PARAMETERS	SYMBOLS	VALUE
INITIAL YOUNG'S MODULUS (kN/m^2)	E_1	12135.0
INITIAL POISSON'S RATIO	ν_1	0.354
FRICTIONAL ANGLE (degrees)	ϕ	27
FAILURE LINE q/p	m_f	1.07
DILATANCY LINE	m_c	0.963
HARDENING CONSTANT	A	0.0012
COHESION (kH/m^2)	c	3.5

(b)

TABLE 5-1: Values of parameters for (a) conventional methods and nonlinear FE analysis (b) proposed elasto-plastic analysis for the mat foundation

PARAMETERS	SYMBOLS	VALUE
SOIL		
INITIAL YOUNG'S MODULUS (kH/m ²)	E	335000.0
INITIAL POISSON'S RATIO	v	0.25
FRICTIONAL ANGLE (degrees)	φ	47.5
FAILURE LINE q/p	m	1.95
DILATANCY LINE	f	
	m	1.6
	c	
HARDENING CONSTANT	A	0.00012
COHESION (kH/m ²)	c	20.0
CONCRETE		
YOUNG'S MODULUS (kH/m ²)	E	2.1(10) ⁷
POISSON'S RATIO	v	0.2
MASS DENSITY (kH/m ²)	γ	24.5
	c	

TABLE 5-II: Values of parameters for elasto-plastic analysis of the concrete gravity dam

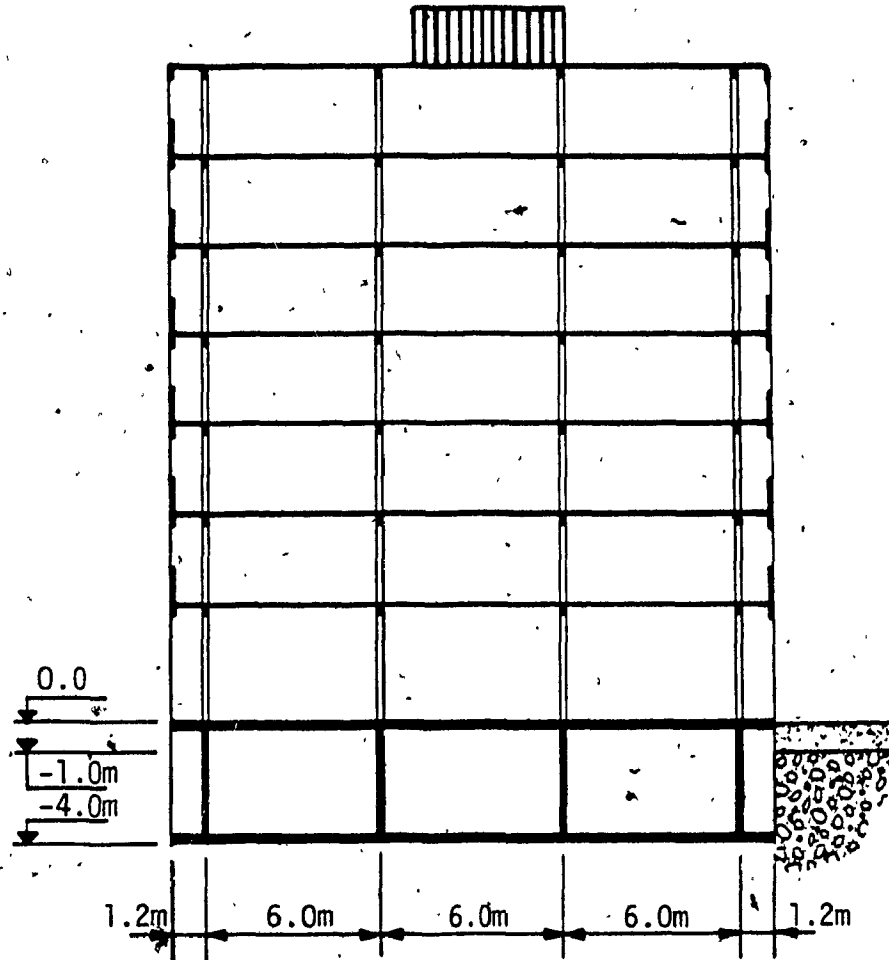


FIG. 5.1: Building and the mat foundation

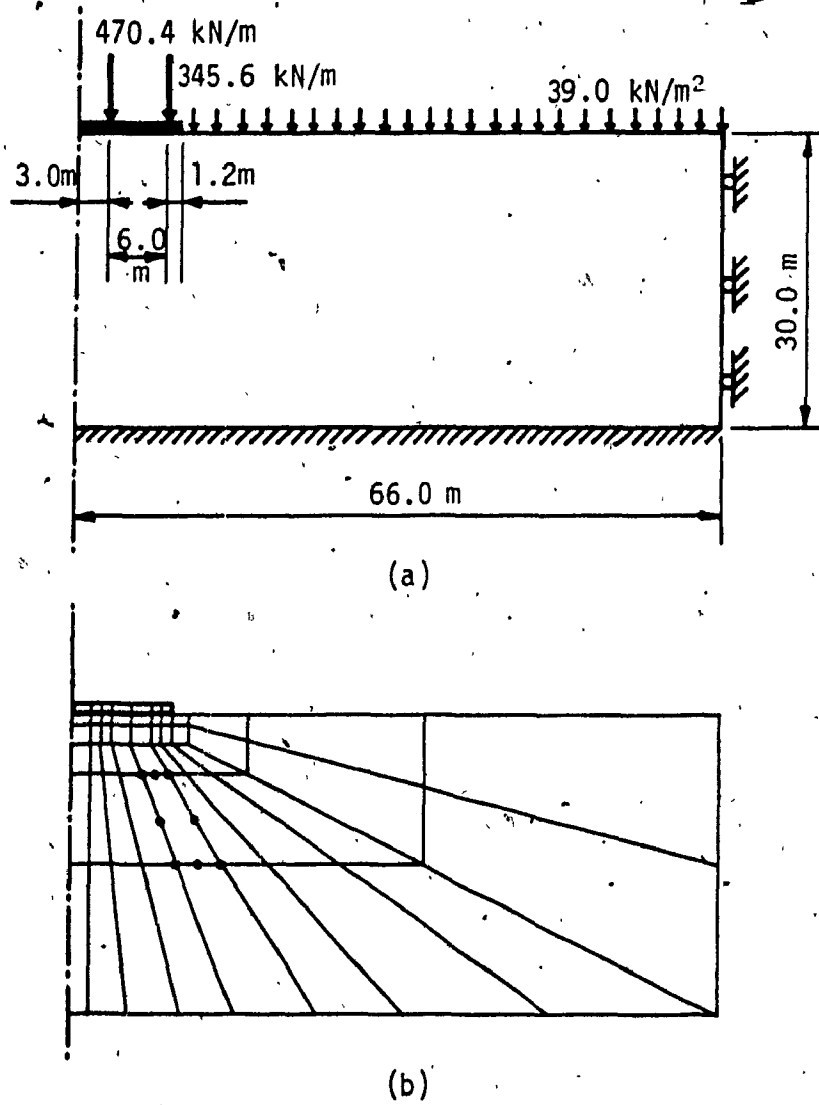


FIG. 5.2: Idealisation for FE analysis (a), and discretization of mat and subsoil (b).

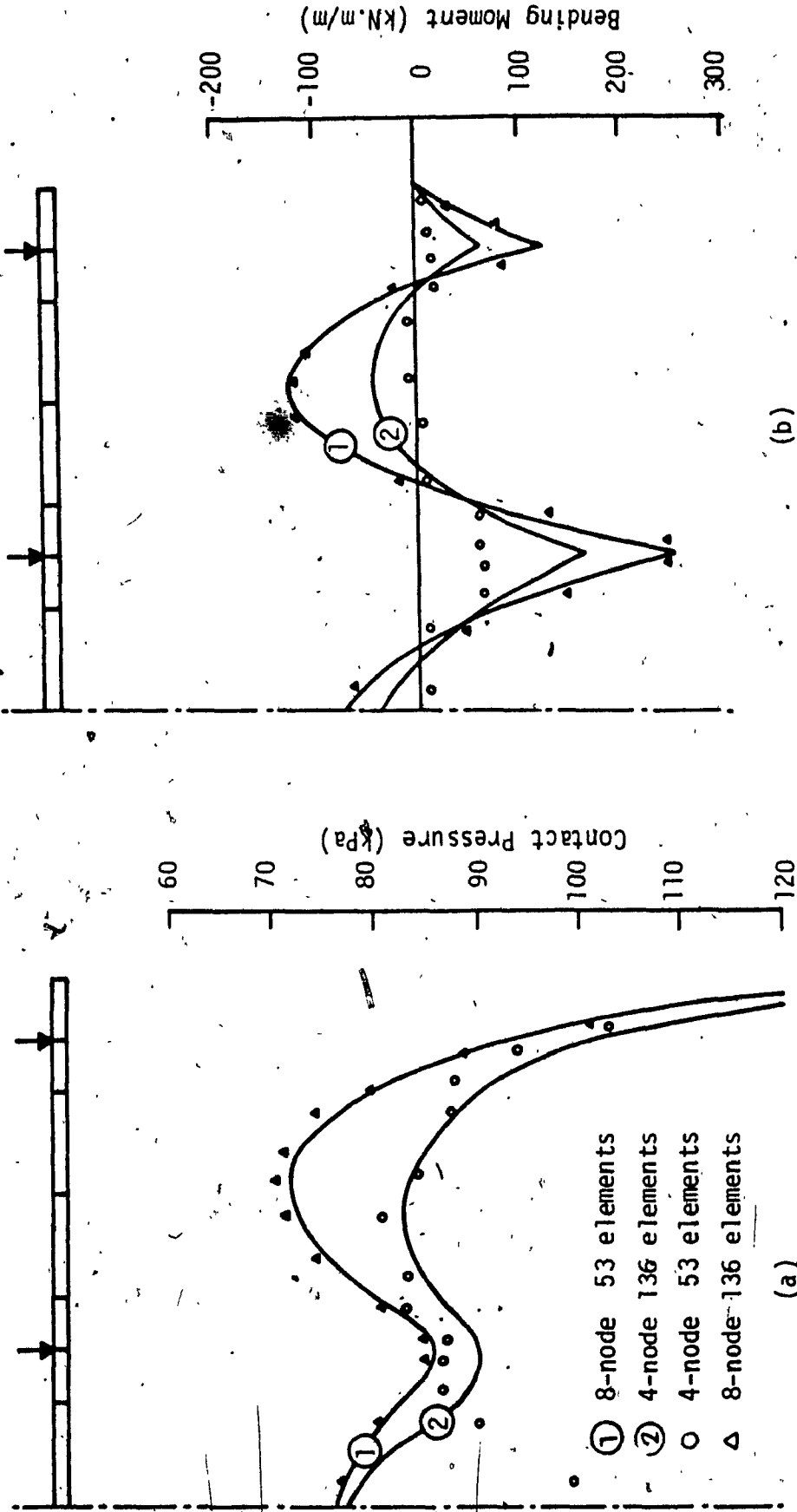


FIG. 5.3: Discretization test: (a) contact pressure; (b) bending moment

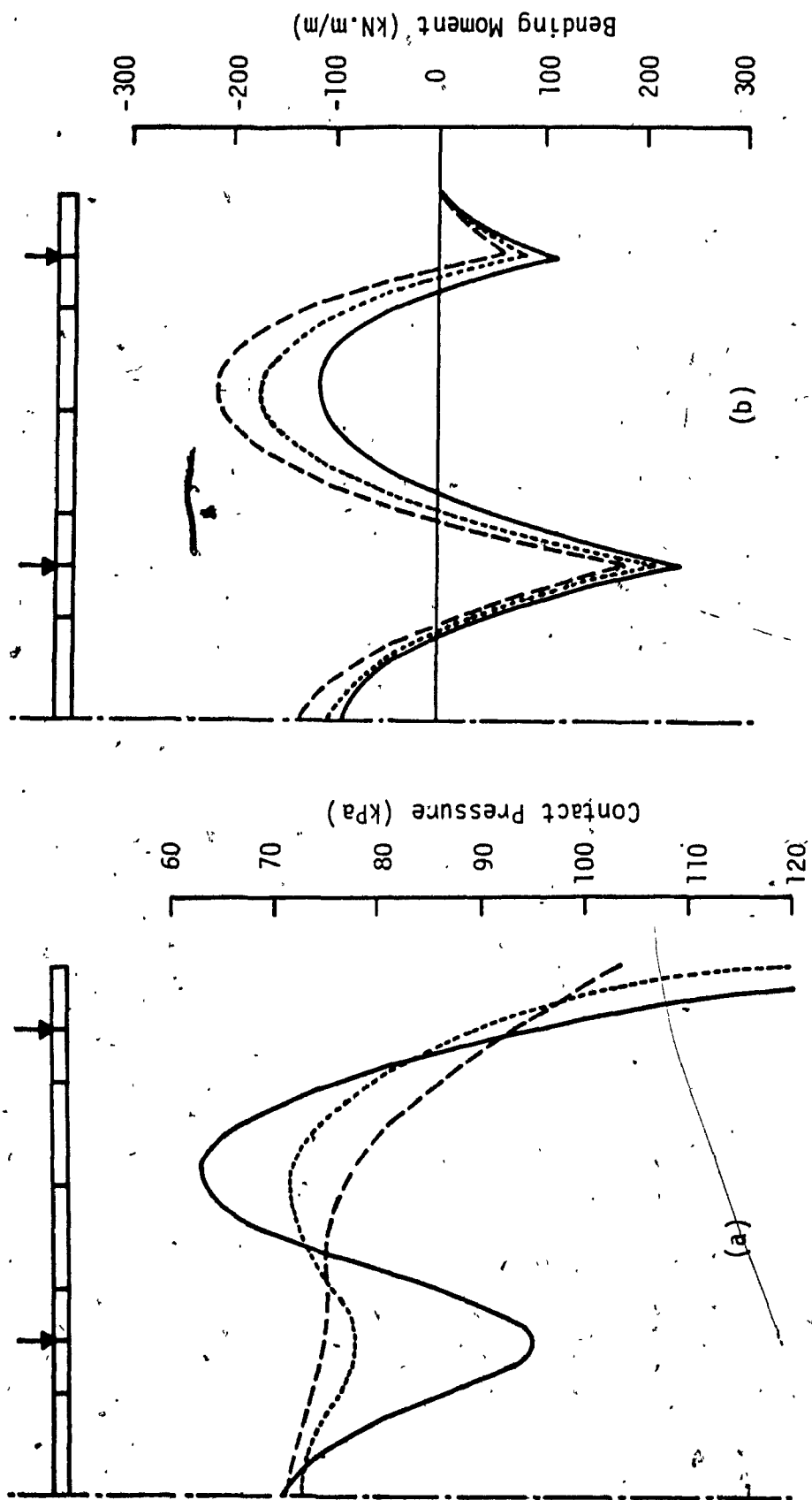
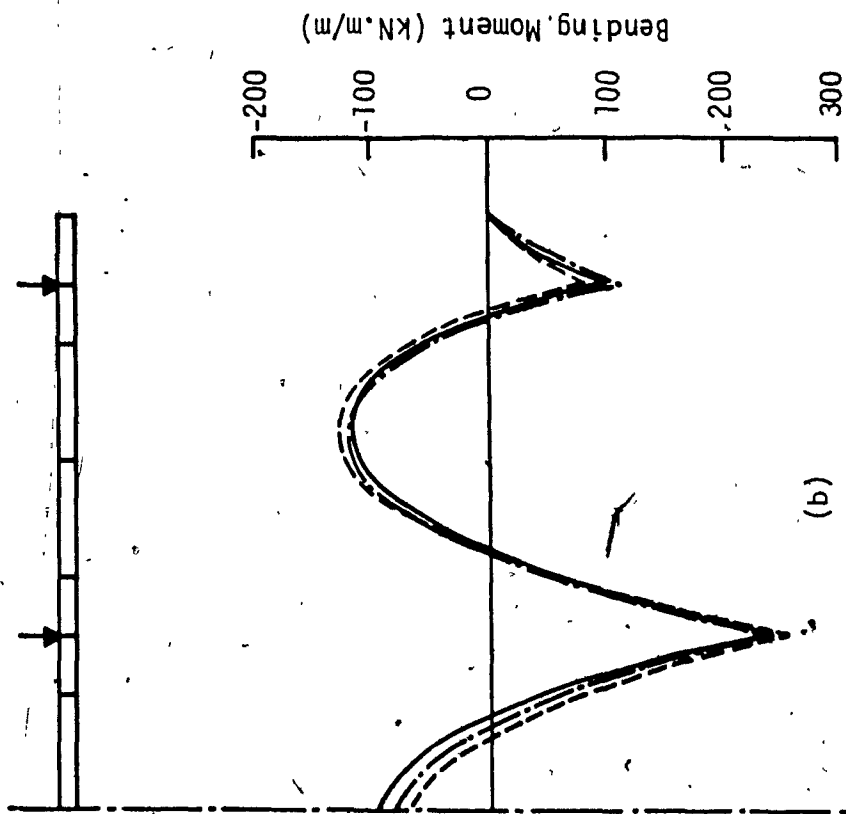
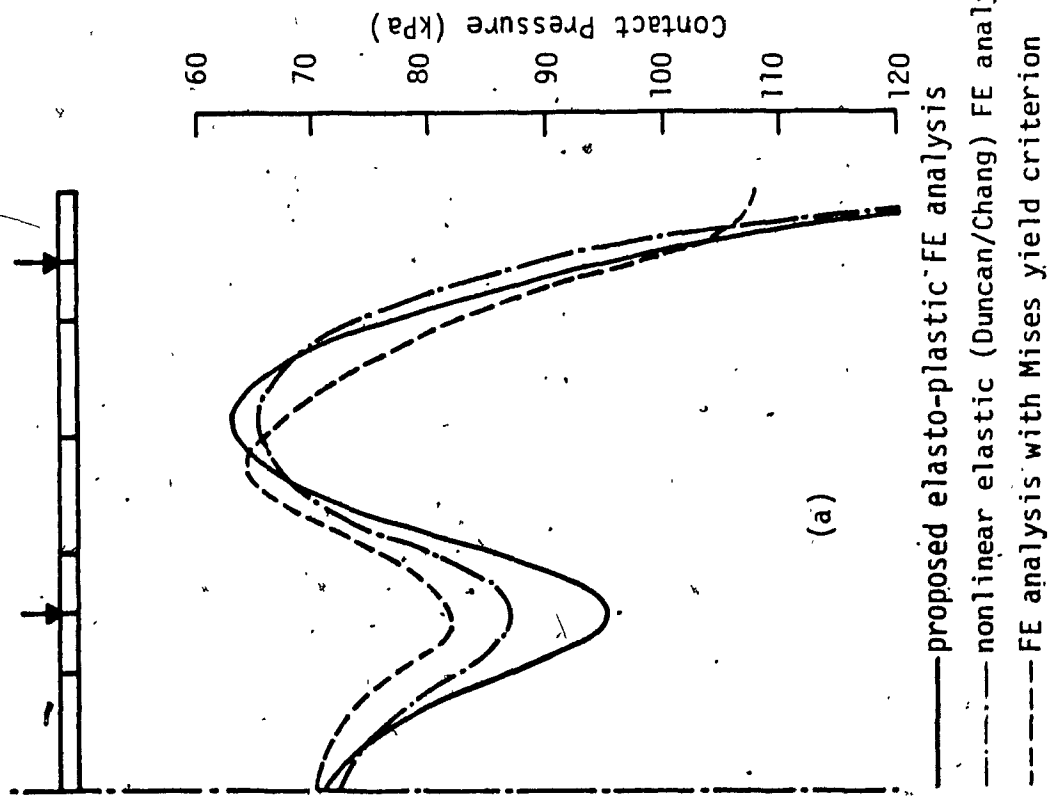


FIG. 5.4: Comparison with conventional methods: (a) contact pressure; (b) bending moment



— proposed elasto-plastic FE analysis
 - - - nonlinear elastic (Duncan/Chang) FE analysis
 - · - FE analysis with Mises yield criterion

FIG. 5.5: Comparison with other FE analyses: (a) contact pressure; (b) bending moment

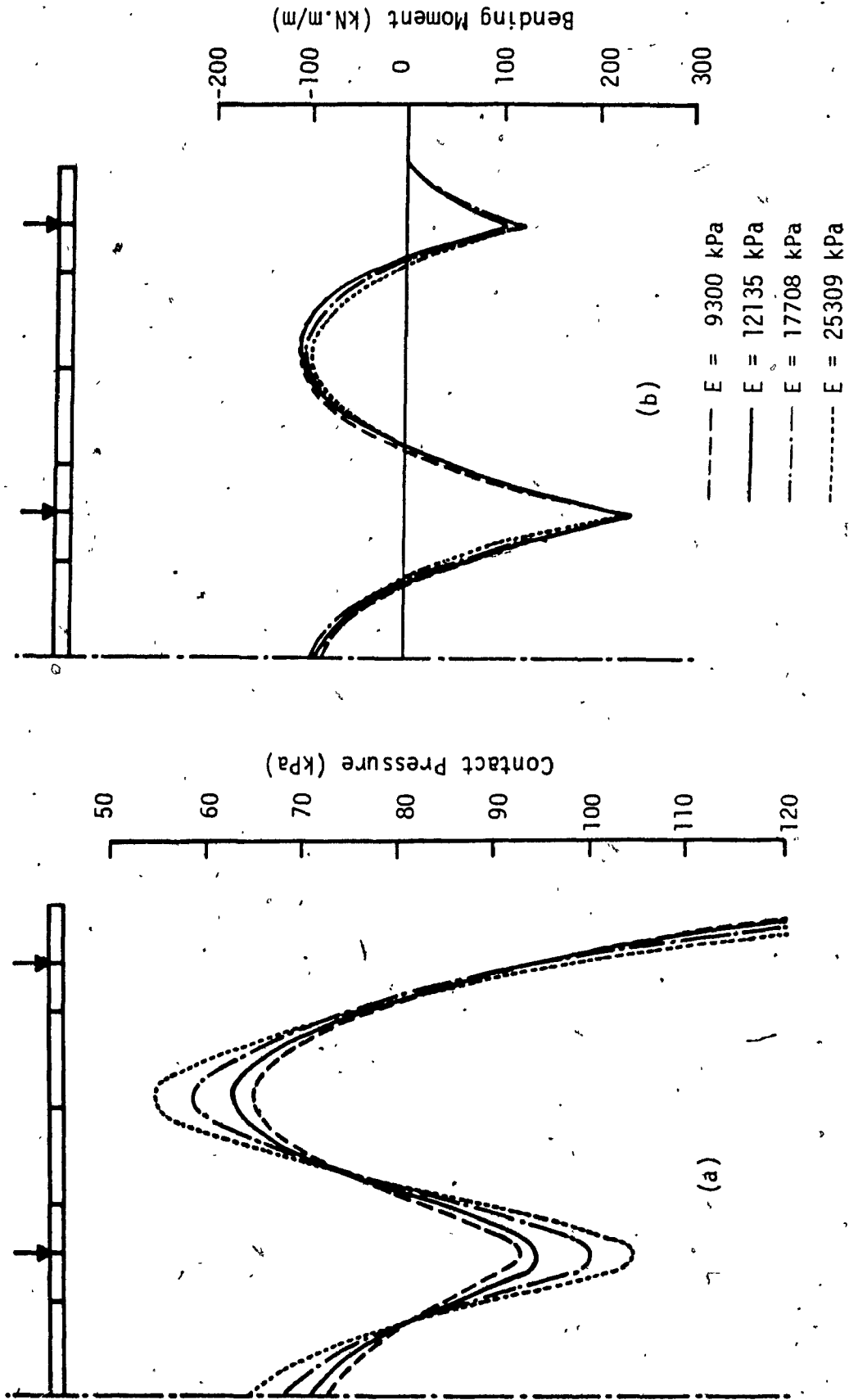


FIG. 5.6: Effect of the initial elastic modulus on: (a) contact pressure; (b) bending moment.

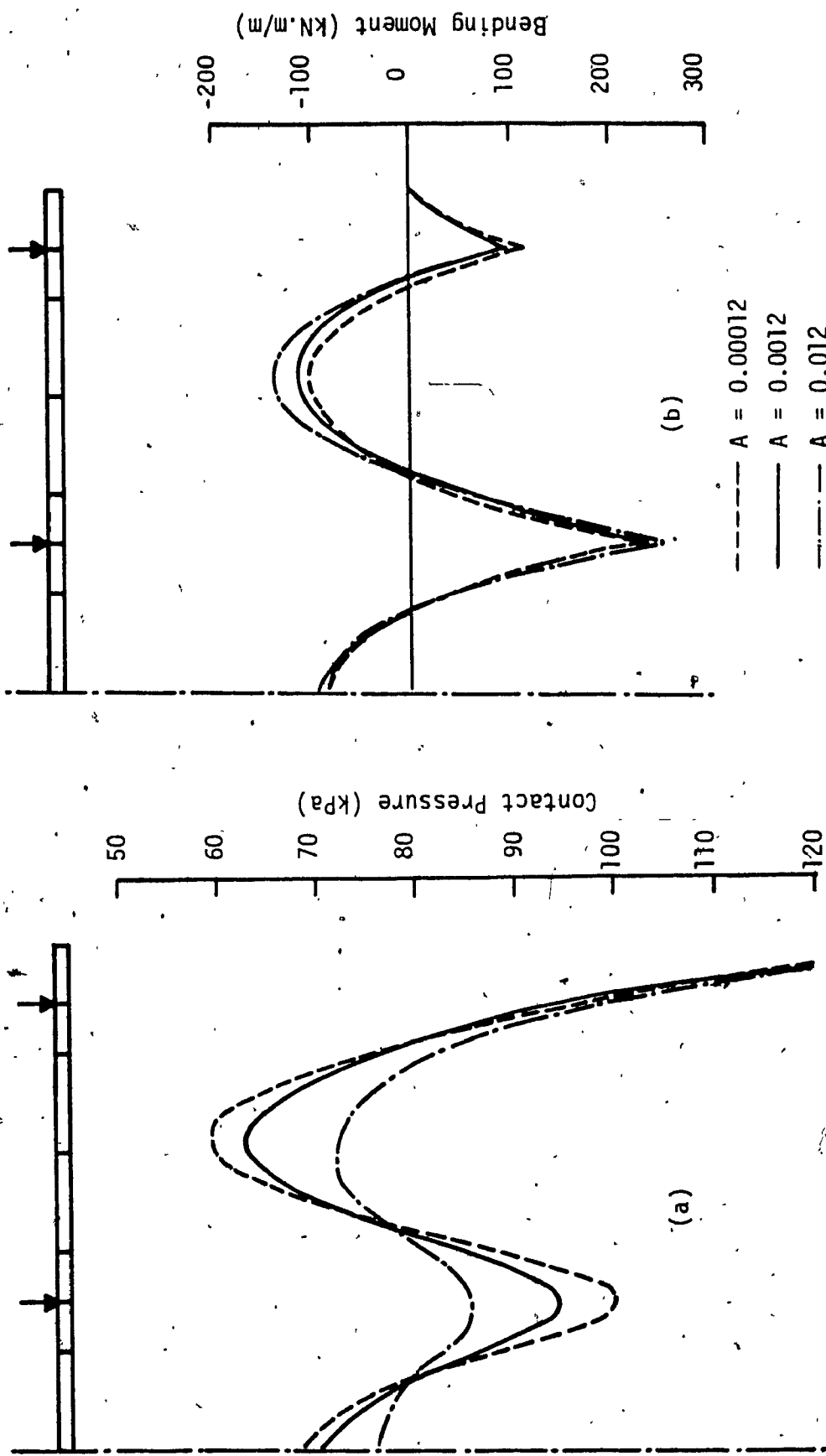


FIG. 5.7: Effect of hardening constant A on: (a) contact pressure; (b) bending moment

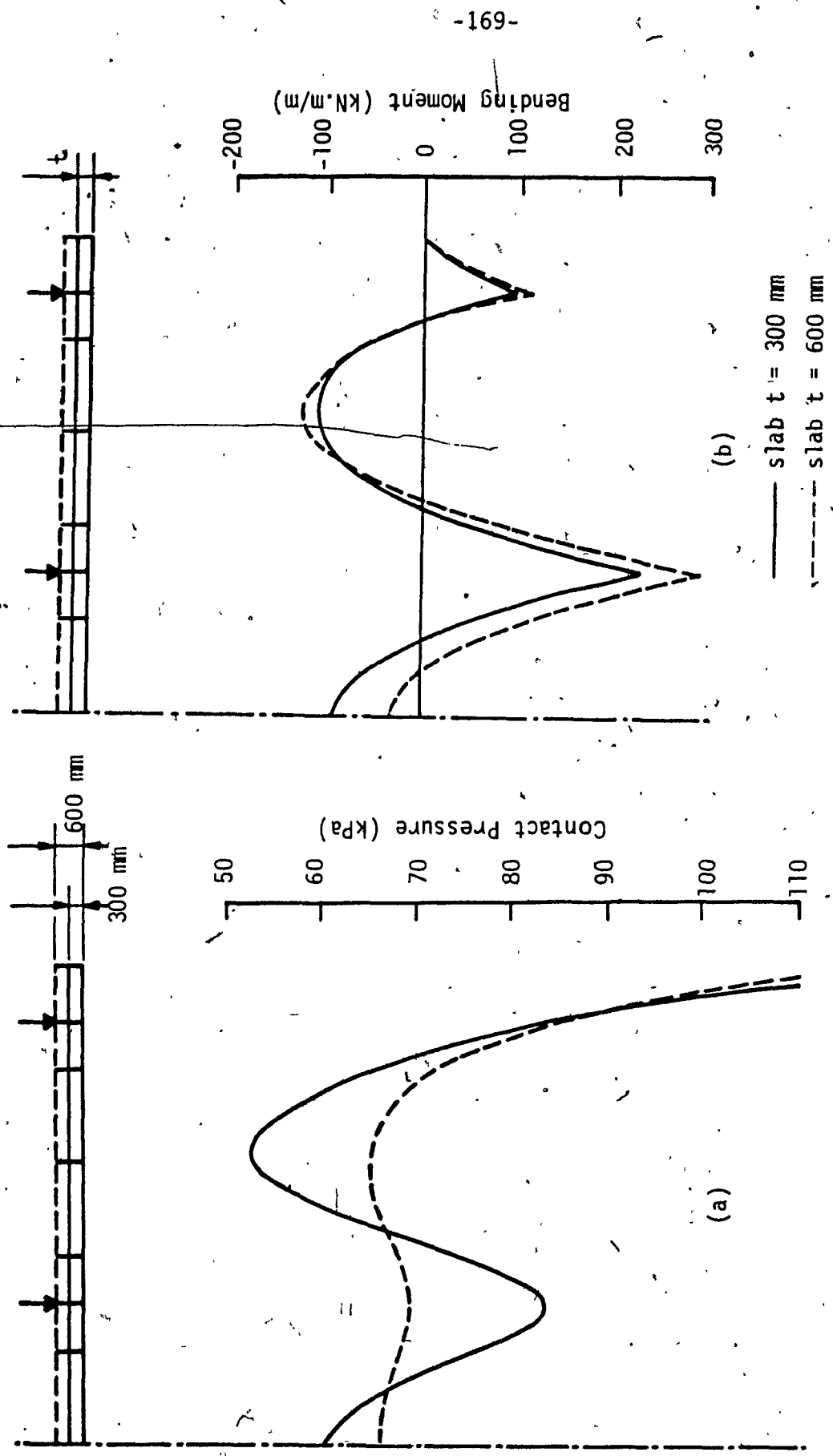


FIG. 5.8: Effect of footing thickness t on: (a) contact pressure (b) bending moment

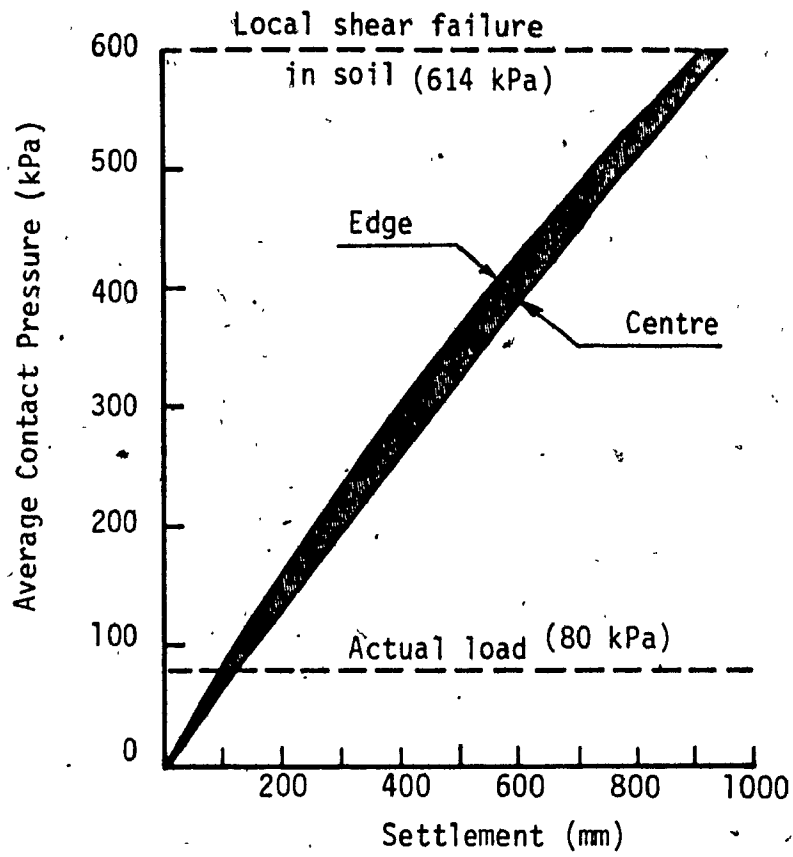


FIG. 5.9: Average contact pressure-settlement diagram for load Δ up to local shear failure in the soil

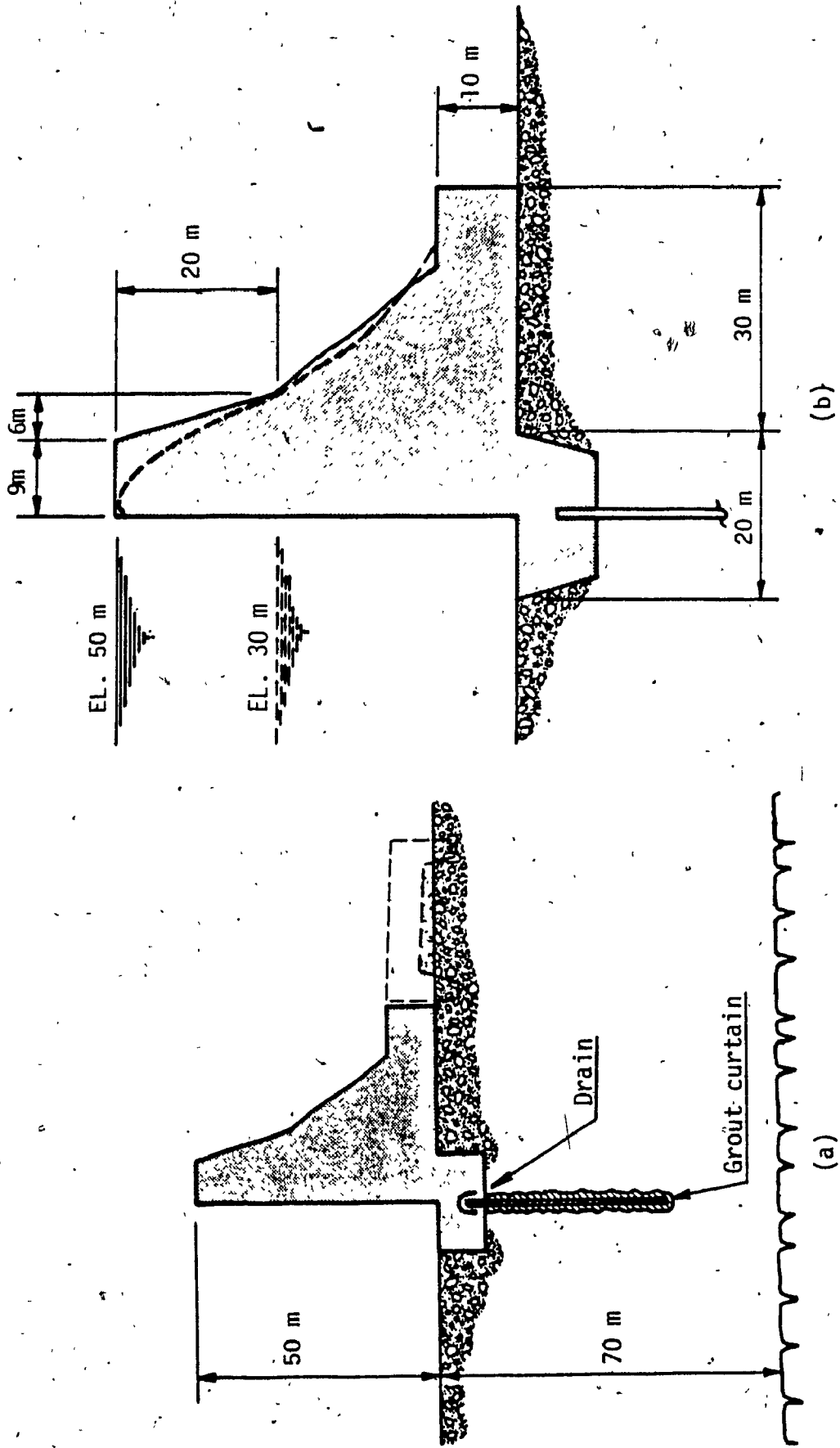
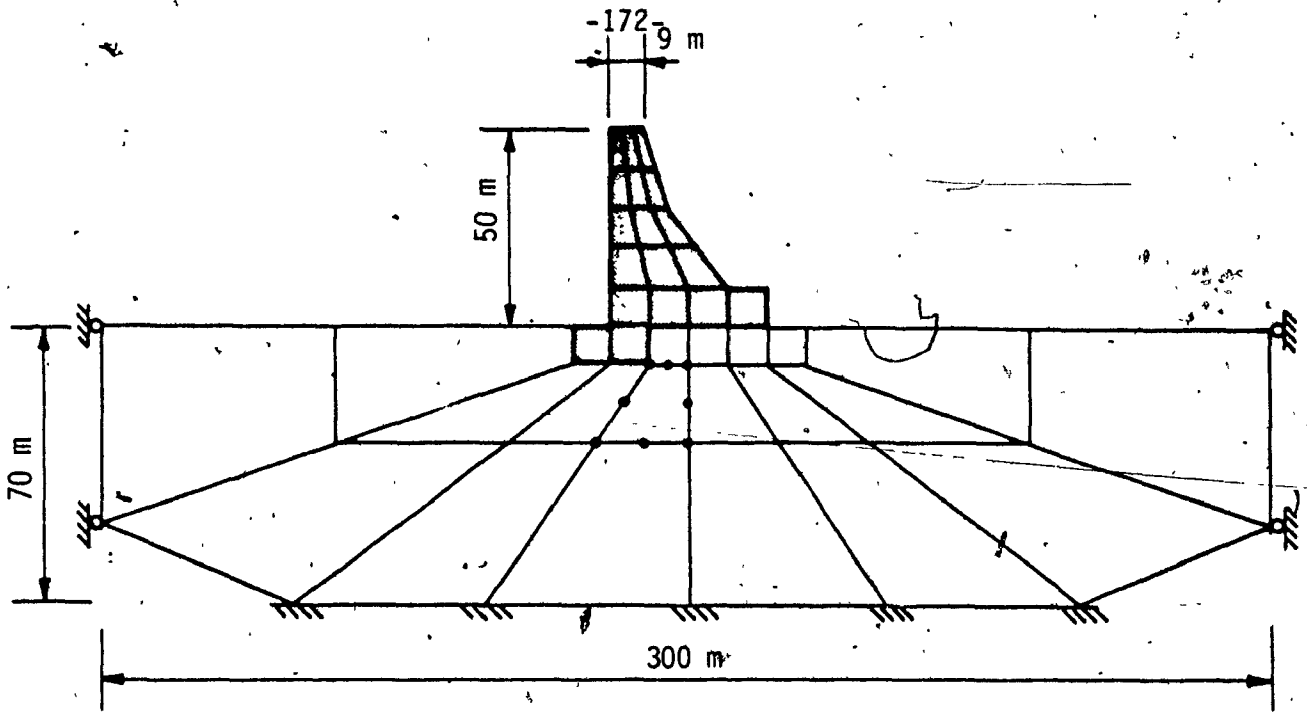
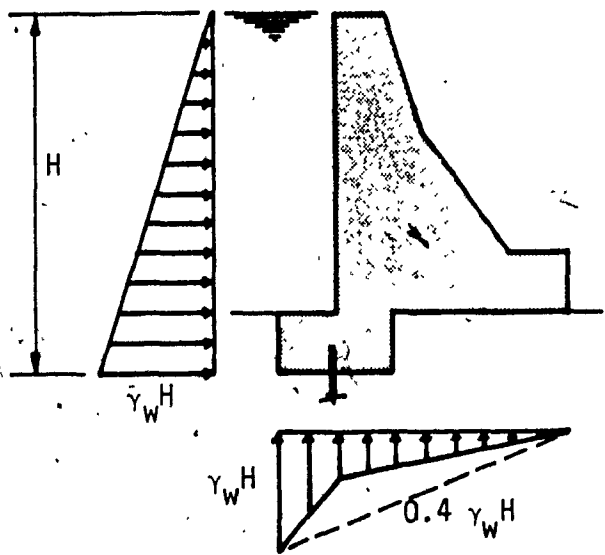


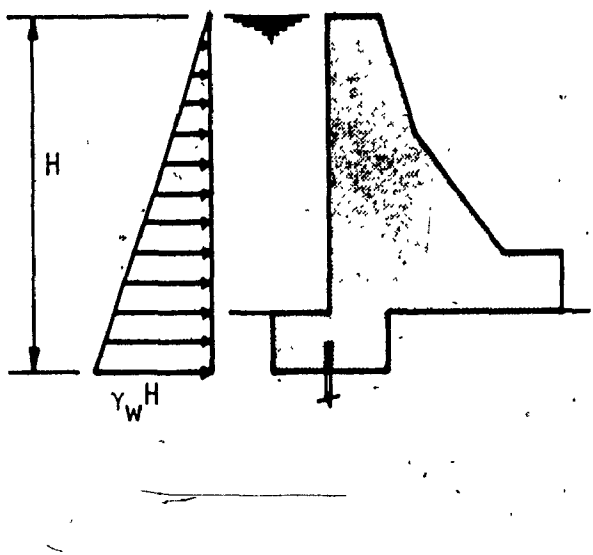
FIG. 5.10: Concrete gravity dam: (a) dam and subsoil; (b) cross-section dimensions



(a)



(b)



(c)

FIG. 5.11: (a) Finite element model used in analysis; (b) and (c) assumed water pressure diagrams

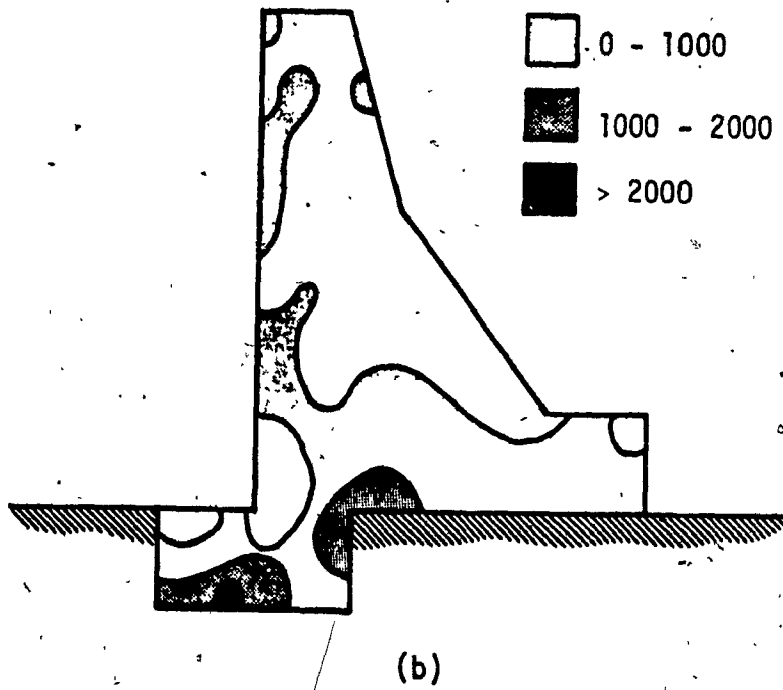
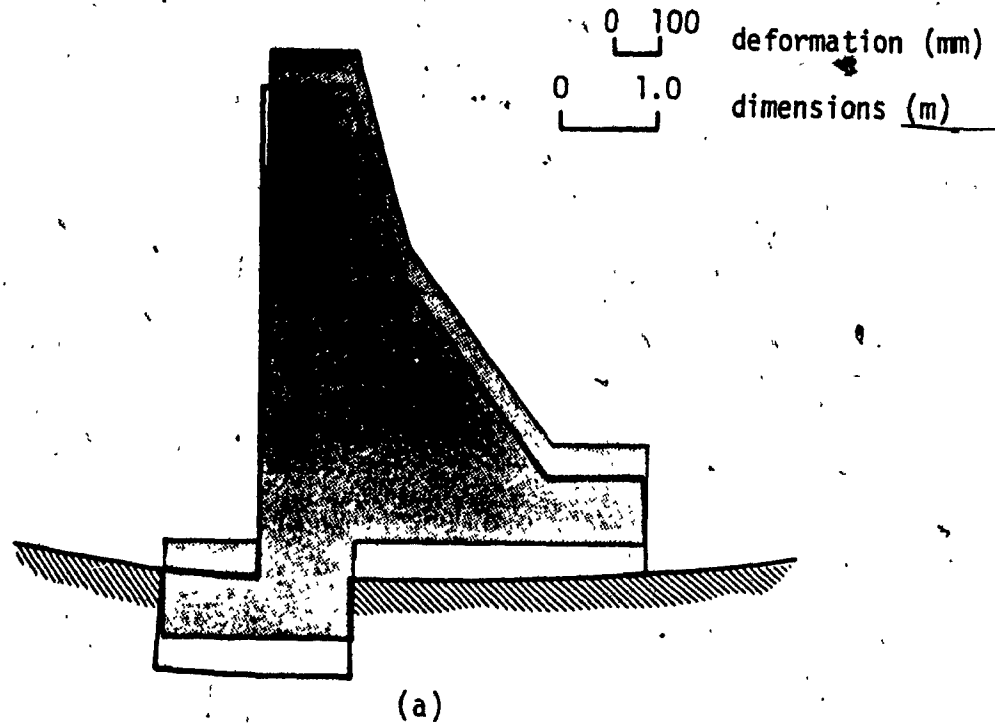
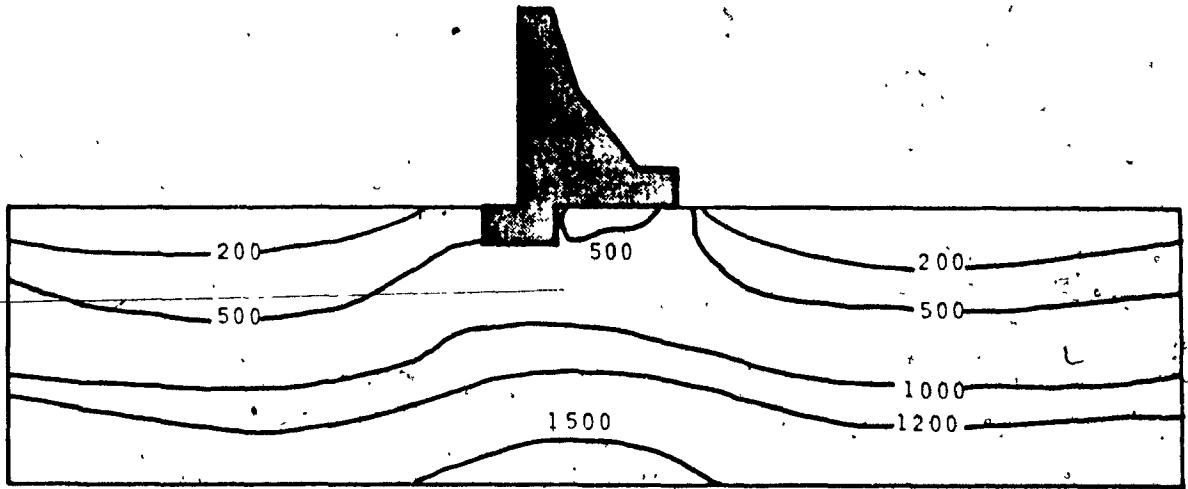
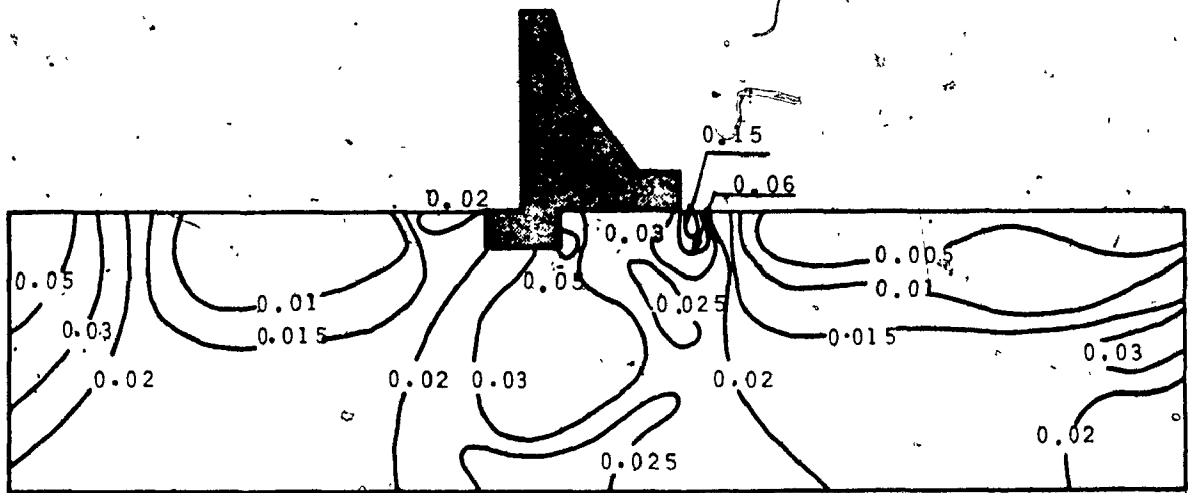


FIG. 5.12: Construction terminated: (a) deformation (b) zones with tensile major principal stresses (kPa)



(a)



(b)

FIG. 5.13: Construction terminated: (a) contours of minor principal stresses (kPa); (b) contours of accumulated plastic strain (%) corresponding to stresses in (a)

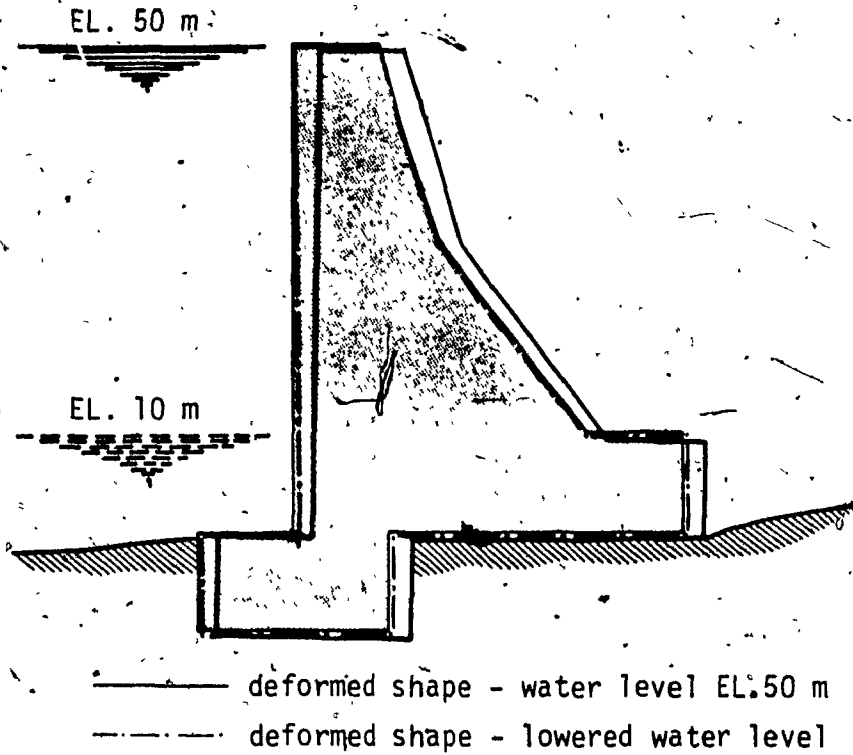
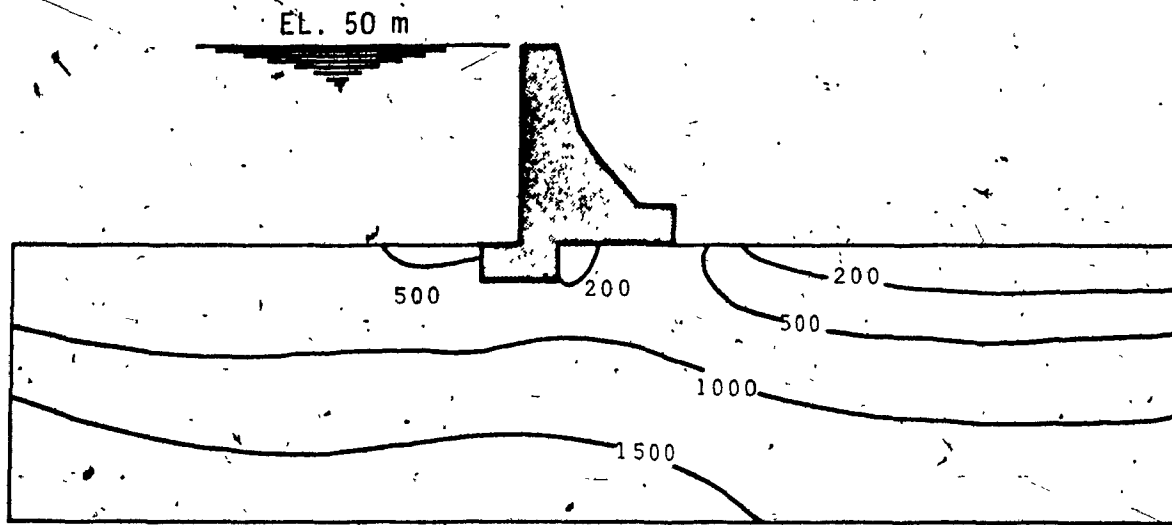
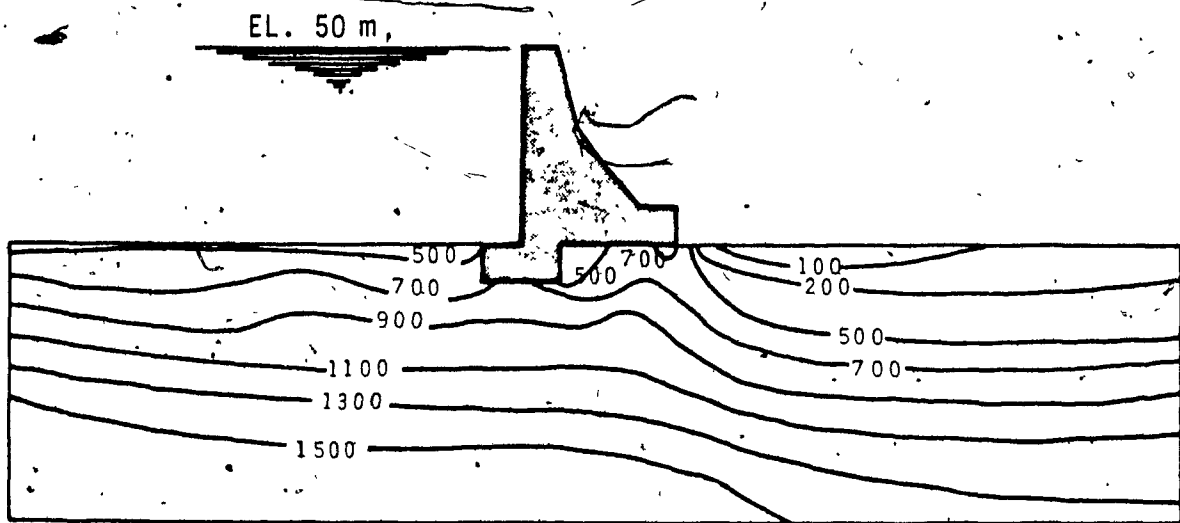


FIG. 5.14: Dam deformation due to first load cycle - water fluctuation 40 m. Uplift pressure with cut-off.



(a)



(b)

FIG. 5.15: Reservoir filled with water, first cycle: (a) contours of minor principal stresses; (b) contours of vertical stresses. Uplift pressure with cut-off.

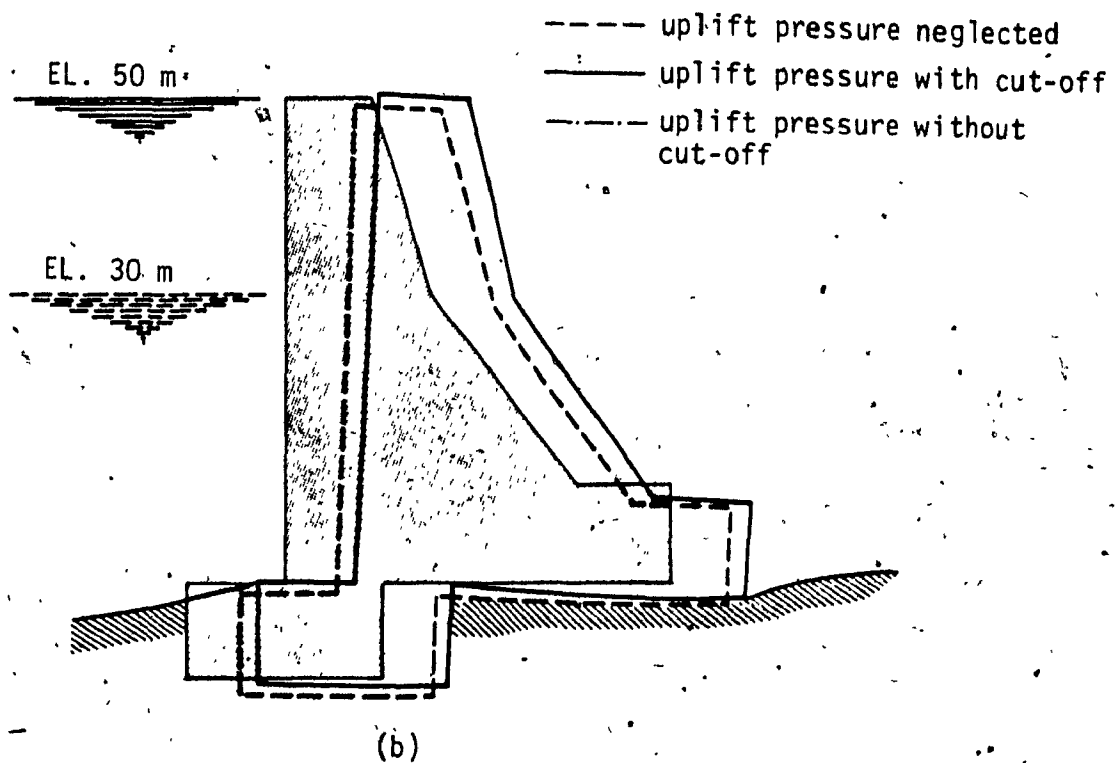
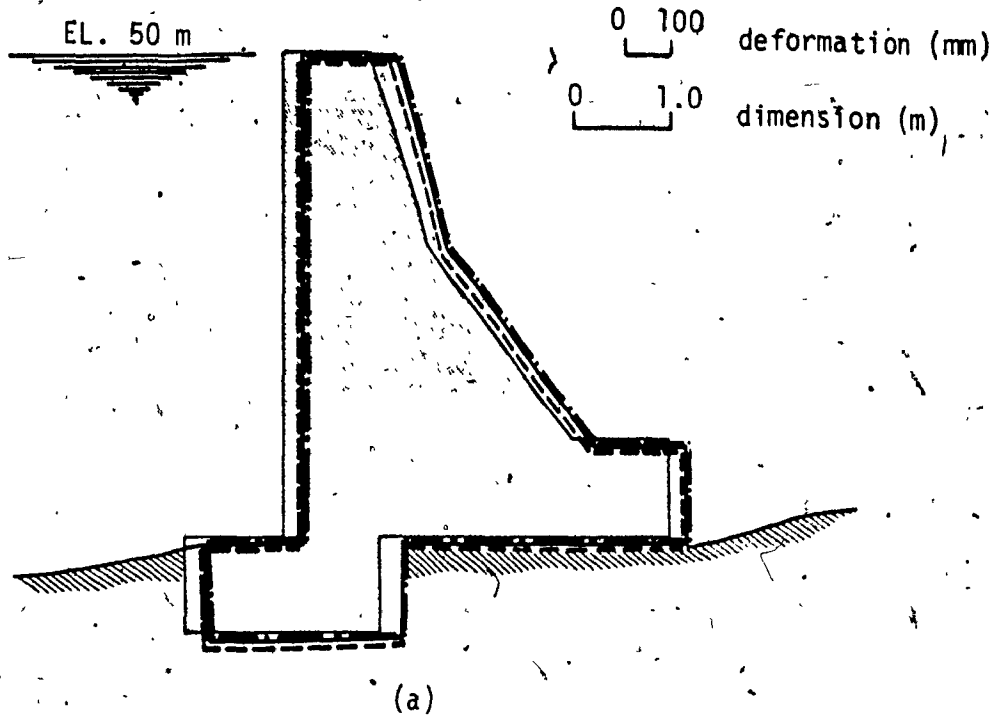


FIG. 5.16: Dam deformation due to different water pressures (water fluctuation 20 m): (a) first loading cycle; (b) twelfth load cycle

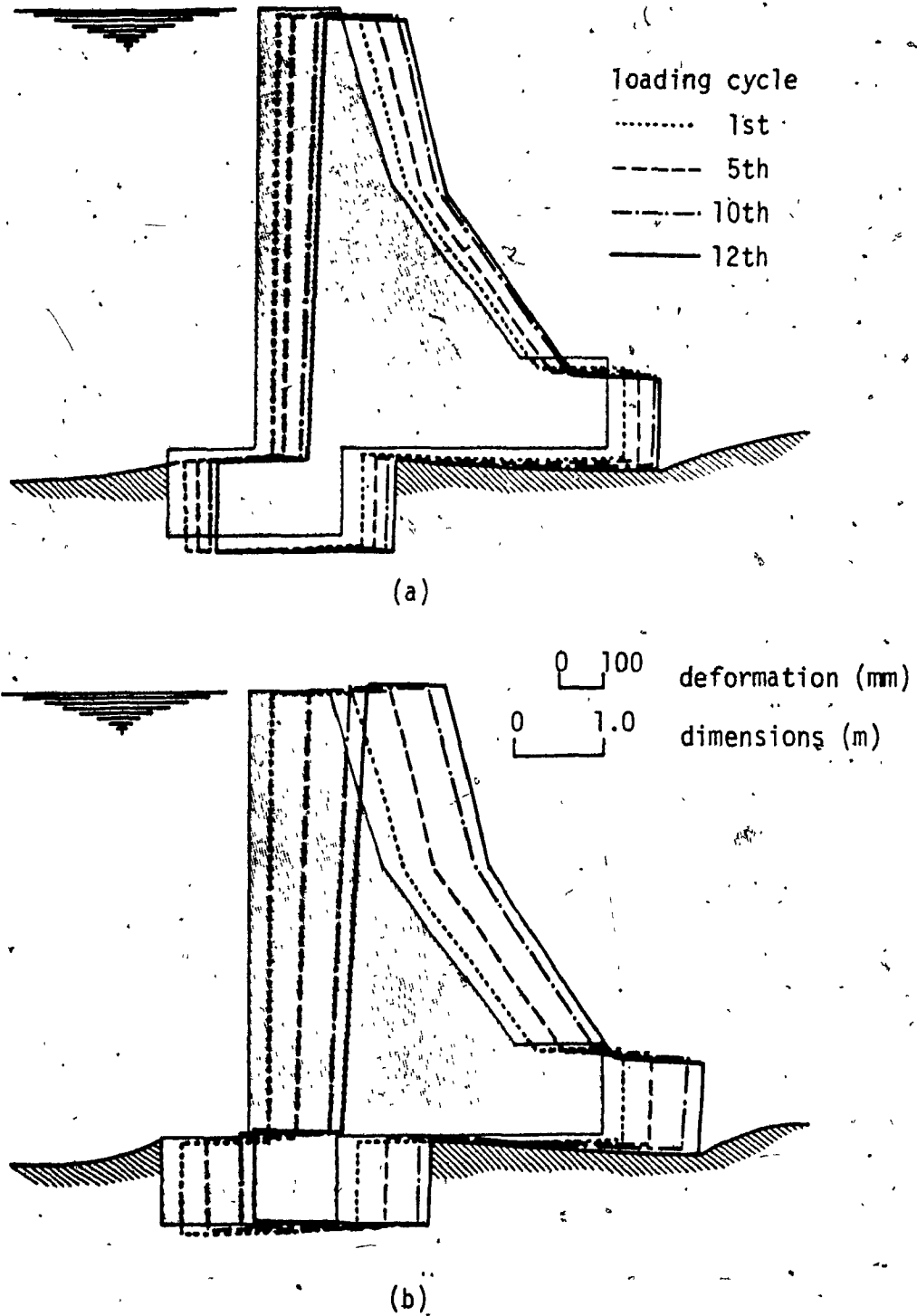


FIG. 5.17: Dam deformation at different loading cycles (water fluctuation of 20 m): (a) uplift pressure neglected; (b) uplift pressure with cut-off

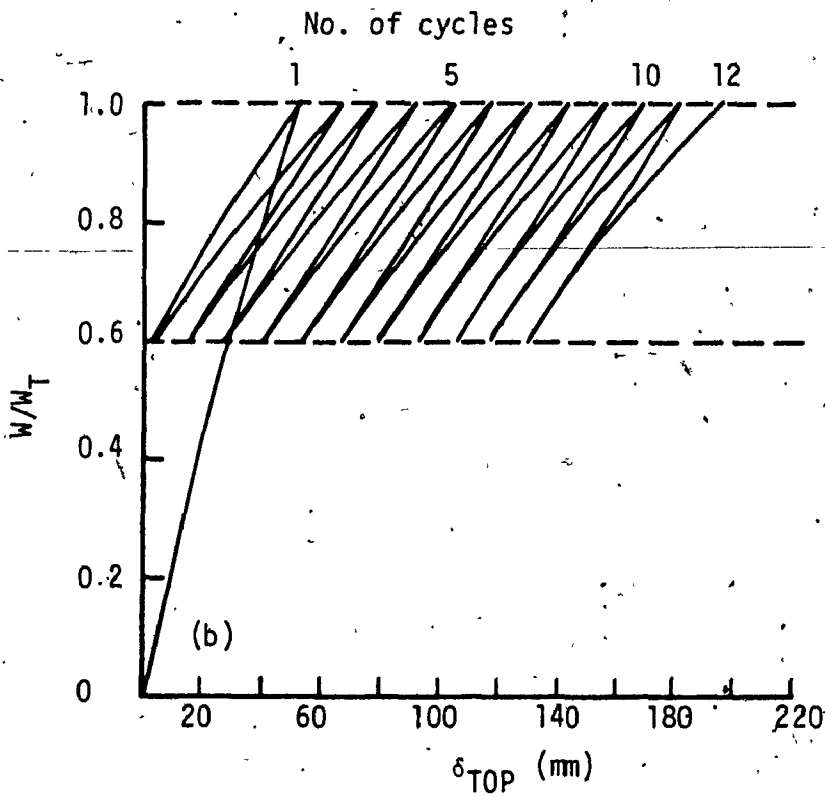
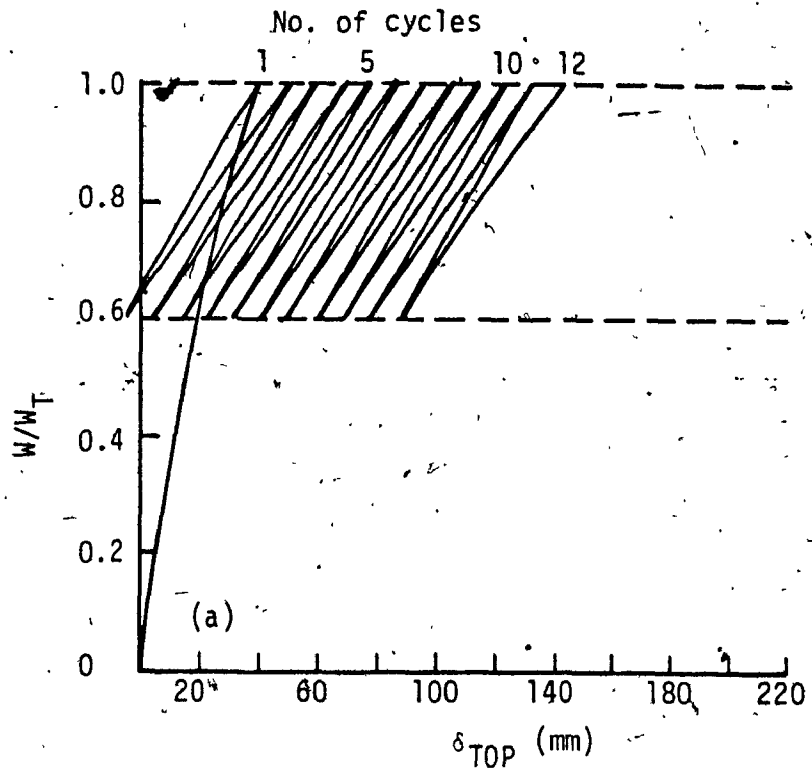


FIG. 5.18: Load-displacement relations for crest (water fluctuation of 20 m): (a) uplift pressure neglected; (b) uplift pressure with cut-off

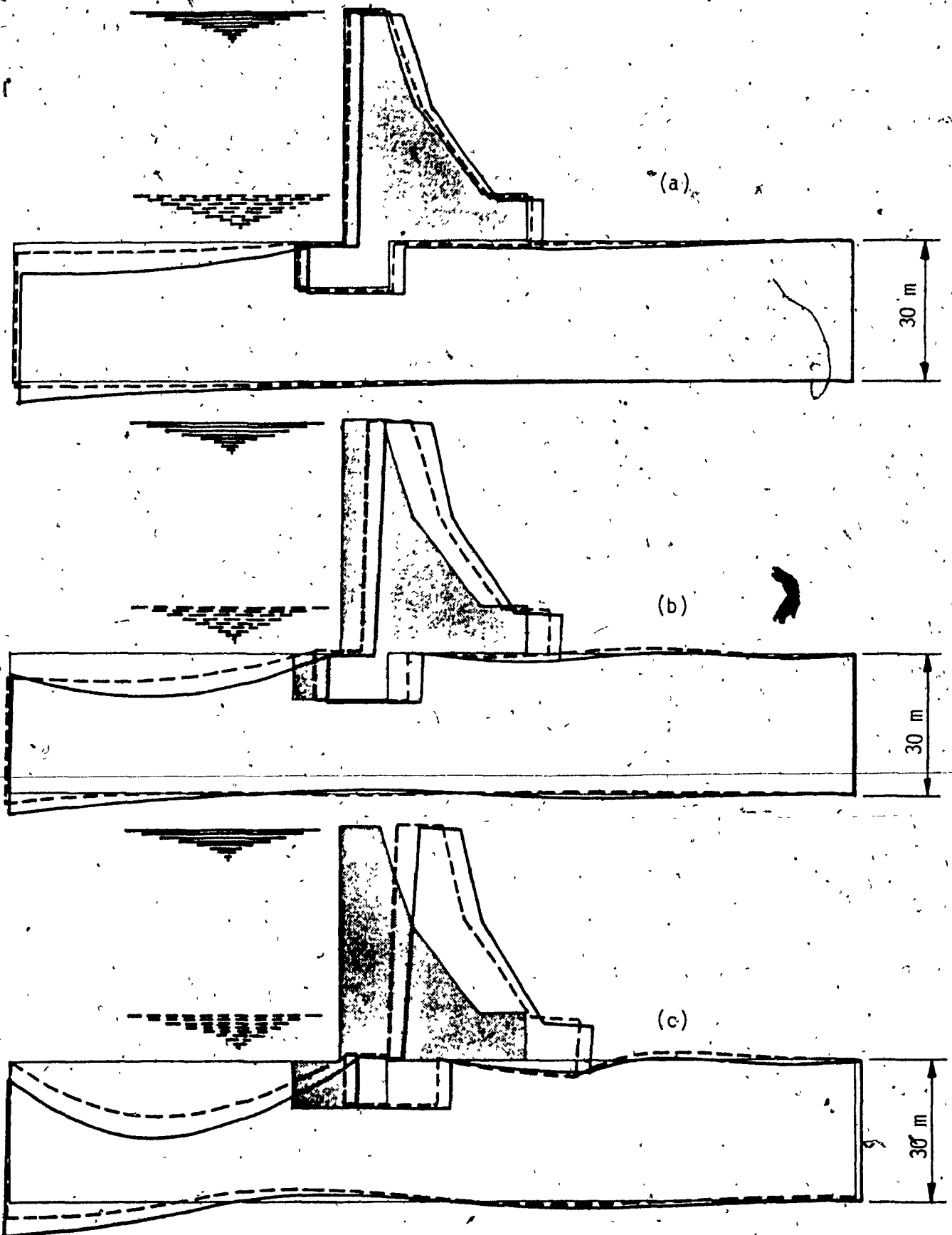
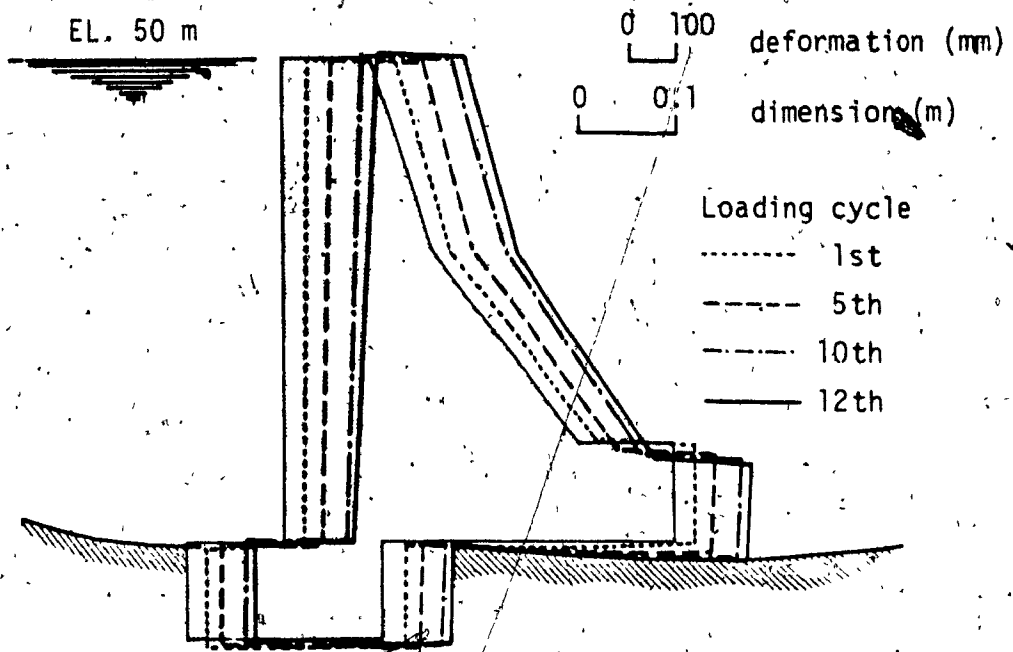


FIG. 5.19: Dam displacement at (a) first, (b) fifth and (c) tenth cycles (water fluctuation 40 m). Uplift pressure with cut-off.



(a)

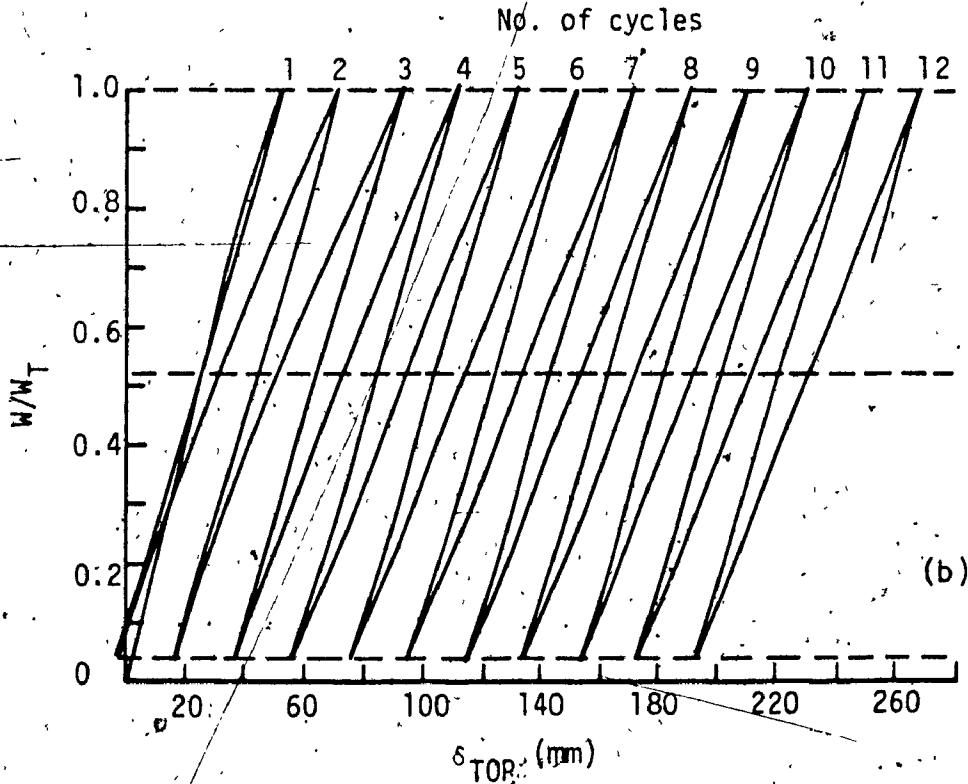
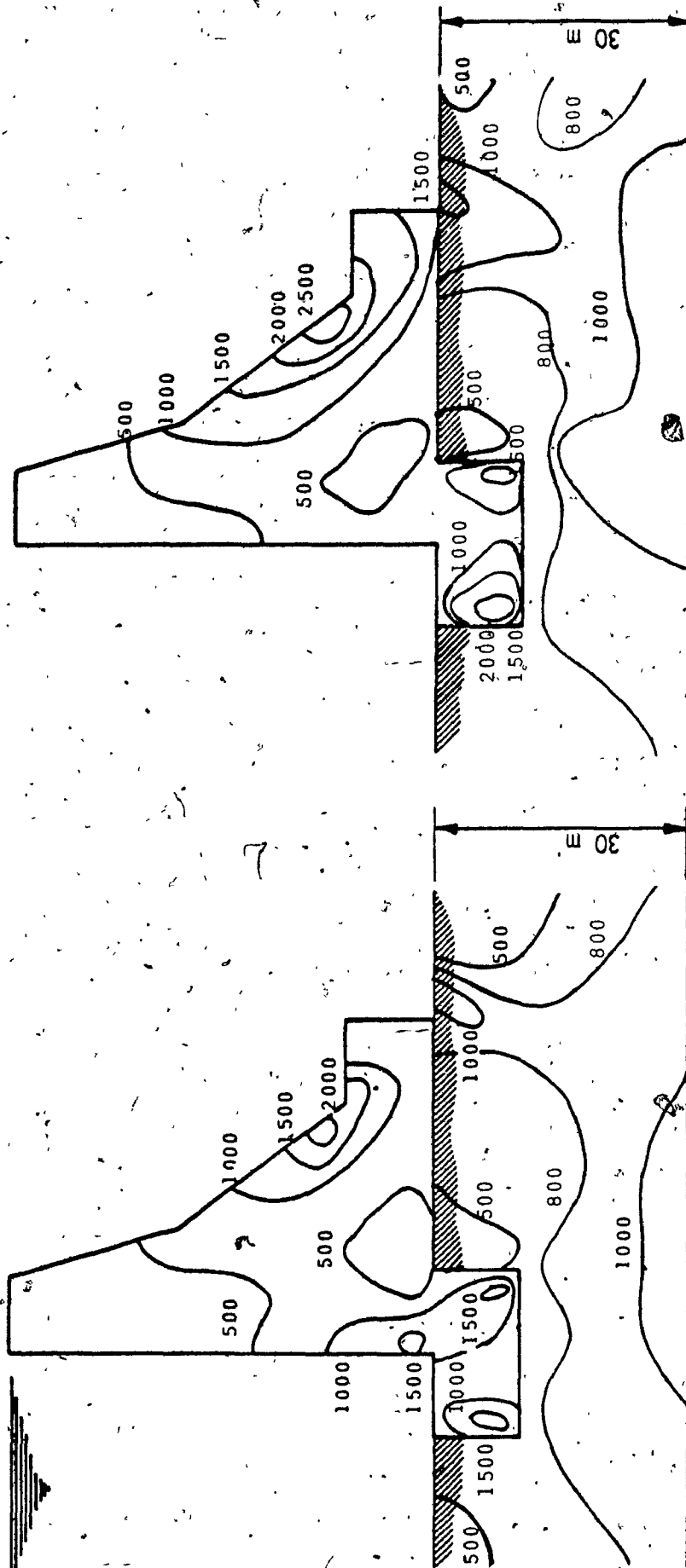


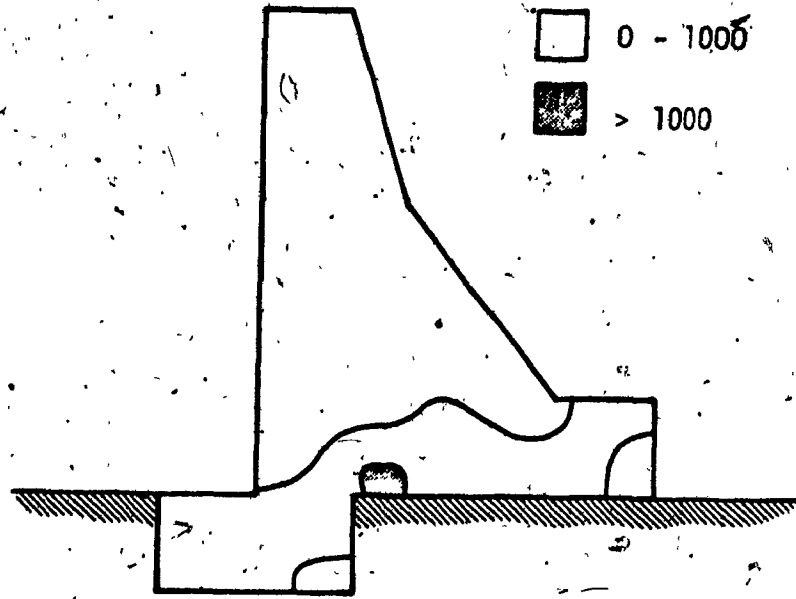
FIG. 5:20: Cyclic deformation of dam: (a) and (b) load displacement relation for crest (water fluctuation 40 m). Uplift pressure with cut-off.



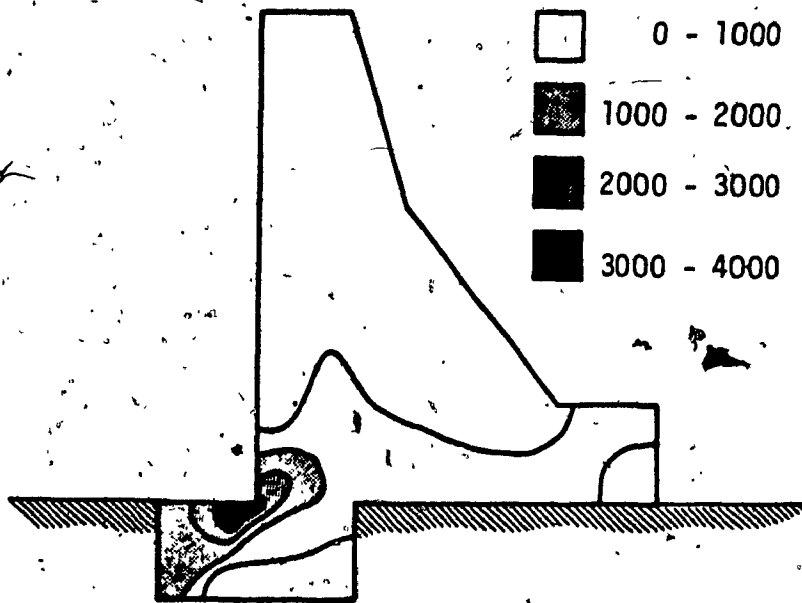
(a)

(b)

FIG. 5.21: Contours of minor principal stresses: (a) first load cycle; (b) twelfth load cycle (for water fluctuation 20 m)

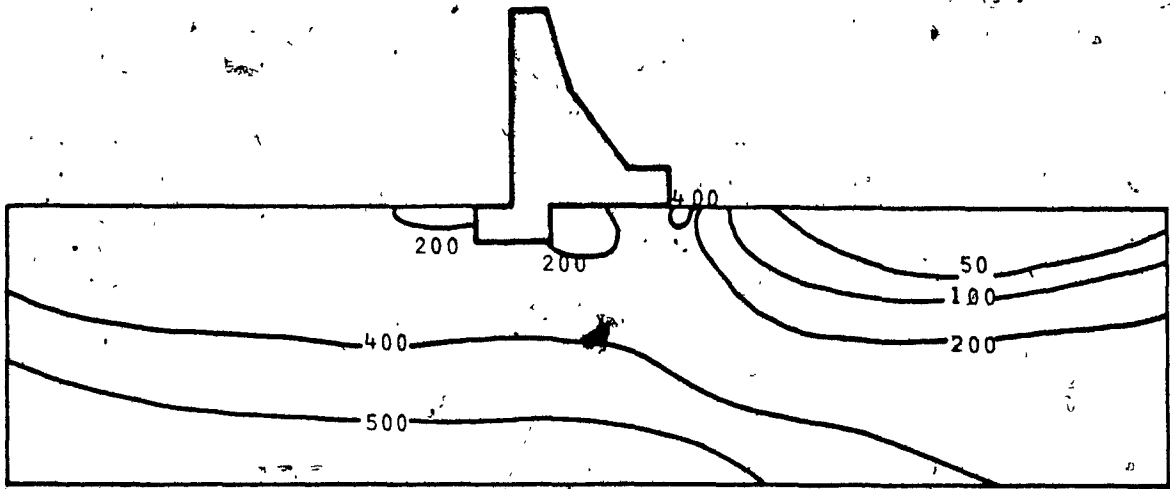


(a)

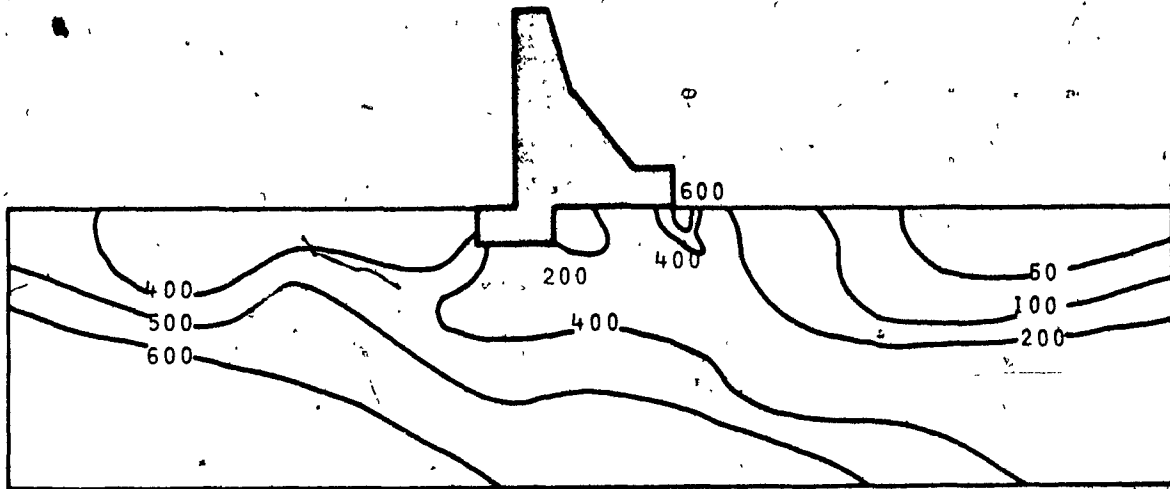


(b)

FIG. 5.23: Tension zones in dam (kPa):
(a) first load cycle;
(b) twelfth load cycle

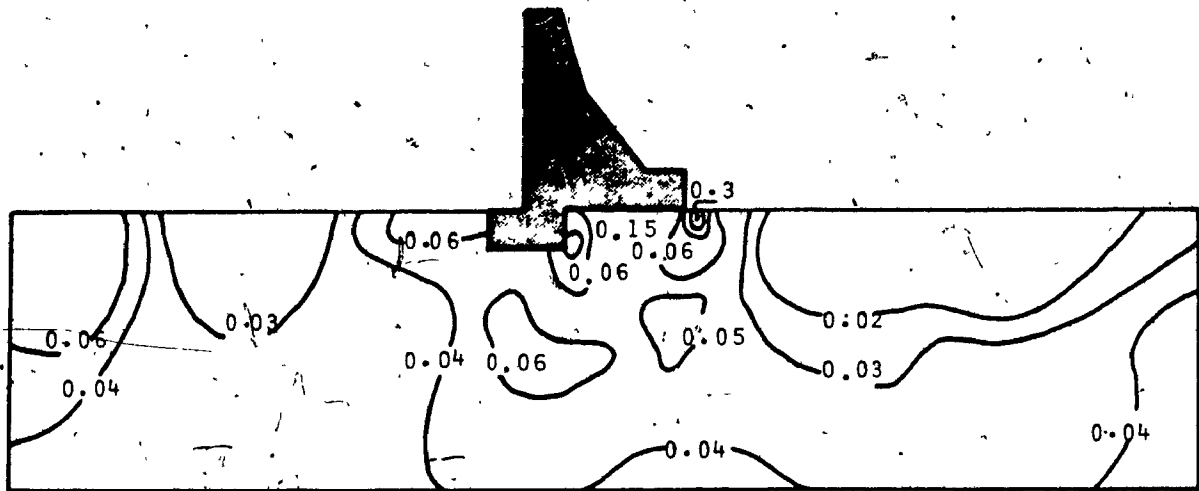


(a)

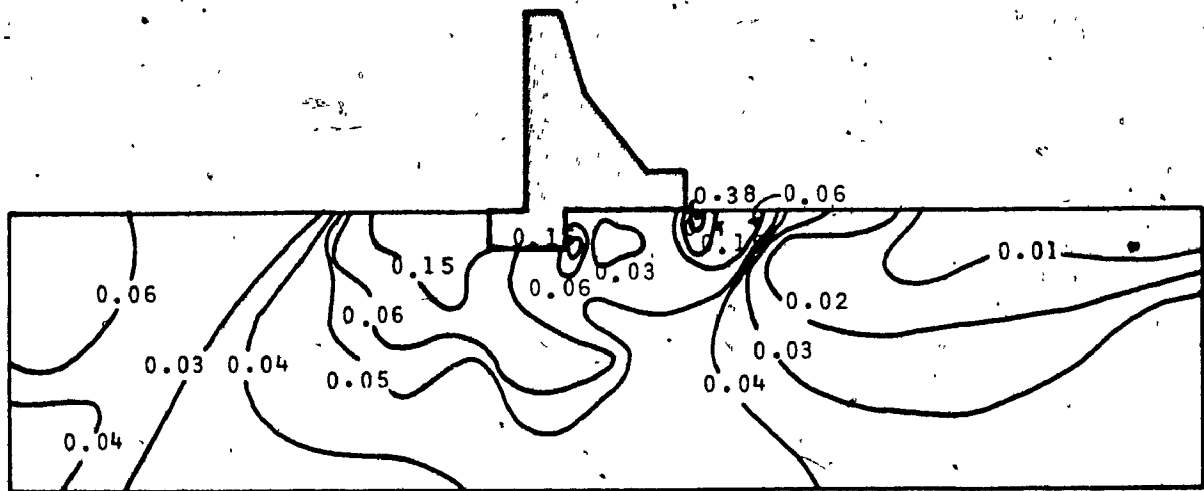


(b)

FIG. 5.24: Contours of maximum shear stresses (kPa): (a) first load cycle; (b) twelfth load cycle



(a)



(b)

FIG. 5.25: Contours of accumulated plastic strain (%) corresponding to stresses in Fig. 5.24: (a) first load cycle; (b) twelfth load cycle

CHAPTER VI

6.0 SUMMARY AND CONCLUSIONS

Constitutive model for granular soil with inherent cohesion have been developed. The model is based on the theory of bounding surface plasticity incorporating a non-associated flow rule and the concept of reflected plastic potential. The formulation constitutes an extension of the work by Poorooshasb and Pietruzziczak and differs from it in a number of aspects; for example, the forms of the yield surface and plastic potential, the mode of accumulation of plastic distortions and the generalized form of the local plastic potential. Also, it is more detailed as it provides the explicit analytical expressions for the gradient tensors and the location of the conjugate stress point, which are required for implementation in a computer code. To examine the validity of the constitutive relations developed here, for monotonic loading, comparisons with the following tests were performed: (a) drained triaxial test on naturally weakly-cemented sands as reported in Ref. 2.3; (b) drained triaxial test on artificially cemented sands with 2% and 5% cement reported in Ref. 2.3 and Ref. 2.4 respectively; (c) undrained triaxial test on loose sand reported in Ref. 2.20. For cyclic loading, the developed model was tested simulating the experiments on cyclic behavior of Fuji sand performed by Ishihara, Tatsuoka and Yasuda (2.17). Good agreement of results in both the monotonic and cyclic load comparisons was obtained. Due to the lack of experimental data on cemented sand deposits under cyclic loading, an extensive simulation of the behavior of a hypothetical similar material was conducted. The simulated behavior showed the expected results. Finally, an extensive parametric study of the developed constitutive relation was conducted

following monotonic or cycling loading histories.

Further, a quadrilateral finite element incorporating the constitutive model was added to the existing element library of the program MIXDYN.

To ensure its validity the newly developed elasto-plastic finite element was used to solve a number of boundary value problems of practical significance.

These included typical problems related to geomechanics (footing on subsoil, analysis of an earth dam during construction), and problems of nonlinear soil-structure interaction (mat foundation on silt, and concrete gravity dam on "soft" foundation).

The model footing 62 mm wide and 320 mm long was rested on cohesionless sand. The results of the analysis were compared with those obtained from small-scale testing and analytical nonlinear-elastic solution published by Duncan and Chang (1.11). They were in close agreement with those from the experiments, while the evaluated load at the end of the experiment was found to be different from that obtained by the analytical solution. In the early loading stage the computed settlements were slightly larger than those from experiments. It was concluded that this deviation is dependent upon the precision in evaluating the initial elastic soil modulus.

In order to ensure reliability and to verify the general applicability of the proposed model, analyses of complex boundary value problems were performed. Problems related to geomechanics as well as nonlinear

soil-structure interaction were analysed. An extensive study on the influence of the elasto-plastic soil properties on the behavior of structures was also conducted. The conclusions reached justify the use of an elaborate soil model in the analyses.

An embankment structure founded on sloped base was analysed first with two different finite element procedures: (a) the proposed elasto-plastic analysis and (b) nonlinear-elastic analysis developed by Kulhawy et al. (1.12). The analyses were carried out by taking into account the sequence of placement of layers of fill during construction. The settlements as well as horizontal movements obtained by the proposed analysis were found to be larger than those by the nonlinear-elastic procedure. This increase in movement was probably due to the shear coupling effect, considered only by the present elasto-plastic model. The effect of the angle of internal friction and cohesion was also examined. It was found that a reduction of 13.5° in the angle of internal friction leads to a 50% increase in settlements. The contours of settlements as well as shear stresses in the dam were obtained by both analyses. A difference of 30% in settlements and 60% in maximum shear stresses was obtained. The contours of settlements were significantly different when the construction sequence was not simulated in the analysis.

The effect of the elasto-plastic foundation medium in problems of static soil-structure interaction was examined next. The analysis of the mat foundation of an eight story building was analysed with the proposed elasto-plastic analysis and results were compared with those obtained from: (a) conventional subgrade modulus, and compression index methods and (b) other finite element procedures assuming nonlinear-elast-

ic and elastic-plastic (von Mises) material behaviors. The stress concentrations beneath the mat foundation calculated by the proposed model were found to be up to 27% higher than those obtained by conventional methods and up to 15% higher from those obtained by the other finite element procedures. Consequently, the bending moments in the mat calculated by the proposed elasto-plastic analysis were up to 52% smaller than those calculated with conventional methods and only 1.2% smaller from those obtained by other finite element methods. The initial elastic modulus did not have a significant effect on the results; however, the hardening constant in the proposed model was found to have a considerable effect on the results. The increase of the mat thickness provided a better distribution of contact stresses. The ultimate bending moment capacity of the mat was found to dictate the failure load.

The versatility of the constitutive proposed model and its finite element implementation were evaluated for a more complex engineering structure. A concrete gravity dam on "soft" foundation was analysed. In particular, the effect of uplift pressure and water fluctuation in the reservoir ~~on the~~ deformations and stress distributions was examined. It was found that to avoid tensile stresses in the concrete dam on "soft" foundation during construction sequence, an adequate geometry of the dam was required. The distribution of stresses developed in the foundation during the construction phase was not significantly affected by the water pressures after the initial water accumulation in the reservoir. Deformations were significantly influenced by the magnitude of the uplift pressure. Up to 39% higher displacements at the crest of the dam were calculated when the uplift pressure was considered. However, the effect

of different uplift pressure patterns on the overall displacements was found not to exceed 7%. Regardless of the presence of uplift pressure, the fluctuation of the water in the reservoir was found to have a considerable effect on both the deformations and stress distributions in the dam and the foundation. Calculated displacements after twelve cycles of 40.0 m water fluctuation were 38% larger compared to those calculated considering water fluctuation of 20.0 m. The stresses in the dam after twelve loading cycles increased by 75%, while the maximum shear stress in the foundation increased by an average of 50%. The accumulated plastic strains in the foundation were found to increase by 27% after twelve loading cycles.

During the course of this research various conclusions have been reached in connection with: (a) the formulation of the developed constitutive model; (b) its finite element implementation in the library of the general purpose program; (c) finite element analysis of problems related to geomechanics and soil structure interaction; (d) the effects on the overall structural behavior from employment of the advanced soil model; (e) the elasto-plastic soil behavior; (f) the influence of cyclic loading on nonlinear soil properties.

The conclusions summarized above show that the objectives of the research effort were accomplished. Undoubtedly, the constitutive relations for the cemented sands are realistic, the finite element model works well at all stages of loading and the proposed nonlinear analysis can be applied to large and complex engineering structures in practice.

6.1 RECOMMENDATIONS FOR FURTHER STUDY

The developed finite element procedure may be used in its present form in performing further studies on complex geotechnical and engineering structures. However, attention should be focussed on factors which have possible effects on the analysis. They are related to: (a) accuracy of experimental and analytical results that form the basis for comparison; (b) influence of soil parameters and precision in their evaluation; and (c) approximations related to the finite element analysis. Therefore, further studies are needed in both analytical and experimental areas. Experiments leading to better evaluation of the behavior of soils are a prerequisite for realistic modeling. Extensive testing on soils simulated in this study is required. The performed tests will allow further improvement of the developed constitutive relations and a closer evaluation of the soil parameters needed in the analysis.

A better understanding of the behavior of the soil modeled here may provide further simplifications of the proposed relatively complex model. This will reduce the amount of effort necessary for its finite element implementation. Tests on full or small scale structures are urgently required to fill the present void in experimental data and to serve as a basis for comparison with the present analytical results.

At the present state, a limited number of general purpose finite element programs are structured for inclusion of more elaborate models of the type developed in this study. Therefore, extensive developments in this area are needed.

The present model has the potential to be very useful in engineering practice and it is hoped that it will attract more attention in the future; especially in further study of complex problems in geomechanics and soil-structure interaction where soil nonlinearity cannot be ignored.

REFERENCES

- 1.1 Desai, R.W., Christian, J.T., (1977) (editors), Numerical Methods in Geotechnical Engineering, McGraw Hill.
- 1.2 Boyce, H.R., "A Non-linear Model for the Elastic Behavior of Granular Materials Under Repeated Loading", International Symposium on Soils Under Cyclic and Transient Loading, Swansea, U.K., Vol. 1, 1980, pp. 285-294.
- 1.3 Girijavallabhan, C.V., and Reese, L.C., "Finite Element Method for Problems in Soil Mechanics", Journal of the Soil Mechanics and Foundations Division, ASCE, Vol. 94, No. SM2, March 1968, pp. 473-496.
- 1.4 Hardin, B.O., and Drnevich, V.P., "Shear Modulus and Damping in Soils: Measurements and Parameter Effects", Journal of the Soil Mechanics and Foundations Division, ASCE, Vol. 98, No. SM6, June 1972, pp. 603-624.
- 1.5 Katona, M.G., Smith, J.M., Odello, R.S., and Allgood, J.R., "CANDE-A Modern Approach for Structural Design and Analysis of Buried Culverts", Report No. FHWA-RD-77-5, Naval Civil Engineering Laboratory, Oct. 1976.
- 1.6 Evans, R.J., and Pister, K.S., "Constitutive Equations for Class of Non-linear Elastic Solids", International Journal of Solids and Structures, Vol. 2, No. 3, 1966, pp. 427-445.
- 1.7 Ko, H.Y., and Masson, R.M., "Non-linear Characteristics and Analysis of Sand", Numerical Methods in Geomechanics, ASCE, 1976, pp. 294-304.
- 1.8 Saleeb, A.F., and Chen, W.F., "Non-linear Hyperelastic (Green) Constitutive Models for Soils, Part I - Theory and Calibration, Part II - Predictions and Comparisons", Proceedings of the North American Workshop on Limit Equilibrium, Plasticity and Generalized Stress-Strain in Geotechnical Engineering, McGill University, Montreal, Canada, May 1980.
- 1.9 Duncan, J.M., Byrne, P., Wong, K.S., and Mabry, P., "Strength Stress-Strain and Bulk Modulus Parameters for Finite Element Analysis of Stresses and Movements in Soil Masses", Report No. UCB/GR/78-02, University of California, Berkeley, April 1978.
- 1.10 Kondner, R.L., "Hyperbolic Stress-Strain Response: Cohesive Soils", Journal of the Soil Mechanics and Foundation Division, ASCE, Vol. 89, No. SM1, Feb. 1963, pp. 115-143.
- 1.11 Duncan, J.M., and Chang, Y.Y., "Non-linear Analysis of Stress and Strain in Soil", Journal of the Soil Mechanics and Foundations Division, ASCE, Vol. 97, No. SMB, Proc. Paper 7513 Sept 1970, pp. 495-498.

- 1.12 Kulhawy, F.H., and Duncan, J.M., "Stresses and Movements in Oroville Dam", Proc., ASCE, 98, No. SM7, pp. 653-665.
- 1.13 Saleeb, A.F., and Chen, W.F., "Constitutive Modeling of Soils-An Overview", ASCE, Conference, Las Vegas, Nevada, April 1982.
- 1.14 Hill R., "The Mathematical Theory of Plasticity", Oxford University Press, London, 1950.
- 1.15 Rendulic L., "Pore-index and pore water pressure", Bauingenieur, Vol.17, No. 559, 1936.
- 1.16 Hvorslev M. J., Physical properties of remolded cohesive soils, Transl. 69-5, U.S. Army Corps of Engineers Waterways Exp. Stn., Vickburg, Miss., June 1969.
- 1.17 Roscoe K.H., Schofield A., Wroth C.P., On the yielding of soils, Geotechnique, Vol.8, 1958, pp. 22-53.
- 1.18 Roscoe K.H., Poorooshasb H.B., A theoretical and experimental study of stress-strain in triaxial compression test on normally consolidated clays, Geotechnique, Vol. 13, 1963, pp. 12-28.
- 1.19 Roscoe K.H., Burland J.B., On the generalized stress - strain behaviour of "wet" clay, in: Engineering Plasticity, J. Heyman, F.A. Leckie (Eds), Cambridge University Press, Cambridge, 1968, pp. 535-609.
- 1.20 Poorooshasb H.B., Holubic I., Sherbourne A.N., On yielding and flow of sand in triaxial compression, Can. Geotechn. Journ., Part I, Vol. 3, 1966, pp. 179-190; Parts 2 and 3, Vol. 4, 1967, pp. 376-397.
- 1.21 Nova R., Wood R., A constitutive model for sand in triaxial compression, Int. Journ. Num. Anal. Meth. Geomech., Vol 3, 1979, pp. 255-278.
- 1.22 Wilde P., Two-invariants dependent model of granular media, Arch. of Mech., Vol. 23, 1977, pp. 517-555.
- 1.23 Poorooshasb H.B., Young R.N., On intersecting yield surfaces, Proc. Int. Symp. Num. Models in Geomech., Zurich, publ. A.A. Balkema, 1982, pp. 157-162.
- 1.24 Prevost J.H., Hoeg K., Effective stress-strain-strength model for soils, Journ. Geotechn. Div. ASCE, Vol. 101 GT3, 1975, pp. 257-278.
- 1.25 Pietruszczak S., Poorooshasb H.B., On modelling of cyclic behaviour of soils, in: Developments in Soil Mechanics and Foundation Engineering - 2, P.K. Banerjee, R. Butterfield (Eds), Applied Science Publishers, 1985, pp. 139-184.

- 1.26 Krieg R.D., A practical two-surface plasticity theory, Journ. Appl. Mech., Vol. 42, 1975, pp. 641-646.
- 1.27 Dafalias Y.F., Popov E.P., A model of non-linearly hardening materials for complex loadings, Acta Mechanica, Vol. 21, 1975, pp. 173-192.
- 1.28 Dafalias Y.F., Popov E.P., Cyclic loading for materials with a vanishing elastic region, Nucl. Eng. Design, Vol. 41, 1977, pp. 293-302.
- 1.29 Dafalias Y.F., Herrmann L.R., Bounding surface formulation of soil plasticity, Soil Mechanics-Transient and Cyclic Loads, John Wiley & Sons, 1982, pp. 253-283.
- 1.30 Carter J.P., Booker J.R., Wroth C.P., A critical state soil model for cyclic loading, Soil Mechanics-Transient and Cyclic Loads, John Wiley & Sons, 1982, pp. 219-252.
- 1.31 Mroz Z., Norris V.A., Zienkiewicz O.C., An anisotropic hardening model for soils and its application to cyclic loading, Int. Journ. Num. Anal. Meth. Geomech., Vol. 2, 1978, pp. 203-221.
- 1.32 Mroz Z., Pietruszczak S., A constitutive model for sand with anisotropic hardening rule, Int. Journ. Num. Anal. Meth. Geomech., Vol. 7, 1983, pp. 203-221.
- 1.33 Poorooshasb H.B., Pietruszczak S., On yielding and flow of sand; a generalized two-surface model, Computers and Geotechnics, Vol. 1, 1985, pp. 35-58.
- 1.34 Ghaboussi J., Momen H., Plasticity model for cyclic behaviour of sands, in: Numerical Methods in Geomechanics, W. Wittke (Ed), publ. A.A. Balkema, 1979, pp. 423-434.
- 1.35 Nova R., Hueckel T., A constitutive model for soil under monotonic and cyclic loading, Soil Mechanics-Transient and Cyclic Loads, 1982, pp. 343-373.
- 1.36 Valanis K.C., A theory of viscoplasticity without a yield surface, Arch. of Mech., Vol. 23, 1971, pp. 517-551.
- 1.37 Bazant Z.P., Bhat P.D., Endochronic theory of inelasticity and failure of concrete, Journ. Eng. Mech. Div. ASCE, Vol. 102, EM4, 1976, pp. 701-722.
- 1.38 Bazant Z.P., Krizek R.J., Saturated sand as an inelastic two-phase medium, Journ. Eng. Mech. Div. ASCE, Vol. 101 EM4, 1975, pp. 317-322.

- 1.39 Perzyna P., Fundamental problems in viscoplasticity, Adv. Appl. Mech., Vol. 9, 1966, pp. 244-368.
- 1.40 Zienkiewicz O.C., Corneau I.C., Viscoelasticity, plasticity approach, Int. Journ. Num. Meth. Eng., Vol. 8, 1976, pp. 821-845.
- 1.41 Akai K., Adachi T., Nishi K., Mechanical properties of soft rocks, Proc. Int. Conf. Soil Mech. Found. Eng., Vol. 1, Tokyo, Japan, 1977, pp. 7-10.
- 1.42 Clough, W.R., Zienkiewicz, C.O., "Finite Element Method in Analysis and Design of Dams". Criteria and Assumptions for Numerical Analysis of Dams, Int. Symposium Proceedings, Swansea, 1975, pp. 285-322.
- 1.43 Bode, G., "A treatise on the calculus of finite differences", 2nd Ed., New York, Dover Publications, Inc., 1960.
- 1.44 Wah, T., Calcote, R.L., "Structural Analysis by Finite Element Difference Calculus", Van Nostrand Reinhold Company, 1970.
- 1.45 Cruse, T.A., "Application of the Boundary Integral Equation Method in Solid Mechanics", Variational Methods in Engineering. Proc. Inst. Conf. Southampton Univ. Press, 1972.
- 1.46 Lachat, J.C., Watson, J.O., "A Second Generation Boundary Integral Equation Program for three Dimensional Elastic Analysis. ASME Conf. on Integral Equation Methods, New York, 1975.
- 1.47 Banerjee, P.K., Cathie, D.N., and Davies, T.G., "Two and three-dimensional Problems of Elastoplasticity", In: Developments in Boundary Integral Methods, Chapter 4, Eds. P.K. Banerjee and R. Butterfield, Applied Science Publishers, 1979.
- 1.48 Crowndall, S.H., "Engineering Analysis", McGraw-Hill, New York, N.Y., 1969.
- 1.49 Finlaison, B.A., "The method of weight residuals and variational principles", Academic Press, New York, 1972.
- 1.50 Turner, M.J., Clough, R.W., Martin, H.C., and Topp, L.J., "Stiffness and Deflection analysis of complex structures", J. Aero Sci. 23, 805-23, 1956.
- 1.51 Ergatoudis, J., Irons, B.M., and Zienkiewicz, O.C., "Curved Isoparametric "quadrilateral" elements for finite element analysis", Int. J. Solids Struct. 4, 31-42, 1968.
- 1.52 Zienkiewicz, O.C., Too, J., and Taylor, R.L., "Reduced integration technique in general analysis of plates and shells", Int. J. Num. Meth. Eng. 3, 275-290, 1971.
- 1.53 Pande, G.H., and Pietruszczak, S., "Sideways Look at the Constitutive Models", Institut of Numerical Methods in Engineering, University College of Swansea, U.K., 1982.

- 1.54 Owen, D.R.J., and Hinton, E., "Finite-Element in Plasticity; Theory and Practice", Pineridge Press Limited, Swansea, U.K., 1980.
- 1.55 Laumans, Q., Schad, H., "Calculation of Raft Foundations on Clayey Silts", Numerical Methods in Geomechanics, Edited by C.S. Desai, Virginia, U.S.A., 1986.
- 1.56 Teng, C.W., "Mat Foundations", in Foundation Engineering Handbook, chapter 17, 1981.
- 1.57 Teng, C.W., "Foundation Design", Prentice-Hall Inc., Englewood Cliffs. N.J., 1962.
- 1.58 Hetenyi, M., "Beams on Elastic Foundations", University of Michigan Press, Ann Arbor, Michigan, 1946.
- 1.59 ACI Committee 436 Report, "Suggested design Procedures for Combined Footings and Mats", ACI Journal, Oct. 1966.
- 1.60 Cheung, Y.K., Nag, D.K., "Plates and Beams on Elastic Foundations Linear and Nonlinear Behavior", Geotechnique, June 1968.
- 1.61 Haddadin, M., "Mats and Combined Footings-Analysis by finite element method", ACI Journal, Dec. 1971.
- 1.62 Creager, P.W., Justin, D.J., "Hydro-Electric Handbook", Second Edition, John Wiley, 1950.
- 1.63 Zienkiewicz, O.C., "The Stress Distribution in Gravity Dams", J. Inst. Civil Eng., 27 (3), 1947, pp. 244-271.
- 1.64 Zienkiewicz, O.C., "The Finite Element Method in Engineering Science", Third Edition, Mc Graw-Hill Book Co., New York, N.Y., 1977.
- 1.65 Sharma, D.H., Nayak, C.G., and Maheshwari, B.J., "Nonlinear Analyses of High Rockfill Dam with Vertical and Inclined Cores". Criteria and Assumptions for Numerical Analysis of Dams, Int. Symposium Proceedings, Swansea, 1975, pp. 533-562.
- 1.66 Clough, R.W., and Woodward, R.J., "Analysis of Embankment Stresses and Deformations", ASCE, Proc., J. of Soil Mech and Found. Division, SM4, 1967.
- 1.67 Alberro, J., "Stress-Strain Analysis of El Infiernillo Dam", ASCE, Specialty Conference on Performance of Earth and Earth Supported Structures", Purdue University, 1972.
- 1.68 Kulhawy, F.H., and Duncan, J.M., "Nonlinear Finite Element Analysis of Stresses and Movements in Oroville Dam", Report No. TE-70-2, Department of Civil Engineering, University of California, Berkeley, 1970.

- 1.69 Nobarri, E.S., and Duncan, J.M., "Movements in Dams due to Reservoir Filling", ASCE, Specialty Conference on Performance of Earth and Earth Supporting Structures, Purdue University, 1972.
- 1.70 Resendiz, D., and Romo, M.P., "Analysis of Embankment Deformations", ASCE, Specialty Conference on Performance of Earth and Earth Supported Structures, Purdue University 1982.
- 1.71 Wright, S.G., Kulhawy, F.H., and Duncan, J.M., "Accuracy of Equilibrium Slope Stability Analysis" ASCE Proce. J. of Soil Mech. and Found. Division SM 10, 1973.
- 1.72 Eisenstein, Z., Krishnayya, V.G., and Morgenstern, N.R., "An Analysis of Cracking at Duncan Dam", ASCE Specialty Conference on Performance of Earth and Earth Supporting Structures, Purdue University, 1982.
- 1.73 Takahashi, M., and Nakayama, K., "The Effect of Regional Conditions in Japan on Design and Construction of Impervious Elements of Rockfill Dams", Eleventh International Congress on Large Dams, Madrid, 1983.
- 1.74 Pant, B., Mokhashi, S.L., Knot, A.S., Thomas, B., and Mathew, P.V., "Some Aspects of the Design of Shear Keys for Dams Founded on Weak Rocks". Criteria and Assumptions for Numerical Analysis of Dams, Int. Symposium Proceedings, Swansea, 1975, pp. 945-960.
- 1.75 Aiken, D.G., "Foundation Problems at Warragamba Dam" Q.28, Proc. 8th ICOLD. P.1109.
- 1.76 Vallarino, E., and Alvarez, A., "Strengthening of Mequinenza Dam to Prevent Sliding", Pt. I and II, Journal of Water Power, 1971, pp. 104-121.
- 1.77 Maddox, J.M., Kinstler, F.L., and Mather, R.P., "Foundation Studies for Meadow Bank Buttress Dam", Proc. 9th ICOLD., Vol.1, 1967, p.123.
- 1.78 Corns, C.F., and Nesbitt, R.H., "Sliding Stability of three Dams on Weak Foundations", Proc. 9th ICOLD, Vol.1, 1967 p.463.
- 1.79 Castillo, M., and Navalon, N., "Mesures Prises pour Ameliorer le Coefficient de Securite concernant la Stabilité de l'appui Rive Droite du Barrage de Terrejon sur le Tage", Proc. 9th ICOLD, Vol. 1, 1967 p. 547.
- 1.80 Corns, C.F., "Stability of Spillway Monoliths, Dworshak Dam", Discussion on 2.37, - Proc. 10th ICOLD, Vol. VI, 1970 p. 497.
- 1.81 Link, H., "The Sliding Stability of Dams", Part I to III, J. of Water Power, 1969, p. 99.
- 1.82 Kaneko, K., "Finite Element Methods Applied for Foundation Analysis of Three Dams in Azusagawa Project", Discussion on Q.37, Proc. 10th ICOLD, Vol.6, 1970 p.507.

- 1.83 Sherlock, P., Discussion on Q.37 - Proc. 10th ICDL., Vol. VI, 1970 P.528.
- 2.1 Lade, P.V., "Elasto-Plastic Stress-Strain Model for Sand", Proceeding of the Workshop of Limit Equilibrium, Plasticity and Generalized Stress-Strain in Geotechnical Engineering", McGill University, 1980, pp. 628-648.
- 2.2 Kryning, D.R., and Judd, W.R., "Principles of Engineering Geology and Geotechnics", McGraw-Hill Publishing Co., Inc., New York, N.Y., 1957.
- 2.3 Clough G.W., Sitar, N., Bachus, R.C., Rad, N.S., "Cemented Sands Under Static Loading", Journal of the Geotechnical Engineering Division, ASCE, Vol. 107, No. GT6, 1981, pp. 799-817.
- 2.4 Dupas, J.M., and Pecker, A., "Static and Dynamic Properties of Sand-Cement", Journal of Geotechnical Engineering Division", ASCE, Vol. 105, No. GT3, 1979, pp. 419-436.
- 2.5 Saxena, S.K., and Lastrico, R.M., "Static Properties of Lightly Cemented Sand", Journal of the Geotechnical Engineering Division, ASCE, Vol. 104, No. GT12, 1978, pp. 1449-1464.
- 2.6 Beckwith, G.H., and Hansen, L.A., "The Calcerous Soil of the Southwestern United States", ASTM, Symposium on Calcerous Soils, Ft. Lauderdale, Fla.; 1981.
- 2.7 Frydman, S., Hendron, D., Horn, H., Steinbach, J., Baker, R., and Shaal, B., "Liquefaction Study of Cemented Sand", Journal of the Geotechnical Engineering Division, ASCE, Vol. 106, No. GT3, 1980, pp. 275-297.
- 2.8 Poulos, H.G., "A Review of the Behavior and Engineering Properties of Carbonate Soils", Research Report No. R381, University of Sydney, Sydney, Aust. 1980.
- 2.9 Rad, N.S., and Clough, G.W., "The Influence of Cementation on the Static and Dynamic Behavior of Sands", Report No.59, John Blume Earthquake Engineering Center, Stanford University, Palo Alto, Calif. 1982.
- 2.10 Salomone, L.A., Singh, H., and Fisher, J.A., "Cyclic Shear Strength of variably Cemented Sands", Proceed of the ASCE Geotechnical Engineering Division Specialty Conference on Earthquake Engineering and Soil Dynamics, Vol. II, Pasadena, Calif. 1978, pp. 819-835.
- 2.11 Yamanouchi, T., Mochinaga, R., Gotoh, K., and Murata, H., "Status of Cutoff Slopes in Pumicer Flow Soil Deposits and their Application to Design Standards for an Expressway", Proceed. of the 9th International Conference on Soil Mechanics and Foundation Engineering, Tokyo, Japan, 1977.

- 2.12 Mitchell, J.K., and Solyman, Z.V., "Time-dependant Strength Gain in Freshly Deposited or Densified Sands", Journal of the Geotechnical Engineering Division, ASCE, Vol. 110, No. GT II, 1984, pp. 1559-1576.
- 2.13 Sitar, N., and Clough, G.W., "Seismic Response of Steep Slopes in Cemented Soils", Journal of Geotechnical Engineering, ASCE, Vol. 109, No. GT2, 1983, pp. 210-227.
- 2.14 Acar, Y.B., EL-Tahir A. EL-Tahir, "Low Strain Dynamic Properties of Artificially Cemented Sand", Journal of Geotechnical Engineering, ASCE, Vol. 112, No. II, November, 1986, pp.1001-1015.
- 2.15 Denisov, N.Y., and Reltov, B.F., "The Influence of Certain Processes on the Strength of Soils", Proc. 5th. Inst. Conf. Soil. Mech. and Found. Engr., Vol. 1, 1961, pp 75-78.
- 2.16 Durante, V.A., and Voronkevich, S.D., "Studies of Sand Deposits for Construction Purposes, " Annals of Moscow University, No. 2; 1955, pp. 131-137.
- 2.17 Lukas, R.G., "Densification of Loose Deposits by Pounding", Journal of the Geotechnical Engineering Division, ASCE, Vol. 106, No. GT4, 1980, pp. 435-446.
- 2.18 Pietruszczak, S., Mroz, Z., "On Hardening Anisotropy of Ko-Consolidated Clays", Int. Journ. Num. Anal. Method. Geomech., 7, 1983, pp. 19-38.
- 2.19 Pietruszczak, S., Stolle, D.F.E., "Non-Linear Seismic Response of Loose Sand Deposits", in Soil Dynamics and Earthquake Engineering, Editors Brebbia, C.A., Cakmak, A.G., Ghaffar. A.M., Springer-Verlag Publ. 1985, pp.3-75.
- 2.20 Baladi, G.Y., and Rohani, B., "An Elastic-Plastic Constitutive Model for Saturated Sand Subjected to Monotonic and/or Cyclic Loadings", Num. Meth. in Geomch. - Third International Conference Aachen, ed, W. Wittke, publ. A.A. Balkema, Vol. 1, 1979, p. 388.
- 2.21 Ishihara, K., Tatsuoka, F., and Yasuda, S., "Undrained Deformation and Liquefaction of Sand under Cyclic Stressses", Soils and Foundations, 15 (1), March, 1975.
- 2.22 William, K.J., and Warnke, E.P., "Constitutive Model for the Triaxial Behavior of Concrete", Seminar on Concrete Structures Subjected to Triaxial Stresses, ISMES, Bergamo, 1972.
- 2.23 Vermeer, P.A., "A Double Hardening Model for Sand", Geotechnical, Vol. 28, 1978, pp. 413-433.
- 3.1 Hughes, T.J.R., Lin, W.K., "Implicit-Explicit Finite Elements in transient analysis: Stability Theory", J. Appl. Mech. 45, 371-374, 1978.

- 3.2 Bathe, K.J., Wilson, E.L., "Numerical Methods in Finite Element Analysis", Prentice-Hall, Englewood Cliffs, New Jersey (1976).
- 3.3 Bowles, J.E., "Analytical and Computer Methods in Foundation Engineering", McGraw-Hill Book Company, New York, 1974.
- 3.4 Banks, D.C., MacIver, B.N., "Variation in Angle of Internal Friction with Confining Pressure", U.S. Army Engineer Waterways Experiment Station, Misc. Paper S-69-12, 1969.
- 3.5 Hvorslev, M.J., "Physical Components of the Shear Strength of Saturated Clays", 1st PSC, ASCE, pp. 169-273, 1960.
- 3.6 Bowles, J.E., "Engineering Properties of Soils and Their Measurement", McGraw-Hill Book Company, New York, 1970.
- 3.7 Bishop, A.W., Henkel, D.J., "The Measurement of Soil Properties in the Triaxial Test", 2nd ed., Edward Arnold, (Publishers) Ltd. London, 1962.
- 3.8 Wineland, J.D., "Borehole Shear Device", 6th PSC, ASCE, Vol. 1, pp. 511-522, 1975.
- 3.9 Arman, A., et al. "Study on the Vane Shear", 6th PSC, ASCE, Vol. 1, pp. 93-120, 1975.
- 3.10 Lee, K.L., "Comparison of Plane Strain and Triaxial Test on Sand", JSMFD, ASCE, Vol. 96, SM3, May, pp. 901-923, 1970.
- 3.11 Vesic, A.B., Clough, G.W., "Behavior of Granular Material Under High Stresses", Journal of Soil Mechanics and Foundation Division, ASCE, Vol. 94 No. SM3, Paper 5954, 1968, pp. 661-688.
- 4.1 Naylor, D.J., Pande, G.N., "Finite Elements in Geotechnical Engineering", Pineridge Press, Swansea, U.K., 1981.
- 4.2 Kulhawy, F.H., Duncan, J.M., Seed, H.B., "Finite Element Analysis of Stresses and Movements in Embankments During Construction", No. TE-69-4, Department of Civil Engineering, University of California, Berkeley, Nov. 1969.
- 4.3 Duncan, J.M., "The Influence of Depth on the Bearing Capacity of Strip Footings in Sand", Thesis presented to the Georgia Institute of Technology, at Atlanta, Georgia, in 1962, in partial fulfillment of the requirements for the degree Master of Science.
- 4.4 Marachi, N., "Strength and Deformation Characteristics of Rockfill Materials", Dissertation presented to the University of California, Berkeley, for the degree of Doctor of Philosophie, 1969.

- 4.5 Ozawa, Y., Duncan, J.M., "Elasto-Plastic Finite Element Analysis of Sand Deformations", 2nd International Conference on Numerical Methods in Geomechanics, Blacksburg, Virginia, June 20-26, 1976, pp. 243-259.
- 5.1 National Building Code of Canada 1985 - Nat. Res. Council. Can. Ottawa, Ontario.
- 5.2 Terzaghi, K., "Theoretical Soil Mechanics", John Wiley & Sons., New York, N.Y., 1943.

APPENDIX A

A1. Listing of the Modified Subroutine RESEPL

```

SUBROUTINE RESEPL (COORD ,DISPL ,EFFST ,ELOAD ,EPSTN ,ITER ,
                  INTGR ,LEONS ,LNODS ,MATNO ,NCRIT ,NMODE ,
                  NDOFN ,NELEM ,NGAUS ,NLAPS ,NMATS ,NNOE ,
                  NPOIN ,NSTR ,NTYPE ,POSGP ,PROPS ,RESID ,
                  STRAG ,STRIN ,STRSG ,WEIGP ,IPRED ,ISTEP ,
                  KUNLD ,ESCUV ,
                  MCALC ,SSIZE ,REVST ,ALPH2 ,GTHEJ ,NEONS ,
                  PPTOT ,ICONS ,RKPLS)
.....
C
C *** EVALUATES RESIDUAL FORCES
C
.....
DIMENSION COORD(NPOIN,1),DERIV(2,9),DMATX(4,4),AVECT(4),MATNO(1),
          PROPS(NMATS,1),DLCOD(2,9),BMATX(4,18),DEVIA(4),DISPL(1),
          LNODS(NELEM,1),GPCOD(2,9),DJACM(2,2),STRAN(4),POSGP(1),
          ELOAD(NELEM,1),CARTD(2,9),SHAPE(9),STRES(4),WEIGP(1),
          STRIN(4,1),ELCOD(2,9),SIGMA(4),SGTOT(4),EFFST(1),
          STRSG(4,1),ELDIS(2,9),DESIG(4),DVECT(4),EPSTN(1),
          STRAG(4,1),RESID(1),LEONS(18,1),INTGR(1),PPTOT(1),
          SSIZE(4,1),REVST(4,1),ALPH2(4,1),ALPA2(4),
          ESCUV(1),
          GTHEJ(1),STREV(4),VECTA(4),STRST(4),ALPA3(4),
          ICONS(1),RKPLS(1)
.....
C
KUNLD = 0
TWOP1 = 6 283185307179586
NEVAB = NMODE * NDOFN
NTQTV = NPOIN * NDOFN
NSTR = 4
DO 530 IELEM = 1, NELEM
IF (INTGR(IELEM) EQ 2 AND ITER GT 1 AND IPRED EQ 1) GO TO 530
DO 540 IEVAB = 1, NEVAB
540 ELOAD(IELEM,IEVAB) = 0.0
530 CONTINUE
C
KGAUS = 0
DO 20 IELEM = 1, NELEM
IF (INTGR(IELEM) EQ 2 AND ITER GT 1 AND IPRED EQ 1) GO TO 20
LPROP = MATNO(IELEM)
C
IF ( NCRIT EQ 5 ) GO TO 610
C
YOUNG = PROPS(LPROP,1)
POISS = PROPS(LPROP,2)
THICK = PROPS(LPROP,3)
UNIAX = PROPS(LPROP,6)
HARDS = PROPS(LPROP,7)
FRICT = PROPS(LPROP,8) * 0.017453292
IF (NCRIT EQ 3) UNIAX = UNIAX * COS(FRICT)
IF (NCRIT EQ 4) UNIAX = 6.0 * UNIAX * COS(FRICT) /
(1.73205080757 * (3.0 - SIN(FRICT)))
IF (NCRIT NE 6) GOTO 620
AMF = 6.0 * SIN(FRICT) / (3.0 - SIN(FRICT))
AMC = PROPS(LPROP,12)
ACON = PROPS(LPROP,13)
CF = HARDS
SPHIF = 3.0 * AMF / (AMF + 6.0)
SMO = CF * SORT(1.0 - SPHIF * SPHIF) / SPHIF
GO TO 620
C *** INS-MODEL ***
610 CONTINUE
RKAPA = PROPS(LPROP,1)
STIFG = PROPS(LPROP,2)
VOIDO = PROPS(LPROP,7)
THICK = PROPS(LPROP,3)
BULK = PROPS(LPROP,15)
BETA = PROPS(LPROP,17)
IRIGO = PROPS(LPROP,18)
C
620 CONTINUE
C
C *** COMPUTE COORDINATE AND INCREMENTAL DISPLACEMENTS OF THE
C ELEMENT NODAL POINTS
C
IPOSN = 0
DO 30 INODE = 1, NMODE
LNODE = LNODS(IELEM,INODE)
DO 30 IDIME = 1, NMODE
IPOSN = IPOSN + 1
NPOSN = LEONS(IPOSN,IELEM)
DISPT = 0
IF (NPOSN NE 0) DISPT = DISPL(NPOSN)
DLCOD(IDIME,INODE) = COORD(LNODE,IDIME) + DISPT
ELCOD(IDIME,INODE) = COORD(LNODE,IDIME)

```

```

30 ELDIS(IDIME,INODE)=DISP1
C
C
IF ( NCRIT NE 5 )
CALL MODPS (DMATX,LPROP,NMATS,NSTRE,NTYPE,PROPS,
TRACE,NCRIT)
C
C
KGASP=0
DO 40 IGAUS=1,NGAUS
DO 40 JGAUS=1,NGAUS
EXISP=POSGP(IGAUS)
ETASP=POSGP(JGAUS)
KGAUS=KGAUS+1
KGASP=KGASP+1
C
C
IF ( NCRIT NE 5 ) GO TO 650
C
C
*** INS-MODEL ***
C
DO 640 ISTR1 = 1, NSTRI
IF ( ISTEP EQ 1 AND IITER EQ 1 ) GO TO 630
STRST(ISTR1) = STRSQ(ISTR1,KGAUS)
GO TO 640
630 CONTINUE
STRST(ISTR1) = STRIN(ISTR1,KGAUS)
640 CONTINUE
TRACE = ( STRST(1) + STRST(2) + STRST(4) ) / 3.0
CALL MODPS ( DMATX, LPROP, NMATS, NSTRE, NTYPE, PROPS,
TRACE, NCRIT )
C
C
650 CONTINUE
C
C
-----
CALL SFR2 (DERIV,MNODE,SHAPE,EXISP,ETASP)
CALL JACOB2 (CARTD,DERIV,DJACB,ELCOD,GPCOD,
IELEM,KGASP,MNODE,SHAPE)
CALL JACOB0 (CARTD,DLCD,DJACM,MDIME,NLAPS,MNODE)
DVOLU=DJACB*WEIGP(IGAUS)*WEIGP(JGAUS)
IF (NTYPE EQ 3) DVOLU=DVOLU*TWOP1*GPCOD(1,KGASP)
IF (NTYPE EQ 1) DVOLU=DVOLU*THICK
CALL BLARGE (BMATX,CARTD,DJACM,DLCD,GPCOD,
KGASP,NLAPS,MNODE,NTYPE,SHAPE)
CALL LINGNL (CARTD,DJACM,DMATX,ELDIS,GPCOD,KGASP,
KGAUS,MOFN,NLAPS,MNODE,NSTRE,NTYPE,
POISS,SHAPE,STRAN,STRES,STRAG,NCRIT)
C
C
*** FOR DISPLACEMENT CONTROL ***
C
C
C
C
END
IF ( NCRIT NE 5 ) GO TO 200
C
C
*** INS-MODEL ***
C
C
***SKIP
IF ( IIRIGD EQ 1 ) GO TO 730
IF ( ISTEP EQ 1 AND IITER EQ 1 ) GO TO 760
IF ( IITER EQ 1 ) GOTO 190
C
ICON1 = ICONS(KGAUS)
SIZ1 = SSIZE(1,KGAUS)
SIZ2 = SSIZE(2,KGAUS)
SIZ3 = SSIZE(3,KGAUS)
ALPA1 = SSIZE(4,KGAUS)
GTET3 = GTHEJ(KGAUS)
DO 660 ISTR1 = 1, NSTRI
STREV(ISTR1) = REVST(ISTR1,KGAUS)
ALPA2(ISTR1) = ALPH2(ISTR1,KGAUS)
660 CONTINUE
661 CONTINUE
IF ( MCALC EQ 0 ) GO TO 670
READ (8) DMATX, VECTA, SIZ3, GTET3, ALPA3, FACTR, FLOW1,
GMEAN
C
C
GO TO 680
C
670 CONTINUE
CALL INSDOP ( SIZ1, SIZ2, SIZ3, ALPA1, ALPA2, ALPA3, DMATX,
STRST, STREV, VECTA, GTET3, GMEAN, LPROP, NMATS,
PROPS, FACTR, FLOW1, ISTEP, IITER, ICON1, RKPLA)
680 CONTINUE
IF ( SIZ3 EQ 0.0 ) GO TO 730
DFUN3 = 0.0
DO 690 ISTR1 = 1, NSTRI
DFUN3 = DFUN3 + VECTA(ISTR1) * STRES(ISTR1)
690 CONTINUE
IF ( DFUN3 GT -1.0E-3 ) GO TO 710
C
C
-----
ERROR = 0.0
DO 695 ISTR1=1,NSTRI
IF (ABS(STREV(ISTR1)) LT 1.0E-2) GOTO 695
CONST = ABS(1.0 - ABS((STRST(ISTR1)+STRES(ISTR1))/STRST(ISTR1)))

```



```
IF (CONST GT ERROR) ERROR=CONST
695 CONTINUE
IF (ERROR LT 0.001) DFUN3=1 0
IF (ITER NE 2) DFUN3=1 0
IF (DFUN3 GT 0 0) GOTO 710
C
ICONS(KGAUS) = 0
SZA2 = SZA3
SZA3 = 0 0
GTET3 = GMEAN
DO 700 ISTR1 = 1, NSTR1
  ALPA2(ISTR1) = ALPA3(ISTR1)
  ALPA3(ISTR1) = STRST(ISTR1)
  STREV(ISTR1) = STRST(ISTR1)
700 CONTINUE
GO TO 730
C
710 CONTINUE
DO 720 ISTR1 = 1, NSTR1
  STRES(ISTR1) = 0 0
  DO 720 USTR1 = 1, NSTR1
    STRES(ISTR1) = STRES(ISTR1) + DMATX(ISTR1,USTR1)*STRAN(USTR1)
720 CONTINUE
C
730 CONTINUE
DO 740 ISTR1 = 1, NSTR1
  STRST(ISTR1) = STRST(ISTR1) + STRES(ISTR1)
740 CONTINUE
C *** IN CASE OF A "RIGID" ELEMENT
C
IF (IRIGD EQ 1) GO TO 760
C
DPDEV = 0 0
FACT1 = 1 0
DTVOL = -(STRAN(1) + STRAN(2) + STRAN(4))
IF (DFUN3 LT -1 0E-3) GOTO 745
STIFK = -(1 0 + VOIDO) / RKAPA * TRACE
DEVOL = -( STRES(1)*STRES(2)+STRES(4) ) / (3.0 * STIFK)
DPVOL = DTVOL - DEVOL
IF (BETA LT 0 1) GOTO 742
DTDEV = 2 0/3 0*SORT(STRAN(1)**2+STRAN(2)**2+STRAN(4)**2-
  STRAN(1)*STRAN(2)-STRAN(1)*STRAN(4)-STRAN(2)*STRAN(4)-
  3 0*STRAN(3)**2)
DEDEV = SORT(STRES(1)**2+STRES(2)**2+STRES(4)**2-STRES(1)*
  STRES(2)-STRES(1)*STRES(4)-STRES(2)*STRES(4)-
  3 0*STRES(3)**2)/(3 0*STIFK)
DPDEV = DTDEV - DEDEV
742 CONTINUE
FACT1 = FACTR*(BETA*DPDEV+(1 0*VOIDO)*DPVOL) + 1 0
SZA1 = SZA1 * FACT1
SZA2 = SZA2 * FACT1
ALPA1 = ALPA1 * FACT1
745 CONTINUE
SSIZE(1,KGAUS) = SZA1
SSIZE(2,KGAUS) = SZA2
SSIZE(3,KGAUS) = SZA3
SSIZE(4,KGAUS) = ALPA1
RKPLS(KGAUS) = RKPLA
DO 750 ISTR1 = 1, NSTR1
  ALPH2(ISTR1,KGAUS) = ALPA2(ISTR1)*FACT1
  REVST(ISTR1,KGAUS) = STREV(ISTR1)*FACT1
750 CONTINUE
PPTOT(KGAUS) = PPTOT(KGAUS)-BULK*DTVOL
C
GTHE3(KGAUS) = GTET3
IF (DFUN3 LT -1 0E-3) GOTO 760
IF ( (FLOW1 LT -1 0E-6*SZA1) AND (ICONS(KGAUS) NE 1) )
  GOTO 760
C
C *** LOWER STRESS POINT ONTO BOUNDARY SURFACE
C
CALL INVAR ( DEVIA, LPROP, NCRIT, NMATS, PROPS, SINT1, SBAR1,
  STRST, VAR31, SIGM1, YIELD )
CALL INSLW ( LPROP, NMATS, PROPS, SINJ1, SIGM1, SBAR1,
  ALPA1, SZA1, STRST )
ICONS(KGAUS) = 1
C
C ***
760 CONTINUE
DO 770 ISTR1 = 1, NSTR1
  STRSQ(ISTR1,KGAUS) = STRST(ISTR1)
770 CONTINUE
C
IF ( IGAUS NE 0 ) GO TO 190
IF (IRIGD EQ 1) GO TO 190
IF (ITER LT 2 OR ITER GT 3) GOTO 190
FORMAT(2X,15HPORE PRESSURE =,E15.5)
WRITE(6,1) PPTOT(KGAUS)
CALL ADUMP ( SSIZE(1,KGAUS), 4, "SSIZE-RES" )
CALL ADUMP ( STRST, 4, "STRST-RES" )
CALL ADUMP ( STRSQ(1,KGAUS), 4, "STRSQ-RES" )
CALL ADUMP ( STRES, 4, "STRES-R" )
```

```

      CALL ADUMP ( STRAN, 4, 'STRAIN-R' )
C
C
C          GO TO 180
C *** NOT INS-MODEL ***
200 CONTINUE
IF (ISTEP.GT 1 OR IITER GT 1) GO TO 160
IF (NCRIT NE 6) GOTO 155
C
DO 157 ISTR1=1,NSTR1
STRSQ(ISTR1,KGAUS) = STRIN(ISTR1,KGAUS)
157 SIGMA(ISTR1) = STRIN(ISTR1,KGAUS)
IF (UNIAX GT 100 0) GOTO 160
CALL INVAR (DEVIA,LPROP,NCRIT,NMATS,PROPS,SINTJ,STEFF,
           SIGMA,THETA,VARJ2,YIELD)
SMEAN = (SIGMA(1)+SIGMA(2)+SIGMA(4))
SPHI = -COS(THETA)*STEFF/(SMEAN/3 -SMO-STEFF*SIN(THETA)/SQRT(3 ))
AM = 6 0*SPHI/(3 -SPHI)
EPSTN(KGAUS) = ACON*AM/(AMF-AM)
GO TO 160
C
155 DO 170 ISTR1=1,NSTR1
170 STRES(ISTR1)=STRES(ISTR1)*STRIN(ISTR1,KGAUS)
160 CONTINUE
PREYS=UNIAX+EPSTN(KGAUS)*HARDS
DO 150 ISTR1=1,NSTR1
DESIG(ISTR1)=STRES(ISTR1)
150 SIGMA(ISTR1)=STRSQ(ISTR1,KGAUS)+STRES(ISTR1)
IF (NLAPS EQ 2 OR NLAPS EQ 0) GO TO 60
IF (UNIAX GT 100 0) GOTO 60
C ---
C ---
CALL INVAR (DEVIA,LPROP,NCRIT,NMATS,PROPS,SINTJ,STEFF,
           SIGMA,THETA,VARJ2,YIELD)
IF (NCRIT NE 6) GOTO 44
AM = AMF*EPSTN(KGAUS)/(ACON*EPSTN(KGAUS))
SMEAN = (SIGMA(1)+SIGMA(2)+SIGMA(4))/3 0
SPHI = 3 0*AM/(6 0*AM)
YIELD=(SMEAN-SMO)*SPHI+(COS(THETA)-SIN(THETA)*SPHI/SQRT(3 ))*STEFF
44 ESPRE=EFFST(KGAUS)-PREYS
IF (ESPRE GE 0 0) GO TO 50
ESCUR=YIELD-PREYS
ESCUR(KGAUS) = ESCUR
IF (ESCUR LE 0 0) GO TO 60
RFACT=ESCUR/(YIELD-EFFST(KGAUS))
GO TO 70
50 ESCUR=YIELD-EFFST(KGAUS)
ESCUR(KGAUS) = ESCUR
IF ( ESCUR GT 0 0 ) GO TO 55
KUNLD = 1
GO TO 60
55 CONTINUE
C
REACT=1 0
70 MSTEP = 1
IF (NCRIT EQ 6) GOTO 75
MSTEP=ESCUR*8 0/UNIAX+1 0
IF (MSTEP GT 10) MSTEP=10
75 ASTEP=MSTEP
REDUC=1.0-RFACT
DO 80 ISTR1=1,NSTR1
SGTOT(ISTR1)=STRSQ(ISTR1,KGAUS)+REDUC*STRES(ISTR1)
80 STRES(ISTR1)=RFACT*STRES(ISTR1)/ASTEP
DO 90 JSTEP=1,MSTEP
CALL INVAR (DEVIA,LPROP,NCRIT,NMATS,PROPS,SINTJ,STEFF,
           SGTOT,THETA,VARJ2,YIELD)
IF (NCRIT EQ 6) FRICT=ASIN(SPHI)
CALL YIELD (AVECT,DEVIA,FRICT,NCRIT,SINTJ,STEFF,
           THETA,VARJ2,0)
IF (NCRIT NE 6) GOTO 82
C
INT = 0
SMEAN = SGTOT(1)+SGTOT(2)+SGTOT(4)
CALL YIELD (STREV,DEVIA,FRICT,INT,AMC,STEFF,THETA,SMEAN,SMO)
82 CONTINUE
C
CALL FLOWPL (AVECT,ABETA,DVECT,HARDS,NTYPE,POISS,YOUNG)
IF (NCRIT NE 6) GOTO 89
C
DENOM= 0
DO 83 ISTR1=1,NSTR1
DENOM=DENOM+STREV(ISTR1)*DVECT(ISTR1)
83 SMEN=(STREV(1)+STREV(2)+STREV(4))/3 0
ALPA3(1) = STREV(1) - SMEN
ALPA3(2) = STREV(2) - SMEN
ALPA3(3) = STREV(3)
ALPA3(4) = STREV(4) - SMEN
PCTR = 0
DO 84 ISTR1=1,NSTR1
84 PCTR = PCTR + ALPA3(ISTR1)*ALPA3(ISTR1)

```

```

FGTR = SORT(2 *FCTR/3 0)
DAM = AMF*ACON/(ACON*EPSTN(KGAUS))**2
SMEN = SME*AN/3 0
HPL = -18 0*(SMEN-SMO-SIN(THETA))*STEFF/SORT(3 0)/
      (6 0*AM)**2*DAM*FCTR
ABETA = 1 0/(HPL*DENOM)
C
89 CONTINUE
AGASH=0 0
DO 100 ISTR1=1,NSTR1
100 AGASH=AGASH+AVECT(ISTR1)*STRES(ISTR1)
DLAMO=AGASH*ABETA
IF(DLAMO LT 0 0) DLAMO=0 0
IF(ISTEP EQ 13 AND IITER EQ 4) PRINT*,
C AM,HPL,ABETA,DLAMO,STREV
C IF(ISTEP EQ 13 AND IITER EQ 4) WRITE(6,1014)
C (DESIG(1),I=1,4)
C IF(ISTEP EQ 13 AND IITER EQ 4) WRITE(6,1014)
C (SIGMA(1),I=1,4)
C IF(ISTEP EQ 13 AND IITER EQ 4) WRITE(6,1014)
C (SGTOT(1),I=1,4)
C IF(ISTEP EQ 13 AND IITER EQ 4) WRITE(6,1014)
C (STRES(1),I=1,4)
C IF(ISTEP EQ 13 AND IITER EQ 4) WRITE(6,1014)
C (AVECT(1),I=1,4)
C1014 FORMAT(7G10 4)
IF (NCRIT NE 6) GOTO 108
IF (DLAMO EQ 0 0) GOTO 60
C
CALL FLOWPL(ISTREV,BBETA,DVECT,HARDS,NTYPE,POISS,YOUNG)
DO 102 ISTR1=1,NSTR1
SIGMA(ISTR1) = STRES(ISTR1)-DLAMO*DVECT(ISTR1)
102 ALPA3(ISTR1) = DLAMO*STREV(ISTR1)
EPSTN(KGAUS) = EPSTN(KGAUS)+DLAMO*FCTR
AM=AMF*EPSTN(KGAUS)/(ACON*EPSTN(KGAUS))
SPHI=3 0*AM/(6 0*AM)
IF(ISTEP EQ 13 AND IITER EQ 4) PRINT*,
C AM
C
IND = 0
IF(ABS(SIGMA(4)) LT ABS(SIGMA(1))) IND=1
IF(ABS(SGTOT(4)) LT ABS(SGTOT(1))) IND=1
IF(IND EQ 0) GOTO 114
C
116 DO 112 ISTR1=1,NSTR1
112 SGTOT(ISTR1)=SGTOT(ISTR1)+SIGMA(ISTR1)
CALL INVAR(DEVIA,LPROP,NCRIT,NMATS,PROPS,SINT3,STEFF,
          SGTOT,THETA,VARJ2,YIELD)
SME = (SGTOT(1)+SGTOT(2)+SGTOT(4))/3 0
FAC = ((SMO-SME)*SPHI)/((COS(THETA)-SIN(THETA)*SPHI/SORT(3 0))
      *STEFF)
SGTOT(1) = FAC*DEVIA(1)+SME
SGTOT(2) = FAC*DEVIA(2)+SME
SGTOT(3) = FAC*DEVIA(3)
SGTOT(4) = FAC*DEVIA(4)+SME
GOTO 90
C
114 CONTINUE
IF(ISTEP EQ 13 AND IITER EQ 4) PRINT*,FAC
C
CON1=(SGTOT(1)-SGTOT(2))*(SIGMA(1)-SIGMA(2))+4 0*SGTOT(3)*
      SIGMA(3)-SPHI*SPHI*(SGTOT(1)+SGTOT(2))*(SIGMA(1)+
      SIGMA(2))+2 0*SPHI*SPHI*SME*(SIGMA(1)+SIGMA(2))
CON2=(SIGMA(1)-SIGMA(2))**2+4 0*SIGMA(3)**2-SPHI*SPHI*(SIGMA(1)+
      SIGMA(2))**2+4 0*SPHI*SPHI*SME*(SIGMA(1)+SIGMA(2))-4 0*
      (SPHI*SME)**2
IF(ABS(CON2) LT 0 1E-6) CON2=1 0
CON3=(SGTOT(1)-SGTOT(2))**2+4 0*SGTOT(3)**2-(SGTOT(1)+
      SGTOT(2))**2*SPHI*SPHI
DD = 4 0*CON1*CON1-4 0*CON2*CON3
IF (DD GT 0 0) GOTO 103
STOP
103 DD = SORT(DD)
FAC1=(-2 0*CON1-DD)/(2 0*CON2)
FAC2=(-2 0*CON1+DD)/(2 0*CON2)
FAC=FAC1
IF ((FAC1 LT 0 0) OR (FAC1 GT 2 0)) FAC=FAC2
IF ((FAC LT 0 0) OR (FAC GT 2 0)) GOTO 116
DO 104 ISTR1=1,NSTR1
104 SGTOT(ISTR1)=SGTOT(ISTR1)+FAC*SIGMA(ISTR1)
IF(ISTEP EQ 13 AND IITER EQ 4) PRINT*,
C FAC,CON1,CON2,CON3
C
GOTO 90
C
108 CONTINUE
C
BGASH=0 0
DO 110 ISTR1=1,NSTR1
BGASH=BGASH+AVECT(ISTR1)*SGTOT(ISTR1)
110 SGTOT(ISTR1)=SGTOT(ISTR1)+STRES(ISTR1)-DLAMO*DVECT(ISTR1)

```

```
EPSTN(KGAUS)=EPSTN(KGAUS)*DLAMD*BGASH/YIELD
90 CONTINUE
CALL INVAR (DEVIA,LPROP,NCRIT,NMATS,PROPS,SINT3,STEFF,
           SGTOT,THETA,VARJ2,YIELD)
IF (NCRIT NE 6) GOTO 96
SME = (SGTOT(1)+SGTOT(2)+SGTOT(4))/3.0
YIELD=(SME-SMO)*SPHI+(COS(THETA)-SIN(THETA)*SPHI/SORT(3))*STEFF
BRING = 1.0
GOTO 98
C
96 CURYS=UNIAX*EPSTN(KGAUS)*HARDS
BRING = CURYS / YIELD
98 DO 130 ISTR1=1,NSTR1
130 STRSQ(ISTR1,KGAUS)=BRING*SGTOT(ISTR1)
EFFST(KGAUS) = CURYS
C*** ALTERNATIVE LOCATION OF STRESS REDUCTION LOOP TERMINATION CARD
C 90 CONTINUE
C***
GO TO 190
60 DO 180 ISTR1=1,NSTR1
180 STRSQ(ISTR1,KGAUS)=STRSQ(ISTR1,KGAUS)*DESIG(ISTR1)
EFFST(KGAUS)=YIELD
C
C*** CALCULATE THE EQUIVALENT NODAL FORCES AND ASSOCIATE WITH THE
ELEMENT NODES
C 190 MGASH=0
DO 140 INODE=1,NNODE
DO 140 IDOFN=1,NDOFN
MGASH=MGASH+1
DO 140 ISTR1=1,NSTR1
TOTPP = PPTOT(KGAUS)
IF (ISTR1 EQ 3) TOTPP=0.0
ELOAD(IELEM,MGASH)=ELOAD(IELEM,MGASH)+BMATX(ISTR1,MGASH)*
(STRSQ(ISTR1,KGAUS)*STRINI(ISTR1,KGAUS)+TOTPP)*DVOLU
140 CONTINUE
40 CONTINUE
20 CONTINUE
C
CALL ACLEAR ( RESID, NTQTV )
C
DO 500 IELEM=1,NELEM
DO 500 IEVAB=1,NEVAB
LMVEB=LEONS(IEVAB,IELEM)
TEMPS = ELOAD(IELEM,IEVAB)
IF ( LMVEB GT NEONS ) TEMPS = -TEMPS
RESID(LMVEB)=RESID(LMVEB) + TEMPS
550 CONTINUE
500 CONTINUE
IF ( NCRIT EQ 5 AND MCALEC EQ 1 ) REWIND 8
C
RETURN
END
```

APPENDIX B

INPUT FOR MATERIAL PARAMETERS

The material parameters required by the soil model are read in the subroutine INPUTD of the program MIXDYN in the following order:

CARD SET 7, MATERIAL CARDS - Three cards for each different material, a total of NMATS*3 cards.

1st Card MATERIAL IDENTIFICATION CARD (15)

Cols. 1-5 NUMAT Material ID number

2nd Card MATERIAL PROPERTIES CARD-(a) (8E10.4)

Cols. 1-10	PROPS (NUMAT, 1)	Young's Modulus
11-20	PROPS (NUMAT, 2)	Poisson's ratio
21-30	PROPS (NUMAT, 3)	Thickness for plane stress problem
31-40	PROPS (NUMAT, 4)	0.
41-50	PROPS (NUMAT, 5)	0.
51-60	PROPS (NUMAT, 6)	0.
61-70	PROPS (NUMAT, 7)	Cohesion
71-80	PROPS (NUMAT, 8)	Friction angle

3rd Card MATERIAL PROPERTIES CARD -(b) (8E10.4)

Cols 1-10	PROPS (NUMAT, 9)	0.
11-20	PROPS (NUMAT, 10)	γ - constant
21-30	PROPS (NUMAT, 11)	δ - constant
31-40	PROPS (NUMAT, 12)	Zero dilatancy line
41-50	PROPS (NUMAT, 13)	A - constant